Thèse de Doctorat de l'Université de Liège
Faculté des Sciences
Unité de Physique Théorique des Matériaux

First principles study of rare-earth nickelates: from bulk to heterostructures

Alain Mercy

présentée en vue de l'obtention du grade de Docteur en Sciences Physique

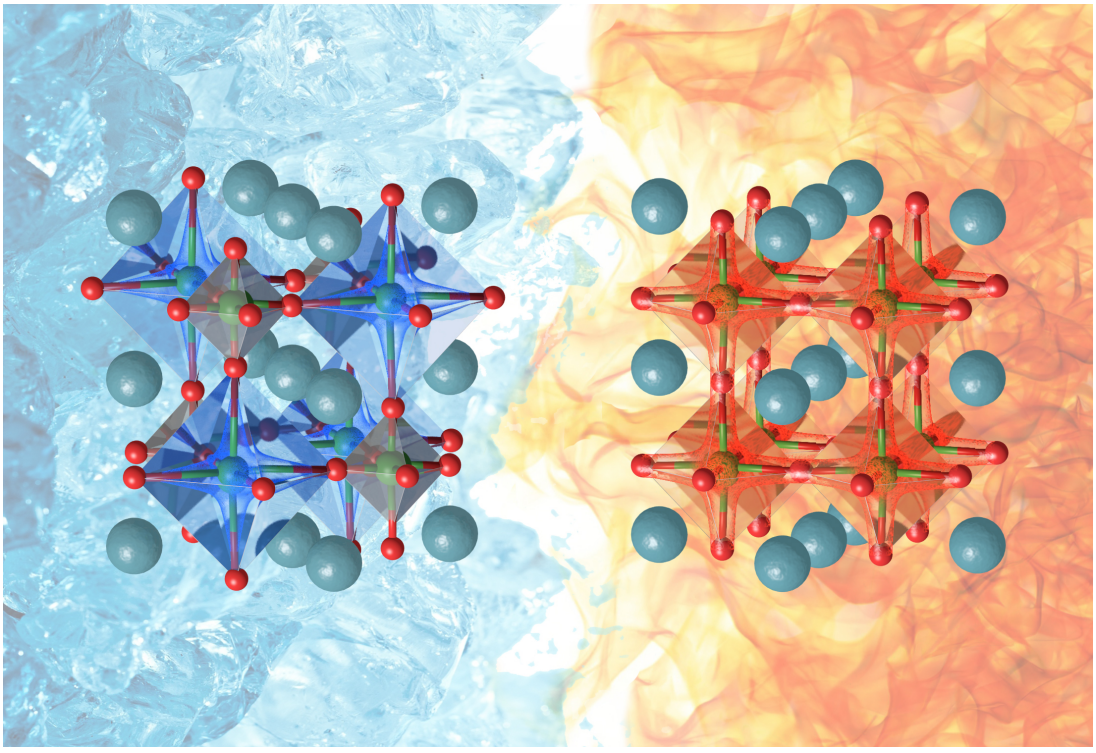

Soutenue en 2020

Directeur:	Philippe	Ghosez
Secrétaire:	Eric	Bousquet
Président:	Matthieu	Verstraete
Examinateurs:	Jorge	Ìñiguez
	Marisa	Medarde
	Bertrand	Dupé

Université de Liège, Département de Physique, Unité Physique Théorique des Matériaux
Allée du six Août, 19 (Quartier Agora) Sart-Tilman, 4000 Liège
Tél : +32 (0)4 366 37 22

Short Table of Contents

Résumé

Le sujet de cette thèse s'est construit en se nourrissant des idées qui ont émergées tout au long de sa réalisation. En effet, au départ, le souhait était d'explorer l'état de l'art pour la famille des nickelates de terre rare dans le but de directement étudier des systèmes complexes comme les hétérostructures dans la perspective de prédire des matériaux pour la micro électronique. L'intérêt se porte sur leur capacité à passer d'une phase métallique à isolante en modifiant la température. Cependant, il s'est très rapidement avéré que la théorie caractérisant ces matériaux, en l'état, n'était pas en mesure d'atteindre cet objectif. Celle-ci ne prenant pas en compte correctement les causes structurelles lors la transition de phase.

Après de longues réflexions au vu des articles existants, le choix s'est porté sur l'étude, dans un premier temps, des nickelates massifs afin de trouver une théorie générale permettant la compréhension de la physique sous-jacente. Pour ce faire, une étude de premiers principes basée sur la théorie de la fonctionnelle de la densité a été menée. Cette étude a été la genèse de la théorie intitulée "l'instabilité de Peierls structurellement déclenchée" permettant d'expliquer la physique de la transition métal-isolant de l'ensemble de la famille. Face au problème posé par les nickelates, cette théorie s'avère révolutionnaire au vu du changement de paradigme au sein du domaine. En effet, en lieu et place d'une approche ne prenant en considération que le comportement des électrons, le choix s'est porté sur la prise en compte des propriétés structurelles **et** électroniques sur un pied d'égalité. Ainsi, il a été montré que ce sont les distorsions structurelles qui poussent les électrons dans une situation favorable pour passer d'un état métallique à isolant. Le comportement de l'ensemble de la famille des nickelates a pu être quantifié à l'aide d'un modèle de Landau construit sur les résultats de premiers principes.

La puissance de cette théorie est telle qu'elle a pu être aisément transposée aux ferrites puis plus généralement aux composés Jahn-Teller. Cette universalité s'avère importante quant à l'approche à entreprendre pour s'attaquer à de tels systèmes. On se rend compte assez aisément qu'une approche en ne considérant que les propriétés de l'atome isolé ne suffit plus.

L'élaboration de cette théorie s'est vue accompagnée d'une étude du magnétisme ainsi que la réalisation de modèles d'Heisenberg caractérisant les propriétés magnétique des nickelates. De plus, par soucis de complétude avec l'expérience, l'analyse des spectres optiques a

été mise en œuvre. Ce laborieux travail de complétion a permis une compréhension poussée des spectres obtenus expérimentalement. Cette analyse appuya l'idée que des modèles simplifiés ne prenant en compte ni les distorsions structurelles ni leur effet sur le comportement électronique ne suffisent pas. De fait, l'effet du champ cristallin se révéla capital pour caractériser le comportement des électrons perturbés par les rayonnements électromagnétiques.

La physique des nickelates étant comprise et validée avec les ferrites, il a été décidé de s'attaquer aux systèmes complexes correspondants à l'idée de départ de cette thèse. C'est dans cette optique que les hétérostructures ont été construites et étudiées à l'aide de la théorie de la fonctionnelle de la densité. En s'appuyant sur le modèle de Landau, il a été démontré qu'en affectant les propriétés structurelles, il est possible de modifier la température à laquelle survient la transition. Ces résultats théoriques sont en accord avec ceux obtenus expérimentalement. L'importance des propriétés structurelles est donc clairement mise en évidence. Cependant, la théorie découverte dans le cadre de cette thèse insiste sur l'obligation de prendre également en compte les causes électroniques de la transition. C'est cette raison qui a amenée à l'utilisation des propriétés électroniques pour ajuster la température de transition à souhait, et même de la doubler. Ce travail concluant cette thèse.

Abstract

The goal of this thesis differs from the one decided at the beginning. Indeed, at first, it was on complex systems such as rare-earth nickelates heterostructures using the available theory. It would have helped experimentalists to predict materials for micro-electronic applications. The focus was set on the metallic insulator phase transition tuning with respect to temperature. However, due to the lack of theory regarding the structural properties, the main objective was unreachable.

Using the literature of that time as an inspiration, the main goal has been refocused toward the discovery of a general theory describing the physics of the metal-insulator phase transition in the nickelates family. To do so, a first-principles study, based on the density functional theory, was carried out. From that point, the "structurally triggered Peierls instability" theory was born. Regarding the nickelates problem, this theory turned out to be a revolutionary new point of view with a change of paradigm inside the field. Indeed, instead of an approach focusing only on the electrons, both electronic **and** structural properties are joined together in an unified approach. Thus, the fact that the structural distortions push the electrons in an advantageous situation to transit from a metallic to an insulator phase has been proven. The whole nickelates family behaviour has been quantified using a suitable Landau model fitted on the first-principles results.

The power of this theory is such that it has been easily transposed to the ferrites and more generally to the Jahn-Teller compounds via the ferrites. This universality turns out to be of high importance regarding the approach to enforce in the fight against such systems. As a matter of fact, considering the properties of isolated atoms is no longer enough.

The elaboration of this theory has been carried out along with the study of magnetic properties and the realization of a Heisenberg model to explain the experimental results. Furthermore, for the sake of comparison with the experimental results, the analysis of the optical spectra have been enforced. This one informs us that the previous models which did not take into account the effect of structural distortion on the electronic behavior are not sufficient. Indeed, the crystal field is crucial to characterize and explain the electronic behavior under optical perturbations.

At this time, the physics of bulk nickelates is understood in a deeper way and validated on ferrites. The next goal is to switch on heterostructures within the density functional theory. Based on the previous Landau model, it has been shown that the transition temperature

is easily modified when affecting the structural properties. Those theoretical results are in line with the experimental ones and the importance of the structural distortion is clearly highlighted. However, this theory also insists on the necessity to also take into account the electronic contribution of the MIT. This is why this electronic contribution was affected to tune the MIT and even split it. This work concludes this thesis.

Remerciements

Je tiens tout particulièrement à remercier Philippe Ghosez de m'avoir offert l'opportunité de réaliser cette thèse. Son attrait pour l'organisation fût pour moi d'un grand intérêt. J'ai eu l'occasion de me découvrir ainsi que de découvrir un monde passionnant rempli d'interrogations. Ce goût pour faire face à cette montagne de questions me fût transmis par Eric Bousquet que je tiens à remercier de tout coeur.

Il va sans dire que je souhaite remercier l'ensemble des collaborateurs, superviseurs et collègues avec qui j'ai pu rentrer en contact et qui m'ont soutenu, guidé et motivé au niveau professionnel. Ainsi, je souhaite remercier Jordan Bieder, Fabio Ricci, Marcus Schmitt, Yajun Zhang, Eric Bousquet, Matthieu Verstraete, Philippe Ghosez, Julien Varignion, Antoine Dewandre, Sébatsien Mawet, Alexandre Martin, Jorge Iniguez, Marisa Medarde, Wen Yi, Ruihao Qiu, Sylvain Petit, Françoise Damay, Jie Wang, Zhaoliang Liao, Nicolas Gauquelin, Manuel Bibes, Gertjan Koster, Claribel Dominguez Ordonez, Jennifer Fowlie, Marta Gibert, Jean-Marc Triscone, Stefano Catalano, Marc Torrent, Sébastien Lemal, Danila Amoroso, Hanen Hamdi, Nicholas Bristowe, William Lafargue-Dit-Hauret, He Xu, Alireza Sasani, Zeila Zanolli, Nicole Helbig, Pedro Melo, Jean-Yves Raty, Andres Camilo Garcia Castro, Hania Djani, Louis Bastogne, Florence Gemine, Carine Garot, Karan Deep, Denis Fontaine et Naihua Miao. Je m'excuse d'avance pour ceux que j'aurais maladroitement oubliés mais depuis quelques années, je ne m'appelle pas bubulle pour rien ;).

Autant au niveau professionnel que personnel, je souhaite remercier un peye français, socialement discutable, nouveau sportif, excellent geek, médiocre gamer, fit, têtu, énervant, attachant, pas net dans sa tête, fatigant, boulanger, masseur et cuistot. Bref Jojo merci pour le bon coup de pied aux fesses en début de thèse ainsi qu'après l'accident et ces excellentes journées passées en ta compagnie. Ce fut TROP BIEN ;). Je suis agréablement surpris et heureux de voir que tu commences à comprendre que le bonheur est en toute chose et qu'il suffit de se poser pour s'en rendre compte. Merci pour ces AOM, CAP, KINE et autres dans le cadre du boulot :D Mes déjeuners préparés le matin me manqueront.

Bien entendu, je ne peux pas ne pas remercier mon second collègue de bureau Alex. J'ai appris à ne pas aimer le hard métal mais apprécier plus profondément la douleur de la course à pied. Un chti est comme chez lui ici et tu en es la preuve. Je suis plus qu'heureux que tu aies pu découvrir les joies de la famille avec Lauranne.

Les collègues de course à pied du Sart-Tilman de longue date tels que Jordan, Antoine

et Alex et de courte date tel que Fabio (éphémère même :p) : encore merci pour ces belles sorties autant froides que chaudes, humides que sèches, dangereuses que sûres.

Amis de calendrier: Toton Fabio, Jojo et Willy la mimole, ce fut un mémorable moment que de me taper une commune honte dans le cadre de la réalisation (merci Antoine pour les photos ;)) du calendrier des physiciens qui se dévoilent. Après ne pas avoir assumé ce calendrier, je prends conscience qu'il en faudrait un nouveau photoshopé :).

Tonton Fabio, je me rends compte que quand je râle je me dis Cristoforo Colombo dans ma tête et ça me sera un traumatisme jusqu'à la fin de mes jours. Tu as intérêt à me ramener de la pana cotta à la maison (surtout au chocolat) car rien que pour ça je me mettrais en ménage avec toi :p. Je pense que nous avons tous les deux été marqués par la possibilité de se faire gronder comme des enfants pour un plan de travail non nettoyé mdr. Surtout, j'apprécierais qu'à l'avenir tu n'oublies pas de mettre du sucre et de la crème dans la sauce bolognaise. C'est dingue que je dois te rappeler les bases ;).

Willy la mimole, tu m'as appris que je n'étais pas très musclé et que je pouvais abandonner l'idée de l'être ;) (mais je suis têtu). Ta rigueur dans la nutrition et ma veulerie dans ce domaine en sont la preuve, je dois le reconnaître. Passer devant le bureau sans faire 15 saluts à la Marry Poppins et un grand Bonjouuuuuuuur du sud me manquent déjà.

Un champion de Labo, un gars avec qui j'ai adoré donner cours. Je regrette ces moments dans la cave a râler et nous rebeller face au système. En tout cas, une chose est sûre: il y a eu du changement mais pas du tout celui auquel on pensait :p. Merci Seb.

Marcus, que de belles discussions et surtout merci de m'avoir fait comprendre que j'avais de riches idées scientifiques et que l'intuition est vraiment quelque chose de génial. Ton approche de la physique fût pour moi un enrichissement sans limite. Ta vision du monde me sera un exemple. J'espère que tu passeras encore de chouettes moments avec Sofia et qu'elle continuera à vous, Hélène et toi, réveiller la nuit :D.

Mon amant, mon tendre chéri, je me dois de te remercier. En effet, au moment où j'ai eu le plus besoin de quelqu'un qui acceptait de s'asseoir à coté de moi à regarder l'évolution des feuilles de noisetiers en silence, tu étais présent sans compter. Quand j'ai souffert comme jamais à la conscience de mon corps meurtri et défectueux, tu as accepté que je l'exprime avec peu de délicatesse quand l'effort devenait vraiment insupportable. De plus, là où l'envie de tout abandonner est arrivée, tu as su trouver les mots simples mais justes. Sans t'en rendre compte, le goût du sport, tu me l'as rendu et c'est ce sport qui m'a sorti la tête de l'eau. Ainsi, c'est à toi que je dois tout cela. Et surtout merci d'avoir épousé une femme aussi douée en massage crânien. Les moments où les maux de tête sont acceptables sont rares mais possible grâce à elle. Je te rappelle que nous ne sommes toujours pas paxé ;). Merci Lou.

Je voudrais remercier l'entièreté de ma famille qui fût présente sans interruption et avec compréhension. Merci à mes parents (directs et indirects), Chloé, mes enfants, tous mes frères et soeurs (de sang et d'alliance ;)), Jeanine, neveux et nièces pour tous ces moments en famille. Se savoir entouré est une chose nécessaire pour l'humain et j'ai la joie de l'être d'une famille formidable ;p. Il y a peu de monde avec qui on sait pouvoir se disputer et

toujours se réconcilier sans en discuter.

Valérie, vous savoir heureux avec Younes et les enfants m'emplit de joie. Même si je l'exprime peu, être parrain d'Inès est pour moi une fierté.

Marjo, je pense que tu as le caractère qui me ressemble le plus. Sans le savoir, tu es un des ciments les plus importants de notre famille. Ta façon de t'exprimer aussi directe nous fait savoir que tu es une personne de confiance et toujours là pour souder la famille.

Merci pour tous ces moments sportifs Phil ;) et surtout les débats philosophiques sur lesquels il nous est impossible de tomber d'accord mais qui nous enrichissent tant. Apprends à te détendre :p A force, tu vas te choper des crampes de cerveaux à argumenter autant :D. Avoir un grand frère se résume facilement: c'est avoir un exemple au quotidien. Merci de m'avoir offert l'opportunité de visiter de si belles contrées à l'île de la Réunion (ou pas, merci Covid-19). Mais surtout, merci d'en revenir afin que l'on puisse se voir plus souvent.

Old bro, Iwan, si je devais te remercier, un livre ne suffirait pas. En attendant, à chaque instant, te savoir heureux me rend heureux. La moitié de ma perception de ce monde dépend de la tienne. Te savoir au soleil amène mon état d'esprit à être lumineux. Surtout n'oublie pas que si je devais avoir confiance en quelqu'un, ça serait toi car depuis ma naissance, je grandis à tes cotés et je connais ta loyauté sans fin ni faille. Une telle joie ne peut être comprise que par peu et je suis heureux de faire partie de ces personnes qui naissent à deux. Avoir une source d'inspiration à ses cotés, depuis le premier souffle de sa vie, ne peut s'expliquer. Cette réussite est pour moi une fierté car j'ai l'occasion de la partager avec toi.

On se doit tous les deux de remercier la vie de nous avoir fait croiser la route du beau gosse du village :D. Brendan, comme un frère, on sait qu'on peut toujours compter sur toi. Que l'on se voit ou non, on sait que tu seras là à la moindre nécessité. Rien que pour cela: merci. À tous les deux: n'oubliez pas de courir car vous devenez mauvais :D. Ta vision du monde et ton audace pour rester en accord avec celle-ci dans la vie de tous les jours est un exemple qu'on imagine ne voir que dans les films. Tout mon respect grand.

Papa, maman, merci d'avoir cru en moi sans perte de conviction là où moi je n'en avais guère plus. Je revois encore ton visage, maman, au coté de celui de Chloé au moment de mon réveil à l'hôpital. Rien que d'y penser les larmes me montent aux yeux et cela m'a confirmé ce que j'ai toujours pensé: j'ai eu l'opportunité d'avoir des parents à l'écoute, compréhensifs et d'une disponibilité sans limite. Ceci n'a pas de prix et j'en ai conscience. Maman, ton choix de te vouer entièrement à nous était très judicieux et je n'aurais pas souhaité qu'il en soit autrement. T'avoir avec nous en permanence fût plus que parfait et nécessaire. Papa, ton parcours est pour moi un exemple et j'ose espérer arriver à la moitié de celui-ci. Je ne te remercierai jamais assez de m'avoir donné le goût du métier manuel autant qu'intellectuel selon un bon équilibre. Merci à vous deux de m'avoir amené là où j'en suis.

Chloé, je ne trouve pas les mots pour décrire mon bonheur à l'idée que l'on partage nos vies. La vie m'a bousculé mais surtout offert la possibilité de me rendre compte à quel point je t'aime et j'ai la chance d'être aimé de toi. Tu m'as offert les plus beaux cadeaux de

tous:Jules et Sofia pour qui je dédie ce travail. On dit que réaliser une thèse, on le fait pour soi. Celui qui a une vision aussi étriquée doit être bien triste. Je le fais certes pour moi mais surtout pour avoir le support suffisant afin de subvenir à vos besoins et en retirer une fierté à travers vous. Ce fut finalement la motivation première dans cette tâche. Sans elle, rien ni personne n'aurait pu me permettre d'aller jusqu'au bout de cette lourde et fastidieuse tâche. Travailler dans un milieu où tous sont convaincus d'être supérieurs n'est pas facile. Au quotidien, vous savoir à l'abri du besoin et heureux m'a permis de tenir. Savoir que ce bonheur familial passait par un effort titanesque de ma part dans le cadre du travail m'a rendu la tâche plus accessible. J'espère trouver ma voie professionnelle afin de m'épanouir complètement. Cependant, sachez qu'au niveau familial, je ne peux espérer mieux car je sais qu'un amour immense m'y attend chaque jour. J'aimerais que ces moments à nous quatre durent à jamais. Sachant que cela ne nous est pas permis, je tente au mieux d'en profiter pleinement malgré les dégats que mon corps (principalement ma tête) a subi et les douleurs ressenties quotidiennement que l'on surmonte ensemble. Souffrir pour rester dans ce bonheur, jamais je ne le regretterai et c'est avec joie que je m'y plonge. Merci à vous trois d'être présents dans ma vie, tout simplement.

Acronyms

Abbreviation	Signification
DFT	Density Functional Theory
BO	Born-Oppenheimer
KS	Kohn Sham
LDA	Local Density Approximation
GGA	Generalized Gradient Approximation
SCF	Self-Consistent Field
BZ	Brillouin Zone
PAW	Projector Augmented Wave
JTH	Jollet Torrent Holzwarth
PBE	Perdew Burke Ernzerhof
PBEsol	Perdew Burke Ernzerhof for Solides
FLL	Fully Localized Limit
DFT+U	Density Functional Theory with Hubbard contribution
DMFT	Dynamical Mean-Field Theory
DOS	Density of States
IFC	Inter atomic Force Constant
DFPT	Density Functional Perturbation Theory
GS	Ground State
MIT	Metal Insulator phase Transition
AFD	AntiFerroDistortive
FM	FerroMagnetic
AFM	AntiFerroMagnetic
PM	ParraMagnetic
M	Metallic
I	Insulator

Part I

Introduction

Introduction

Calcium titanate[1] was first discovered by Gustav Rose who gave it the name of perovskite in memory of the Russian crystallographer Perovski. Nowadays, perovskite is the generic name that refers to crystals of chemical formula ABX_3 where an octahedral cage made by X anions surrounds the B cation (see figure 1). In oxides, corner-shared octahedral cages oxygens at the X site (other cases such as fluorides are also possible[2]) surround B cations located at its center. Usually this B cation is a transition metal with partially filled d electronic levels[3]. In the case of this thesis, I will focus on the nickel cation which has seven electrons over the ten available states in the $3d$ shell. The A cation lies between those cages. In the case of nickelates system, the A cation is a rare earth element ($R = \{La, Pr, ..., Y\}$). Thus, I will study the $R\mathrm{NiO}_3$ oxide family.

The interest for the field of those nickelates compounds relies on their metal-insulator transition and shines through the regularity and the number of reviews[4–7]. First synthesised by Demazeau[8] in 1971, the will to use in practice those materials for electronic device is nowadays realistic[9–11].

The aristotype phase of perovskites is the cubic $Pm\bar{3}m$ phase as depicted in figure 1. A good indicator for the appearance of an eventual structural distortion is the Goldschmidt[12] factor t that is given by

$$t = \frac{r_R + r_O}{\sqrt{2}(r_{Ni} + r_O)} \tag{1}$$

where r_R, r_O, r_{Ni} are the atomic radii of the rare-earth, oxygen and nickel atoms.

If $t < 1$, such as for nickelates[5], the octahedral cages will distort to decrease the distance between the rare-earth and the oxygen (see eq. 1). The main distortions consist of rotations of the octahedral cages around the nickel atom. The origin of those distortions is purely geometric (inert) and does not depend on the properties of the atoms except the size. Thus, to go a step further to understand the complete physics of nickelates, the role of the electrons has to be considered. This is the story of this thesis.

Nickelates exhibit a metal to insulator phase transition[13] (MIT) at a critical temperature T_{MI}. The T_{MI} evolves with the R cation size: the larger the cation is, the lower the T_{MI} is. Experimentally[14, 15], this transition is accompanied by a modification of the structural properties. The distortions consist in a "breathing" of the octahedral cages around the

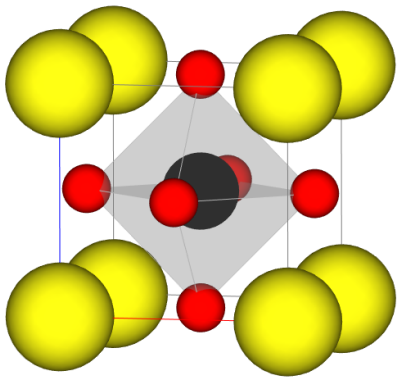

Figure 1 | Cubic $Pm\bar{3}m$ phase of the $YNiO_3$ perovskite compound. R, Ni and O are in yellow, black and red respectively.

nickel atoms according to a rock-salt pattern. This pattern corresponds to one small octahedral cage of oxygen (small nickel) surrounding by large octahedral cages (large nickel) and reciprocally this distortions is linked to a differentiation of the two corresponding nickels.

The physics behind the behaviour of those systems is still under debate[16–18]. Due to the small charge disproportionation between the two nickel sites, both experimentally[19] and theoretically[20] observed, the underlying explanation of the MIT is not trivial. To unveil the physics linked to this MIT is the first main goal of this thesis. It is the reason why I focus on the nickelates compounds.

Experimentally, Medarde et al.[13] clearly observed a correlation between the octahedral rotation distortions and the T_{MI}. Because the distortion depends on the R size, it depends on the tolerance factor t. Thus, the T_{MI} is discussed as a function of the tolerance factor (see figure 2 adapted from Mercy et al.[17]).

The MIT is often associated a site-selective Mott transition[21], explained by a negative charge transfer. This view is supported by calculations[21–24] focusing on the electronic properties with a fixed and non relaxed structural phase. This is questionable since the MIT is concomitant to a structural distortion.

In Mercy et al.[17], I propose to make use of DFT+U calculation in order to treat self-consistently the electronic an structural degrees of freedom. Keeping in mind the close link between the MIT and the structural behaviour experimentally observed, I discovered that the physics of the nickelates phase transition can be explained by a structurally triggered Peierls instability[17]. The key ingredient is that both electronic and structural degrees of freedom have to be treated simultaneously at 0K.

Nowadays, DFT appears as a powerful tool to study the MIT in peroskites[18] and most recent work better discuss the interplay between electronic and structural degrees of freedom.

The MIT seems to be of second order in presence of small rare-earth cation and of first order for the big rare-earths such as Nd and Pr. Concerning the small rare earth cations, Garcia-Munoz et al.[25] observed an additional phase transition. Indeed, at the magnetic

level, $R\mathrm{NiO}_3$ exhibit a transition from a paramagnetic phase to a specific anti-ferromagnetic phase at the Curie temperature ($T_c < T_{MI}$). The magnetic propagator vector is $\left(\frac{1}{4}\frac{1}{4}\frac{1}{4}\right)$ and the magnetic configuration is named S-type (see figure 10.3 page 147) which is mainly characterised by a fourth-neighbours anti-ferromagnetic interaction[26].

In the case of big rare-earth cations, both the metal insulator and the magnetic phase transitions are concomitant ($T_{MI} = T_c$). The appearance of this magnetic phase has been explained by Lee et al.[27] as a nearly nested spin density wave which justifies the first order nature of the transition.

The S-type magnetic configuration has been suggested[28] as having each nickel site magnetic in the low temperature ordered phase. If all the sites are magnetic with two inequivalent magnetic sites, the inversion symmetry is broken and it leads to a ferroelectric phase [29]. This behaviour is allowed near the phase transition as discussed by Gawryluk et al.[30]. However, it has recently been shown that the distinction between a model with and without a magnetic moment on the two inequivalent nickels is not trivial. Indeed, the case without magnetic moment for the nickel in the small octahedral cage is proposed[31] too.

The full phase diagram of bulk Nickelates is summarized in figure 2. The difference between the small and large cation behaviour at MIT is highlighted. Thus, there is only one phase transition ($T_{MI} = T_c$) from a paramagnetic metallic phase (PM-M) to an ordered anti-ferromagnetic insulating phase (AFM-I) for $t_R > t_{Nd}$ and no phase transition for *La*. When $t_R < t_{Nd}$, a new intermediate paramagnetic and insulating phase (PM-I) appears (between T_c and T_{MI} with $T_c < T_{MI}$). In this thesis, I will study the whole phase diagram with a strong focus on the MIT portion highlighted by the black arrow.

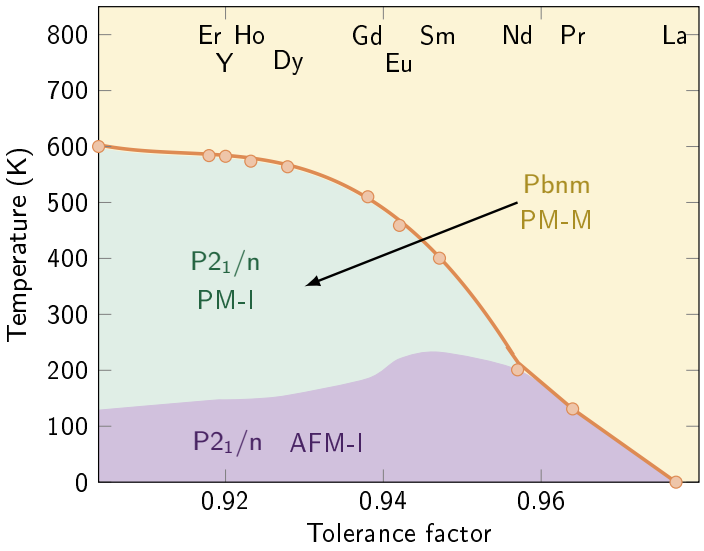

Figure 2 | Phase diagram for the bulk Nickelates family. In yellow, the paramagnetic metallic phase (PM-M). In green, the paramagnetic and insulating phase (PM-I). In purple, the S-type ordered antiferromagnetic insulating phase (AFM-I)

To monitor and modulate the physical properties such as the discussed MIT and mag-

netic phase transition, instead of bulk system, thin film are used. Indeed, the T_{MI} is sensitive to external perturbations (e.g. external pressure[4], internal pressure[32] (chemical), strain constrain[6], light illumination[33], electric field[34]) more easily applicable to such geometries. Another interesting way to deal with the change of T_{MI} is the solid solution[35] that allows to adjust the rare earth atomic composition to explore a wide range of tolerance factors directly linked to the T_{MI}.

A new approach consists of taking advantage of ordered heterostructure in two different ways. The first one plays with the octahedral cage rotations to affect the T_{MI} in ordered systems. It is the Tilt Control Layer (TCL) technique[33]. The second one modifies the electronic properties of the system to affect the T_{MI}[36]. Those two ways to work on heterostructure are the second main goal of this thesis which is a great step to reach usable electronic device in practice. Recently, Georgescu et al.[37] managed to play on both electronic and structural parameters.

In this thesis, after giving brief overview of the theoretical framework (see chapter 1), I will focus on the physics behind the MIT (see chapter 4), the optical properties (see chapter 5) and the magnetism (see chapter 6) to theoretically unify the nickelates behaviour. Then, this general theory will be extended to the ferrites family (see chapter 7) for the sake of transportability. This study will be the opportunity to extend our theory to the famous Jahn-Teller family[38] to review the paradigm of those systems: the system has to be seen as a whole and not focused on the individual properties even if useful as a first thought. Using heterostructures, I will prove that both structural (see chapter 8) and electronic (see chapter 9) properties can be used to tune T_{MI}. At the end, the general conclusion (see chapter V) is dispensed.

Part II

Theoretical background and methods

1 | Density Functional Theory

This chapter is devoted to the theories and methods used to study Nickelate compounds but not only. Because of the large amount of books, e.g. [3, 39–41], I can not be exhaustive. However, I will give the necessary informations to understand the results obtained in this thesis.

When one wants to study a system composed by atoms (electrons and nuclei) at nano scale, one has to go beyond classical physics such as Newton. This classical theory fails to describe such systems. To try to be predictive at this microscopic level, one has to solve the Schrödinger equation which is the core of the modern quantum physics[42]. To be able to work on complex systems (more than two electrons), some approximations are needed and the formalism is adapted. Here, starting with that famous equation, I will address the Density Functional Theory (DFT).

This chapter is organised as follow. I will explain how to go from the complex Schrödinger equation to solvable DFT equations. The consequences of the applied approximations will be addressed too. Moreover, after this first section, I will shortly introduce some useful crystal properties such as metal, insulator, phase transition and magnetism.

In this thesis, I decided to use the code named **Abinit**[43–45] which implements the DFT formalism to calculate properties for Nickelates compounds. The details of usage of this code will be addressed step by step among the theory in separated boxes. For those who are less interested about the **Abinit** tool, you can skip those boxes.

1.1 From intractable Schrödinger equation to solvable DFT equations

1.1.1 Schrödinger for solids: a many body problem

To study and understand the physics behind matter (such as Nickelate compounds e.g.), one has to remember that the goal is to study material systems at atomic scale. One consists of N_e electrons and N_i nuclei. Those particles are described by a distribution function $\Psi(\overrightarrow{r}, \overrightarrow{R})$ where electrons are distributed at the positions $\overrightarrow{r}$ ($\overrightarrow{r} = \left\{\overrightarrow{r_i}\right\}$, $i = 1, ..., N_e$) and nuclei at the positions $\overrightarrow{R}$ ($\overrightarrow{R} = \left\{\overrightarrow{R_k}\right\}$,$k = 1, ..., N_i$)). The probability P to find a set of particles in a given state is directly linked to this distribution function and given by $P = \left|\Psi(\overrightarrow{r}, \overrightarrow{R})\right|^2$. Here, the

nuclei can be considered as an entity by itself neglecting the subnuclear interactions so that they are characterised just by their mass, size and charge. However, the reason why this entity is assumed stable is not the goal of this thesis and has to be accepted. In other words, the Coulombic interaction and the kinetic energy are the only relevant terms for our study.

The equation to be solved at the microscopic level to obtain the stationary ground state of a system of N_e electrons and N_i nuclei is the time-independent (the Hamiltonian has no explicit time dependency) Schrödinger equation:

$$\hat{H}\Psi(\overrightarrow{r},\overrightarrow{R}) = E\Psi(\overrightarrow{r},\overrightarrow{R}) \tag{1.1}$$

where E is the total energy and H is the Hamiltonian. This Hamiltonian describes particles and the interaction between those particles. For the present systems, it is

$$\hat{H} = \hat{T}_i + \hat{T}_e + \hat{U}_{ie} + \hat{U}_{ee} + \hat{U}_{ii} \tag{1.2}$$

where $\hat{T}_i$ and $\hat{T}_e$ are the kinetic energy operators of the nuclei and electrons respectively, $\hat{U}_{ie}$, $\hat{U}_{ee}$ and $\hat{U}_{ii}$ are the Coulombic interaction between nuclei-electrons, electrons-electrons and nuclei-nuclei respectively. All the operators only apply on electrons and nuclei states. They can be expressed in atomic unit (a.u.) as[1]

$$\hat{T}_e(\overrightarrow{r}) = -\sum_{i}^{N_e} \frac{1}{2}\nabla^2_{\overrightarrow{r_i}} \tag{1.3}$$

$$\hat{T}_i(\overrightarrow{R}) = -\sum_{k}^{N_i} \frac{1}{2M_k}\nabla^2_{\overrightarrow{R_k}} \tag{1.4}$$

$$\hat{U}_{ii}(\overrightarrow{R}) = \sum_{k<k'}^{N_i} \frac{Z_k Z_{k'}}{\left|\overrightarrow{R_k} - \overrightarrow{R_{k'}}\right|} \tag{1.5}$$

$$\hat{U}_{ee}(\overrightarrow{r}) = \sum_{i<i'}^{N_e} \frac{1}{\left|\overrightarrow{r_i} - \overrightarrow{r_{i'}}\right|} \tag{1.6}$$

$$\hat{U}_{ie}(\overrightarrow{R,r}) = -\sum_{j,k}^{N_e,N_i} \frac{Z_k}{\left|\overrightarrow{r_j} - \overrightarrow{R_k}\right|} \tag{1.7}$$

Because the nucleus mass is much larger than the electronic one ($M \gg m_e$), the electronic system adiabatically adapts its distribution to nuclei arrangement[2]. Therefore, the nuclei kinetic energy $\hat{T}_i$ can be neglected in the Hamiltonian. This is the famous and so called Born-Oppenheimer (B-O) approximation[46]. At this stage, there is no differential operator on the nuclei positions ($\overrightarrow{R}$). Thus, $\overrightarrow{R}$ can be considered as an imposed parameter to solve the electronic Schrödinger equation. In other words, the electronic configuration can be

[1] I will use the atomic unit, i.e. m_e=$\hbar$=e=1 where m_e is the electron mass, $\hbar = \frac{h}{2\pi}$ for which h is the Planck constant and e^- is the electron charge.

[2] the kinetic energy is equal to zero and can be treated as a perturbation

calculated for a given set of nuclei position. The Hamiltonian can be rewritten in terms of a nucleic contribution and an electronic contribution as

$$\hat{H} = \hat{H}_{el} + \hat{H}_i \tag{1.8}$$

where $\hat{H}_i$ is a constant. $\hat{H}_{el}$ is the associated electronic part still to be solved and reads

$$\hat{H}_{el} = \hat{T}_e + \hat{U}_{ee} + \hat{U}_{ei} \tag{1.9}$$

Because of the parametrisation in term of $\overrightarrow{R}$, the Coulombic interaction between nuclei is a constant. It is the reason why it is not written in the electronic Hamiltonian[3]. However, if it is zero, only systems with the same nuclei distribution can be compared.

The final consequence of the B-O approximation is the total wave function can be rewritten as a product of two independent wave functions (electrons and nuclei)[4]:

$$\Psi(\overrightarrow{r}, \overrightarrow{R}) \approx \Psi_e(\overrightarrow{r})\Psi_n(\overrightarrow{R}) \tag{1.10}$$

where $\Psi_e(\overrightarrow{r})$ is the electronic wave function for a given nuclei distribution $\Psi_n(\overrightarrow{R})$. The associated Schrödinger equation to be solved as a many-body problem is given by

$$\left(-\sum_i^{N_e} \frac{1}{2}\nabla^2_{\overrightarrow{r_i}} - \sum_k^{N_i} \frac{1}{2M_k}\nabla^2_{\overrightarrow{R_k}} + \sum_{k<k'}^{N_i} \frac{Z_k Z_{k'}}{\left|\overrightarrow{R_k} - \overrightarrow{R_{k'}}\right|} + \sum_{i<i'}^{N_e} \frac{1}{\left|\overrightarrow{r_i} - \overrightarrow{r_{i'}}\right|} - \sum_{j,k}^{N_e,N_i} \frac{Z_k}{\left|\overrightarrow{r_j} - \overrightarrow{R_k}\right|} \right) \Psi_e(\overrightarrow{r}) = E_{el}\Psi_e(\overrightarrow{r}) \tag{1.11}$$

Due to the complexity of this equation (caused by the electron-electron interaction), one can not solve it. In the next section, I will introduce a new and more tractable approach for real usage.

[3] In the **Abinit** code, the ion-ion Coulombic interaction is in the electronic contribution but not written for the sake of simplicity.

[4] Despite this approximation, I would like to insist both electronic and nuclei distribution are important to understand the physics

In the Abinit world #1 Structural Parameters

To make the numerical calculations to study systems composed of electrons and nuclei, I use a Code named **Abinit**[43–45]. The electronic problem is solved at fixed nuclei position thanks to the B-O approximation. To do so, I have to give the nuclei position and their properties (mass and charge) to the code.
In the Input file of **Abinit**((see Table 1.1), The number of atoms is given by the *natom* flag. Then, the number of types of atoms is informed thanks to the *ntypat*.

natom	5
ntypat	3
znucl	39 28 8
typat	1 2 3 3 3

Table 1.1 | An example of **Abinit** input for $YNiO_3$ cell composition

To know we have different kinds of atoms is not sufficient. I have to explicitly inform the code what are those atoms thanks to their nuclei charge with *znucl* that has to be repeated *ntypat* times to remain consistent (see Table 1.1). To announce to the code the order of atoms, I will use *typat* repeated *natom* times.
You can see on Table 1.1, an example of an input file with the above parameters.

1.1.2 Density Functional Theory

The many-body electronic wave function is complicated because it is a function of 3 N_e variables. At this stage, solving it for systems such as Nickelates with more than two electrons is impossible. Hohenberg, Kohn and Sham[47, 48] reassessed the problem using a new formalism and a new approach to deal with such systems. Hohenberg and Kohn[47] demonstrated two fundamental theorems for the present theory.

Hohenberg and Kohn[47] Concerning the first theorem, they proved the density of the system $n(\overrightarrow{r})$ is uniquely defined in presence of an external potential $V_{ext}(\overrightarrow{r})$. Thus, they explicitly mentioned the energy of the system can be referred to a unique functional of the density that is given by

$$E_{el}[n(\overrightarrow{r})] = \int V_{ext}(\overrightarrow{r})n(\overrightarrow{r})d\overrightarrow{r} + F[n(\overrightarrow{r})] \tag{1.12}$$

where the electron-nucleus Coulombic interaction is usually defined in the external potential term $V_{ext}(\overrightarrow{r})$. In the functional term $F[n(\overrightarrow{r})]$, the Coulombic interaction and the unknown kinetic contribution of the electrons are contained. Nevertheless, due to the non trivial form of those two last terms, it is impossible to write the equation for the system of interest.

The second theorem states the ground state electronic density minimizes the energy functional $E_{el}[n(\overrightarrow{r})]$ of the system.

$$E_0[n_0(\overrightarrow{r})] = \min_n \left\{E_{el}[n(\overrightarrow{r})]\right\} \tag{1.13}$$

where $n_0(\overrightarrow{r})$ is the electronic density of the ground state.

This minimisation is of high importance because if it is possible to get the lowest total energy, the related density is the ground state one.

Even if we have changed the formalism (density instead of wave function), the equation is still unsolvable. Indeed, the expression of the kinetic energy as a functional of the density is unknown. To be able to solve this system with this new formalism, we have to go a step further.

Kohn and Sham[48] Because the density $n(\overrightarrow{r})$ is uniquely defined for the given nuclei configuration through $V_{ext}(\overrightarrow{r})$, they[48] suggested that there is an artificial system of independent particles having the same density. It allows to work with N_e functions $\phi_i(\overrightarrow{r})$ of 1 variable where $\overrightarrow{r}$ is limited to the 3 space coordinates instead of 1 tricky $\Psi_e(\overrightarrow{r})$ function of N_e variables. In other words, thanks to this *ansatz*, one works with independent Kohn-Sham electron wave functions $\phi_i(\overrightarrow{r})$. The problem previously induced by the complicated form of the wave function $\Psi(\overrightarrow{r}, \overrightarrow{R})$ clearly disappears[5]. To give the same density as for the real system, the independent particles have to be immersed in the external potential and an effective potential $V_{eff(\overrightarrow{r})}$ such that

$$\left(V_{ext}(\overrightarrow{r}) - \frac{\nabla^2}{2} + V_{eff}(\overrightarrow{r})\right)\phi_i(\overrightarrow{r}) = \epsilon_i\phi_i(\overrightarrow{r}), \forall i \in \{1, ..., N_e\} \tag{1.14}$$

which is a classical eigenvalue problem. The resolution of the problem is now replaced by this resolution of N_e equations instead of one complicated equation. Thus, the Kohn-Sham

[5] One will have to remember the density is relevant for the physics of our problem but not the wave functions $\phi_i(\overrightarrow{r})$

equations to be solved are

$$\begin{cases} \left(V_{ext}(\overrightarrow{r}) - \dfrac{\nabla^2}{2} + \displaystyle\int \frac{n(\overrightarrow{r}')}{\left|(\overrightarrow{r}' - \overrightarrow{r})\right|} d\overrightarrow{r}' + \frac{\delta E_{xc}[n(\overrightarrow{r})]}{\delta n(\overrightarrow{r})} \right) \phi_i(\overrightarrow{r}) = \epsilon_i \phi_i(\overrightarrow{r}), \forall i \in \{1, ..., N_e\} \\ n(\overrightarrow{r}) = \displaystyle\sum_i^{N_e} \phi_i^\star(\overrightarrow{r}) \phi_i(\overrightarrow{r}) \end{cases} \tag{1.15}$$

The energy functional for this equivalent independent particles system is given by[6]

$$E_{el}[n(\overrightarrow{r})] = \int V_{ext}(\overrightarrow{r}) n(\overrightarrow{r}) d\overrightarrow{r} - \sum_i^{N_e} \int \phi_i^\star(\overrightarrow{r}) \frac{\nabla^2}{2} \phi_i(\overrightarrow{r}) + \frac{1}{2} \int \int \frac{n(\overrightarrow{r}) n(\overrightarrow{r}')}{\left|(\overrightarrow{r} - \overrightarrow{r}')\right|} d\overrightarrow{r} d\overrightarrow{r}' + E_{xc}[n(\overrightarrow{r})] \tag{1.16}$$

At this level, the kinetic energy contribution and the Coulombic interaction term of independent particles is easy to evaluate. However, this contribution is the one of independent particles and not the one of the real system. The interacting part of both kinetic and Coulombic terms has to be added in another contribution called the correlation term included in $E_{xc}[n(\overrightarrow{r})]$ which is the tricky part. The exact form of this correlation contribution to keep the density of the artificial system equals to the real one is actually unknown. However, if it was known, a solvable system of equations is obtained. Despite the impossibility to get the exact correlation term, several approximations have been proposed. Fock[49] gives the exact form of the exchange contribution. Nevertheless, in practice, it is laborious to calculate. Thus, it will be approximated and added to the correlation contribution in the so called exchange correlation term $E_{xc}[n(\overrightarrow{r})]$.

Exchange Correlation term The most commonly used is the Local Density Approximation (LDA) [50]. The exchange-correlation functional reads

$$E_{xc}^{LDA}[n(\overrightarrow{r})] = \int n(\overrightarrow{r}) E_{xc}^{hom}[n(\overrightarrow{r})] d\overrightarrow{r} \tag{1.17}$$

where $E_{xc}^{hom}[n(\overrightarrow{r})]$ is the energy of a homogeneous electronic gas. The LDA means the electronic density is supposed homogeneous around a given space point $\overrightarrow{r}$[51]. However it is important to notice the density still depends on the position. Furthermore, the environment at each $\overrightarrow{r}$ is different.

As an extension, Perdew et al.[52] have created the Generalised Gradient approximation (GGA). Its main goal is to take into account the variation of the neighbourhood density like

[6] The kinetic contribution of this system should be written as $T_e[n(\overrightarrow{r})]$ to be a functional of the density. However we do not know the form of this term. Because of the simplicity of solving this term applied on independent wave function, I keep it in this form.

$$E_{xc}^{GGA}[n(\overrightarrow{r})] = \int n(\overrightarrow{r}) E_{xc}\left[n(\overrightarrow{r}), \left|\nabla n(\overrightarrow{r})\right|, \left|\nabla^2 n(\overrightarrow{r})\right|\right] d\overrightarrow{r} \tag{1.18}$$

Because we do not know the exact form of this exchange correlation term except for the homogeneous electron gas, there is no warranty this approximation is better than the LDA one.

Self-consistent resolution The resolution of the Kohn-Sham equations is made following the variational method (see eq. 1.1.2). The energy of this ground state can be reached in a self consistent approach (Self-Consistent Field (SCF) procedure).

In the initialisation step (in black in figure 1.1), the structural parameters to create the external potential $V_{eff}(\overrightarrow{r})$ are provided. From random wave functions, a first density guess is initialized using equation 1.1.2.

Then, the loop starts the SCF calculation (yellow loop in figure 1.1). From the electronic density, the potential $V_{eff}(\overrightarrow{r})$ discussed in the equation 1.1.2 is calculated. It allows to solve the Kohn-Sham equations (see equation 1.1.2). From the new Kohn-Sham independent particles wave functions, the new density is calculated. If the difference between the two last obtained densities does not reach the chosen tolerance, the density is not converged and the loop iterates. To avoid divergence, the next density for the next iteration consists of a mixing of the previous one and the new density.

If the calculation is converged, the loop exits (in red in figure 1.1).

Here, I introduced the DFT formalism. It is to remind there are different approaches to deal with solids such as Hartree-Fock [49, 53] with the Slater[54] determinant producing a full antisymmetric wave function of independent particles to get an exact exchange contribution or Hybrid[55] (mixing DFT and exact Hartree-Fock) e.g. to fight with electronic problem.

The DFT formalism with to the Kohn Sham *ansatz* is useful to study solids. Even though this mathematical formalism is solvable, it is quite time consuming[7] for a large system. The main reasons are the number of electrons with different behaviour. Moreover, the integrals that are in theory infinite and continuous have to be discretized in practice. In the next section, I will unveil the way to deal with these problems.

[7] Even a long thesis has to be done during a limited and finite period of time

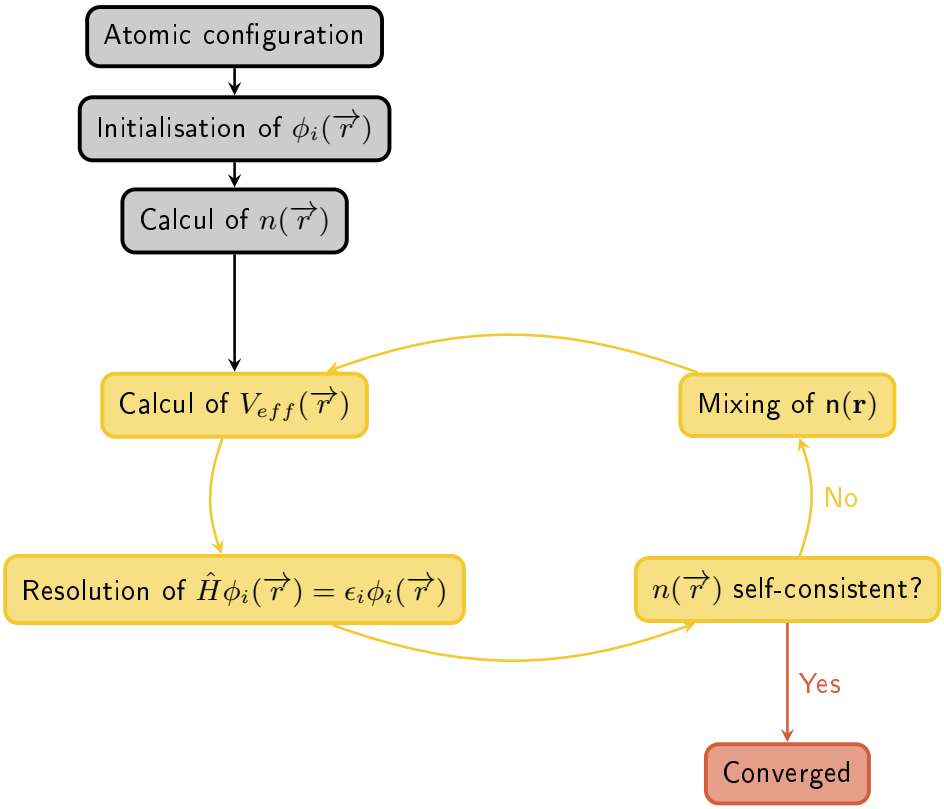

Figure 1.1 | Schemas of the SCF procedure. In black, the initialisation step. In yellow, the SCF loop with criterion. In red, if the criterion is satisfied, the last step.

In the Abinit world #2 Minimizing the energy

The choice of the convergence criterion is usually imposed on the density. However, in **Abinit**, this tolerance can be forced on the wave functions ($tolwfr$), the potential ($tolvrs$), the forces ($toldff$) or the energy ($toldfe$ in Hartree in Table 1.2) too. In case of non convergence and to avoid an infinite loop[a], a maximal number of step must be imposed via *nstep*.

$toldfe$	10^{-10}
$nstep$	200

Table 1.2 | An example of **Abinit** choice of criterion for the SCF cycle on the energy.

[a] Or at least until you get a message from the (High Performance Computer) HPC job scheduler.

1.2 Periodic discrete system

1.2.1 First Brillouin Zone

From now on, I will focus on crystals: systems for which a specific atomic pattern is periodically repeated along the three space directions[41]. The smallest pattern to describe the entire crystal is named the primitive cell. Coming from the theory of diffraction[41], in correspondence to the real space, an analogous reciprocal space can be defined exploiting the idea of Bloch [41] to describe the periodic properties of a crystal. Bloch[41] demonstrated the wave function is a product of a periodic function and a plane wave such as

$$\Psi_{\vec{k}}(\vec{r}) = e^{i\vec{k}\cdot\vec{r}}\, u_{\vec{k}}(\vec{r}) \tag{1.19}$$

where $\vec{k}$ is a vector of the reciprocal space also called wave vector, $e^{i\vec{k}\cdot\vec{r}}$ is a plane wave and $u_{\vec{k}}(\vec{r})$ a periodic function. The vector $\vec{k}$ is directly linked to a given electronic distribution in real space which is described by its wave length $\lambda = \frac{2\pi}{|\vec{k}|}$. In theory, all the electronic distributions in space are possible implying that the number of $\vec{k}$ vector to be treated is infinite. However, thanks to the periodic discretization of the atoms in real space, the reciprocal space can be restricted to a single called the Brillouin Zone (BZ)[41]. Taking a k-point from any another zone does not add any information.

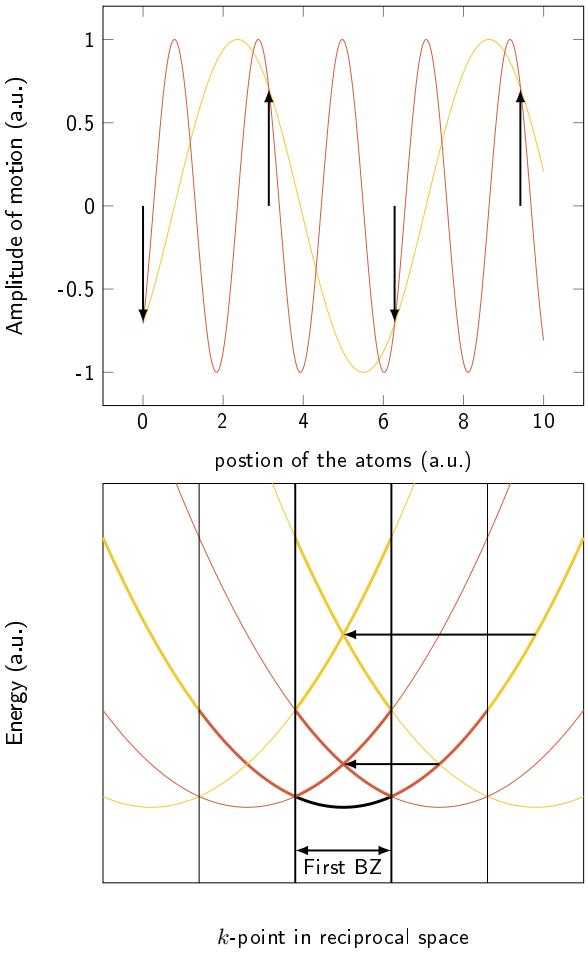

Figure 1.2 | Top: Description of atomic motions (Black arrow) in real space in the case of a linear chain with a wave function inside the Brillouin Zone (yellow) and another one from outside (Red). Bottom: Energy for the free electron in reciprocal space with first BZ highlighted. The folding in the first BZ for the center is described by the arrows.

In this paragraph, I slightly digress to explain the concept of the Brillouin zone thanks to the atomic motions. The top picture in figure 1.2 shows a case of collective atomic displacements in a linear mono atomic chain correctly described with either one k-point in the Brillouin zone (yellow curve) or one k-point from another zone (red curve). The first one has the largest λ able to correctly characterize the atomic pattern and belongs to the First Brillouin zone. For the sake of simplicity, this zone is centered around $\Gamma = (0, 0, 0)$.

Coming back to the electronic distribution, the energy dispersion of the free electrons $E(k) = \frac{k^2}{2}$ is depicted in the lower sketch of figure 1.2. The solution of the Schrödinger equation for the free electrons[41] are plane waves that will be of main use in the next section. As for the atoms, all the information is in the first Brillouin zone. The whole parabola is available inside it: it is folding in the first Brillouin zone as highlighted with the arrows in figure 1.2.

In the most general case (no plane wave), the complete description of any electronic behaviour can be restricted to the first BZ. This description gives the electronic band structure

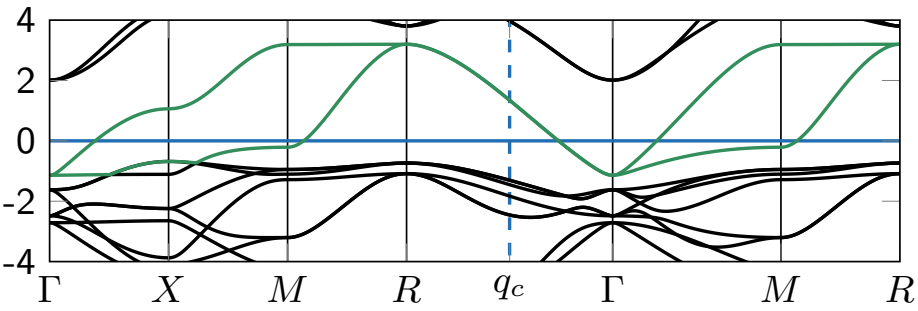

Figure 1.3 | Example of band structure in the first 3D Brillouin zone for $YNiO_3$ in the cubic phase (see Supplementary in chapter 10 for details).

as in the example shown in picture 1.3.

Taking into account all the previous considerations, for a system of independent particles as the Kohn-Sham states, the i^{th} wave function integral is limited over the first Brillouin zone

$$\phi_i(\vec{r}) = \int_{BZ} e^{i\vec{k}\cdot\vec{r}} u_{i\vec{k}}(\vec{r}) d\vec{k} \tag{1.20}$$

In practice, this integral is evaluated using a summation restricted to a discrete number of k-points.

$$\phi_i(\vec{r}) = \sum_{\vec{k}}^{BZ} e^{i\vec{k}\cdot\vec{r}} u_{i\vec{k}}(\vec{r}) \tag{1.21}$$

The finite set of k-points inside the first Brillouin zone is chosen by defining the grid of k-points. Methods to sample the BZ have been developed by Monkhorst and Pack[56] e.g..

The mathematics coming into play for a periodic system ease the solution of the problem. In the following, I will present one basis used to construct crystal thanks to the plane waves.

In the Abinit world #3 Brillouin Zone

The number of k-point which is necessary to correctly simulate the physics of our studied system has to be determined. Step by step, the number of k-point[a] is increased and when the difference of the total energy, e.g., between the chosen grid of k-points and a calculation with a huge grid (impossible to use for all the calculations because of the simulation

time), is small enough to obtain the desired physical properties, the calculation is said to be "converged". Thus, some convergence tests have to be realised.

To set the number of k-point in the Brillouin zone along each reciprocal space direction, the flag *ngkpt* is used as in the example on Table 1.3. However, because of the crystal symmetries, the number of k-points to treat can be decreased. Indeed, the k-point giving the same results by symmetry are considered only once. To do so, the *kptopt* flag determined the symmetry operations that have to be applied and for which the default value (1) takes into account all the symmetries.

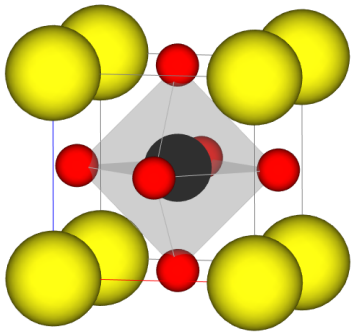

Figure 1.4 | Cubic phase of the $YNiO_3$ Perovskite compound. Y, Ni and O are in yellow, black and red respectively.

acell	1.0	1.0	1.0
rprim	7.12	0.0	0.0
	0.0	7.12	0.0
	0.0	0.0	7.12
xred	0.0	0.0	0.0
	0.5	0.5	0.5
	0.0	0.5	0.5
	0.5	0.0	0.5
	0.5	0.5	0.0
ngkpt	12	12	12
kptopt	1		

Table 1.3 | An example of **Abinit** input with the atomic position in the repeated box and the linked grid of k-point.

[a] Be sure all the other parameters are converged to avoid correlated problem

1.2.2 Basis for the Kohn-Sham wave functions

Because the electronic interactions are screened by the other electrons and nuclei in space, their distributions are limited in space and thus the number of k-points of interest is limited too. The i^{th} Kohn-Sham wave function reads

$$\phi_i(\overrightarrow{r}) = \sum_{\overrightarrow{k}}^{BZ} e^{i\overrightarrow{k}\cdot\overrightarrow{r}} u_{i\overrightarrow{k}}(\overrightarrow{r}) \tag{1.22}$$

The periodic function $u_{\overrightarrow{k}}(\overrightarrow{r})$ of the i^{th} Kohn-Sham wave function is expanded on a plane waves basis such as

$$u_{i\overrightarrow{k}}(\overrightarrow{r}) = \sum_{\overrightarrow{G}} e^{i\overrightarrow{G}\cdot\overrightarrow{r}} u_{i\overrightarrow{k}}(\overrightarrow{G}) \tag{1.23}$$

where $\overrightarrow{G}$ is a vector of the reciprocal space and is a combination of the three primitive vectors.

The i^{th} Kohn-Sham wave function finally reads

$$\phi_i(\overrightarrow{r}) = \sum_{\overrightarrow{k}\,\overrightarrow{G}}^{BZ} e^{i(\overrightarrow{k}+\overrightarrow{G})\cdot\overrightarrow{r}} u_{i\overrightarrow{k}}(\overrightarrow{G}) \tag{1.24}$$

This series 1.23 is convergent in theory. In practice, because the electronic distribution in real space does not oscillate at an infinite frequency, plane waves that oscillate too much are neglected and the series is truncated.

As shown in picture 1.5 for the plane waves, due to the energy dispersion $E(G) = \frac{G^2}{2}$, the bigger the $\overrightarrow{G}$ vector is, the higher the corresponding energy is. For a given $\overrightarrow{k}$ vector, the linked $\overrightarrow{k} + \overrightarrow{G}$ vector describing the oscillation increase too. Once the desired accuracy to describe the electron distribution is reached, the summation over $\overrightarrow{G}$ is truncated. Here, the limitation of the plane waves basis is discussed for the chosen grid of k-point[8]. Thus, for a given k-point of the first Brillouin zone, one has $\frac{\left|\overrightarrow{k}+\overrightarrow{G}\right|^2}{2} <$ cutoff Energy as a basis.

Concerning the discussion of the first Brillouin zone, I would like to show that, thanks to picture 1.5, all the informations concerning the energy dispersion are available inside it. As mentioned in the previous section, the parabola is folding in the first Brillouin zone. For

[8] For each k-point, the energy cutoff is different. When, in practice, you test the needed value of the cut-off energy, be careful you have a big enough grid of $k$point on which you test it! In other words, as always, when you test a parameter, be sure the others are converged

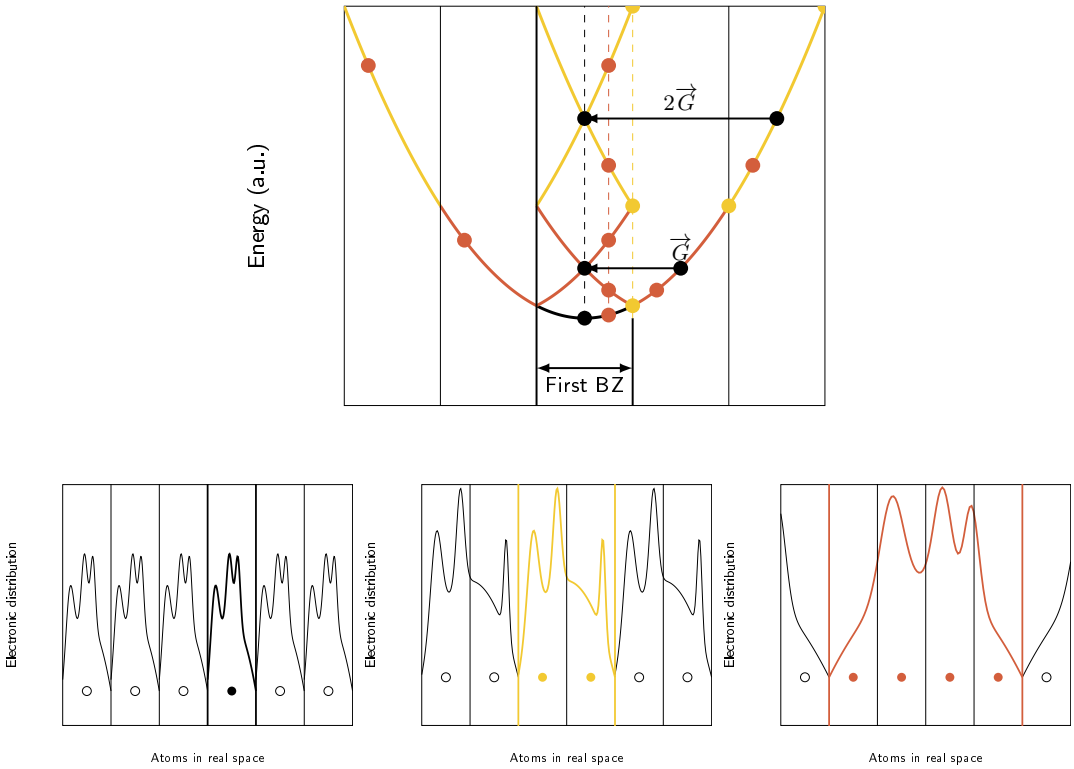

Figure 1.5 | Top: Energy dispersion of the plane waves basis. In black, the bullets corresponding to the center of zone. In yellow, the ones corresponding to the zone border. In red, the intermediate case at the middle of the two others. Bottom: From left to right are the corresponding electronic distribution to be described with the corresponding basis in real space for the black, yellow and red bullets from the energy dispersion respectively.

a given k-point, the expansion of the plane wave basis is limited to a cutoff energy. The energy corresponding to the chosen number of plane waves as basis for a given k-point are highlighted by bullets in figure 1.5 along with their equivalents out of the first BZ. The higher the last chosen energy is (i.e. bullets), the more oscillating the plane wave is. Even if the information of the energy dispersion is available in the first BZ, looking at eq. 1.23, the summation is truncated on the $\vec{G}$ vector. So, in practice, one has to work on the whole reciprocal space delimited by the cutoff energy.

As discussed in the previous section, each k-point corresponds to different spatial electronic distribution. In picture 1.5, three k-points are discussed. Γ is the center of the zone and corresponds to the dashed black line that describes an electronic distribution $u_{i\vec{0}}(\vec{G})$ limited to one primitive cell and repeated in all three directions. To correctly describe this distribution, a number of plane waves corresponding to the black bullets are taken into account. If the electronic distribution is limited to two cells (yellow in figure 1.5), the used plane waves are the ones linked to the yellow bullets in the first BZ. The third case correspond to a periodic electronic distribution spread on four cells for which the basis of plane waves is given by the red bullets.

Although both the basis and the number of k-points are limited, it is still hard to get

accessible properties in human time due to the behaviour of some electrons: the ones close to the nuclei named core electrons and electrons far from the nuclei named valence electrons which are responsible for the bond between two atoms. The core electrons oscillates too much to be described with a reasonable number of plane waves. In opposite, the valence electrons distribution needs less plane waves to be described. The next section introduces the approximations to override those problems.

In the Abinit world **#4** Plane Wave Basis set

The flag to set the number of plane waves for the basis is *ecut* in Hartree by default.

```
ecut  20
```

Table 1.4 | An example of **Abinit** input with the energy cutoff (Hartree).

1.2.3 Core electrons and smoothing

The needed energy cutoff can be hard to reach in practice because the core electrons (close to the nuclei) are oscillating in a too fast way. To overpass this problem, two approximations are used in two different approaches explained in the following paragraphs.

Pseudopotential The first approximation is the frozen core approximation. Because the electrons close to the nuclei are not supposed to play a main role in the chemical properties of the materials (eg. they are not responsible for the bonds), it is assumed that they keep their properties as for the isolated atom[9]. It allows us to precalculate them and thus decrease the needed energy cutoff to describe the valence electrons.

The second one is about the valence electrons (assumed important for the study of a material) that still oscillate much around the nuclei (see picture 1.6). To deal with this issue, the potential of those electrons is smoothed around the nuclei and is called the pseudopotential. The most famous pseudopotential is the Norm-Conserving one: despite the modification of the potential, the norm of the wave function is preserved. In the next paragraph, another approximation which is supposed to better describe the local properties around the nuclei is discussed.

[9]It is not obvious to distinguish and define core and valence electrons because it depends on the desired properties and external conditions

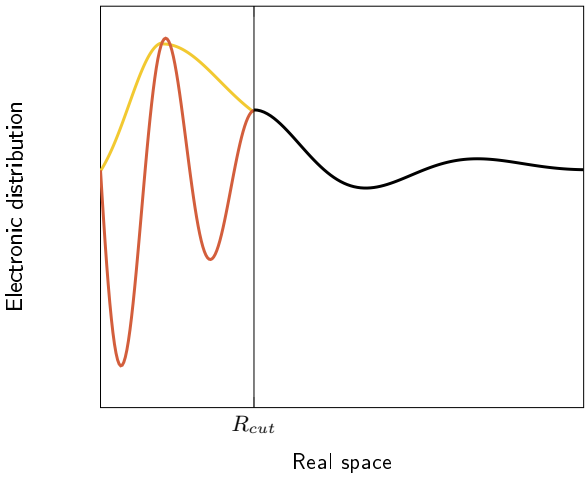

Figure 1.6 | Above the critical radius R_{cut} the unchanged electronic potential. Below R_{cut}, the unchanged electronic potential in red that oscillates too much and the modified one in yellow to create the pseudopotential.

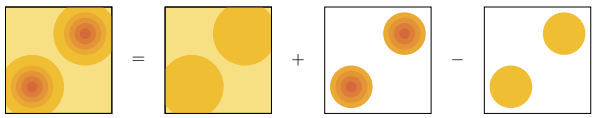

Figure 1.7 | Schematic description of the PAW formalism as discussed in the main text.

Projector Augmented Wave approach Blöchl[57] wanted to find a way to get the accuracy of an all electrons calculation with a small computational cost. He created the Projector Augmentation Wave approach. Because the plane waves are of great interest to treat the delocalized valence electrons, he proposed an approach where the previous norm conserving pseudopotential is improved in the region around the nuclei (the core region) but kept outside this region. To better characterized the core electrons and the behaviour of the valence electrons around the nuclei (in a spherical region centered around the nuclei), localised functions are used for the basis instead of plane waves.

The region in which the correction is done is called the augmentation region or the spherical non overlapping region. In this region, the PAW calculation is performed with both the local basis and the plane waves. Therefore, to avoid the double counting, the plane wave contribution in this region is subtracted as shown on picture 1.7 from[58]. A new and more accurate grid is defined to subtract this plane wave contribution. Associated to this double grid, a new energy cutoff is defined.

The main goal of this method is to retrieve an all electrons description. Furthermore, because the local basis correctly describes the core region, the plane wave basis can be reduced. Namely, the energy cutoff to construct the delocalized basis is clearly smaller and consequently the calculation is faster.

Due to the local basis to describe the electrons close to the nuclei, this method is usually used to describe electrons which are localized such as d or f electrons even if it is not the

initial goal of this approach. To deal with those specific electrons, we have additional methods explicitly created for them such as the Hubbard model[59] and the dynamical mean field theory (DMFT)[60]. In the next section, I will present the first one that has been used in this thesis.

In the Abinit world #5 Projector Augmented Wave

PAW as implemented by Torrent [61] has been used for the description of Nickelates compounds. We use the JTH atomic data[62] available on the Abinit Web Site[63] within the GGA approach developed by Perdew et al.[52] and adapted for solid (PBEsol[64]).

1.3 Electron Correlations

When electrons are localized, their spatial distribution is limited. Due to the Coulombic interaction, it costs a lot of energy to have another electron in the same region. Systems with this behaviour are named correlated electron systems. The approximation of the exchange correlation term is usually not adapted for such systems. Thus, the d or f electrons which are localized are usually not correctly described. To deal with correlated systems, more suitable models are proposed.

In this study, a Hubbard[59] correction is added in the model. We can write it as

$$\hat{H}_{Hubbard} = \frac{1}{2} \sum_{m',m} U_{m',m} \hat{n}_{m'} \hat{n}_m \tag{1.25}$$

where $U_{m',m}$ is the cost of energy to get the electrons m and m' on the same atom and $\hat{n}_m$ and $\hat{n}_{m'}$ are the density operators of the m and m' correlated electrons respectively.

The discussed local basis in the PAW approach is useful to create Wannier functions[65] which are suitable to add this correlation contribution.

The Hubbard term is a correlation correction but already partially taken into account in the Exchange Correlation term. Thus, again, the double counting must be evaluated and substracted. There are different methods to remove the correlation contribution equivalent to the Hubbard term in the Exchange correlation term. In this work, the Full Localised Limit (FLL) double counting discussed by [66] is used.

In the Abinit world #6 Hubbard Term

Using PAW, the new energy cutoff inside the spherical region is given by *pawecutdg*. A specific convergence study has to be done like for *ecut*.

At least three flags to use the Hubbard term (U) in the PAW formalism as implemented in **Abinit**[67] have to be set. To use the Hubbard term (U) in the PAW formalism, as implemented by Amadon et al.[67], a minimum of three flags have to be set. The chosen formalism is the one developed by Liechtenstein[68]. To activate the Hubbard correction and use the FFL double counting, *usepawu* is set at 1.

The electrons on which you want to add the correction have to be specified thanks to the flag *lpawu*. It gives the value of the angular momentum for each species as in Table 1.5. A value equals to -1 means you do not want to add a correction. The amplitude of the interaction (U, the screened coulomb interaction) between electrons corresponding to the ones chosen by *lpawu* is given by *upawu*.

pawecutdg	38			
usepawu	1			
lpawu	-1	2	-1	
upawu	0	1.5	0	eV

Table 1.5 | An example of **Abinit** input with the details for the PAW method with Hubbard correction.

2 | Physical properties in DFT

2.1 Magnetism

DFT equations can be easily generalized for including magnetism by considering two densities (one for each channel, i.e., spin *up* and spin *down*).

In the Abinit world #7 Magnetism

Each spin moment for each atom is specified with the flag *spinat*. It has three values for the x, y and z directions. One line for each atom in the same order as for the *xred* flag as shown in table 2.3.
A collinear system (all magnetic moments aligned along the same direction) can be seen as a scalar magnetization. *nspden* sets to 2 impose a scalar magnetization with two spin densities (one up and one down). The third column of the *spinat* flag is used for the amplitude of the scalar magnetic moment. For a collinear spin-polarized system, the flag *nsppol* is set to 2 to mention there are two separated wavefunctions corresponding to the two spin channels. If it is unpolarized, an antiferromagnetic configuration is described and wavefunctions have only one independent spin channel (*nsppol* = 1).

nsppol	1		
nspden	2		
spinat	0	0	1
	0	0	-2
	0	0	0
	0	0	0
	0	0	0

Table 2.1 | An example of **Abinit** input for the spin moment (Bohr magneton) in a collinear case.

2.2 Electronic dispersion and density of states

DFT approach allows to get the minimum of energy for a given structure. Here, I will discuss about the density of state (DOS) and the electronic dispersion, also called electronic band structure.

The electronic behaviour is summarized in the BZ of the reciprocal space. But to characterize the whole BZ, only a representative path is chosen. The energy of the electrons depends on the wave vector $\overrightarrow{k}$ and is given by $\epsilon(\overrightarrow{k})$: the eigenvalues of the electronic Hamiltonian at $\overrightarrow{k}$. Plotting those values with respect to $\overrightarrow{k}$ draws the electronic band structure in the BZ such as in figure 2.1. Because electrons cannot be in the same quantum state, there is only one electron by band, by k-point and by spin.

The occupied bands are named valence bands. The highest energy corresponding to the last occupied valence state is called the Fermi Level. By definition, all the valence bands are below this Fermi level. Above this Fermi level, the unoccupied bands are named conduction bands. If an electron is inside an unoccupied band (eg. due to temperature), any electrical perturbation induces a motion and is the reason why those bands are called the conduction bands. The electrons in the valence band are also responsible for the bonding properties.

If there is a range of forbidden energies (i.e. a gap) between the valence and conduction bands, the system is insulator. In this situation, to fill the conductions bands, the gap energy has to be exceeded. On the contrary, if there is no gap, the system is said metallic.

In DFT, one has to be careful about the electronic band struture. Even if they are used to interpret the physics, they do not have a real meaning for the real system. Indeed, they are constructed from the Kohn-Sham Hamiltonian. And only the electronic density has a physical meaning but not the independent KS wave functions. Moreover, the bands above the Fermi level are for the excited electrons. However, DFT is only able to deal with the ground state properties.

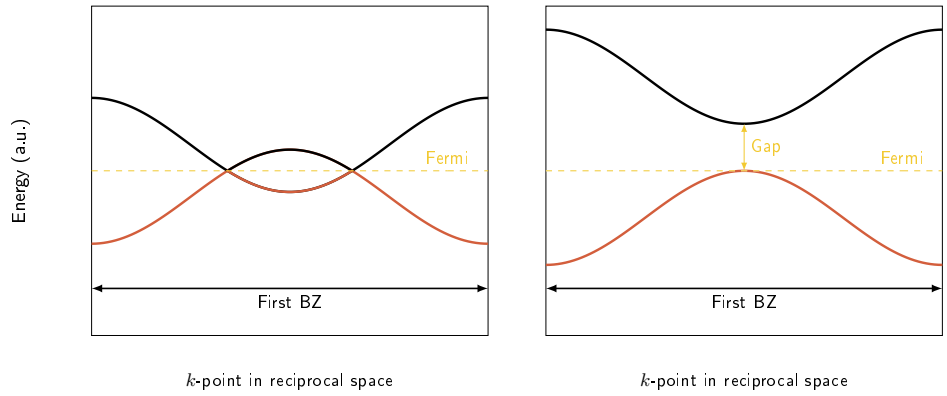

Figure 2.1 | Electronic band structure. In black, the conduction band. In red, the valence bands. In yellow, the Fermi level. Left: Metallic case. Rigt: Insulator case with the gap which is highlighted in yellow.

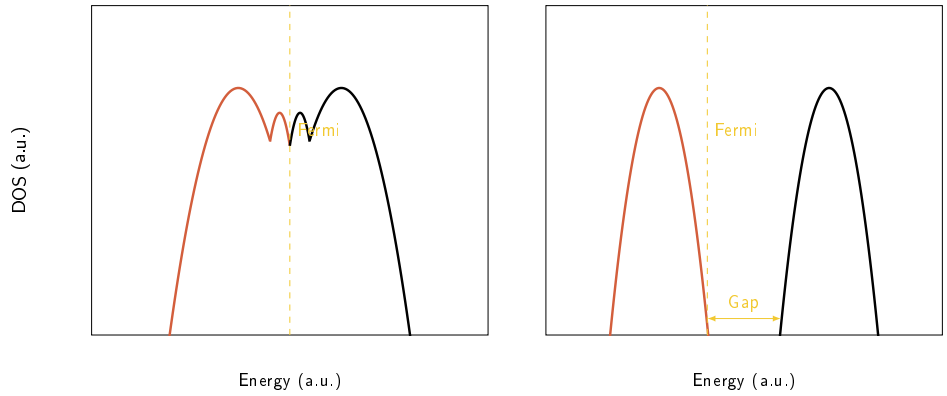

Figure 2.2 | Density of state of: Left: Metallic case and Rigt: Insulator case with the gap which is highlighted in yellow. In black, the conduction states. In red, the valence states. Yellow line, the Fermi level.

An additional tool to the electronic dispersion is the density of states as depicted on picture 2.2. It represents the number of available states for a given energy. To calculate the DOS at that given energy, the electronic states with this energy are integrated over the $\overrightarrow{k}$ space. If desired, the projected DOS on the angular momentum of each atom can be obtained as it will be done during this thesis.

2.3 Forces

In classical physics, forces are responsible for the motion of objects. In our case, the objects are the atoms and they undergo a force. Until now, DFT was helpful to get the electronic behaviour (electronic ground state) for a given atomic structure. However, there was no warranty the structure was the one corresponding to the minimum of energy named global ground state. Thanks to the Hellmann-Feynman theorem[69, 70], the forces are directly and analytically accessible thanks to the GS wave functions. The forces are given by $F^a_{\kappa\alpha} = -\frac{\partial E}{\partial \tau^a_{\kappa\alpha}}$

where α is the cartesian spatial direction, a the label for the cell position of the atom κ and $\tau^a_{\kappa\alpha}$ is the atomic displacement.

From those forces (obtained at the end of the SCF cycle), we can find the direction to the global ground state (minimum of energy). A relaxation consists of successively moving the atoms in order to minimize those forces and reach the minimum of energy. In material science, forces and stresses are different. The first one is responsible for the motion of the atoms, while the second one, even if coupled to atomic motions, is directly linked to the size and the shape of the unit cell. They can be relaxed independently or simultaneously.

In the Abinit world #8 Forces

The flag *ionmov* allows to relax the atomic positions. There are several algorithms to reach the ground state from the knowledge of the forces. The one used for this thesis is the BFGS minimization [71–74] with setting *ionmove* to 2. To relax the size and the shape of the cell, there is the flag *optcell*. If the calculation is not able to converge, you can limit the number of iterations thanks to the *ntime* flag. To avoid relaxation for which the change of cell size is too drastic, *dilatmx* can be imposed. Indeed, the chosen energy cutoff would not stay consistent with the new size. To smooth the edge of the plane wave basis during the relaxation, a smearing has to be imposed on the energy cutoff thanks to the *ecutsm* flag.
The criterion to be reached is on the forces (on the atoms) and stresses (on the cell) thanks to *tolmxf* (alternatively on the energy with *tolmxde*).

optcell	2
ionmov	2
ntime	1000
dilatmx	1.2
ecutsm	0.1
tolmxf	10^{-5}

Table 2.2 | An example of **Abinit** input for the relaxation of the atoms and the cell.

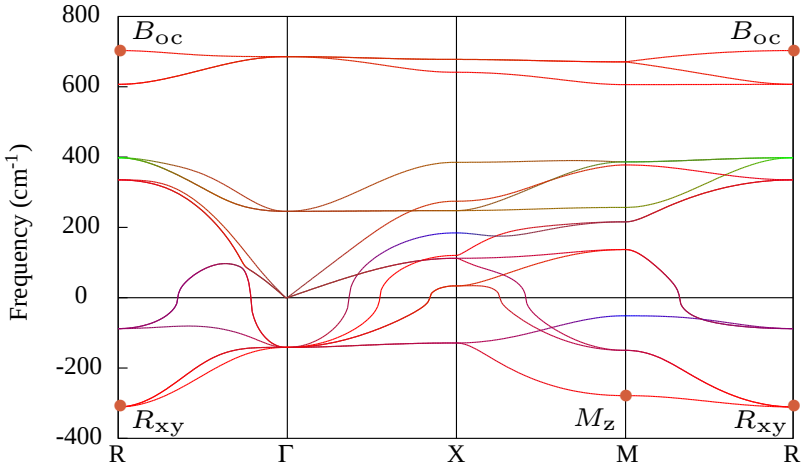

Figure 2.3 | **Cubic phonon dispersion curve of $YNiO_3$.** Phonon dispersion curve for the $Pm\bar{3}m$ phase of $YNiO_3$ (see Chapter 10 for details), at the $P2_1/n$ ground state volume and for a FM spin ordering (U=1.5 eV). Colors have been associated to the curves according to the involvement of each cation in the eigendisplacement of each mode (*R* in blue, Ni in green and O in red). Imaginary frequencies (unstable modes) appear as negative values.

2.4 Phonon

Thanks to the knowledge of the electronic density, as we have seen, we can analyse and get forces about the structural properties. However, in condensed matter, to analyse the dynamical stability, the forces on individual atom are used but also the collective displacements around the equilibrium positions[1] named phonons. The strength of the collective displacements is characterised by the inter atomic force constants (IFC) given by

$$C^{a,b}_{\kappa\alpha,\kappa'\beta} = \frac{\partial^2 E[\overrightarrow{R^a_\kappa}]}{\partial u^a_{\kappa\alpha} u^b_{\kappa'\beta}} \tag{2.1}$$

where α, β are the cartesian spatial directions, a and b are the labels for the cell position of the atom κ and κ' respectively. $\overrightarrow{R^a_\kappa}$ is the equilibrium atomic position and $u^a_{\kappa\alpha}$ is the displacement compared to $\overrightarrow{R^a_\kappa}$. It is the second derivate of the energy and so directly linked to the curvature of the energetic landscape. If the IFC is positive, it means the collective displacement is stable and the atomic structure would come back to its equilibrium state under a perturbation. *A contrario*, if it is negative, the system goes away from the unstable equilibrium state to gain energy and reach another minimum.

Due to the crystal periodicity as discussed for electron, the description of all the collective displacements can be summarized in the Brillouin zone in the phonon dispersion such as in figure 2.3.

From IFC, you define[75]:

[1] The formalism concerning the phonons are only available for an equilibrium structure (forces on the atom have to be zero!)

$$\tilde{D}_{\kappa\alpha,\kappa'\beta}(\overrightarrow{q}) = \frac{\tilde{C}_{\kappa\alpha,\kappa'\beta}(\overrightarrow{q})}{\sqrt{M_\kappa M_{\kappa'}}} \tag{2.2}$$

with $\tilde{C}_{\kappa\alpha,\kappa'\beta}$ the Fourier transform of the IFC $C^{a,b}_{\kappa\alpha,\kappa'\beta}$ as the dynamical matrix at $\overrightarrow{q}$ and write the dynamical equation:

$$\sum_{\kappa'\beta} \tilde{D}_{\kappa\alpha,\kappa'\beta}(\overrightarrow{q})\gamma_{m\overrightarrow{q}}(\kappa'\beta) = \omega^2_{m\overrightarrow{q}}\gamma_{m\overrightarrow{q}}(\kappa\alpha) \tag{2.3}$$

as an eigenvalue problem where $\overrightarrow{q}$ is the wave vector[2]. The eigen energies are $\omega_{m\overrightarrow{q}}$ the associated phonon frequencies and the corresponding eigen vectors are $\gamma_{m\overrightarrow{q}}(\kappa\alpha)$ the eigen displacements.

There are two methods to calculate the IFC: The analytical one is the one based on the perturbation theory on DFT named Density functional Perturbation theory (DFPT)[76].The other one is a finite a numerical calculation of the numerical calculation of the derivatives called frozen phonon approach.

In the Abinit world #9 Phonon

DFPT is available in **Abinit**[77–81] and is analytical. However, even if nowadays available, this method was not available in the GGA+PAW formalism during this thesis. Because of that, I use the finite method. To do so, the **Phonopy** toolkit[82] was employed to generate structures then calculated by **Abinit**. From the outputs of **Abinit**, the dynamical matrix is extracted with **Phonopy** to get the phonon band structure.

2.5 Optical conductivity

The real part of the optical conductivity allows to reach interesting information about the electronic behaviour. Indeed, we have access to states that can be excited by optical perturbations. The Fermi's golden rule[83] informs what transitions is allowed for the impulsion operator (velocity). In practice, the detailed electronic configuration is not accessible from the optical spectrum but in the other way, the DOS can be used to know which transitions may be responsible of which peaks.

[2] Same BZ as for electrons but not named $\overrightarrow{k}$ to avoid confusing formalism

In the Abinit world #10 Optical Properties

The optical properties studied thanks to Abinit are calculated using the implementation by Mazevet [84, 85] in PAW and explained on the **Abinit** Web Site [63]. The Post process has been done thanks to the Agate[86] software with the Kubo-Greenwood[87, 88] formula.

2.6 Conclusion

Thanks to the DFT formalism, it is possible to study the electrons and nuclei for the ground state properties. Nickelates family will be studied in term of structural, electronic, magnetic and optical properties. I would like to remind DFT is at oK for the ground state only. In the next section, I will introduce a theory allowing to model the effects of temperature from DFT results.

In the Abinit world ABINIT Summary

Here is an example of input to relax the ferromagnetic configuration in the cubic phase for $YNiO_3$. **Abinit** boxes 1, 2, 3, 4, 6, 7 and 8 are used to create the input. Linked to what is mention in 2.2, you can specify the kind of electronic occupation thanks to *occopt* flag. Because the studied system can be metallic and insulator during the relaxation and or the SCF cycle, *occopt* sets to 3 imposes a Fermi-Dirac smearing *tsmear* to help the calculation at a numerical level.

natom	5				
ntypat	3				
znucl	39	28	8		
typat	1	2	3	3	3
acell	1.0	1.0	1.0		
rprim	7.12	0.0	0.0		
	0.0	7.12	0.0		
	0.0	0.0	7.12		
xred	0.0	0.0	0.0		
	0.5	0.5	0.5		
	0.0	0.5	0.5		
	0.5	0.0	0.5		
	0.5	0.5	0.0		
toldfe	10^{-10}				
nstep	200				
ngkpt	12	12	12		
kptopt	1				
occopt	3				
tsmear	0.001				
ecut	20				
pawecutdg	38				
usepawu	1				
lpawu	-1	2	-1		
upawu	0	1.5	0	eV	
nsppol	1				
nspden	2				
spinat	0	0	1		
	0	0	-2		
	0	0	0		
	0	0	0		
	0	0	0		

optcell	2
ionmov	2
ntime	1000
dilatmx	1.2
ecutsm	0.1
tolmxf	10^{-5}

Table 2.3 | An example of **Abinit** input with the electronic occupation in black.

3 | Phase transition Temperature in Nickelates

A phase transition is typically described by an order parameter that evolves from zero to a non-zero-value at the transition. This order parameter is a physical property of the system that can be either macroscopic or microscopic.

3.1 Landau Theory

The Landau theory[89] gives a generic method to describe the phase transition from a macroscopic and phenomenological point of view. To describe the macroscopic behaviour of the system, the knowledge of the microscopic one is not necessary.

In the Landau theory, the main assumption is that the free energy can be developed as a polynomial expansion of the order parameter identical for the system below and above the transition temperature. This means that the energy must stay invariant under the symmetry operations of the most symmetric phase. The free energy F, corresponding to the competition between the entropy S and the internal energy $U(F = U - TS)$, typically reads for cubic perovskites

$$F(Q_M) = \alpha_0 + \frac{1}{2}\alpha_M Q_M^2 + \frac{1}{4}\beta_M Q_M^4 + \frac{1}{6}\epsilon_M Q_M^6 \tag{3.1}$$

where Q_M is the order parameter. α_0, β_M and ϵ_M are assumed constant and $\alpha_M = \gamma_M(T_{0M} - T)$ where T_{0M} is the temperature of the phase transition with γ_M positive. The temperature dependence of α_M affects the curvature of the energy in function of Q_M. Indeed, an instability appears when the curvature around Q_M=0 is negative ($\frac{\partial^2 F}{\partial Q_M^2} < 0$).

When β_M>0, it is possible to stop the expansion at the fourth order and the phase transition is said of second order. This leads to a unique phase transition temperature. However, when β_M<0, it is necessary to expand up to the sixth order (with $\beta_M < 0$ and $\epsilon_M > 0$) and the transition is first order. The main difference with the second order is the transition typically experiences an hysteresis cycle. This means the behaviour of the order parameter depends on whether the system is cooled down or warmed up as observed in picture 3.1.

In our case, the second order phase transition is of main interest. As it will be explained in chapters 4 on the Metal-Insulator Phase transition and 5 on the optical properties, it is

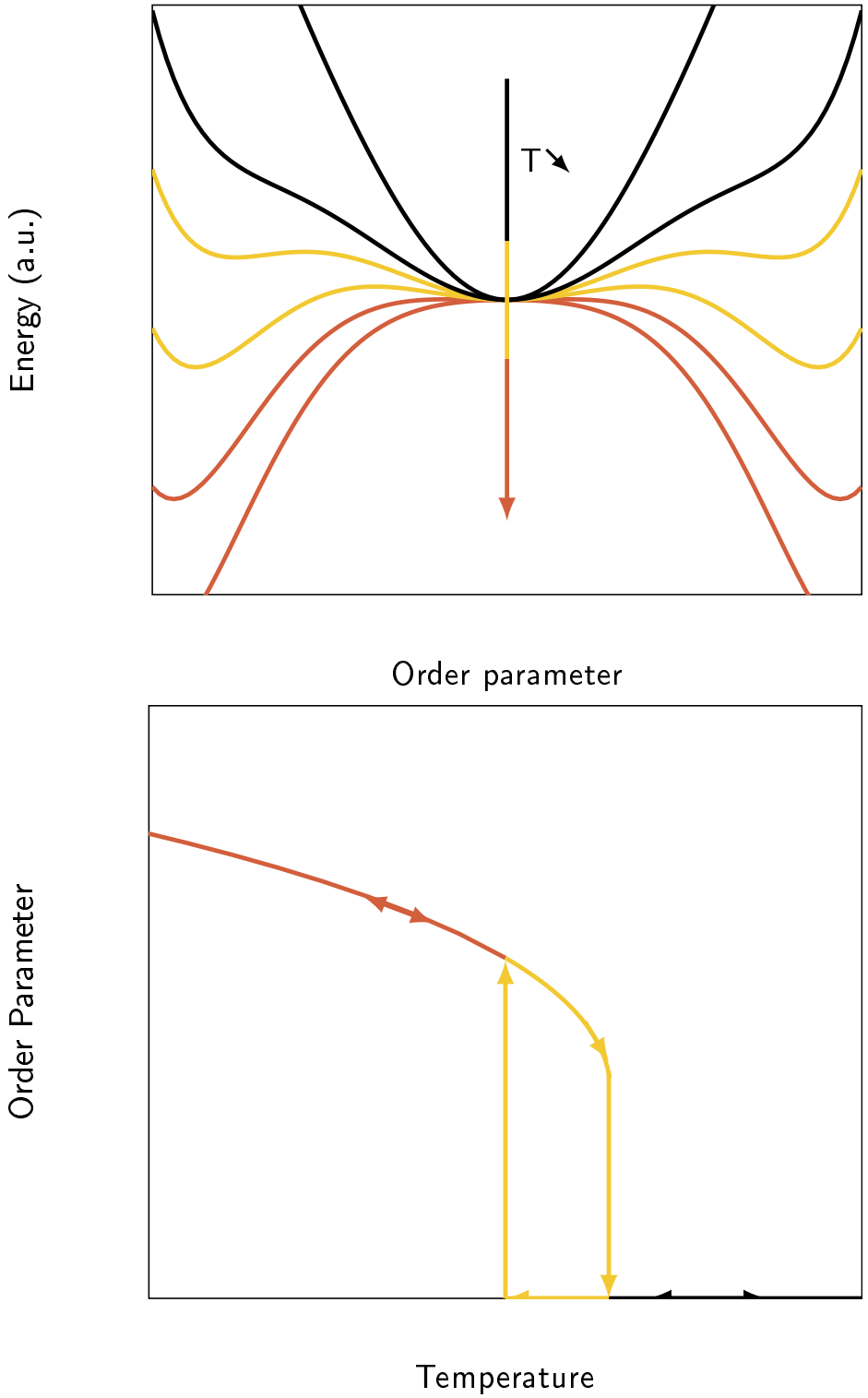

Figure 3.1 | Top:First order phase transition from high temperature (Black) to low temperature (Red) crossing the hysteresis region (Yellow). Bottom: Evolution of the linked order parameter as a function of the temperature. The heating and cooling paths are highlighted by arrows.

not clear in literature what the order of the transition should be for the case of the small size rare-earth cations. However, it is clearly of first order in the case of big cation but, as explained in the chapter 4, it is due to the magnetism. This latter case is not the main goal of this thesis

In more complex systems, a given order parameter can be triggered by a second one. It means it does not really evolve in temperature by itself but thanks to an other parameter. By example, an order parameter Q_B can be affected by the parameter Q_M from eq. 3.1. The coupling between Q_B and Q_M is expressed with a bi-quadratic term that preserves the symmetry like

$$\begin{aligned} F(Q_M, Q_B) = \alpha_0 &+ \frac{1}{2}\ \gamma_M(T_{0M} - T)Q_M^2 + \frac{1}{4}\beta_M Q_M^4 \\ &+ \frac{1}{2}\alpha_B Q_B^2 + \frac{1}{4}\beta_B Q_B^4 \\ &+ \frac{1}{2}\lambda_{MB} Q_M^2 Q_B^2 \end{aligned} \tag{3.2}$$

where α_B, β_B and λ_{MB} are constant. Although there is no explicit dependence in temperature for the Q_B order parameter, it is the evolution of Q_M through the bi-quadratic coupling λ_{MB} term that will trigger the change of Q_B from a zero to a non-zero value.

Even more sophisticated, two parameters can evolve in temperature, be coupled and both trigger a third parameter Q_B:

$$\begin{aligned} F(Q_M, Q_R, Q_B) = \alpha_0 &+ \frac{1}{2}\ \gamma_M(T_{0M} - T)Q_M^2 + \frac{1}{4}\beta_M Q_M^4 \\ &+ \frac{1}{2}\ \gamma_R(T_{0R} - T)Q_R^2 + \frac{1}{4}\beta_R Q_R^4 \\ &+ \frac{1}{2}\alpha_B Q_B^2 + \frac{1}{4}\beta_B Q_B^4 \\ &+ \frac{1}{2}\lambda_{MR} Q_M^2 Q_R^2 + \frac{1}{2}\lambda_{MB} Q_M^2 Q_B^2 + \frac{1}{2}\lambda_{RB} Q_R^2 Q_B^2 \end{aligned} \tag{3.3}$$

where γ_R is positive and β_R, λ_{MR}, λ_{RB} are constant.

In this thesis, the studied system is describe thanks to this kind of equations and we reveal the microscopic origin behind this behaviour.

3.2 Metal-Insulator transition

As discussed in the introduction, the nickelate family exhibits a Metal-Insulator phase transition (except $LaNiO_3$ which is always metallic). As defined in the Landau theory section, a phase transition is determined by the change of a physical property from zero to a non-zero value. In this specific case, a possible order parameter is the electronic gap. Because the gap width is linked to a structural distortion, this structural distortion is another possible order parameter and will be the one that will be discussed in this thesis.

Concerning the Metal-Insulator phase transition, the available DFT tools as previously discussed (section 2.2) allow the characterisation of both insulating and metallic phases but

at 0K. Here, the insulating phase is a semi-conductor. However, it is important to notice that the nickelates are not usual semi-conductors. Indeed, in the case of metal-insulator phase transitions such as for nickelates, there is a drastic change in the electronic band structure with the disappearance of the gap when reaching the high temperature phase. The very difference is that in the case of semi-conductors, the electronic band structure does not drastically change with temperature: the gap is always present in temperature but small enough gap allowing thermal excitations.

3.3 Magnetic transition

Magnetic properties of nickelates are not trivial. At high temperature, they exhibit a Curie paramagnetism. That is to say all the magnetic atoms have a magnetic moment but not organized because of the temperature.

Usually, when decreasing the temperature, the magnetic configuration is not random anymore. In some systems, the ordered phase is a ferromagnetic configuration: all the magnetic moments are aligned along the same direction. However, in some other systems, from one site to another the magnetic moments can be opposite but still following an organised pattern. Nickelates belong to this later kind of configuration named antiferromagnets. Other configurations such as ferrimagnetics[90] are not discussed here.

In the case of perovskites, the magnetic moment is usually created by the atom inside the octahedral oxygen cages which is the Nickel atom[1] in our case. The antiferromagnetic configuration at low temperature is described in picture 3.2 and is usually named S or E'-type. It corresponds to an "up-up-down-down" spin arrangement along the 3 pseudocubic directions. It is important to notice that if one magnetic moment over two is equal to zero, the inversion symmetry is not broken and the system remains non polar. As it will be discussed later, this is the case at 0K but not necessary closed to the transition as clearly suggested in the Gawryluk paper[30].

The goal is to describe the magnetic interactions responsible for this kind of ground state configuration. The pair interactions between magnetic moments can be characterised by an Heisenberg model:

$$E_{ex} = -2 \sum_{i,j} J_{ij} S_i S_j \tag{3.4}$$

where E_{ex} is the exchange energy and J_{ij} is the exchange interaction between the magnetic moment S_i on site i and the magnetic moment S_j on site j. A positive value of J means that a ferromagnetic configuration is favorable for the considered pair of atoms. Instead, a negative value gives rise to an antiferromagnetic configuration. To correctly describe such S-type configuration like in nickelates, 6 pair interactions (a 6J model) until the fourth neighbours

[1] We are not focusing on the magnetic properties from the f electrons from the A-cation which could be of high importance in such systems but mainly at low temperature.

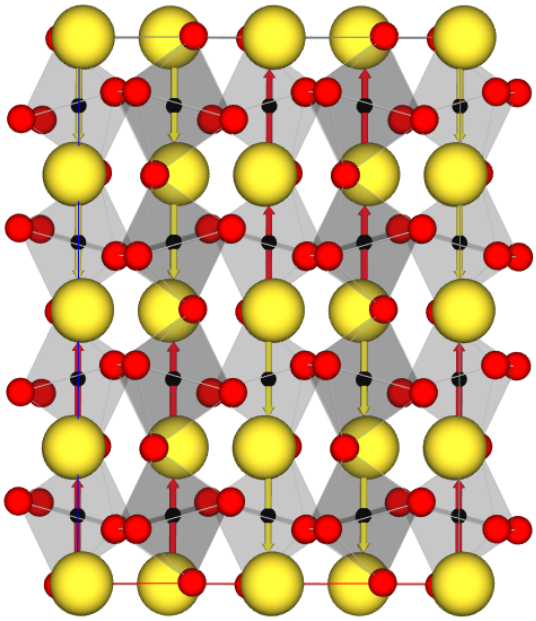

Figure 3.2 | **Ground State spin configuration for $YNiO_3$.** Spin order associated to the E'-type antiferromagnetic (AFM-E') ground state.

need to be taken into account to properly characterise the anisotropy of the magnetic interactions as explained in details in chapter 6.

Part III

Structurally triggered metal-insulator transition

4 | Structurally triggered MIT in rare-earth nickelates

Alain Mercy[1], *Jordan* Bieder[1,2], *Jorge* Íñiguez [3] and *Philippe* Ghosez[1]

[1]Theoretical Materials Physics, Q-MAT, CESAM, University of Liège, B-4000 Liège, Belgium [2]CEA DAM-DIF, F-91297 Arpajon, France [3]Department of Materials Research and Technology, Luxembourg Institute of Science and Technology, L-4362 Esch/Alzette, Luxembourg

Introduction to the article

Nature communications 8(1), 1-6 (2017)

Nowadays, all the Material Research community wants to focus on applications and deal with heterostructures and superlattices to access novel properties like interface coupling and strain tuning. However, to be able to work on such systems, it is mandatory to correctly understand the underlying fundamental physics. Thus, I decided to first study the bulk properties of nickelates. Here is the summary of my investigation on the MIT.

4.1 Abstract

Rare-earth nickelates form an intriguing series of correlated perovskite oxides. Apart from $LaNiO_3$, they exhibit on cooling a sharp metal-insulator electronic phase transition, a concurrent structural phase transition and a magnetic phase transition toward an unusual antiferromagnetic spin order. Appealing for various applications, full exploitation of these compounds is still hampered by the lack of global understanding of the interplay between their electronic, structural and magnetic properties. Here, we show from first-principles calculations that the metal-insulator transition of nickelates arises from the softening of an oxygen breathing distortion, structurally triggered by oxygen-octahedra rotation motions. The origin of such a rare triggered mechanism is traced back in their electronic and magnetic properties, providing a united picture. We further develop a Landau model accounting for the metal-insulator transition evolution in terms of the rare-earth cations and rationalising how to tune this transition by acting on oxygen rotation motions.

4.2 Introduction

First synthetized in 1971 [8], rare-earth nickelates (RNiO$_3$, with R = rare earth) are appealing for various applications [91, 92] and the possibility to tune their properties in epitaxial films and heterostructures [7] has recently fuelled an even larger interest [93–95]. RNiO$_3$ compounds belong to the family of perovskite oxides with a reference $Pm\bar{3}m$ cubic structure (Fig. 4.1a), nevertheless not directly observed. Apart for LaNiO$_3$, which always keeps a metallic $R\bar{3}c$ phase and will not be further discussed here, all RNiO$_3$ adopt at reasonably high temperature a metallic $Pbnm$ orthorhombic phase [5]. This phase, rather ubiquitous [96] amongst perovskites with small Goldschmidt tolerance factor [5], t, corresponds to a distortion of the cubic structure arising from the appearance of combined anti-phase rotations of the oxygen octahedra along the x and y directions, R_{xy} (Fig. 4.1b), with the same amplitude Q_R and in-phase rotations of the oxygen octahedra along z, M_z (Fig. 4.1c), with amplitude Q_M.

In this phase, all Ni atoms are equivalent and formally in a Jahn-Teller active d^7 (likely $t_{2g}^6 e_g^1$ low spin) configuration. Surprisingly, although compatible with the $Pbnm$ symmetry, cooperative Jahn-Teller distortions do not appear. Instead, at a temperature T_{MI} which strongly evolves with the R cation (i.e with t) [4], RNiO$_3$ compounds exhibit an electronic metal-insulator transition (MIT), which was shown to be concurrent with a structural transition from $Pbnm$ to monoclinic $P2_1/n$ symmetry [97]. This symmetry lowering is accompanied with the appearance of a breathing distortion of the oxygen octahedra, B_{OC} (Fig. 4.1d), which alternatively expand and contract with amplitude Q_B, according to a rock-salt pattern. This gives rise to two types of Ni sites with long and short Ni–O bonds respectively.

At low temperature (100-200K), RNiO$_3$ compounds finally show a magnetic phase transition toward an unusual E'-type antiferromagnetic (AFM) spin order identified by a Bragg vector $\mathbf{q} = (1/4, 1/4, 1/4)$ in pseudocubic notation [27, 97, 98]. For large cations (R = Nd and Pr), the Néel temperature $T_N = T_{MI}$ and the system goes directly from paramagnetic metal (PM-M) to AFM insulator (AFM-I). For smaller R cations, T_N is much lower than T_{MI}; the two phase transitions are decoupled and the system goes through an intermediate paramagnetic insulating phase (PM-I).

The origin of the MIT has been widely debated in the literature [21, 99–103]. It was sometimes interpreted as a charge disproportionation at Ni sites [104] : $2(d^7) \rightarrow d^8 + d^6$. However, the importance of Ni $3d$ – O $2p$ hybridization – i.e., transfer of electrons from O to Ni and formation of oxygen holes ($\underline{L}$) keeping Ni in a d^8 configuration (i.e., $d^{8-n} \approx d^8\underline{L}^n$) – was evoked early on [100]. Nowadays, the MIT is usually viewed as a charge ordering of the type $2(d^8\underline{L}^1) \rightarrow (d^8) + (d^8\underline{L}^2)$ [21, 105, 106]. In this scenario, B_{OC} appears important to stabilise the charge ordering and open the gap. As suggested in Ref. [107] and confirmed from statistical correlation techniques [108], R_{xy} and M_z are also expected to play an active role. However, a complete picture linking electronic, structural and magnetic properties is yet to emerge.

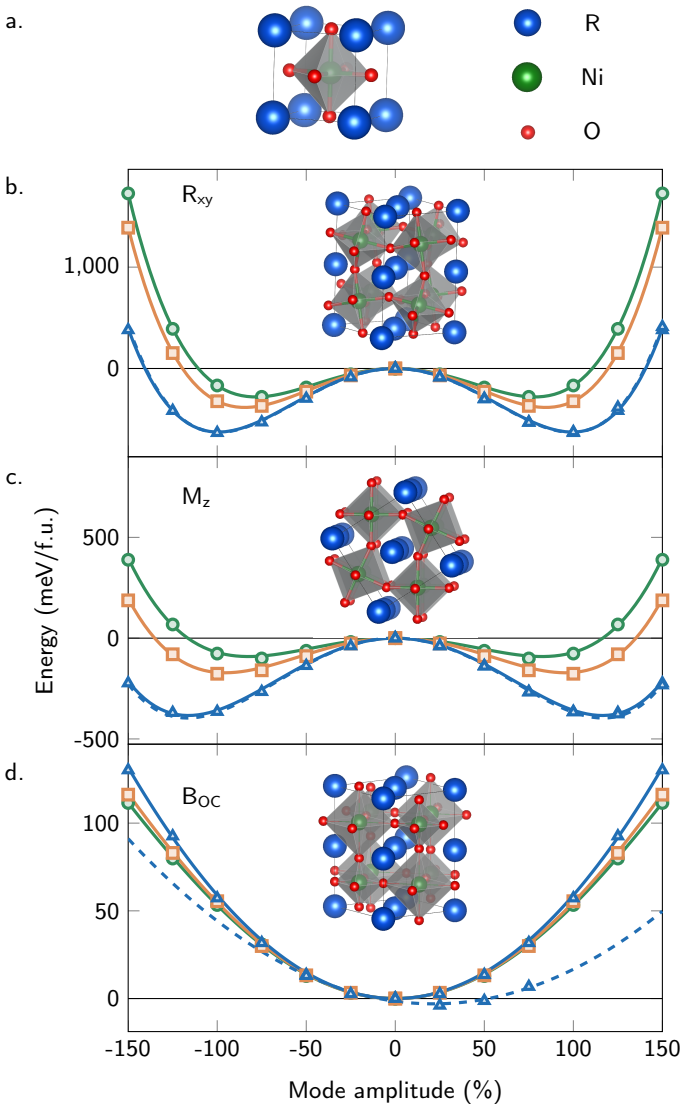

Figure 4.1 | **Reference cubic perovskite structure and most relevant atomic distortions.** (**a**) Sketch of the reference $Pm\bar{3}m$ cubic perovskite cell of $R\mathrm{NiO_3}$ compound with R at the corner, Ni at the centre and O atoms at the middle of the faces, forming corner-shared octahedra surrounding the B atoms. Starting from this reference, three main atomic distortions drive the system successively to the $Pbnm$ and then $P2_1/n$ phases : (**b**) anti-phase rotations of oxygen octahedra of same amplitudes about x and y axis (R_{xy}), (**c**) in-phase rotations of oxygen octahedra about z axis (M_z), (**d**) breathing of the oxygen octahedra (B_{OC}). The energy wells associated to the freezing of individual distortion of increasing amplitude in the cubic phase are shown for different R cations, associated to distinct tolerance factor t, and either a ferromagnetic (full line) or E'-type antiferromagnetic (dashed line, only for R =Y) spin arrangement : $\mathrm{YNiO_3}$ (t = 0.920, blue), $\mathrm{GdNiO_3}$ (t = 0.938, orange) and $\mathrm{SmNiO_3}$ (t = 0.947, green). The atomic distortions are normalised to their amplitude in the $P2_1/n$ AFM-E' ground state of $\mathrm{YNiO_3}$. Calculations are done for each compound in a cubic phase that has the same volume as the ground state.

Unlike recent theoretical studies which were focusing specifically on the electronic properties [21, 102, 103, 105], we investigate here self-consistently the electronic and structural degrees of freedom of RNiO$_3$ compounds from density functional theory calculations (DFT, see Methods). Specific care was given to the validation of our approach, which turns out to provide an unprecedented agreement with experimental data. Focusing on YNiO$_3$, we show (Supplementary Note 10.1-10.4) that not only the atomic structure but also the AFM-E' ground state, the estimated T_N and the electronic bandgap of the insulating phase are very accurately reproduced, making therefore our approach a method of choice to shed light on the interlink between these different features.

4.3 Results

4.3.1 Energetics of individual lattice distortions

We start from the reference $Pm\bar{3}m$ cubic structure. Inspection of the phonon dispersion curves (Supplementary Note 10.4-10.5) reveals dominant structural instabilities at R (ω_R = 310i cm^{-1}) and M (ω_M = 278i cm^{-1}) points of the Brillouin zone (BZ), which are associated respectively to the R_{xy} and M_z distortions responsible for the $Pbnm$ phase. These imaginary frequencies ω_i are linked to a negative energy curvature α_i at the origin ($\alpha_i \propto \omega_i^2 < 0$) and to a typical double-well (DW) shape of the energy when freezing R_{xy} and M_z distortions of increasing amplitude within the cubic structure, as illustrated in Fig. 4.1. These wells are nearly independent of the spin order but strongly evolve with the R cation : they become shallower when R size increases, consistently with a reduction of the related distortion amplitudes in the $Pbnm$ phase.

In contrast, the B_{OC} motion, corresponding to another phonon at R, is stable and extremely stiff (in fact the stiffest mode with ω_B = 700 cm^{-1}), in line with the single well (SW) shape illustrated in Fig. 4.1. Decreasing R-cation size tends to stabilise slightly further B_{OC}, in apparent contradiction with the observed increase of T_{MI}. As illustrated for YNiO$_3$, switching from ferromagnetic (FM) to AFM-E' spin order reduces slightly the curvature but does not reverse it; instead it shifts the SW to lower energy [27], yielding a finite Q_B at the minimum. Although B_{OC} tends to make the system insulating, this amplitude (25% of ground-state's value) is however not large enough to open a gap (more than 75% would be required). This shows that B_{OC} and the magnetic order only cannot explain the MIT by themselves.

4.3.2 Mode coupling and triggered mechanism

Our central result is presented in Fig. 4.2 where we report the evolution of the B_{OC} energy well of YNiO$_3$ at various fixed amplitudes of oxygen rotation motions. It highlights that, although initially stable (SW), B_{OC} is progressively destabilized (DW) by the appearance of R_{xy} and M_z. As illustrated in the inset, α_B is renormalized into $\tilde{\alpha}_B$ which evolves linearly

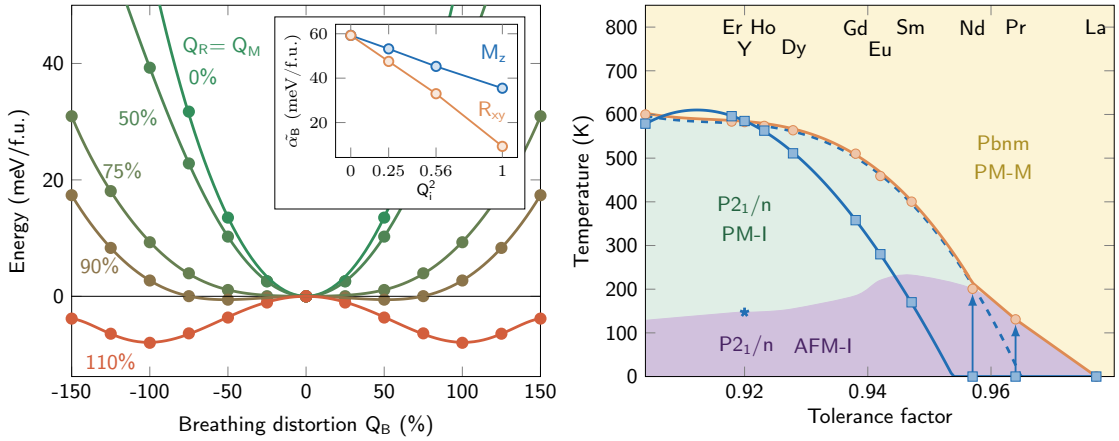

Figure 4.2 | **Triggered mechanism and nickelate phase diagram** (**a**) Evolution of the energy E in terms of the amplitude of the breathing distortion (Q_B) for fixed amplitudes of oxygen rotations ($Q_R = Q_M$ from 0% to 110%) in the FM cubic phase of $YNiO_3$ (same volume as the ground state). It highlights the softening of the energy well associated to B_{OC}, triggered by the oxygen rotations R_{xy} and M_z. Inset : Linear evolution of the energy curvature at the origin, $\tilde{\alpha}_B$ along Q_B, in terms of the square of the amplitude of the individual distortions Q_R (orange) and Q_M (blue). (**b**) Phase diagram of $RNiO_3$ compounds in terms of their tolerance factor t and the temperature T. It includes 3 phases : a metallic $Pbnm$ paramagnetic phase (PM-M, yellow area), an insulating $P2_1/n$ paramagnetic phase (PM-I, green area) and an insulating $P2_1/n$ E'-type AFM phase (AFM-I, magenta area). The yellow line and dots show the experimental evolution of T_{MI} with the tolerance factor t. The blue line and squares is the prediction of the simple Landau model fitted on the first-principles data (FM order). The dashed blue line is the fit of the Landau expression of $T_{MI}(t)$ on experimental data. The blue star is the magnetic phase transition predicted for $YNiO_3$ from first-principles. The blue arrows indicate the correction to be applied on T_{MI} for large cations when properly incorporating the change of magnetic order.

with Q_R^2 and Q_M^2. The slope associated to Q_R is twice as large as that related to Q_M, attesting that each of the three individual rotations similarly affects B_{OC}. This behavior arises from the presence in the energy expansion of cooperative ($\lambda < 0$) bi-quadratic coupling terms between B_{OC} and oxygen rotations ($E \approx \lambda_{Bi} Q_B^2 Q_i^2$, $i = R, M$) which, being the lowest-order couplings allowed by symmetry, should give rise to the appearance of B_{OC} through a triggered phase transition according to Holakovsky [109]. The same behavior is observed independently of the magnetic order (Supplementary Note 10.8). From now we focus on representative FM results while coming back to the role of magnetism later.

4.3.3 Landau model and phase diagram

To further assess the relevance of such a triggered mechanism in nickelates, we built a Landau model including R_{xy}, M_z and B_{OC} degrees of freedom [108], restricting to lowest coupling terms and assuming temperature dependence of the oxygen rotations only :

$$\begin{aligned} E &= \gamma_R(T - T_{0R})Q_R^2 + \beta_R Q_R^4 + \lambda_{BR} Q_B^2 Q_R^2 \\ &+ \gamma_M(T - T_{0M})Q_M^2 + \beta_M Q_M^4 + \lambda_{BM} Q_B^2 Q_M^2 \\ &+ \alpha_B Q_B^2 + \beta_B Q_B^4 + \lambda_{MR} Q_M^2 Q_R^2. \end{aligned} \tag{4.1}$$

Within this model, R_{xy} and M_z appear at T_{0R} and T_{0M}. On cooling, they progressively develop within the $Pbnm$ phase and renormalize the energy curvature α_B of B_{OC} as made clear when grouping the Q_B^2 terms in Eq. (1):

$$\tilde{\alpha}_B = \alpha_B + \lambda_{BM} Q_M^2 + \lambda_{BR} Q_R^2 \tag{4.2}$$

When reaching a critical amplitude at which $\tilde{\alpha}_B = 0$, they trigger the appearance of B_{OC} and produce concurrent structural and metal-insulator phase transitions. The phase transition appears to be second order within this model, which is however too simple to be conclusive on this point (Supplementary Note 10.10).

All parameters and their evolution with R were directly fitted from first-principles; only Curie temperatures were uniformly scaled to reproduce the experimental T_{MI} of $YNiO_3$ (Supplementary Note 10.8). The phase diagram of nickelates as predicted within this model is reported in Fig. 4.2. This figure demonstrates that the cooperative coupling of B_{OC} with R_{xy} and M_z is a key mechanism that, by itself, accounts for the experimentally observed evolution of T_{MI} with the tolerance factor.

Hence, the MIT in nickelates turns out to be a concrete example of triggered phase transition[110, 111], a kind of transition never identified before in simple perovskites. Indeed, although bi-quadratic interactions are generic in this class of compounds, different distortions usually compete and exclude each other [96]. The cooperative coupling of B_{OC} with oxygen rotations pointed out here is therefore an unusual and intriguing feature, whose origin is now traced back in the electronic band structure.

4.3.4 Electronic origin of the triggered mechanism

In the cubic phase, as expected from the formal Ni $3d^7$ ($t_{2g}^6 e_g^1$) occupancy, the Fermi energy E_f crosses levels of dominant Ni $3d$-e_g character (i.e. anti-bonding Ni $3d$- O $2p$ states); such levels form an isolated and rather dispersive set of two e_g bands, shifted above the t_{2g} levels by the crystal field (Fig. 4.3). Forcing into this cubic structure a B_{OC} distortion, associated to a phonon at $\mathbf{q}_R = (1/2, 1/2, 1/2)$, can open a gap at $\mathbf{q}_c = (1/4, 1/4, 1/4)$ within the e_g bands but well above E_f and without any direct impact on the metallic character and the occupied states. Nevertheless, the oxygen rotation motions substantially affect the e_g bands (Fig. 4.3), reducing their bandwidth and yielding a progressive down shift of the e_g levels at $\mathbf{q}_c$. As the rotations gradually increase and the bandwidth decreases, B_{OC} more substantially pushes down the electronic states around E_f, providing a progressive gain of electronic energy which, in turn, results in the softening of ω_B. The critical rotation amplitude at which B_{OC} becomes unstable ($\tilde{\alpha} = 0$) is precisely that at which the e_g levels at $\mathbf{q}_c$ cross E_f. At these amplitudes, the electronic system itself becomes unstable; the appearance of B_{OC} is favored and opens a gap at E_f, making the system insulating. As such, the MIT can therefore be interpreted as a Peierls instability but one that is not initially present and has been triggered by oxygen rotations.

4.4 Discussion

For compounds with small R cations, Q_R and Q_M are large and able to produce the MIT at relatively high temperatures, well above T_N. For large cations (R = Nd, Pr), oxygen rotations are reduced and, from our Landau model (built on FM results), no more sufficient to trigger the MIT (Figure 4.3). However, as previously mentioned, the AFM-E' spin order is compatible by symmetry with B_{OC} and induces its appearance as an improper order (linear shift of B_{OC} SW, Fig. 4.1d). Hence, although not opening a gap in the cubic phase, the onset of the AFM-E' order in the *Pbnm* phase of $NdNiO_3$ and $PrNiO_3$ promotes the occurrence of the MIT almost triggered by the rotations. In these compounds, we have therefore $T_{MI} = T_N$; the transition is more abrupt and first-order [5]. Such active role of magnetism for large cations is supported by the experimental results and discussion in Ref. [112]. It is also confirmed by our first-principles calculations on $NdNiO_3$, showing that the predicted T_{MI} is rescaled when including the change of magnetic order: while the system prefers to stay in the *Pbnm* metallic phase when imposing a FM order, it switches to the $P2_1/n$ phase when adopting a AFM-E' order. The cooperative effect of the magnetic order remains true for small cations but without any impact on T_{MI} ($> T_N$).

In conclusion, the concurrent electronic and structural transitions at T_{MI} in $RNiO_3$ compounds take the form of a Peierls instability which, primarily, is structurally triggered by the oxygen rotation motions R_{xy} and M_z and, eventually, is further assisted by the appearance of the E'-type AFM magnetic ordering. Our Landau model, and its possible extension

to incorporate explicitly strain degrees of freedom neglected here for simplicity, provides a simple and useful quantitative tool to estimate and interpret how T_{MI} can be tuned toward the monitoring of oxygen rotation motions R_{xy} and M_z when making solid-solutions [4], applying pressure [5] or playing with the epitaxial strain and the orientation of the substrate in thin films [35]. Our findings are relevant to other families of perovskites like $A^{2+}Fe^{4+}O_3$ compounds [113]. For instance, they can explain why $CaFeO_3$, which exhibits oxygen rotations, undergoes a MIT while $SrFeO_3$ and $BaFeO_3$, which stay cubic, remain metallic. In addition, the same physics is also inherent to manganites like $LaMnO_3$, suggesting a close competition between charge and orbital orderings in this family compounds. However, the situation is slightly different in bismutate like $BaBiO_3$, in which B_{OC} is intrinsically unstable in the cubic phase [114].

4.5 Methods

First-Principles calculations

First-principles calculations were performed in the framework of Density Functional Theory (DFT) [47, 48] using a Projected Augmented Wave (PAW) approach [57] as implemented within the ABINIT package [43–45, 61]. The calculations relied on the Generalized Gradient Approximation using the PBEsol [115] exchange-correlation functional. We worked within a collinear spin approximation. We included a Hubbard correction U = 1.5 eV [68] on the 3*d* orbitals of Ni atoms. A special care has been devoted to the determination of the appropriate U parameter (Supplementary Note 10.1-10.4).

We made use of JTH atomic potentials [62]. For the wave-functions, we used an energy cutoff of 24 Ha (38 Ha for the second grid in the PAW spheres), which guarantees a convergence better than 1 meV on the total energy. The Brillouin-zone was sampled with *k*-point meshes equivalent to a $12 \times 12 \times 12$ grid in the 5-atoms unit cell. During structural relaxations, thresholds of 10^{-5} Ha/bohr on the maximum force and of 10^{-7} Ha/bohr^3 on the maximum stress have been considered.

Structural Analysis

The Goldschmidt tolerance factor, [12], $t = d_{R-O}/\sqrt{2}d_{Ni-O}$, of $RNiO_3$ compounds were determined using Nicole Benedek's tool [116] relying on a bond valence model [117] to calculate d_{R-O} and d_{Ni-O}, respectively the ideal *R*–O and Ni–O bond lengths in the cubic perovskite structure.

Symmetry-adapted mode analysis have been performed with AMPLIMODE [118, 119]. The modes are normalized to their amplitude in the $P2_1/n$ AFM-E' ground state. This normalization is such that in cubic phase (volume of the ground state) Q_R = 100% corresponds to rotation angles $\phi_x = \phi_y = 11.33^o$ (Ni-O-Ni angle of 157.33^o) , Q_R = 100% corresponds to a rotation angle $\phi_z = 12.12^o$ (Ni-O-Ni angle of 155.75^o) and Q_B = 100% corresponds to

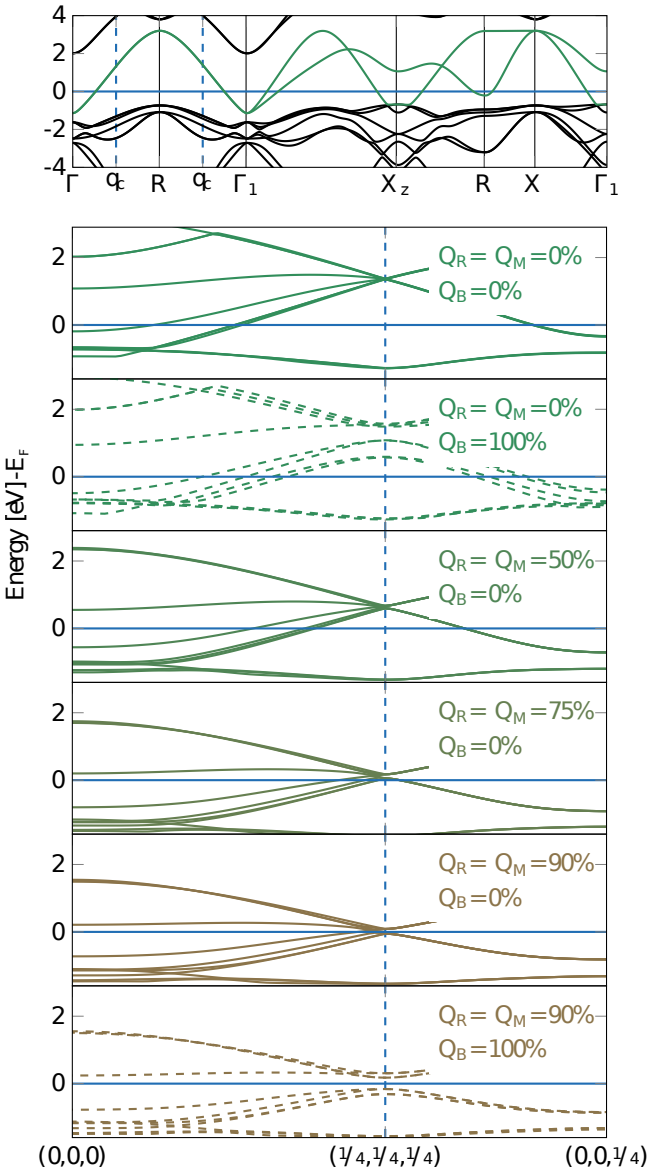

Figure 4.3 | **Electronic properties** a. Electronic dispersion curves of $YNiO_3$ along different high symmetry line of the Brillouin zone of the $Pm\bar{3}m$ phase (FM case, majority spins): $\Gamma = (0,0,0)$, $X = (1/2,0,0)$, $M = (1/2,1/2,0)$ and $R = (1/2,1/2,1/2)$. The Ni 3d e_g bands are highlighted in green. The Fermi energy corresponds to the horizontal blue line. The point $q_c = (1/4,1/4,1/4)$ is located by vertical dashed blue lines. (b) Evolution of the electronic dispersion curves around the Fermi energy E_f (FM order, majority spins) when freezing into the $Pm\bar{3}m$ phase increasing amplitudes of oxygen rotations ($Q_R = Q_M$ from 0% to 90%, lines) and eventually adding the breathing distortion ($Q_B = 100\%$, dashed lines). The graph connects high-symmetry points (coordinates in pseudocubic notations) in the Brillouin zone of the $Pbnm$ or $P2_1/n$ 20-atom cell, in which bands have been folded respect to (a).

oxygen displacements $d_O = 0.0358$.

Landau model

The Landau model parameters have been fitted for $YNiO_3$, $GdNiO_3$ and $SmNiO_3$ on first-principles data using in each case a FM cubic phase (volume of the ground state) and interpolated for the other compounds. T_{MI} was determined analytically (Supplementary Note 10.6-10.9).

4.6 Acknowledgements

The authors thank Y. Zhang, E. Bousquet, F. Ricci, M. Verstraete, J.-Y. Raty, S. Catalano and J. Varignon for fruitful discussions. This work was supported by FRS-FNRS project HiT4FiT and ARC project AIMED. J.I. acknowledges support form FNR Luxembourg Grant P12/4853155 "COFERMAT". Calculations have been performed on the Céci facilities funded by F.R.S-FNRS (Grant No 2.5020.1) and Tier-1 supercomputer of the Fédération Wallonie-Bruxelles funded by the Walloon Region (Grant No 1117545). They also took advantage of HPC resources from the French Research and Technology Computing Center (CCRT) and from the PRACE project Megapasta.

Conclusion of the article

The main breakthrough that I would like to emphasise is that both electronic and structural contributions are of great importance. Indeed, the rotation modes trigger the breathing mode by renormalising the curvature. Concomitantly, the electron-phonon coupling modifies the electronic distribution which undergoes the gap opening.

This concomitance occurs through the $\frac{1}{4}\frac{1}{4}\frac{1}{4}$ electronic propagation vector that provides a way to tune the MIT via the structural and/or the electronic properties. However, before digging deeper, I will study the optical conductivity and the magnetism in bulk Nickelates.

5 | Optical Spectrum

Alain Mercy[1], *Jordan* Bieder[1], *Wen* Yi [1] and *Philippe* Ghosez[1]

[1]Theoretical Materials Physics, Q-MAT, CESAM, University of Liège, B-4000 Liège, Belgium

Introduction to the article

On arXiv:2004.01100 and submitted on PRB Rapid Communications (2020)

Although I was able to describe the whole nickelates family with DFT+U, Peil et al.[23] suggests that DFT+U is not able to treat nickelates. Furthermore, and amazingly, they mention that our theory is wrong because it describes a second order phase transition while they cite two papers[120, 121] where one suggest a first order transition and the other suggest a second order for the small rare-earth cation. In this paper, supported by optical spectra calculations in DFT+U, I refute their arguments and try to be persuasive enough that DFT+U is totally capable of studying nickelates and equivalent systems.

5.1 abstract

Based on the electronic band structure obtained from first principles DFT calculations, the optical spectra of yttrium and neodymium nickelates are computed. We show that the results are in fair agreement with available experimental data. We clarify the electronic transitions at the origin of the first two peaks, highlighting the important role of transitions from t_{2g} states neglected in previous models. We discuss the evolution of the optical spectra from small to large rare-earth cations and relate the changes to the electronic band structure.

5.2 Introduction

ABO_3 perovskites form a broad and technologically important family of compounds[3, 122–124]. Depending of A and B cations, they can exhibit a wide range of distinct behaviors – ferroelectricity, piezoelectricity, multiferroism, metal-insulator transition, ... – making them attractive for various device applications [9, 95].

Amongst perovskites, rare-earth nickelates, $RNiO_3$, show on cooling an unusual and very complex phase diagram combining structural, electronic and magnetic phase transitions. Except for $LaNiO_3$ which remains always in a metallic paramagnetic rhombohedral phase [34], other $RNiO_3$ compounds typically show on cooling concurrent structural and electronic transitions from an orthorhombic *Pbnm* metallic phase to a monoclinic $P2_1/n$ insulating phase [4, 5, 99]. The structural distortion accompanying this metal-insulator transition (MIT) consists in a *breathing* distortion of the corner-shared NiO_6 oxygen octahedra, yielding a 3-dimensional checkerboard arrangement of large (Ni_L) and small (Ni_S) cages compatible with a related charge ordering. The temperature of the MIT is moreover directly linked to the *R* cation size, or equivalently to the Goldschmidt tolerance factor[12], and ranges from 100 K for $PrNiO_3$ to 600 K for $YNiO_3$ [122, 125]. Additionally, these compounds also show a low-temperature magnetic transition from paramagnetic to an E'-type antiferromagnetic order [25]. Depending again of the cation size, this magnetic transition can be either independent (small cations) or concurrent (large cations) to the structural and electronic transitions.

There has been a long debate about the origin and mechanism of the MIT in these compounds[126]. It was sometimes considered as a Mott-Hubbard transition[100]. In line with the appearance of the breathing lattice distortion, it was also related to a formal d^8/d^6 charge ordering at the nickel sites, requiring a negative U [104, 127]. It was however further shown that the electronic configuration is better described by a d^8/d^8L^2 occupation for the two nickels. From this, the MIT has been seen as a site-selective Mott transition [21, 128]. Relying on its strong dependence with oxygen rotation motions, the MIT was also recently re-interpreted as a structurally triggered Peierls transition, linked to an electron-phonon coupling [17]. Although some controversies remain, these views are not necessarily in contradiction and it seems now accepted that a proper picture[126] should consider together electronic and atomic degrees of freedom [16, 17, 23].

One concrete way of probing experimentally the metal-insulator transition of nickelates is from optical conductivity measurements [102, 129, 130]. Indeed, the opening of a gap and the changes in the electronic structure of the conduction bands taking place at the MIT significantly affect the optical spectrum. Moreover, the effect of magnetism on the optical conductivity can also be probed [37]. One limitation of optical conductivity measurements is however that, although they successfully provide a global view on the electronic structure and its modifications, they do not provide direct access to a "state-by-state" analysis. Proper interpretation of optical spectra therefore typically requires to combine measurements with electronic band structure calculations allowing to assign measured peaks to specific electronic transitions.

Optical spectra of nickelates [102] have, up to now, only been reported on thin films[102, 129, 130]. They appear characterised, close to the conductivity edge, by a first main peak with a shoulder followed by a second peak in a range of 2 eV. Other more complicated features then appear at higher energies, but are however sensitive to the substrate [130].

Relying on DMFT calculations[24] restricted to Ni-e_g states only, the first peak was assigned to inter-site electronic transitions from Ni_L to Ni_S sites at the Mott gap while the second peak was interpreted as coming from the opening of a Peierls pseudogap at larger energy linked to the breathing distortion[102, 128].

As recently discussed, density functional calculations reproduce rather the MIT transition as a Peierls-type transition. Relying on that, it was recently stated [23] that the DFT band structure is not compatible with the observed optical spectra of nickelates, further suggesting that DFT cannot properly handle the physics of these compounds.

Here, we show that DFT calculations correctly reproduce the experimental optical spectra of nickelates, properly accounting for the first peak and its shoulder as well as the second peak. Doing so, we further clarify that the second peak was erroneously assigned to the Peierls pseudo-gap. We highlight that the second peak is related to t_{2g}-e_g transitions, missed in previous analysis based on a simple low-energy model including e_g levels only.

5.3 Methods

Our calculations are performed within the DFT[47, 48] formalism as implemented in the Abinit software package[43–45, 131]. We work within the Projected Augmented Wave (PAW) method [57], relying on the atomic data from the JTH table[62]. The following valence and semi-core electrons are explicitly included in the calculations : Y $5s^2 5p^6 5d^1 6s^2$, Nd $5s^2 5p^6 5d^1 6s^2$, Ni $3s^2 3p^6 3d^9 4s^1$ and O $2s^2 2p^4$. We use the GGA-PBE-sol[115] exchange-correlation functional. In order to better describe the electronic correlations of the localized Ni $3d$ electrons, a mean field Hubbard correction is included in the Lichtenstein formalism[114] as implemented in Abinit [67]. We adopt the Hubbard correction $U = 1.5$ eV which was previously shown to provide accurate description together of the structural, magnetic and electronic properties of $YNiO_3$ [17]. The same value is then used for $NdNiO_3$, with the assumption that it is only slightly dependent of the tolerance factor[16]. Calculations are moreover performed within the collinear spin approximation.

We adopt a plane-wave basis set with an energy cut-off of 24 Ha and a grid of special k-points equivalent to $12 \times 12 \times 12$ in the 5-atoms unit cell. This guarantees a level of convergence of 1 meV/f.u. on the total energy. The relaxations are converged up to a maximum force of 5.10^{-5} Ha/bohr and a maximum stress of 5.10^{-7} Ha/bohr^3. In order to correctly describe the insulating and metallic phases, we use a Fermi-Dirac occupation of the electronic states, with a smearing temperature of 300 K.

The real part of the optical conductivity is computed using the Kubo-Greenwood formalism[85]. Using Agate [ref], the origin of the peaks is then related to specific electronic transitions that are analysed from density of states projected on specific atomic orbitals. From that, an interpretation is provided in terms of e_g/t_{2g} transitions. Although conventional and appealing, this interpretation has to be taken with care and considered as only qualitative. Indeed, assessing the role of individual atomic orbital in the optical spectra is complicated

Modes	$YNiO_3$		$NdNiO_3$	
	DFT	EXP	DFT	EXP
R_2^-	0.124	0.127	0.091	0.072
R_5^-	1.494	1.492	1.040	1.146
M_2^+	1.132	1.153	0.532	0.807

Table 5.1 | Comparison of the theoretical (DFT) and experimental (EXP) amplitudes (Å) of the dominant lattice distortions with respect to the cubic reference in the $P2_1/n$ AFM-E' phase of $YNiO_3$ ($t = 0.92$) and $NdNiO_3$ ($t = 0.96$), as quantified with Amplimodes [118, 119]
.

by the amount of transitions (various k-points and energy bands) contributing to the optical spectrum at a given energy. Furthermore, the rotation and deformation of the oxygen cages make only approximate the decomposition into e_g/t_{2g} states. Finally, we have to keep also in mind the strong hybridisation between Ni 3d and O 2p states. The most hybridized t_{2g} and e_g levels are marked by a * in what follows.

5.4 Results and Discussion

5.4.1 Ground state properties

Because of the strong interplay between structural, magnetic and electronic degrees of freedom in rare-earth nickelates, we cannot address their electronic and optical properties without evoking at first their structural and magnetic properties.

The high-temperature prototypical reference phase of $RNiO_3$ nickelates is a priori the $Pm\bar{3}m$ cubic perovskite structure but it should only appear at very high temperatures and has never been observed experimentally. The observed high-temperature metallic phase is of $Pbnm$ symmetry. It appears as a small distortion of the cubic reference involving mainly rotations (M_3^+ mode) and tilts (R_5^- mode) of the NiO_6 octahedra (see Table 5.1 for $NdNiO_3$ and $YNiO_3$). At the MIT, the system evolves from $Pbnm$ to $P2_1/n$ symmetry. This $P2_1/n$ phase differs from the $Pbnm$ phase by the appearance of the breathing distortion of the oxygen cages (R_2^- mode) yielding the appearance of large (Ni_L) and small (Ni_S) NiO_6 cages distributed according to a rocksalt pattern.

Here, all the calculations are done in the E' antiferromagnetic (AFM-E') ground state configuration corresponding to a ($\uparrow$, 0, $\downarrow$, 0) spin arrangement with a propagator vector of ($\frac{1}{2}$,0,$\frac{1}{2}$) in the $Pbnm$ setting. As previously discussed [17], DFT calculations predict the correct magnetic and structural ground states. Moreover, they provide very accurate description of the structural distortions (see Table 5.1) and the obtained values for the magnetic exchange parameters give a Néel temperature in good agreement with experimental data[17].

In the cubic reference phase, according to the octahedral environment of the nickel atoms, the crystal field already splits the Ni 3d levels into three lower-energy t_{2g} and two

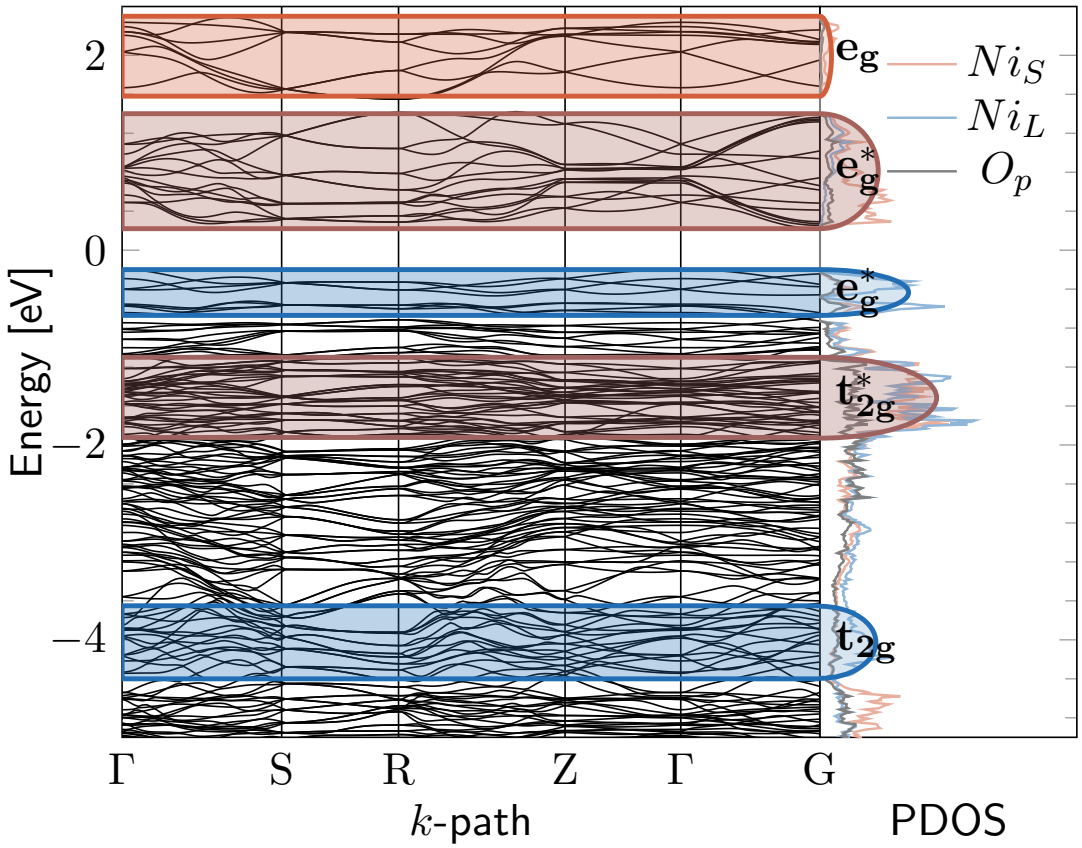

Figure 5.1 | Electronic band structure of the insulating $P2_1/n$ AFM-E' phase of $YNiO_3$ as obtained from DFT calculations and related projected density of states (pDOS). For oxygen, the projection is illustrative and made on a single atom. Interpretation in terms of e_g and t_{2g} states is highlighted thanks to colored ellipse. The color is defined from the dominant large (blue) or small (red) nickel contribution.

higher-energy e_g states. In the $Pbnm$ and $P2_1/n$ phases, oxygen rotations and tilts and related cell-shape deformations further increase the splitting between t_{2g} and e_g states. The $t_{2g} - e_g$ splitting being linked both to the Ni-O distance and the amplitude of the structural distortions, it increases from large to small rare-earth atom compounds.

We focus here on the optical spectra of the insulating $P2_1/n$ AFM-E' phase. The electronic band structure in this phase and related projected density of states are depicted in Figure 5.1 for $YNiO_3$. Although some minor differences can appear in the distributions of the highest e_g states, this figure is representative of DFT calculations. In this phase, the valence states close to the Fermi level are dominantly e_g states at Ni_L sites. Moreover, in such DFT calculations, the lowest conduction states are dominantly e_g states of the Ni_S site while, contrary to another study, empty e_g states at Ni_L are at higher energy. The gap does therefore not appear as a Mott gap between e_g states at Ni_L but rather as a Peierls gap between e_g states from Ni_L to Ni_S, directly proportional to the amplitude of the breathing distortion. Since the latter is triggered by rotation and tilt motions, the gap increases as the tolerance factor decreases. We further notice that activation of the breathing distortion also opens a pseudo-gap in the upper e_g conduction bands.

5.4.2 Optical Spectra

Since the electronic band structure of nickelates is sensitive to the tolerance factor, we compare now optical spectra for representative compounds with small and large rare-earth cations. We consider at first $NdNiO_3$ ($t = 0.96$) and compare our results to experimental data from Ruppen et al.[102]. Then, we study the case of $YNiO_3$ ($t = 0.92$) and compare the spectra of both compounds, relating changes to the evolution of the band structure.

$NdNiO_3$

The projected electronic density of states around the Fermi level and the optical spectrum of $NdNiO_3$ are reported in Fig. 5.2. We identify a first main peak (peak A in red) in the optical spectrum at an energy of about 0.8 eV, consistently with the value of the energy gap. This peak is associated to transitions from the occupied e_g^* states of Ni_L to the unoccupied e_g^* states of Ni_S (across the Peierls gap) as shown in the projected band structure on Fig. 5.2*a*. Then, a second peak (peak C in blue) appears at an energy of about 1.6 eV and is related to transitions from t_{2g}^* states at Ni_S to the lowest unoccupied e_g^* states of Ni_S.

This assignment of the first and second peaks is different from the intepretation of Ruppen *et al.* [102] who were relating the first peak to transitions between e_g states at Ni_L (Mott gap) and the second peak to transitions between e_g states at Ni_L and Ni_S (Peierls pseudogap).

It is worth mentioning that our DFT calculations also reproduce a pseudogap in the unoccupied e_g states and we identify a peak (B in green) related to transitions from e_g^* states at Ni_L to e_g states above the pseudo-gap, in the same range of energy, but the intensity related to these transitions is much too small to explain alone the second peak.

Then, we finally identify additional peaks at higher energies, originating from two main kinds of transitions. The peaks D (purple) and E (pink) in figure 5.2 correspond to transitions from occupied t_{2g}^* at Ni_S to e_g states above the pseudo-gap and from deeper t_{2g} states at Ni_L to e_g^* just above the gap, respectively.

Comparison with experimental data (inset in Fig. 5.2b) highlights that, contrary to what was sometimes suggested[23], DFT optical spectra are not incompatible with measurements. They not only reproduce the first and the second peaks but even the intriguing shoulder observed in the second part of the first peak. From our calculations, this shoulder is related, on the one hand, to transitions from occupied e_g^* states to the upper part of empty e_g^* states and, on the other hand, to transitions from the states between the labelled e_g^* and t_{2g}^* bands (more related to the t_{2g}^* states) and the empty e_g^* bands.

It should moreover be noticed that, as previously discussed, the fixed value of U used in the present study was not optimized for $NdNiO_3$ but simply transferred from $YNiO_3$. As highlighted in Table 1, this yields a small overestimate of the breathing distortion. Slightly reducing U, would reduce the breathing distortion and the bandgap and would yield slightly more spread peaks, still improving the quantitative agreement with experiment.

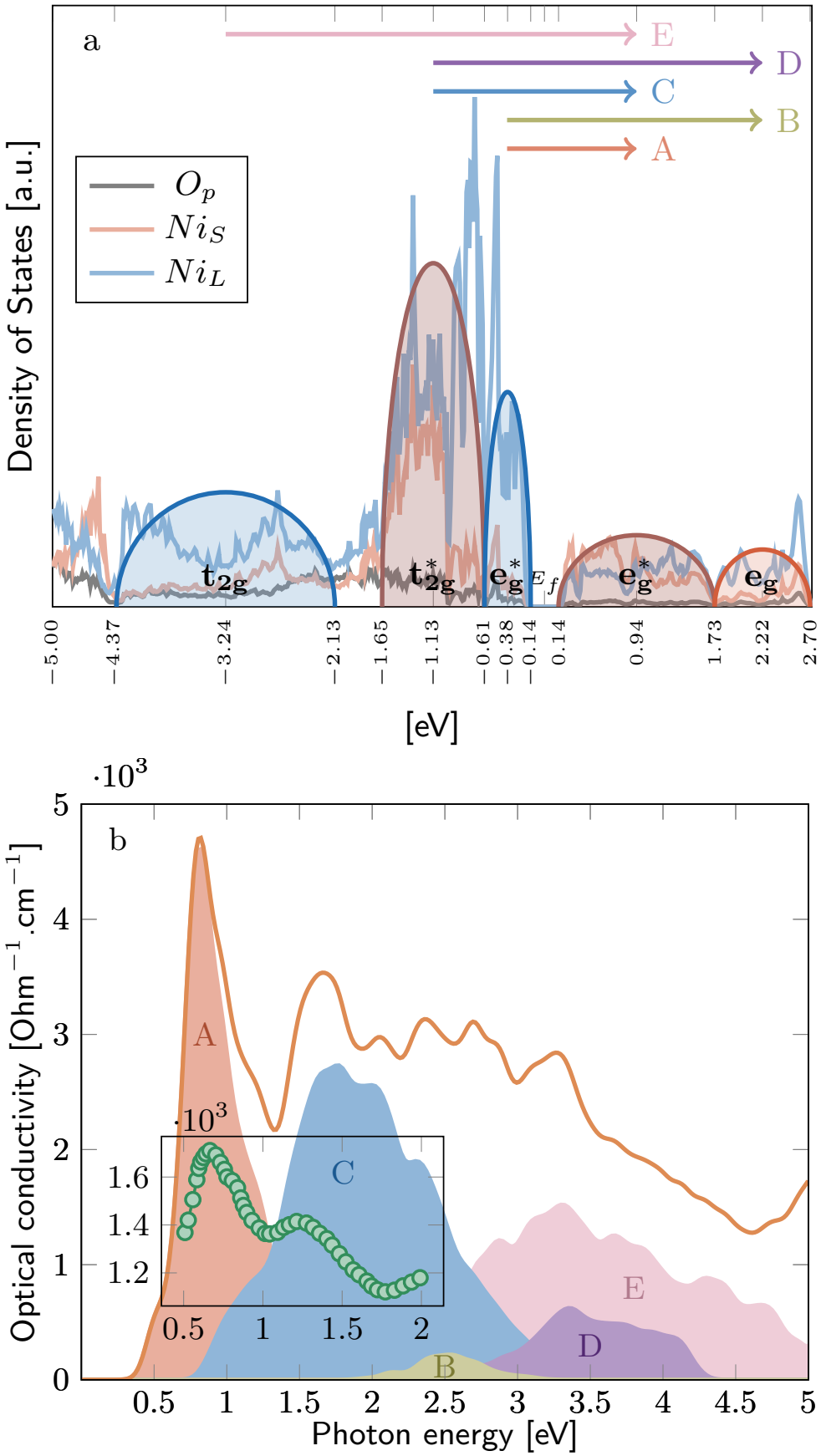

Figure 5.2 | (a) Projected DOS of $NdNiO_3$ in its $P2_1/n$ AFM-E' ground state, highlighting the main electronic transitions contributing to the optical spectrum. Only one oxygen contribution is shown. (b) Optical Spectrum of $NdNiO_3$ in its $P2_1/n$ AFM-E' ground state and related individual contributions, as labelled in (a). Inset: Experimental optical spectrum at 100K[102].

Although it was not necessarily guarantee nor obvious, this illustrates that the DFT band structure of rare-earth nickelates is compatible with optical measurements on these compounds. It also highlights the importance of considering explicitly t_{2g} states while interpreting these data, which was missing in some previous models restricted to e_g states.

$YNiO_3$ and comparison

The projected electronic density of states around the Fermi level and the optical spectrum of $YNiO_3$ are reported in Fig. 5.3. The shape and interpretation of the peaks are similar to $NdNiO_3$. Now, the location of the peaks is slightly modified according to the evolution of the electronic band structure.

Since the breathing distortion (Table 5.1) and the bandgap are larger for small rare-earth atoms, the first peak appears at a slightly larger energy for $YNiO_3$ than $NdNiO_3$ (see Fig. 5.4 for the comparison). This is in line with the experimental evolution of the optical spectrum from $NdNiO_3$ to $SmNiO_3$ [102].

Then, the evolution of the second peak is even more drastic. Moving from $NdNiO_3$ to $YNiO_3$, the Ni–O distances are reduced and the oxygen rotations are increased yielding a larger $t_{2g} - e_g$ splitting and moving the C peak at larger energy.

Finally, as can be seen in Fig. 5.4, due to various other additional contributions, the modification of the full spectrum from $NdNiO_3$ to $YNiO_3$ is even more dramatic than what would have been be anticipated from the shift of the A and C peaks only.

5.5 Conclusion

In this paper, we have reported the optical spectra of rare-earth nickelates, deduced from the DFT electronic band structure reproducing the bandgap as a Peierls gap. Contrary to what was recently suggested [23], we show that the optical spectrum of $NdNiO_3$ is in fair agreement with available experimental data and reassigned the peaks highlighting the role of t_{2g}-e_g transitions neglected from previous models. We also highlight significant change of the position of the second peak from large to small rare-earth nickelates.

5.6 Acknowledgement

We thank Vanina Recoules for helpful discussions on spectroscopy. This work was supported by the ARC project AIMED from University of Liège and the PDR project PROMOSPAN from F.R.S.-FNRS Belgium. Computational resources were provided by the Consortium des Equipements de Calcul Intensif (CECI), funded by the F.R.S.-FNRS under the Grant No. 2.5020.11 and the Tier-1 supercomputer of the Fédération Wallonie-Bruxelles funded by the Walloon Region under the Grant No. 1117545.

A.M. and J.B. contributed equally to this work.

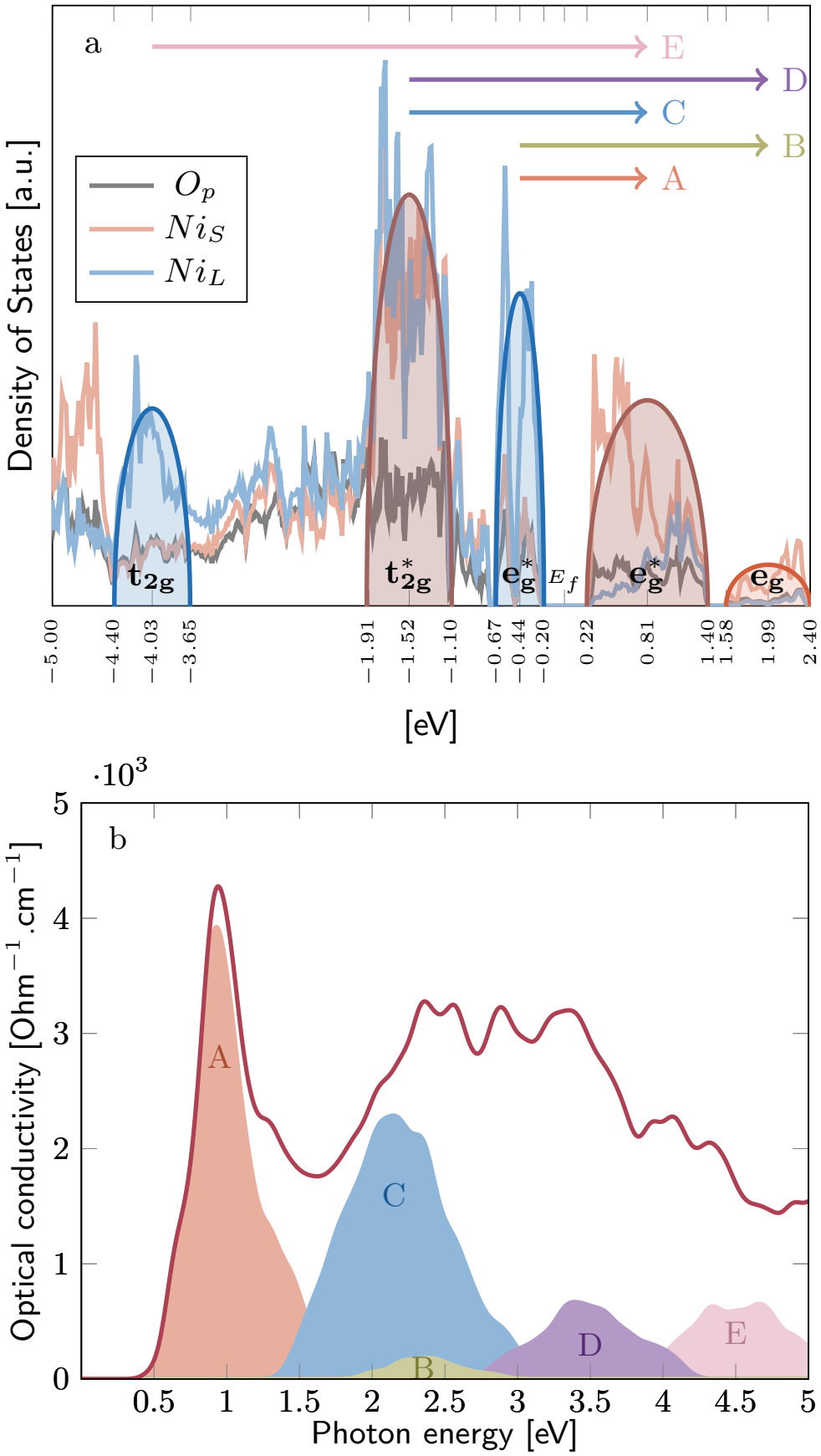

Figure 5.3 | (a) Projected DOS of $YNiO_3$ in its $P2_1/n$ AFM-E' ground state, highlighting the main electronic transitions contributing to the optical spectrum. Only one oxygen contribution is shown. (b) Optical spectrum of $YNiO_3$ in its $P2_1/n$ AFM-E' ground state and related contributions as labelled in (a).

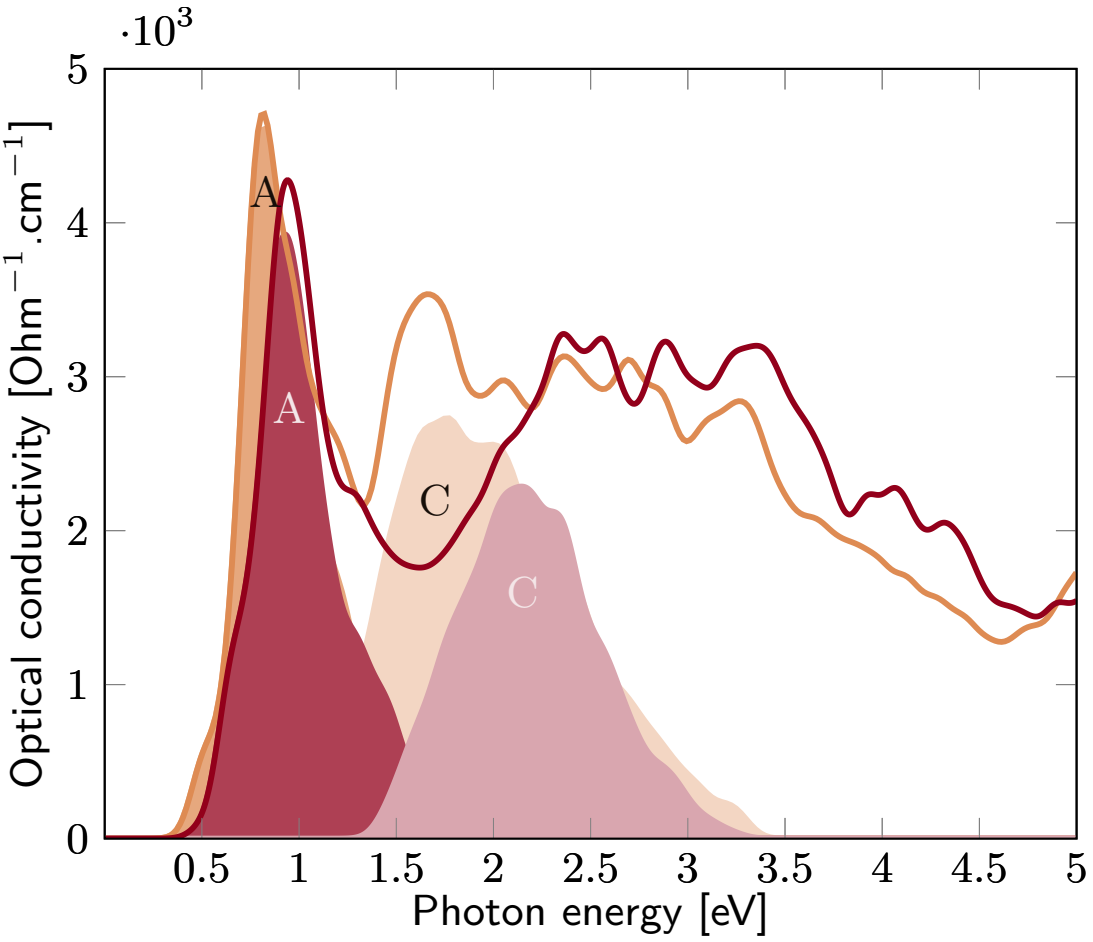

Figure 5.4 | Comparison of the optical spectra of $NdNiO_3$ (orange) and $YNiO_3$ (red) in their $P2_1/n$ AFM-E' ground state.

Conclusion of the article

In this paper, I have shown that DFT+U is capable of reproducing the experimental optical spectra. In our framework, the characteristic double peaks is characterised by both t_{2g} and e_g bands. To rub it in, in the next chapter, the focus will be on the magnetic properties.

6 | Magnetic Properties

Alain Mercy[1], *D.* Gawryluk[2], *F.* Damay[3], *S.* Rols[4], *J.* Embs[5], *Y.* Zhang[1], *J.* Bieder[1], *D.* Sheptyakov[5], *E.* Canevet[5], *S.* Petit[3], *M.* Medarde[2] and *Philippe* Ghosez[1]

[1]Theoretical Materials Physics, Q-MAT, CESAM, University of Liège, B-4000 Liège, Belgium [2]Laboratory for Multiscale Materials Experiments,Paul Scherrer Institut, 5232 Villigen PSI, Switzerland [3]Laboratoire Léon Brillouin, CEA, CNRS, Université Paris-Saclay, CE-Saclay, Gif-sur-Yvette, France [4]Institut Laue Langevin, 71 avenue des Martyrs, CS 20156 -38042 Grenoble CEDEX 9, France [5]Laboratory for Neutron Scattering and Imaging, Paul Scherrer Institut, 5232 Villigen PSI, Switzerland

Introduction to the article

This paper is a draft to be submitted. For submission, more details will be added to complete the study.

The role of magnetism on the small rare-earth cation in the Nickelates family seems secondary (see chapter 4). However, it plays a role in the nickelates properties as clearly discussed in literature by the mean of the optical spectra (see chapter 5. Indeed, the optical spectra are affected due to the change in the electronic distribution for small rare-earth cations at the occurrence of the magnetic transition. Furthermore, they even play a major role in the triggering of the MIT for large rare-earth as already explained in chapter 4. Thus, here, I will focus on characterizing the magnetic ground state configuration in Nickelates which is under active debates as discussed in the introduction of the current chapter. For this purpose, I will make a simple Heisenberg model describing the magnetic properties of Nickelates. Taking benefits of this additional property analysis, the capability of DFT+U to deal with nickelates will be reinforced.

Moreover, we highlight that the obtained quantitative theoretical results are fully compatible with experimental results, what allows to discard some previously suggested models.

6.1 Abstract

In materials intrinsically close to the boundary between localized and itinerant electronic behaviour, the increasing mobility of the electrons by approaching this limit may have an important impact in the magnetic interactions and hence in the magnetic order. Perovskite

nickelates, where controlled A-site cation tuning allows to approach this limit from the localized side, constitute a puzzling example were the periodicity of the magnetic order is preserved in the full localized region. Here we investigate the nature of the magnetic ground state of $YNiO_3$, representative of the most localized side of the nickelate phase diagram. By combining elastic and inelastic neutron scattering with ab-initio calculations we show that both, theory and experiment are consistent with a collinear antiferromagnetic ground state with half of the Ni sites carrying zero magnetic moment. The magnon excitations are well described by a Heisenberg model involving 2^{nd} and 4^{th} neighbour exchange interactions, whose values, determined ab-initio, provide an excellent agreement with the experimental data.

6.2 Introduction

The coupling between magnetic moments in insulating oxides with on-site Coulomb energies U much larger than the bandwidth W (i.e. $W/U << 1$ limit) is generally well described in terms of the superexchange interactions. This mechanism is however expected to break down when approaching the crossover from localized to itinerant behaviors. Moreover, double exchange or RKKY interaction, characteristic of magnetic metals, may coexist in the crossover region.

The family of $RNiO_3$ nickelate perovskites (with R either a rare earth element or Y, Pb, Bi, Tl) appears as an ideal playground to investigate this region without doping. While on the one side $LaNiO_3$ is an itinerant paramagnetic metal and on the other side $TlNiO_3$ is a localized antiferromagnet insulator, other $RNiO_3$ compounds display a spontaneous metal-insulator transitions (MIT) at temperatures T_{MIT} that, depending of the size of the R cation, ranges from 130 to 600 K. This MIT is accompanied with a structural breathing distortion and can be concomitant or not with a magnetic transition to a unique AFM order. T_{MIT} can further be finely tuned by either chemical substitution, high pressure, electrical field, dimensional confinement, epitaxial strain or tilt engineering. This makes these compounds attractive not only for fundamental investigations but also for numerous applications, including thermochromic devices and resistive memories as summarized by Catalano et al.[126].

From a fundamental perspective, some open questions remain regarding the physics of nickelates. Some of them relate to the nature of the mechanism(s) at the origin of the spontaneous electronic localization observed below T_{MIT}. The MIT is often explain as a site selective Mott transition[21] but it was recently re-intrepreted as a structurally-triggered Peierls instability[17]. Other questions concern the exact nature of the AFM order. It is also not clear how superexchange, which is usually the main magnetic interaction in insulators, may be affected by the intrinsic proximity of the RNiO3 family to the metallic state.

The magnetic structure, believed to be common to the whole family, has been reported for R =Pr, Nd, Sm, Eu, Dy, Ho and Y. It is characterized by the propagation vector k = $(\frac{1}{4}, \frac{1}{4}, \frac{1}{4})$

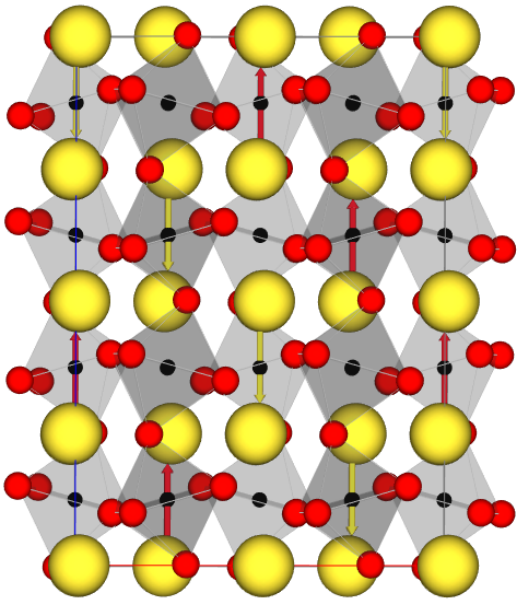

Figure 6.1 | Magnetic Ground state of $YNiO_3$ with a magnetic propagation vector k = $(\frac{1}{4}, \frac{1}{4}, \frac{1}{4})$with half of Nickel sites with no magnetic moment.

referred to the pseudocubic parent perovskite cell, see [112] and Fig. 6.1, and presents a number of very peculiar characteristics.

The first of them is the remarkable stability of the magnetic propagation vector against the "degree" of charge/bond disproportionation, which changes continuously along the series[132].The increase of the Ni-O-Ni superexchange angle of more than 20 degrees by moving from Lu to La, adding to the change of the amplitude of the magnetic moment, implies drastic differences in the strength of exchange interactions across the series, which, surprisingly does not result in any change of the magnetic periodicity. As a comparison, several different magnetic ground states with both commensurate and incommensurate propagation vectors are observed in the isostructural RMnO3 family, were a similar variation of the superexchange angle is observed between the two end members. This could be due to the fact that superexchange, - in principle the expected leading magnetic interaction in insulators- may slowly break down in the RNiO3 family by moving from Lu to La due to the increasing stability of the metallic state. Recent work by Goodenough et al. [17] suggests that this could be the case for nickelates with R = Sm, Nd and Pr, for which other, longer-range interactions typical from metals may become significant. (mention Keimer)

6.3 Crystal structure at 10K

The evolution of the $YNiO_3$ crystal structure across the MIT has been investigated in the past using neutron powder diffraction [97, 120], and the lattice anomalies at T_{MIT} interpreted in terms of changes in the Ni-O interatomic distances and Ni-O-Ni superexchange angles. Here we use instead the symmetry-adapted distortion mode formalism, which enables the

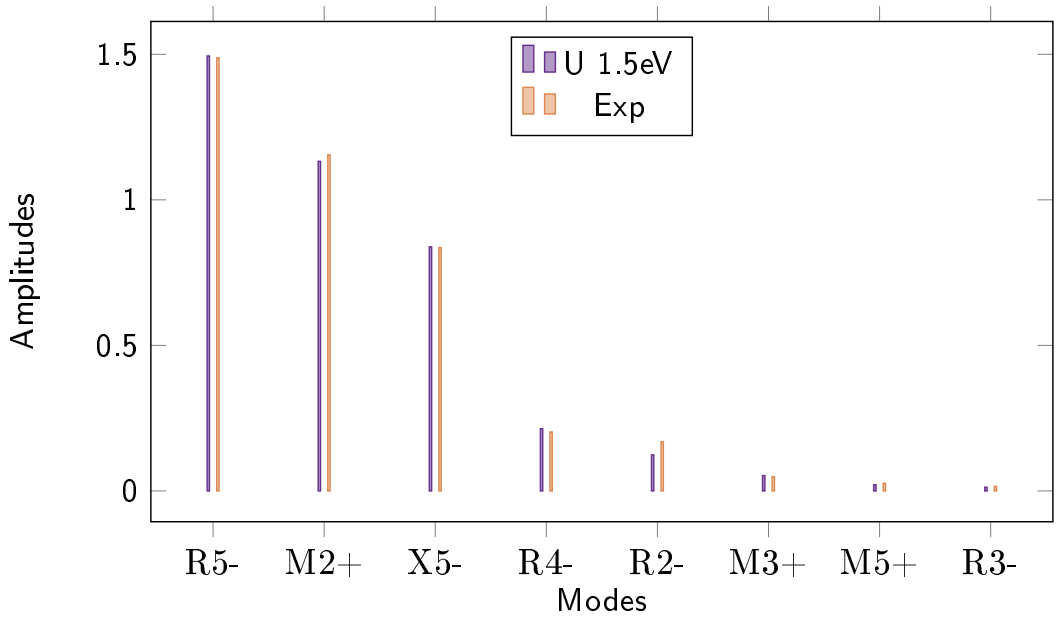

Figure 6.2 | Comparison of the experimental (Orange) and theoretical (Purple) structural properties in term of modes.

decomposition of the global distortion of the crystal structure into contributions from the different modes with symmetries given by the irreducible representations (*irreps*) of $Pm-3m$, the space group of the undistorted perovskite structure.

In the metallic phase ($T > T_{MIT} = 600K$, space group (SG)$Pbnm$), the main contribution to the orthorhombic distortion comes from the appearance of out-of-phase (R_5^-) and in-phase (M_2^+) rotations of the octahedral oxygen cages surrounding the nickel sites, with smaller contribution of other distortion modes of X_5^-, R_4^- and M_3^+ symmetry (see Fig. 6.2). Below T_{MIT} the symmetry of the lattice changes from orthorhombic to monoclinic (SG $P2_1/n$). The leading structural response to the electronic localization is the appearance of a breathing distortion of R_2^- symmetry involving the existence of alternating NiO_6 octahedra with long and short average Ni-O distances [120]. Other distortion modes of R_3^- and M_5^+ symmetry are also allowed in the insulating phase, but their amplitudes remain marginal even at RT, i.e., 300 degrees below T_{MIT} [17, 97, 120]. A comparison between the experimental mode amplitudes thanks to our neutron powder diffraction at 10K and those calculated using DFT is shown in Fig. 6.2. No significant deviations from the $P2_1/n$ symmetry, predicted to occur in the Néel state ($T < T_N = 150$ K) [30, 133], could be observed within our experimental resolution. Furthermore, it has to be noticed that the agreement for the lattice constant between experimental and theoretical results are below 0.8% and thus excellent.

6.4 Magnetic structure

The first, and to date only neutron diffraction investigation of the $YNiO_3$ magnetic structure was carried out by Alonso and co-workers in 1999 [97], who described it using the

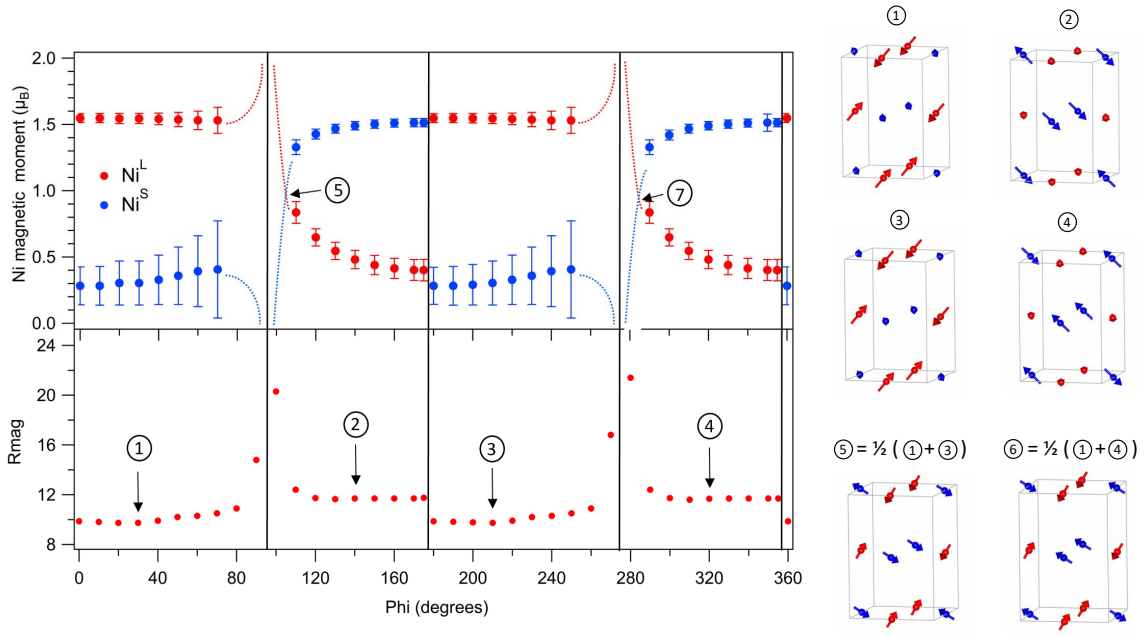

Figure 6.3 | Stability of the magnetic structure. On the left: fit of experimental data with at the top the magnetic moments of the nickel sites and at the bottom the corresponding "Rmag" factor. On the right: Magnetic configuration linked (thanks to the bullets with number) to the corresponding fit from left.

collinear model [98]. Here we present the first experimental reinvestigation of the $YNiO_3$ magnetic ground state since 20 years, with particular emphasis in the compatibility of the two proposed models with the experimental data. For this purpose we took advantage of the availability of a powder sample of excellent quality and much larger (~ 12 g) than the specimen used in ref. [97] (~ 800 mg). We also used a longer wave length (λ = 3.80008), a smaller $2\theta_{step}$ (0.1°) and a very high counting statistics (36 h), aimed to improve the visibility of the magnetic reflections and to decrease the degree of superposition in the powder diffraction patterns.

To our best knowledge, the only rigorous discussion of the possible magnetic structures of the Ni sublattice in $RNiO_3$ perovskites, characterized by the propagation vector $\mathbf{k}$ = (1/2, 0, 1/2) was reported by J.L. Garcia-Muñoz et al. in 1994 using the SG *Pbnm*.[98]. Here we revisit this analysis for the monoclinic SG $P2_1/n$. We also investigate the stability of the different models and their implication for the exchange interactions at the origin of the magnetic order.

As shown on picture 6.3, for a given site (either Ni^L or Ni^S) there is a restriction on the relative orientation of the two symmetry-related Ni moments: they can only be collinear, either parallel, or anti-parallel. Their absolute direction is in contrast no restricted.

Furthermore, the relative orientation between the Ni^L and Ni^S magnetic moments is not subject to any symmetry constrain and has to be determined experimentally. This is an important difference with the previous analysis using *Pbnm*, where it could only form an

angle of 0, $\pi/2$, or π.

Then ,the splitting of the *Pbnm* orbit 4*b* makes the Ni^L and Ni^S magnetic moments symmetry-unrelated. Hence, they can take completely different values. In contrast, the *Pbnm* symmetry contemplates only two possibilities: all moments identical, or, in the case on non-equal moment solutions, two of them equal to zero.

6.4.1 Comparison with the experiment

Next, we checked the compatibility of the experimental data with the magnetic structures.

Given the absence of general extinction conditions associated to the propagation vector $\mathbf{k} = (\frac{1}{2}, 0, \frac{1}{2})$ in the *Pbnm* setting, a preliminary trial-and-error series of fits using configurations fulfilling the above mentioned conditions was used to explore the absolute orientation of the Ni magnetic moments. We found that for both Ni sites, the moments are most likely confined to the **a-c** plane, perpendicular to the monoclinic screw axis 2_1. This finding, in agreement with previous reports, was confirmed subsequently suggesting a high on-site anisotropy for this specif direction.

Next, we explored the coupling between magnetic moments of the Ni^L and Ni^S sites with phases 0 and π, i,e, those giving rise to collinear arrangements. There are four possibilities as depicted on figure 6.3 right. We note that *all* of them are combinations of basis functions belonging to different *irreps*. This contrasts with the behaviour expected in a second order phase transition, were the order parameter (here the staggered magnetization) is usually described with a single *irrep*. We note also that the problem disappears if one of the two Ni sites does not carry magnetic moment! Moreover, if we impose a zero magnetic moment on the small nickel site, the Rmag factor for the fit is close to be not change and still better than the non collinear configuration.

In a third series of fits, we explored the evolution of the goodness of the fit for non-collinear arrangements, i.e., with arbitrary phases ϕ between the magnetic moments of Ni^L (red) and Ni^S (blue) sites (note that the phase between two blue (two red) sites along **a** and **c** is given by the propagation vector). Only four values of ϕ can reproduce the neutron powder diffraction data: $\phi = 0$, $\pi/4$, π and $\phi = 3\pi/4$. The first and the third correspond to the collinear orders discussed in the previous paragraph, whereas the second and the fourth are non-collinear square spirals. In the case of the non-collinear configuration, there is only one possibility where the magnetic moments are equals. Indeed, if not, the magnetic moment for the small nickel is larger than the large nickel which is not physic (not compatible with nowadays DFT+U and DMFT results). Furthermore, if all the nickel sites are magnetic, the symmetry is $P2_1$ and not yet observed at the knowledge of the authors. If observed, this would be a clear information to suggest a magnetic configuration with a magnetic moment on each nickel site and a polar GS.

The fits, where the modulus of the Ni^L and Ni^S magnetic moments were refined independently for every value of ϕ, reveal also an interesting fact, not reported previously: the

collinear model requires the Ni^L and Ni^S moments to be as different as possible, whereas a fit with the square spiral model is only possible if the two moments are identical.

From all those results, the best ground state configuration seems to have the propagation vector $k = (\frac{1}{4}, \frac{1}{4}, \frac{1}{4})$ with half of the nickel sites (small nickel) with no magnetic moment. Furthermore, a preferential direction (ac plane) suggests a large anisotropy for the magnetic and large nickel site.

6.4.2 DFT results

Using the best value of the Hubbard term U equals to 1.5 eV[17], the importance of the fourth neighbours interaction and the structural distortion allowing a $\frac{1}{2}0\frac{1}{2}$ magnetic propagator in the *Pbnm* setting is highlighted. Furthermore the role of the second neighbours will be discussed too.

As already discussed in the previous section, the magnetic ground state can be seen as a first step as ↑↑↓↓ chains along the three pseudocubic directions. Starting from this magnetic configuration in collinear DFT calcluation, the structure relaxes in a ↑ 0 ↓ 0 configuration instead of ↑↑↓↓ (see figure 6.1). It means there is no magnetic moment on the nickel in the small octahedral cages which is fully compatible with the experimental results of the previous section.

The starting configuration breaks the inversion symmetry giving the P21 space group. However, the obtained result implies the maintain of the inversion symmetry and the P21n phase so. The Ground state of $YNiO_3$ is non polar so.

The next discussed results quantitatively describe this magnetic configuration from DFT simulations that will be used to characterize and explain the further experimental results.

Heisenberg model

To understand how much the magnetic interaction is important or not in this material, we decided to use the Heisenberg model given by:

$$E_{ex} = -2 \sum_{i,j} J_{ij} S_i S_j \tag{6.1}$$

where E_{ex} is the exchange Energy and J_{ij} is the exchange interaction between the magnetic moment S_i on site i and the magnetic moment S_j on site j.

Four different models are tested. We call them the 2J, 4J, 5J and 6J models. All of them impose a rock salt configuration for the magnetism because the ab initio results inform us that half of the nickel atoms have no magnetic moment. In the usual "cubic-like" point of view, we consider the second and fourth neighbours which are magnetic. Indeed the first and third neighbours have no magnetic moment as already mentioned.

The 2J model supposes an isotropic interaction for both second and fourth neighbours. It means a "cubic-like" symmetry as depicted on figure 6.4. Thus, J_2 corresponds to the

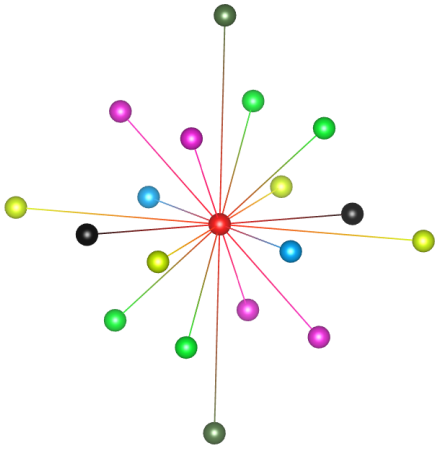

Figure 6.4 | Representation of the exchange interactions between Ni atoms. Because of the rock-salt configuration, Ni with no magnetic moment are not represented. The Black-Red lines correspond to J_{2a} and the Blue-Red lines to J_{2b}. These are the in plane second neighbours interactions. Looking at the Green-Red lines and the Purple-Red lines, we have the J_{2c1} and J_{2c2} out-of plane second neighbours interactions respectively. About the fourth neighbours interactions we have the in plane (J_{4ab})represented by the Yellow-Red lines and the out-of plane (J_{4c}) by the Khaki-Red lines.

interaction between the second neighbours and J_4 between the fourth ones. The main problem with the 2J model is the inability to make the difference between the S1, S2, T1 and T2 magnetic configuration.

Concerning the 4J and the 5J models, the fourth neighbours interaction is still supposed isotropic. Only one J_4 is needed in these cases. However, the second neighbours interaction is not. Indeed, looking at the S1 magnetic GS, we clearly see that the interaction along the a and b direction are different (AFM and FM respectively). In such a way, a J_{2a} and a J_{2b} terms are added to describe this anisotropy linked to the difference between the size of the a and the b lattice parameters. Furthermore, the interaction distance for the out-of plane atoms is different too. Thus, the J_{2c} term is added in the Heisenberg expression and we get the 4J model. At this level we have a "P_{bnm}-like" symmetry. On figure 6.4, we see this behaviour (see black and blue directions). Using the 4J model we can make the difference between the (S,T)1 and the (S,T)2 magnetic configurations. Of course, the main difference is the propagation along the a and b axes of the magnetism. Indeed, the (S,T)1 type are FM along b and AFM along a. A contrario, (S,T)2 type are FM along a and AFM along b. A weakness in the 4J model is not solved yet. Doubtlessly, we are able to make the difference between the (S,T)1 and the (S,T)2 state but not between the S and T types yet.

To do so, the 5J model is necessary to describe the S1 and T1 difference (or S2 and T2). We consider an anisotropy between out-of plane atoms (J_{2c} is split). The atoms along the 111, 1-11, -11-1 and -1-1-1 are equivalent (J_{2c1}) and the atoms along the -1-11, -111,11-1 and 1-1-1 too (J_{2c2}) as depicted on figure 6.4 (see green and purple directions). We have now a "$P21_n$-like" symmetry linked to the shear angle (the out-of-plane axis is not perfectly perpendicular to the in plane parameter like in P_{bnm}). In these three models (we only consider anisotropy

2J		4J		5J		6J	
J_2 (12)	1.11	J_{2a} (2)	-0.15	J_{2a} (2)	-0.15	J_{2a} (2)	-0.12
		J_{2b} (2)	0.91	J_{2b} (2)	0.91	J_{2b} (2)	0.95
		J_{2c} (8)	1.33	J_{2c1} (4)	1.52	J_{2c1} (4)	1.64
				J_{2c2} (4)	1.15	J_{2c2} (4)	1.28
J_4 (6)	-1.33	J_4 (6)	-1.23	J_4 (6)	-1.23	J_{4ab} (4)	-1.66
						J_{4c} (2)	-0.25
T_{Neel}^{Mean}	124		147		170		166
T_{Neel}^{Ising}	168		138		164		147

Table 6.1 | Summary of the 2J, 4J, 5J and 6J models. In parentheses we have the number of neighbours involved for the considered J terms. Values for the different J with U=1.5 eV. Then the Néel temperature using Mean Field theory called T_{Neel}^{Mean}. We have the Néel temperature from the Ising model called T_{Neel}^{Ising}.

for the second neighbours), we improve the ability to discriminate the different magnetic states. However, we do not totally correctly (even of close to be the case) fit the ab initio results.

The main result is that the fourth neighbour interaction is antiferromagnetic. It is in line with the Goodenough-Kanamori rules that inform us the d^8-d^8 superexchange through the oxygen p orbital is antiferromagnetic and of about tens meV. However, as also mentioned by Goondenough-Kanamori, the superexchange between two d^8 cations (large nickel) through two oxygens and a non magnetic site (small nickel) keep the interaction antiferromagnetic but an order of magnitude smaller. This is fully in agreement with the obtained ab-initio results for which the amplitude of superexchange is about a few meV for the fourth neighbours interaction.

For this purpose, we add the anisotropy between in plane and out-of plane interaction for the fourth neighbours (see fig 6.4). This is the so called "6J" model[1]. As a summary, we have the figure 6.4 and the table 6.1.

The results of the Heisenberg Model with U=1.5 eV for the energy of each magnetic state for the four models compared to ab initio results is in the figure 6.5. As expected, the 2J model is unable to describe the anisotropy in the magnetism of nickelates. Again, the 4J model is, as expected, able to find the right GS but unable to find S1 as the only magnetic GS too. Both S1 and T1 are predicted as being the GS. At the end, the 5J model with the magnetic interaction anisotropy with out-of plane second neighbours gives the right GS which is the S1 type[2]. It just underestimates the energy and predicts it is more stable than it really is. Hence we confirm our 5J model is suitable to describe the magnetism compare to ab initio calculations. The 6J model renormalised all the coefficients and takes into account the anisotropy along the c direction for the fourth neighbours too. The best model of course

[1] It has to be noticed the in plane fourth neighbours interaction is the most important one. This suggests we should keep the specific magnetic propagation vector in thin films as experimentally observed.

[2] We clearly see a frustration is still available on the out-of-plane second neighbours.

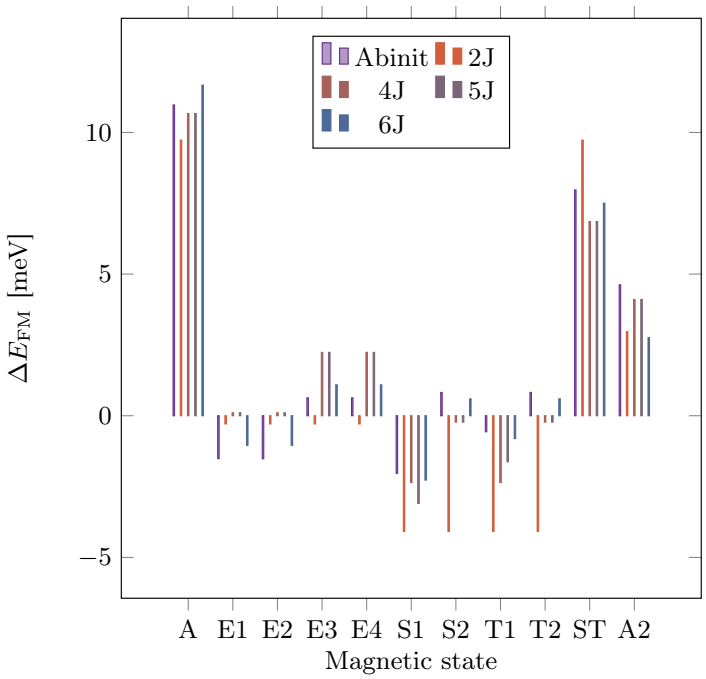

Figure 6.5 | Heisenberg results vs ab initio results. The energy difference when taking the FM configuration as being the reference.

is the one with the most important number of relevant parameters.

The intersite anisotropy for the magnetic interaction is one of the reason why we use more sophisticated model with more parameters but not only. Indeed, using a 2J model induces frustration. Experimentally[26], they made a 2J model knowing the Néel temperature and the Curie temperature of $NdNiO_3$ and they get thanks to Mean Field Theory a value for the interaction between second neighbours and between the fourth ones. The J_2 is 4.1 meV and the J_4 is 8.3 meV. It is to be noticed if we impose fourth neighbours to be antiferromagnetic (common to both theoretical and experimental results), it is impossible to have all the second neighbours with a ferromagnetic configuration or an antiferromagnetic configuration. Thus it justifies the creation of the 4J, 5J and 6J models. Thus, to satisfy this antiferromagnetic interaction between the fourth neighbours, the second neighbours interaction will adapt as a function of the distance between them. Because the a parameter is smaller than the b one, we will have a ferromagnetic interaction along b. Moreover, we have, as mentioned before, a shear affecting the out-of plane interaction. As a function of this, we pass from the S1 to the T1 type magnetic configuration. This would suggest, as discussed inLu et al. [26], this is the fourth neighbours interaction which is responsible for the magnetic configuration and is responsible for the $(\frac{1}{4},\frac{1}{4},\frac{1}{4})$ magnetic propagator[3]. As for experimental results from Lu et al. [26], we will use Mean Field theory to calculate the Néel temperature.

[3]In this paper[26], they try to describe the non collinear phase which is different from the collinear one discussed here. Indeed, all the nickel sites are magnetic in the experimental paper.

Mean Field theory

Using Mean field Theory, we obtain the critical temperature. We use the same method as Lu et al.[26] based on Smart[90]. It is the temperature between the antiferromagnetic (our Ground state) and the paramagnetic phase (high temperature magnetic configuration).

In the "cubic-like" symmetry it is given by:

$$T_{Neel} = -\frac{2Z_4 J_4 S_4(S_4+1)}{3k_b} \tag{6.2}$$

where k_b is the Boltzmann constant and Z_4 is the number of fourth neighbours.

It considers a cubic phase without any anisotropy for the interaction. It is suitable for the 2J model and the predicted value is 124 Kelvin. It is smaller than the experimental value of 150K. The experimentally obtained J values using the same model for a temperature of 150K are more important than us. However, the main problem is the fact they use only a 2J model we know insufficient to correctly describe the magnetic Ground State.

For the 4J model, we go a step further than in Lu et al. paper[26] with the "$Pbnm$-like" symmetry, we have:

$$\begin{aligned} T_{Neel} = \quad & -\frac{2Z_{2a}J_{2a}S_{2a}(S_{2a}+1)}{3k_b} + \frac{2Z_{2b}J_{2b}S_{2b}(S_{2b}+1)}{3k_b} \\ & -\frac{2Z_4 J_4 S_4(S_4+1)}{3k_b} \end{aligned} \tag{6.3}$$

where Z_{2a} is the number of second neighbours with interaction J_{2a} and Z_{2b} is the number of second neighbours with interaction J_{2b}.

For the 5J model, reaching the "$P2{1}_{n}$-like" symmetry, we have:

$$\begin{aligned} T_{Neel} = \quad & -\frac{2Z_{2a}J_{2a}S_{2a}(S_{2a}+1)}{3k_b} + \frac{2Z_{2b}J_{2b}S_{2b}(S_{2b}+1)}{3k_b} \\ & -\frac{2Z_{2c1}J_{2c1}S_{2c1}(S_{2c1}+1)}{3k_b} + \frac{2Z_{2c2}J_{2c2}S_{2c2}(S_{2c2}+1)}{3k_b} \\ & -\frac{2Z_4 J_4 S_4(S_4+1)}{3k_b} \end{aligned} \tag{6.4}$$

where Z_{2c1} is the number of second neighbours with interaction J_{2c1} and Z_{2c2} is the number of second neighbours with interaction J_{2c2}.

At the end, for the 6J model renormalising the fourth neighbours interaction, we have:

$$\begin{aligned} T_{Neel} = \quad & -\frac{2Z_{2a}J_{2a}S_{2a}(S_{2a}+1)}{3k_b} + \frac{2Z_{2b}J_{2b}S_{2b}(S_{2b}+1)}{3k_b} \\ & -\frac{2Z_{2c1}J_{2c1}S_{2c1}(S_{2c1}+1)}{3k_b} + \frac{2Z_{2c2}J_{2c2}S_{2c2}(S_{2c2}+1)}{3k_b} \\ & -\frac{2Z_{ab}4J_{ab}4S_{ab}4(S_{4ab}+1)}{3k_b} - \frac{2Z_{4c}J_{4c}S_{c4}(S_{4c}+1)}{3k_b} \end{aligned} \tag{6.5}$$

where Z_{4ab} is the number of fourth neighbours with interaction J_{4ab} and Z_{4c} is the number of fourth neighbours with interaction J_{4c}.

The obtained temperature are summarized in the table 6.1. The four models correctly reproduce the Néel temperature. We have a competition between the fourth neighbours that

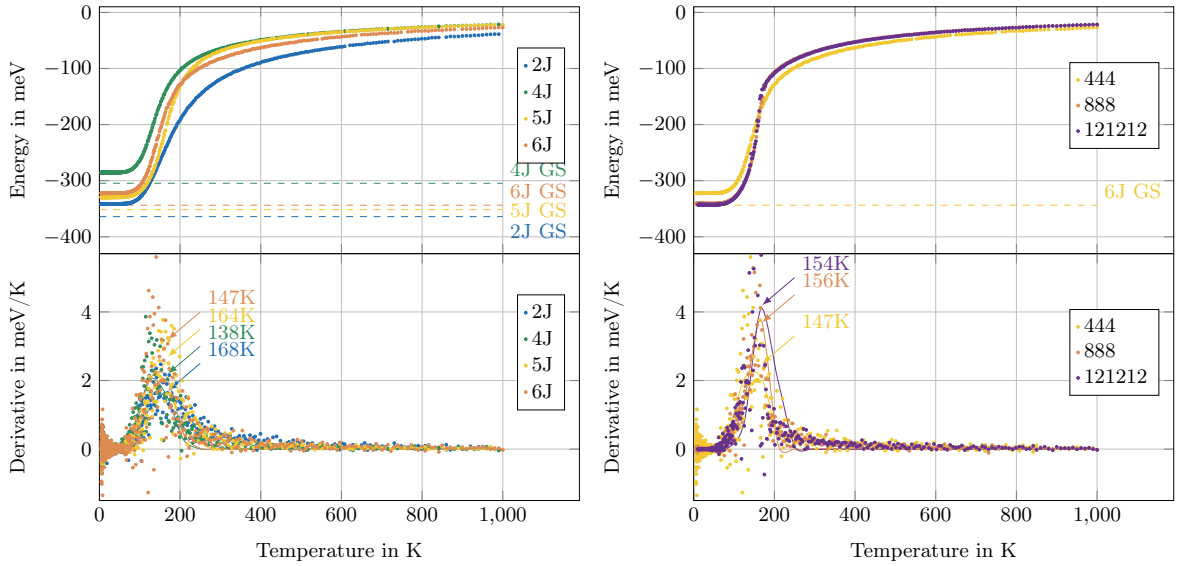

Figure 6.6 | On the left: evolution as a function of the number of J parameters. On the right: The effect of the box size. At the top: Evolution of the energy as a function of the temperature for the three models in a 444 box. At the bottom, the evolution of the derivative and the Gaussian fit.

impose the phase transition (the higher the J are, the highest the T_N is) and the frustration of the second neighbours (the best the J of the magnetic interaction for the second neighbours corresponds, the less the fourth neighbours interaction has to fight with them to impose the specific magnetic propagation vector.).

Ising Model

In this Ising model, we impose the rock-salt configuration and the spin to be collinear (they can only flip between 1 and -1) to stay coherent with the previous ab initio and Heisenberg studies. Then, we impose the values of the J obtained thanks to the discussed Heisenberg investigation. Starting with a 4×4×4 box, we obtain the four models are suitable to describe the magnetic Ground State and the effect of the temperature. The results for the energy show we have the paramagnetic phase at high temperature. When the magnetic interaction is enough important compared to the temperature, the magnetic GS appears and we have the phase transition. We see this transition on figure 6.6 page 88 thanks to the calculation of the derivative of this energy as a function of the temperature from which we obtain a peak at the temperature corresponding to the phase transition. Fitting the plot with a Gaussian equation we get a temperature of 168K, 138K, 164K and 147K for the 2J, 4J, 5J and 6J model respectively. All these values are closed and in good agreement with the experiment values.

To avoid the boarding effect, using the 6J model, we increase the box. So a 4×4×4, a 8×8×8 and a 12×12×12 boxes are used to calculate the effect on the temperature. Increasing the box induces a small shift of the critical temperature phase transition and a narrowing of the Gaussian fit in the derivative appears. This means a better estimation of the phase transition. For the 6J model, the obtained value for the 12×12×12 box is 154K in excellent

magnetic configuration	k point 1	k point 2
S1	$\frac{1}{4}\frac{3}{4}\frac{3}{4}$	$\frac{3}{4}\frac{1}{4}\frac{1}{4}$
S2	$\frac{1}{4}\frac{3}{4}\frac{1}{4}$	$\frac{3}{4}\frac{1}{4}\frac{3}{4}$
T1	$\frac{1}{4}\frac{1}{4}\frac{1}{4}$	$\frac{3}{4}\frac{3}{4}\frac{3}{4}$
T2	$\frac{1}{4}\frac{1}{4}\frac{3}{4}$	$\frac{3}{4}\frac{3}{4}\frac{1}{4}$

Table 6.2 | Localisation of the peak in the reciprocal space for the four magnetic configurations with a $\frac{1}{4}\frac{1}{4}\frac{1}{4}$ magnetic propagator.

agreement with the desired 150K[26].

To ensure the fact we have the right Ground state, a Fourier transform is applied to the magnetic configuration at each step of the simulation and the average value of the coefficients is given for each temperature. Starting to cool down the material, two peaks increase (in the 5J and the 6J) and are maximum after the phase transition. All the other coefficients are equal to 0 below the critical temperature. These points are $\frac{1}{4}\frac{3}{4}\frac{3}{4}$ and $\frac{3}{4}\frac{1}{4}\frac{1}{4}$ in the reciprocal space. The peaks are localised at different positions of the reciprocal space for each of the S1, S2, T1 and T2 complex magnetic configurations as shown in table 6.2 page 89.

We have the S1 type as the predicted GS from the Ising models with 5J and 6J. This is in agreement with the ab initio and experimental results again. For the 4J model we can have the peaks corresponding to S1, T1 or a combination of them as well. For the 2J model we obtain peaks referring to the four S and T type or a combination of them. This is, again, because the structural anisotropy in these compounds needs such a complex magnetic configuration to satisfy the antiferromagnetic fourth neighbours interaction.

If the spin orientation are not imposed to be aligned, the T_N is sensitive to an on-site anisotropic term named "A". If this term is small (A of about a few meV), the Néel temperature is divided by 2. However, imposing a high on-site anisotropy (A around 60 meV), we recover the T_N of collinear spins. This would suggest, the magnetic GS is collinear with an on-site anisotropy of about 60meV[4]. This on-site anisotropy is in agreement with the preferential direction in the (ac) plane in experiments.

As a conclusion, both DFT+U=1.5eV, Heisenberg study and Ising (collinear and non collinear) investigation correctly describe the magnetism of the bulk $YNiO_3$ compound. The magnetic Ground state is the S1 type and the phase transition temperature is estimated at 147K with no magnetic moment on the small nickel site. Because a 2J model lets to a frustration for the second neighbours configurations, complex models are needed. Knowing this, we can conclude as the complex magnetism needs 6 parameters to be correctly described and is mainly driven by the fourth neighbours interaction. The Néel temperature depends on the subtle competition with the fourth neighbours interaction and the frustration between the second neighbours ones. From the knowledge of those J parameters, we will characterize the experimental inelastic neutron scattering results in the next section.

[4]The T_N is saturated for small and large value of on-site anistropy for a range between about 70K to about 200K.

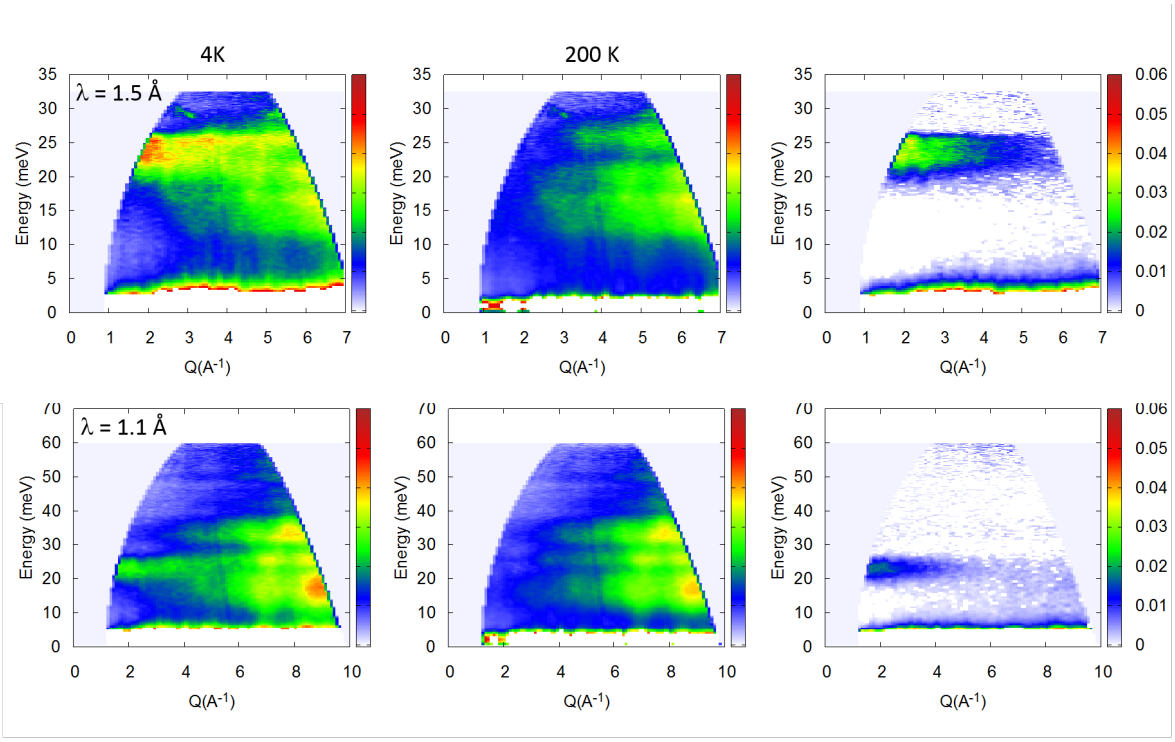

Figure 6.7 | IN4 data at 5 and 200 K and for two different wavelengths. The right column shows the difference between 5 and 200K, unraveling the magnetic contribution.

6.4.3 Inelastic neutron scattering

The raw data, corrected for the detailed balance factor, are shown on Figure 6.7a and 6.7b. Both show a strong contribution which grows with both Q (reciprocal space vector) and temperature, clearly due to the phonon density of states. An additional contribution arises at low Q and relatively high energy of about 25 meV. Its spectral weight decreases with increasing Q, as expected in the case of a magnetic signal because of the decrease of the form factor. Figure 6.7c shows this magnetic contribution obtained by taking the subtraction between the two corrected raw data at 4K and 200K. It takes the form of a nearly flat mode, yet, more precisely, it is characterized by a wavy shape, with minima at 1.9, 2.4 and 3.1 AA^{-1} and maxima at 2.2 and 2.9 AA^{-1}. Furthermore, in the Q-E range unveiled by neutron scattering, no magnetic intensity is observed below about 20 meV. The lack of signal in this range is confirmed by the FOCUS data, carried out with lower incident energies.

We tentatively attribute this magnetic contribution to the powder average spin wave spectra developing below the Néel temperature. Should this hypothesis be correct, an acoustic branch would be expected, going soft at the magnetic main Bragg peak. As a result, the lack of intensity at low energy is in apparent contradiction with this simple spin wave hypothesis. However, it is still compatible with the neutron data provided the acoustic branch stems from the ferromagnetic zone center Q=0 and is characterized by a large enough celerity.

Numerical calculations based on the theory have been developed. The exchange cou-

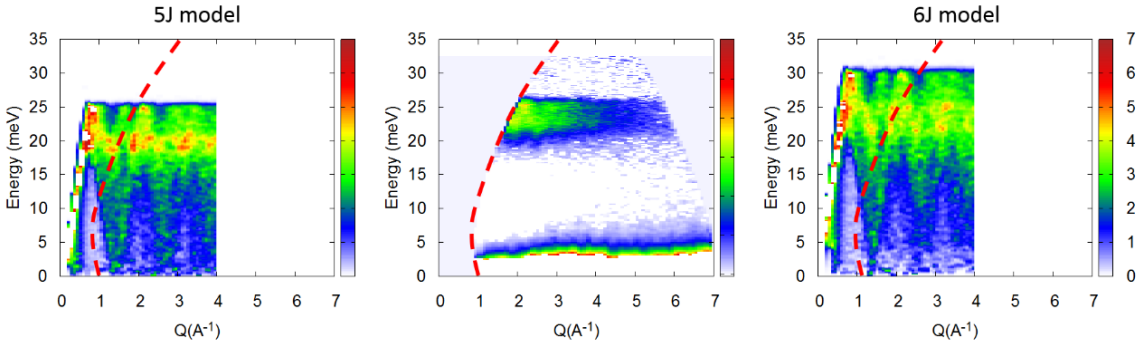

Figure 6.8 | Experimental data compared to the powder averaged spin wave spectra in the 5J and 6J models.

plings that we shall consider are defined as in the previous theoretical section. We basically find (2J model) that the magnetic ground state configuration results from the competition between a ferromagnetic J_2 and an antiferromagnetic J_4. More refined calculations (4J model) show that J2 must be actually recast using different values J_{2a}, J_{2b} and J_{2c}, since they correspond to different exchange paths. J_{2b} and J_{2c} show only little change, while J_{2a} becomes weakly antiferromagnetic. The 5J and 6J models further refine the description of J_4 and J_{2c} as discussed in the previous theoretical section.

To further test this modeling, the spin wave excitations spectrum was calculated numerically in the classical Holstein-Primakov approach using the Spinwave software developed at LLB, for the 5J and 6J models. The neutron cross section was then powder averaged by integrating over the solid angle defining the wavevector Q. This integration was carried out by a numerical sampling over a sphere of constant modulus based on a Fibonacci algorithm. As shown in Figure 6.8, a qualitative agreement is obtained for both models. The nearly flat band at about 25 meV, its weaky dispersive shape, as well as the lack of strong scattering at low energy are quite well captured by the different models. These calculations also predict a very strong acoustic branch stemming from Q=0 (due to the ferromagnetic character), which is however intrinsically invisible to neutrons.

6.5 Discussion

We have shown the obtained magnetic GS from DFT+U and neutron powder diffraction are fully compatible and is collinear with a $(\frac{1}{4},\frac{1}{4},\frac{1}{4})$ magnetic propagation vector with no magnetic moment on the small nickel site.This configuration is not polar.

We have highlighted that DFT properly fit experimental data from inelastic neutron scattering and provides realistic J parameters. It is a further validation of the ability of static DFT+U to properly model ReNiO3 compounds.

6.6 Conclusions

This paper clarifies that the highly-debated magnetic ground state of bulk $YNiO_3$ is compatible with a non-polar collinear $\uparrow 0 \downarrow 0$ order and provides useful and realistic J parameters.

6.7 Methods

6.7.1 Sample preparation and characterization

The $YNiO_3$ polycrystalline sample used in this work was synthesized using a high-pressure oxygen-gas setup [134, 135] recently relocated at the Paul Scherrer Institut (PSI) in Villigen, Switzerland, following a method based in the procedures described in refs. [30, 136]. Laboratory x-ray powder diffraction (Siemens D8 Advance, CuKα) indicated excellent crystallinity and the absence of impurities within the detection limit of this technique. The metal-to-insulator T_{MIT} and Néel T_N temperatures, probed respectively using differential scanning calorimetry (DSC, Netzsch DSC 204F1) and SQUID magnetometry (MPMS XL, Quantum Design), were respectively 600 K and 150 K (T_N), both measured by heating.

6.7.2 Neutron powder diffraction

The neutron powder diffraction (NPD) measurements were carried out at the Swiss Spallation Neutron Source (SINQ) of the PSI. A large ($\sim$ 12g) $YNiO_3$ polycrystalline sample was introduced into a cylindrical vanadium can (D = 6 mm, H = 5 cm) and mounted on a He cryostat, whose contribution to the powder diffraction patterns was eliminated using oscillating radial collimators. Diffraction patterns were collected at RT and 10 K at the high resolution diffractometer HRPT [137] (primary beam collimations $\alpha_1 = 12'$; Ge(511) λ = 1.494 Å (Q_{max} = 8.33 Å^{-1}); $2\theta_{step} = 0.05°$). The measurements were performed after a stabilization time of 15 minutes with total acquisition times of $\sim$ xx hours per temperature. The wavelength was refined using a NAC standard sample. An additional pattern with high statistics (39 h) was collected on the cold neutron diffractometer DMC [138] (pyrolytic graphite (002); λ = 3.80008 Å; $2\theta_{step} = 0.1°$). The presence of higher harmonics (less than 1%) was further minimized using a Berillium filter. The exact value of the wavelength was adjusted to match the lattice parameters refined in HRPT at 10K.

All powder diffraction data were analyzed with the Rietveld package FullProf Suite [139]. Below T_N new reflections corresponding to the $\boldsymbol{k}$ = (1/2, 0, 1/2) magnetic propagation vector were observed. To describe them, a second phase was added to the fits. We used the magnetic form factor of Ni^{3+} for all Ni sites [140].

6.7.3 Inelastic neutron scattering

Inelastic neutron scattering measurements have been carried out both at IN4 (ILL, France) and at FOCUS (PSI, Switzerland). IN4 was operated with different wavelength depending

on the desired Q-E range, namely at 1.1, 2.2, 1.5 and 3 $\mathbf{r}A^{-1}$. A 12 g powder sample was loaded in an aluminium container (8 mm in diameter) and attached to the cold finger of a standard cryostat. The spectra have been recorded at 4 and 200 K.

6.7.4 First-principles simulations

Abinit software [43–45] is used to do first principle calculations[47, 48] within the Projector Augmented Wave (PAW) [57] method with GGA-PBEso l atomic data based on JTH pseudo potential[61, 115]. We consider core and valence electrons for Y, Ni and O. We have $5s^2 5p^6 5d^1 6s^2$ for yttrium, $3s^2 3p^6 3d^9 4s^1$ for nickel and $2s^2 2p^4$ for oxygen. Having a Perovskite $Y^{3+}Ni^{3+}O^{2-}$, we in average have $5s^2 5p^6$ for yttrium, $3s^2 3p^6 3d^7$ for nickel and $2s^2 2p^6$ for oxygen.

Our results are in such a way the energy difference between two different magnetic states and structures is converged below 1 meV for a 5 atoms unit cell ($1\frac{meV}{f.u.}$). For this purpose, an energy cutoff of 24 Hartree for the plane waves basis and a equivalent 12×12×12 grid of k-point in the 5 atoms unit cell are imposed. The forces in the 80 atoms unit cell are of 5.10^{-5} $\frac{Hartree}{bohr}$ for the relaxation and the stress is of 5.10^{-7} $\frac{Hartree}{bohr^3}$. We constrain a collinear spin configuration for the Ni ion for all the calculations. A smearing of 300K was imposed too. The scheme of the DFT+U[114] is used to correctly describe the d correlated electrons of the Ni atoms.

Conclusion of the article.

I showed the magnetic configuration is driven by the fourth neighbours interaction. This is directly linked to the $\frac{1}{4}\frac{1}{4}\frac{1}{4}$ *electronic propagation vector. The magnetic ground state configuration is related to the structural distribution and explained through symmetry considerations.*

Now that the quality of DFT+U results has been demonstrated, the same framework will be employed to extend the structurally triggered Peierls instability theory to the ferrites.

7 | From charge- to orbital-ordered MIT in alkaline-earth ferrites

Yajun Zhang[1,2], *Michael Marcus* Schmitt[1], *Alain* Mercy[1], *Jie* Wang[2] and *Philippe* Ghosez[1]

[1]Theoretical Materials Physics, Q-MAT, CESAM, University of Liège, B-4000 Liège, Belgium [2]Department of Engineering Mechanics, School of Aeronautics and Astronautics, Zhejiang University,38 Zheda Road, Hangzhou 310007, China

Introduction of the article

Physical Review B 98(8), 081108 (2018)

Ferrites are an academic family of compounds to explicitly show the role of the rotations in the gap opening. Indeed, from compounds without rotation to compounds with large amplitude of rotations, I will highlight their involvement in the breathing triggering. Moreover, by applying strain constrains, the Peierls instability mechanism can be transposed to the Jahn-Teller distortions.

7.1 Abstract

While $CaFeO_3$ exhibits upon cooling a metal-insulator transition linked to charge ordering, $SrFeO_3$ and $BaFeO_3$ keep metallic behaviors down to very low temperatures. Moreover, alkaline-earth ferrites do not seem prone to orbital ordering in spite of the d^4 formal occupancy of Fe^{4+}. Here, from first-principles simulations, we show that the metal-insulator transition of $CaFeO_3$ is structurally triggered by oxygen rotation motions as in rare-earth nickelates. This not only further clarifies why $SrFeO_3$ and $BaFeO_3$ remain metallic but allows us to predict that an insulating charge-ordered phase can be induced in $SrFeO_3$ from appropriate engineering of oxygen rotation motions. Going further, we unveil the possibility to switch from the usual charge-ordered to an orbital-ordered insulating ground state under moderate tensile strain in $CaFeO_3$ thin films. We rationalize the competition between charge and orbital orderings, highlighting alternative possible strategies to produce such a change of ground state, also relevant to manganite and nickelate compounds.

7.2 Introduction

ABO_3 perovskite oxides, with a transition metal at the B-site, form a vast class of functional materials, fascinating by the diversity of their unusual properties [3, 122, 123]. Amongst them, different families of compounds with a formal e_g^1 occupation of the d orbitals at the B-site, like rare-earth manganites ($d^4 = t_{2g}^3 e_g^1$ in $R^{3+}Mn^{3+}O_3$, with R a rare-earth element), rare-earth nickelates ($d^7 = t_{2g}^6 e_g^1$ in $R^{3+}Ni^{3+}O_3$), or alkaline earth ferrites ($d^4 = t_{2g}^3 e_g^1$ in $A^{2+}Fe^{4+}O_3$, with A = Ca, Sr or Ba) are similarly prone to show metal-insulator transitions (MIT). However, the mechanism behind such a transition can be intriguingly different from one family to the other.

$RNiO_3$ (except R=La) and $RMnO_3$ compounds crystallize in the same metallic *Pbnm* $GdFeO_3$-type phase at sufficiently high-temperature. This phase is compatible with their small tolerance factor and labeled ($a^-a^-c^+$) in Glazer's notation[141]. It differs from the aristotype cubic perovskite structure, only expected at very high temperature and not experimentally observed, by the coexistence of two types of atomic distortions: (i) in-phase rotation of the oxygen octahedra along z direction (M_z) and (ii) anti-phase tilts of the same oxygen octahedra with identical amplitude around x and y directions (R_{xy}). On the one hand, $RNiO_3$ compounds show on cooling a MIT ($T_{MIT} = 0 - 600K$) concomitant with a structural transition from *Pbnm* to $P2_1/n$ [4]. This lowering of symmetry arises from the appearance of a breathing distortion of the oxygen octahedra (B_{oc}), recently assigned to a structurally triggered mechanism [17] and producing a kind of charge ordering (CO)[21, 104, 105, 142]. On the other hand, $RMnO_3$ compounds also exhibit on cooling a MIT ($T_{MIT} \approx 750K$) but associated to orbital ordering (OO) and linked to the appearance of Jahn-Teller distortions (M_{JT}) compatible with the *Pbnm* symmetry [143, 144].

In comparison, $AFeO_3$ compounds do not behave so systemically and adopt seemingly different behaviors. While $SrFeO_3$ and $BaFeO_3$ keep the ideal cubic perovskite structure and show metallic behavior at all temperatures [145, 146], $CaFeO_3$, which crystallizes above room temperature in a *Pbnm* $GdFeO_3$-type phase, exhibits a behavior similar to nickelates. At 290K, a MIT takes place at the same time as its symmetry is lowered to $P2_1/n$ due to the appearance of a breathing distortion [147, 148]. A variety of explanations have been previously proposed to elucidate the MIT in $CaFeO_3$, including orbital hybridization [113], electron-lattice interactions [149, 150], and ferromagnetic coupling [151]. However, no net picture has emerged yet to rationalize its behavior and that of other ferrites.

Here, we show from first-principles calculations that the CO-type MIT in bulk $CaFeO_3$ arises from the same microscopic mechanism as in the nickelates and must be assigned to a progressive triggering of B_{oc} atomic distortions by M_z and R_{xy} atomic motions. We demonstrate that this triggered mechanism is universal amongst the ferrite family and that an insulating phase can be induced in metallic $SrFeO_3$ from appropriate tuning of oxygen rotations and tilts. Going further, we reveal that CO and OO compete in $AFeO_3$ compounds and we unveil the possibility to switch from CO-type to OO-type MIT in $CaFeO_3$ thin films

under appropriate strain conditions. This offers a convincing explanation for the enormous resistivity at room-temperature recently found in $CaFeO_3$ films grown on $SrTiO_3$ [152].

7.3 Methods

Our first-principles calculations relied on density functional theory (DFT) as implemented in VASP [57, 153]. We worked with the PBEsol [115] exchange-correlation functional including U and J corrections as proposed by Liechtenstein [154]. We used $(U|J) = (7.2|2.0)$eV, a plane-wave energy cutoff of $600eV$ and Monkhorst-Pack[155] k-point samplings equivalent to 12×12×12 for a 5-atoms cubic perovskite cell. The lattice parameters and internal atomic coordinates were relaxed until atomic forces are less than 10^{-5}eV/Å. The phonon dispersion curves were calculated with $2\times2\times2$ supercells using finite displacement method. A special care was devoted to the determination of appropriate U and J parameters, which is discussed in detail in the Supplementary Material 11. We found the combination $(U|J) = (7.2|2.0)$eV provides good simultaneous description of the structural (lattice constant and distortion amplitudes), electronic (insulating ground- state) and magnetic (AFM spiral-type ground state very close in energy to the FM configuration) properties of $CaFeO_3$.

7.4 Bulk $CaFeO_3$

In order to clarify the mechanism behind the $P2_1/n$ insulating ground state of $CaFeO_3$, we first focus on the phonon dispersion curves of its parent cubic phase (Fig. 7.1a). Calculations are reported in a ferromagnetic configuration, which is representative to unravel the essential physics. On the one hand, Fig. 7.1a) shows expected unstable phonon modes at M point (M_2^+, $\omega_M = 181i\text{cm}^{-1}$) and R point ($R_5^-$, $\omega_R = 197i\text{cm}^{-1}$) of the Brillouin zone, related respectively to the M_z and R_{xy} distortions yielding the *Pbnm* phase. On the other hand, it attests that the R_2^- mode related to the B_{oc} distortion is significantly stable ($\omega_B^2 = 343\text{cm}^{-1}$), so questioning the origin of its appearance in the $P2_1/n$ phase.

The answer is provided in Fig. 7.1d), reporting the evolution of the energy with the amplitude of B_{oc} (Q_B) at fixed amplitudes of M_z (Q_M) and R_{xy} (Q_R). It demonstrates that, although initially stable (single well – SW – with a positive curvature at the origin $\alpha_B \propto \omega_B^2 > 0$) in the cubic phase, B_{oc} will be progressively destabilized (double well – DW – with a renormalized negative curvature at the origin $\tilde{\alpha}_B < 0$) as M_z and R_{xy} develop in the *Pbnm* phase. The curvature $\tilde{\alpha}_B$ changes linearly with Q_M^2 and Q_R^2 ($\tilde{\alpha}_B = \alpha_B + \lambda_{BM}Q_M^2 + \lambda_{BR}Q_R^2$) so that its evolution must be assigned to a *cooperative* biquadratic coupling ($\lambda_{BM}, \lambda_{BR} < 0$) of B_{oc} with M_z and R_{xy} as highlighted by the following terms in the Landau-type energy expansion around the cubic phase:

$$E \propto \alpha_B Q_B^2 + \lambda_{BM} Q_M^2 Q_B^2 + \lambda_{BR} Q_R^2 Q_B^2 \tag{7.1}$$

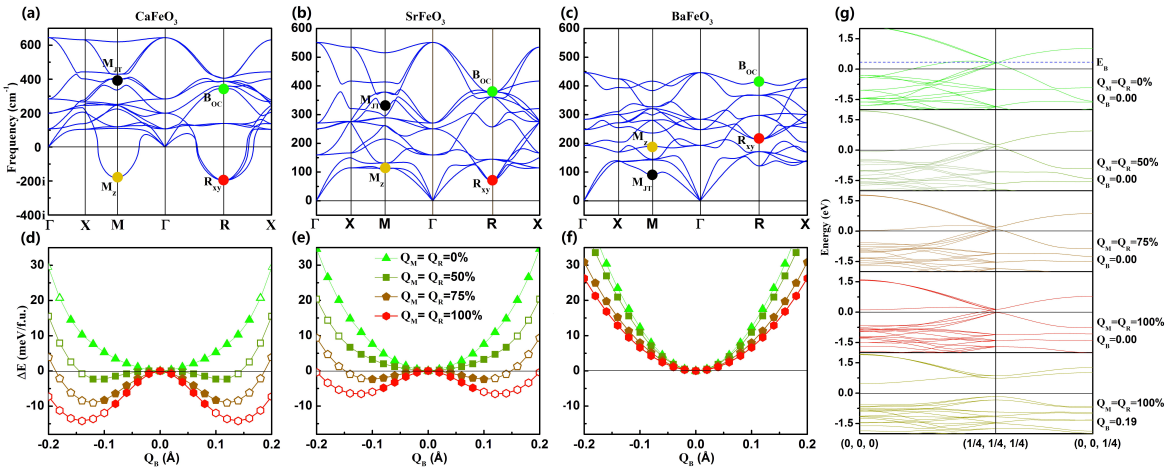

Figure 7.1 | (a-c) Phonon dispersion curves of cubic $CaFeO_3$ (a), $SrFeO_3$ (b), and $BaFeO_3$ (c) on which most relevant modes are pointed. (d-f) Evolution of the energy with respect to the breathing distortion amplitude (Q_B) at fixed rotation (Q_M) and tilts (Q_R) amplitudes in $CaFeO_3$ (d), $SrFeO_3$ (e), and $BaFeO_3$ (f). Opened (resp. filled) symbols denote insulating (resp. metallic) states. (g) Electronic band structure of $CaFeO_3$ along selected lines of the $Pbnm$ or $P2_1/n$ Brillouin zone (coordinates in pseudo-cubic notations) for different amplitude of disortions. All results were calculated with FM spin order and using a fixed cubic cell with the same volume as the ground state. Distortion amplitudes are normalized to those calculated by *ISODISTORT*[156] in the $CaFeO_3$ AFM ground state.

For large enough amplitudes of M_z and R_{xy}, B_{oc} becomes unstable and will spontaneously appear in the structure. In Fig. 7.1d) we further notice that the amplitude of B_{oc} required for making the system insulating decreases for increasing M_z and R_{xy}, yielding therefore an insulating $P2_1/n$ ground state.

This behavior is point by point similar to that reported recently in rare-earth nickelates by Mercy *et al.*[17] who subsequently assigned the MIT to a structurally triggered phase transition, in the sense originally defined by Holakovský [109]. In Ref. [17], the unusual cooperative coupling of B_{oc} with M_z and R_{xy} at the origin of this triggered mechanism was moreover traced back in the electronic properties of nickelates and further related to a type of structurally triggered Peierls instability.

Fig 7.1g) shows that this explanation still hands for ferrites. In the cubic phase of $CaFeO_3$ (Fe^{4+} with formal occupation $d^4 = t_{2g}^3 e_g^1$), the Fermi energy, E_F, crosses anti-bonding Fe $3d$ – O $2p$ states with a dominant e_g character. Activation of B_{oc} can open a gap in these partly occupied e_g bands at $q_B = (1/4, 1/4, 1/4)$, but around an energy E_B initially above E_F. The role of R_{xy} and M_z is to tune Fe $3d$ – O $2p$ hybridizations in such a way that E_B is progressively lowered towards E_F. As they develop into the structure, activating B_{oc} affects more and more substantially energy states around E_F and yields an increasing gain of electronic energy explaining the progressive softening of ω_B. The e_g bandwidth in $CaFeO_3$ being smaller than in the nickelates, E_B is initially closer to E_F consistently with a softer ω_B and the smaller amplitude of R_{xy} and M_z required to destabilize B_{oc}.

7.5 Bulk SFO and BFO

The triggered mechanism highlighted above further straightforwardly explains the absence of MIT in other alkaline-earth ferrites. Because of their larger tolerance factors and as confirmed from the absence of unstable mode in their phonon dispersion curves (Fig. 7.1b) and c)) $SrFeO_3$ and $BaFeO_3$ preserve their cubic structure down to zero Kelvin[145, 146] and so do not spontaneously develop the oxygen rotation and tilts mandatory to trigger the MIT. The cooperative coupling of B_{oc} with M_z and R_{xy} remains however a generic features of all ferrite compounds.

As illustrated in Fig. 7.1e) and 7.1f), B_{oc} is progressively destabilized when increasing artificially the amplitudes of M_z and R_{xy} distortions in $SrFeO_3$ and $BaFeO_3$. Since, in the cubic phase of these compounds, ω_B is originally at frequencies slightly larger than in $CaFeO_3$ (ω_B = 362cm^{-1} in $SrFeO_3$ and ω_B = 415cm^{-1} in $BaFeO_3$), larger distortions are required to induce the MIT. In $SrFeO_3$, amplitudes of M_z and R_{xy} corresponding to 75% of their ground-state values in $CaFeO_3$ are nevertheless enough to force an insulating ground state. In $BaFeO_3$, the cooperative coupling is less efficient and much larger amplitudes would be required.

This highlights the possibility of inducing a MIT in $SrFeO_3$ thin films or heterostructures under appropriate engineering of oxygen rotation and tilts. Moreover, it provides a vivid explanation to the decrease of T_{MIT} experimentally observed in $Ca_{1-x}Sr_xFeO_3$ solid solutions as x increases [157]. For increasing Sr concentrations, the average tolerance factor increases and the mean amplitudes of M_z and R_{xy} decrease. This analysis is supported by DFT calculation at 50/50 Ca/Sr composition using an ordered supercell along the [001] direction (see Supplementary Materials 11).

7.6 Charge Order vs. Orbital Ordering

The mechanism of the MIT being clarified, it remains intriguing why $CaFeO_3$ ($t_{2g}^3 e_g^1$) prefers to exhibit a breathing distortion (B_{oc}) and CO as $RNiO_3$ compounds ($t_{2g}^6 e_g^1$) rather than a Jahn-Teller distortion (M_{JT}) and OO as $RMnO_3$ compounds ($t_{2g}^3 e_g^1$). In Ref. [158] Whangbo *et al.* argue that B_{oc} is favored in $CaFeO_3$ by the relatively strong covalent character of the Fe-O bond while the M_{JT} distortion is preferred in $LaMnO_3$ by the weak covalent character of the Mn-O bond. Relying on this analysis, we anticipate that weakening the covalence by increasing the Fe-O distance might potentially favor Jahn-Teller distortions and OO in $CaFeO_3$. To realize practically this idea, we investigated the role of tensile epitaxial strain on the ground state of $CaFeO_3$ thin films.

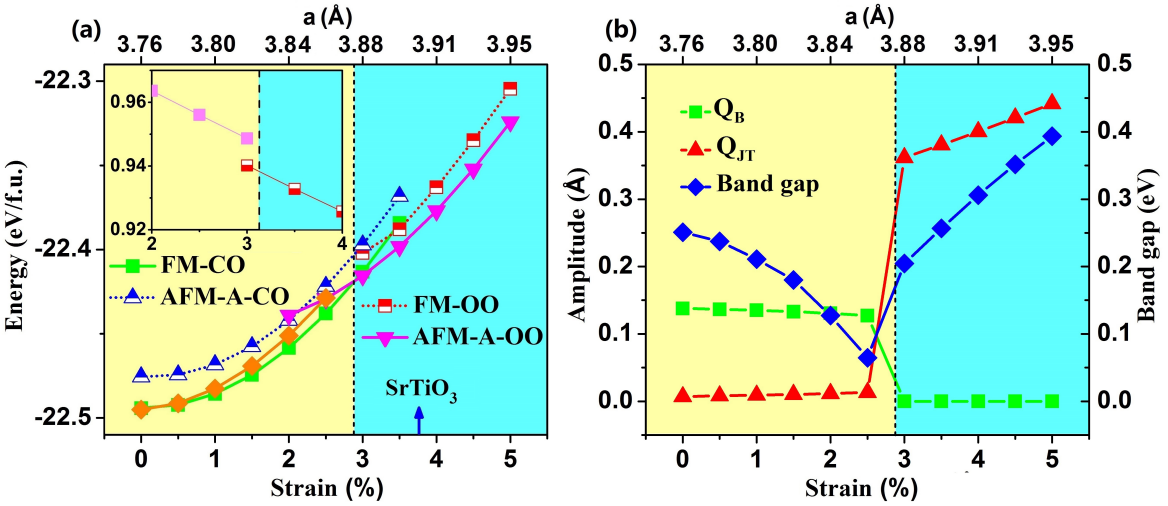

Figure 7.2 | (a) Total energy as a function of tensile strain (or in-plane lattice constant) for $CaFeO_3$ epitaxial films with c-axis out-of-plane, in CO and OO states with either FM or A-type AFM spin ordering; FM CO state with the long c-axis in-plane is plot in orange curve for comparison. It highlights a change of ground state from FM-CO phase (yellow area) to A-type AFM-OO phase (blue area). Inset: c/a ratio of the ground state structure as a function of strain. (b) Evolution of Q_B (green), Q_{JT} (red) and band gap (blue) as a function of strain (or in-plane lattice constant).

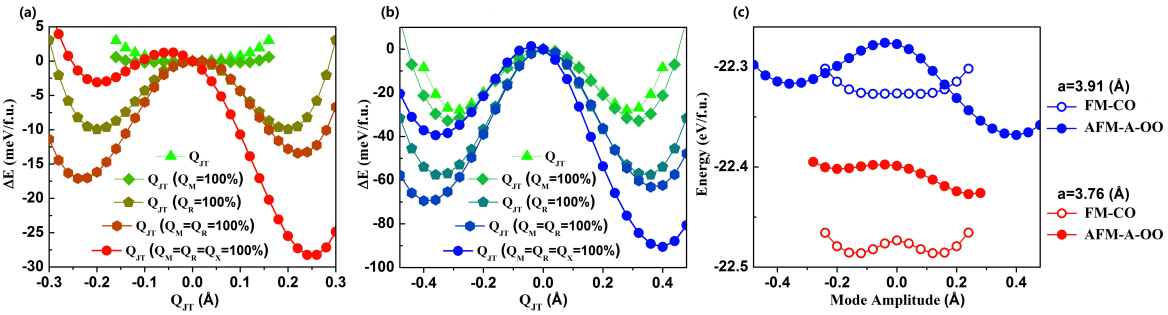

Figure 7.3 | Evolution of the energy with Jahn-Teller distortion amplitude Q_{JT} in AFM-A magnetic order and at fixed amplitudes of other distortion (see legend) for $CaFeO_3$ epitaxial films under strain of (a) 0% (a = 3.76 Å) and (b) 4% (a = 3.91 Å).(c) Evolution of the total energy as a function of Q_B in FM-CO state (open symbol) and Q_{JT} in A-type AFM-OO state (filled symbol) for $CaFeO_3$ thin film under 0% (a = 3.76Å, red) and 4% (a = 3.91Å, blue) strains. Q_M, Q_R and Q_X are fixed to their amplitudes in the relevant phase (except for the FM-CO state at 4% which cannot be stabilized and for which we kept positions in the A-type AFM-OO phase) phase, the corresponding mode amplitude of A-type AFM-OO is fixed for the filled symbol) and 4% (a = 3.91Å, blue curves with fixed Q_M, Q_R and Q_X of of A-type AFM-OO phase, since the initial CO phase converges to OO phase after optimization under such strain) strains.

7.7 $CaFeO_3$ Thin films

The phase diagram of $CaFeO_3$ films epitaxially grown on a cubic perovskite (001)-substrate is reported Fig. 7.2a). The evolution of the energy with the lattice constant of the substrate is shown for FM and A-type AFM orders with either charge or orbital ordering. Although S- and T-type spiral magnetic orders (not shown here) possess a slightly lower energy at the bulk level, the FM order becomes quickly the GS under small tensile strain; C-type and G-type AFM order are much higher in energy and not shown. Both possible orientations of the orthorhombic ($a^-a^-c^+$) oxygen rotation pattern, with the long c-axis either in-plane or out-of-plane were also considered: while c-axis in-plane is favored at zero strain, c-axis out-of-plane becomes more stable under tensile strains.

Fig. 7.2a) confirms our guess and demonstrate the possibility of switching from a CO to an OO ground state in $CaFeO_3$ using strain engineering: under increasing tensile strain, the ground state of the film changes from an insulating FM-CO $P2_1/n$ configuration at small strain to an insulating A-type AFM-OO *Pbnm* configuration above 3% tensile strain (a=3.88Å). Fig. 7.2b) highlights the strain evolution of B_{oc} and M_{JT} distortions together with the change of band gap. Under increasing tensile strain, B_{oc} slightly decreases and is abruptly suppressed at the phase transition; at the same time, the band gap – already reduced in this FM phase – decreases, although much faster than B_{oc} and the transition appears precisely when the bandgap converges to zero. Conversely, M_{JT} is nearly zero below 3% tensile strain while it suddenly appears at the transition and then continuously increases. Amazingly, the amplitude of M_{JT} (0.37 Å) in a $CaFeO_3$ film grown on a $SrTiO_3$ substrate (a = 3.905 Å) is comparable to that of bulk $LaMnO_3$ (0.36 Å). Such similar amplitude suggests that the T_{MIT} associated to the OO state in strained $CaFeO_3$ films might be much larger than the T_{MIT} associated to the CO state in bulk and comparable to the one of $LaMnO_3$ (T_{MIT} = 750K).

Our findings provide a convincing explanation for the insulating character of $CaFeO_3$ films on $SrTiO_3$ at room temperature and for the absence of CO MIT in the 100-300K temperature range as recently pointed out in Ref.[152]. They suggest that the presence of OO MIT at higher temperature should be investigated. A key feature, highlighted in the inset in Fig. 7.2a), is the jump of c/a ratio at the transition boundary, which provides another concrete hint for experimentalists to probe the CO-OO transition.

7.8 Competition between Charge and Orbital Ordering

To rationalize the emergence of an OO ground state in $CaFeO_3$ films, we quantify the lowest-order couplings of M_{JT} with other distortions in a Landau-type free energy expansion and investigate their sensitivity to magnetic order and epitaxial strain :

$$E \propto \alpha_{JT} Q_{JT}^2 + \lambda_{MJ} Q_M^2 Q_{JT}^2 + \lambda_{RJ} Q_R^2 Q_{JT}^2 + \gamma Q_R Q_X Q_{JT} \tag{7.2}$$

Amplitudes (Å)	Q_{JT}	Q_B	Q_M	Q_R	Q_X
a = 3.76Å-CO	0.007	0.137	0.788	1.111	0.440
a = 3.76Å-OO	0.256	0.000	0.717	1.194	0.457
a = 3.91Å-OO	0.400	0.000	0.676	1.309	0.552
Energies (meV/fu)	$\Delta E_{JT}^{(1)}$	$\Delta E_{JT}^{(2)}$	$\Delta E_{JT}^{(3)}$	ΔE_{JT}	ΔE_{AFM-A}
a = 3.76Å-OO	4.4	-43.6	-15.8	-55.0	74.5
a = 3.91Å-OO	-104.3	-80.9	-31.0	-216.2	49.3

Table 7.1 | Top: Amplitudes of dominant distortions in the relaxed CO (FM) and OO (AFM-A) phases of $CaFeO_3$ epitaxial films under 0% (a = 3.76Å) and 4% (a = 3.91Å) tensile strain. Bottom : Energy contributions associated to the different terms in Eq.(7.2), obtained from the amplitudes of distortion reported above.

The first term quantifies the *proper* harmonic energy contribution $\Delta E_{JT}^{(1)}$ associated to the appearance of M_{JT}. The second and third terms in Eq. (7.2) account for a change of energy $\Delta E_{JT}^{(2)}$ in presence of M_z and R_{xy}, linked to their lowest bi-quadratic coupling with M_{JT}. Finally, sizable anti-polar motions of the Ca cations and apical oxygens (X_{AP} mode of amplitude Q_X, see Table 7.1), which are driven by M_z and R_{xy}[159], couple in a trilinear term with R_{xy} and M_{JT} (last term in Eq.(7.2)). This coupling produces an energy lowering $\Delta E_{JT}^{(3)} < 0$, through a so-called *hybrid improper* mechanism yeilding an asymmetry in the M_{JT} energy well [1]. Compendiously, appearance of a M_{JT} distortion requires $\Delta E_{JT} = \Delta E_{JT}^{(1)} + \Delta E_{JT}^{(2)} + \Delta E_{JT}^{(3)} < 0$.

In bulk $CaFeO_3$, α_{JT} is large ($\omega_{JT}(FM)$ = 390 cm^{-1}) in the FM cubic phase, which prohibits ΔE_{JT} to become negative for sizable amplitudes of M_{JT}. Switching to the A-type AFM spin order tremendously lowers α_{JT} ($\omega_{JT}(AFM-A)$ = 144 cm^{-1}) but simultaneously increases the total energy by ΔE_{AFM-A}. The stabilization of an OO phase with M_{JT} against the CO phase with B_{oc} so depends eventually on the counterbalance between ΔE_{AFM-A} and ΔE_{JT}.

This is quantified for epitaxial thin films in Fig. 7.3 and Table 7.1. Under negligible tensile strain (a= 3.76 Å, Fig. 7.3a), with A-type AFM order, ω_{JT} is even softer than in bulk $CaFeO_3$, yielding $\Delta E_{JT}^{(1)} \approx 0$. Then, similarly to what was discussed for B_{oc} in bulk compounds, R_{xy} and M_z trigger M_{JT} ($\lambda_{MJ}, \lambda_{RJ} < 0$), yielding $\Delta E_{JT}^{(2)} < 0$. Finally, the hybrid improper coupling with X_{AP} and R_{xy} provides a further $\Delta E_{JT}^{(3)} < 0$. However, although globally negative, ΔE_{JT} cannot overcome ΔE_{AFM-A}(Fig. 7.3c). Under large tensile strain (a= 3.91 Å, Fig. 7.3b) α_{JT} is significantly reduced by coupling with the epitaxial tetragonal strain e_{tz} ($\alpha_{JT} \propto \gamma_{tJ} e_{tz} + \lambda_{tJ} e_{tz}^2$ [160]), yielding a huge negative $\Delta E_{JT}^{(1)}$. Then, although λ_{MJ} and λ_{RJ} are reduced and γ remains unaffected (see Supplementary Materials 11), $\Delta E_{JT}^{(2)}$ and $\Delta E_{JT}^{(3)}$ are increased roughly by a factor of 2, mainly due to the increase of Q_{JT}. Globally, $|\Delta E_{JT}|$ in A-type AFM order is now much larger than ΔE_{AFM-A}, which moreover has been slightly

[1] The coexistence of M_z and R_{xy} already produces an asymmetry in the energy well through the term $E \propto \delta Q_R^2 Q_M Q_{JT}$. However, this asymmetry is in the negligible range of 1 meV (see Fig. 7.3a-b), and is not further discussed here.

reduced, and the OO phase with M_{JT} is stabilized against the CO phase with B_{oc} (Fig. 3c). We notice that Q_M and Q_R are not strongly affected by strain so that the stabilization of the OO phase must be primarily assigned to the strain remormalization of α_{JT}. $E_{JT}^{(2)}$ and $\Delta E_{JT}^{(3)}$ play however an important complementary role and tuning Q_M and Q_R would offer an alternative strategy to stabilize the OO phase.

7.9 Conclusions

We have rationalized the appearance of a CO-type MIT in alkaline-earth ferrites. We have shown that, in $CaFeO_3$, such a MIT arises from the triggering of B_{oc} by M_z and R_{xy} and that this mechanism can induce a CO insulating ground state in $SrFeO_3$ under appropriate tuning of M_z and R_{xy}. Going further, we found that OO is also incipient to $CaFeO_3$ and that an OO-type MIT can be ingeneered in thin films under moderate tensile strain. We have shown that the appearance of the OO-type insulating ground state arises from a delicate balance between different energy terms, suggesting different strategies to stabilize it. Interestingly, the emergence of the OO phase in ferrites is the result of a purely structural instability and we did not find any gradient discontinuity in the energy (corner point), fingerprint of the electronic instability usually associated to OO phases[161]. Such a structural stabilization of the OO phase might offer a reasonable explanation to the emergence of an OO phase in other materials like $RNiO_3$ compounds [162][2].

7.10 Acknowledgements

This work was supported by the FRS-FNRS PDR project HiT4FiT and ARC AIMED. M.S. and Y.Z. acknowledge financial support from FRIA (Grants No.1.E.070.17. and No. 1.E.122.18.). Computational support fromCéci funded by F.R.S.-FNRS (Grant No. 2.5020.1) and Tier-1supercomputer of the Fédération Wallonie-Bruxelles fundedby the Walloon Region (Grant No. 1117545). J.W. acknowl-edges financial support from NSFC (11672264 and 11621062)and the Fundamental Research Funds for the Central Univer-sities (2018XZZX001-05).

Conclusion of the article

Ferrites family allows us to validate the structurally triggered Peierls instability theory discovered thanks to the nickelates family. Moreover, this study illustrates the common mechanism between the Jahn-Teller and Breathing distortions.

From the analysis on both ferrites and nickelates, in the future, I expect a theory describing both breathing and Jahn-Teller as being only one theory. Indeed, it is time to consider those properties in a collective view and not in an isolated atom view. It will be a challenging change of paradigm for the Jahn-Teller community.

[2] Xu He et.al, in press.

At this stage, bulk properties are deeply understood. In the next part, experimental application will take advantage of them to predict and describe the MIT tuning.

Part IV

Validation of this theory to constrained compounds

8 | Modulation tilt control engineered metal-insulator transitions in perovskite nickelates for room temperature optical switching

Zhaoliang Liao[1], *Nicolas* Gauquelin[2], *Robert* J. Green[345], *Knut* Müller-Caspary[2], *Ivan* Lobato[2], *Lin* Li[1], *Sandra* Van Aert[2], *Johan* Verbeeck[2], *Mark* Huijben[1], *Mathieu* N. Grisolia[6], *Victor* Rouco[6], *Ralph* El Hage[6], *Javier* E. Villegas[6], *Alain* Mercy[7], *Manuel* Bibes[6], *Philippe* Ghosez[7], *George* A. Sawatzky[34], *Guus* Rijnders[1], and *Gertjan* Koster[1]

[1]MESA Institute for Nanotechnology, University of Twente, 7500 AE Enschede, The Netherlands [2]Electron Microscopy for Materials Science (EMAT),University of Antwerp, 2020 Antwerp, Belgium [3]Quantum Matter Institute, University of British Columbia, Vancouver, V6T 1Z4, Canada [4]Department of Physicsand Astronomy, University of British Columbia, Vancouver, V6T 1Z4, Canada [5]Department of Physics and Engineering Physics, University of Saskatchewan,Saskatoon, S7N 5E2, Canada [6]Unité Mixte de Physique CNRS/Thales, Université Paris-Saclay, 91767 Palaiseau, France [7]Theoretical Materials Physics,Quantum Materials Center (Q-MAT), Complex and Entangled Systems from Atoms to Materials (CESAM), Université de Liège, B-4000 Liège, Belgium

8.1 Introduction to the article

PNAS 115, 9515 (2018)

The triggered phase transition theory studied on bulk nickelates explicitly mentions the rotation modes can be tweaked to tune the T_{MIT}. Here, the obtained experimental results in heterostructures with artificially modified rotations will be explained by the previously developped bulk Landau model.

8.2 Abstract

In transition metal perovskites ABO_3 the physical properties are largely driven by the rotations of the BO_6 octahedra, which can be tuned in thin films through strain and dimensionality control. However, both approaches have fundamental and practical limitations due to discrete and indirect variations in bond angles, bond lengths and film symmetry by using commercially available substrates. Here, we introduce modulation tilt control as a new approach to tune the ground state of perovskite oxide thin films by acting explicitly on the oxygen octahedra rotation modes, i.e. directly on the bond angles. By intercalating the prototype $SmNiO_3$ target material with a tilt-control layer, we cause the system to change the natural amplitude of a given rotation mode without affecting the interactions. In contrast to strain and dimensionality engineering, our method enables a continuous fine-tuning of the materials properties. This is achieved through two independent adjustable parameters: the nature of the tilt-control material (through its symmetry, elastic constants and oxygen rotation angles) and the relative thicknesses of the target and tilt-control materials. As a result, a magnetic and electronic phase diagram can be obtained, normally only accessible by A-site element substitution, within the single $SmNiO_3$ compound. With this unique approach, we successfully adjusted the metal-insulator transition (MIT) to room temperature to fulfill the desired conditions for optical switching applications.

8.3 Introduction

Oxide heterostructures offer unprecedented opportunities to manipulate the interplay between spin, charge, orbital and lattice degrees of freedom, leading to many novel electronic phases which are hard or even impossible to be realized in bulk materials ([9, 94, 163–167]). To date, strain and dimensionality are two main approaches used to engineer properties of heterostructures (in oxides ranging from dielectric or ferroelectric insulators to superconductors). While both can strongly modify the physical response of the materials ([9, 163–166]), they suffer several limitations, in particular in the context of oxide perovskites whose physical properties are largely driven by the metal-oxygen bond angles ([4, 168, 169]). First, the strain and dimensionality engineering are both discrete handles with restricted tuning possibilities. The strain is applied through the growth on a handful of commercial substrates that have preset lattice constants and the small lattice mismatch that is required for coherent epitaxial growth further limits the choice of substrates. Dimensionality is tuned by reducing the number of unit cells one-by-one and a significant effect only occurs when the thickness is in the range of a few unit cells. Second, the strain often acts in an indirect manner: it will influence the bond angles, but also the bond lengths which can result in non-systematic behavior.

The nickelates have been attracting enormous attention owing to their intriguing properties ([4, 34, 94, 95, 106, 165, 170, 171]). One of the remarkable properties is the metal-

insulator transition (MIT), which in the bulk can be continuously adjusted by tolerance factor or external pressure ([4, 172]), serving as fascinating platform for both fundamental physics investigation and synaptic applications ([17, 34, 91, 95, 106, 170–173]). Very recently, Mercy et al. identified that the breathing mode responsible for the MIT in the perovskite nickelates is triggered by octahedral rotations and tilts ([17]). This makes the nickelates an ideal system for exploring emergent functionalities through the direct control of angles between neighboring octahedra.

In this work, we introduce modulation tilt control as a novel approach to tune the ground state of nickelate thin films by directly acting on the oxygen octahedral rotation modes. Through intercalating the target material with a tilt-control layer (TCL) as shown by the sketch in Fig. 8.1, the natural amplitude of a given rotation mode will be modified in order to retain the connectivity of octahedral network ([174, 175]), leading to strong propagation of the tilt around the in-plane axes. As also shown in Fig. 8.1A, a less tilted TCL can significant reduce the tilt in the target material. If the tilt of TCL is similar to target material, the structure modulation effect then will be very small (see Fig. 8.1B). Additionally, the decay nature of tilt propagation should allow us to modulate the tilt by changing the thickness of the target material. In contrast with strain and dimensionality engineering, our method enables a pseudo-continuous fine-tuning of the materials properties. This is achieved through two independent adjustable parameters: the nature of the tilt-control material (through its symmetry, elastic constants and oxygen rotation angles) and the relative thicknesses of the target and tilt-control materials. In a prototypical system where we combine $SmNiO_3$ (SNO) with TCLs in fine period TCL/SNO superlattices, we are able to directly act on the SNO octahedral rotation mode and therefore continuously tune the MIT. Our results show for the first time that a magnetic and electronic nickelate phase diagram, normally built through A-site element substitution, can be demonstrated in a single SNO compound through the transfer of tilt patterns. This remote control of ground state properties, not through doping but here through the transfer of tilt patterns can be viewed as a structural analogue of modulation doping in semiconductors. This approach paves a way for novel phases in oxides that remain inaccessible by simple composition modulations. Moreover, it offers a novel method to adjust materials to meet practical conditions for applications.

8.4 Results

8.4.1 Experimental Results

Nickelate superlattices (SL) were grown on atomically flat $NdGaO_3$ (NGO) (110) substrates by pulsed laser deposition (SI Appendix, Section 12.1). $LaFeO_3$ (LFO) was chosen as the TCL layer because LFO is less tilted than SNO, and it also shares same polar nature and orthorhombic symmetry as SNO. Additionally, a large compressive strain (1.8%) enforced by the NGO substrate will further reduce the tilt of LFO ([176, 177]). Therefore, a strong

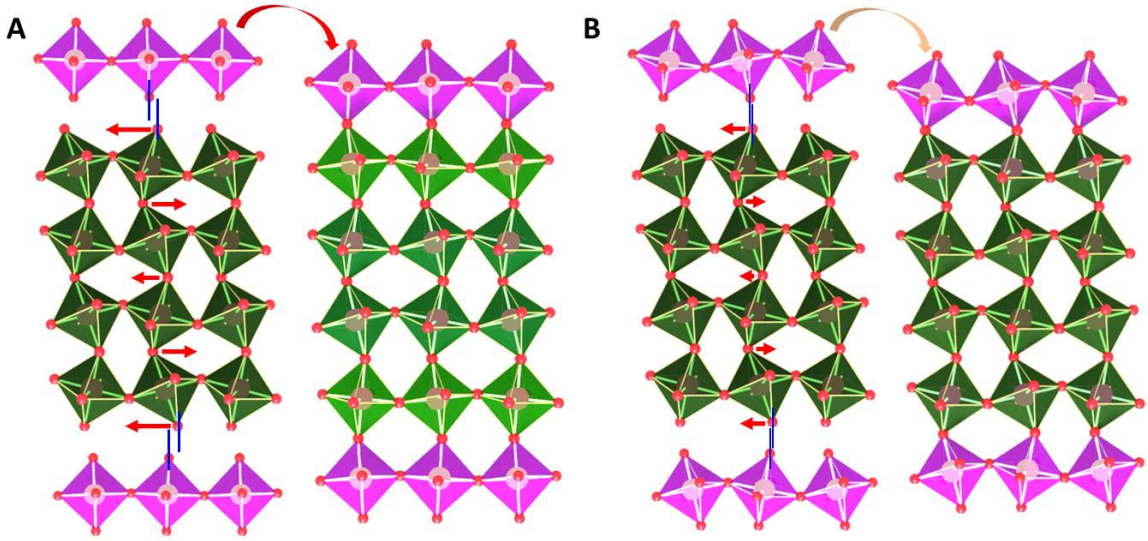

Figure 8.1 | **Octahedral tilt pattern modulation.** Schematic view of octahedral tilt modulation (green layer) by introducing a tilt-control-layer (purple layer) having (A) less tilting and (B) more tilting. Here, an orthorhombic structure ($a^+b^-b^-$) is used for demonstration. The red arrows and their length indicate the direction and amount of the rotation angle change, respectively, which are necessary to match tilt control layer. A smaller tilt change in interior layers is due to the decay nature of interfacial geometry constraint.

tilt modulation of SNO by LFO can be expected. Four unit cells (uc) LFO were deposited first and subsequently the $(LFO_1/SNO_n)_m$ superlattices (noted as LFO_1-SNO_n) were grown starting from SNO. The total SNO thickness (n×m) was maintained at ∝40 uc. The SNO films and LFO_1-SNO_n superlattices share the same orthorhombic symmetry as characterized by x-ray diffraction (SI Appendix, Section 12.2). Due to the presence of LFO, the LFO_1-SNO_n superlattices are found to exhibit less structural distortion compared to pure SNO films.

The layer resolved lattice distortion of nickelate superlattices was investigated by scanning transmission electron microscopy (STEM). The orthorhombic symmetry produces out-of-phase tilts of amplitude (α_T) and in-phase rotations of amplitude (α_R) around the in-plane [1-10] and [001] axis respectively. These rotational behaviors are revealed microscopically by resolving the oxygen sites in the annular bright field (ABF) images (see Fig. 8.2A-B). The limited contrast difference between LFO and SNO in STEM images is due to the similarity in atomic number for Sm and La, as well as Ni and Fe, but the chemical contrast can be resolved by electron energy loss spectroscopy (EELS) (SI Appendix, Section 12.3-12.4). The ABF image of the (1-10) plane displays significantly elongated and blurred oxygen sites, which are consistent with the signature of out-of-phase rotation which generates two very close oxygen columns (O1 and O2) (see Fig. 8.2A). In the (001) plane, the atomically resolved oxygen sites clearly confirm the in-phase rotational behavior around the [001] axis (see Fig. 8.2B).

Using statistical parameter estimation theory to quantify the atomic positions from a STEM image, we are able to obtain detailed, layer resolved lattice structure parameters

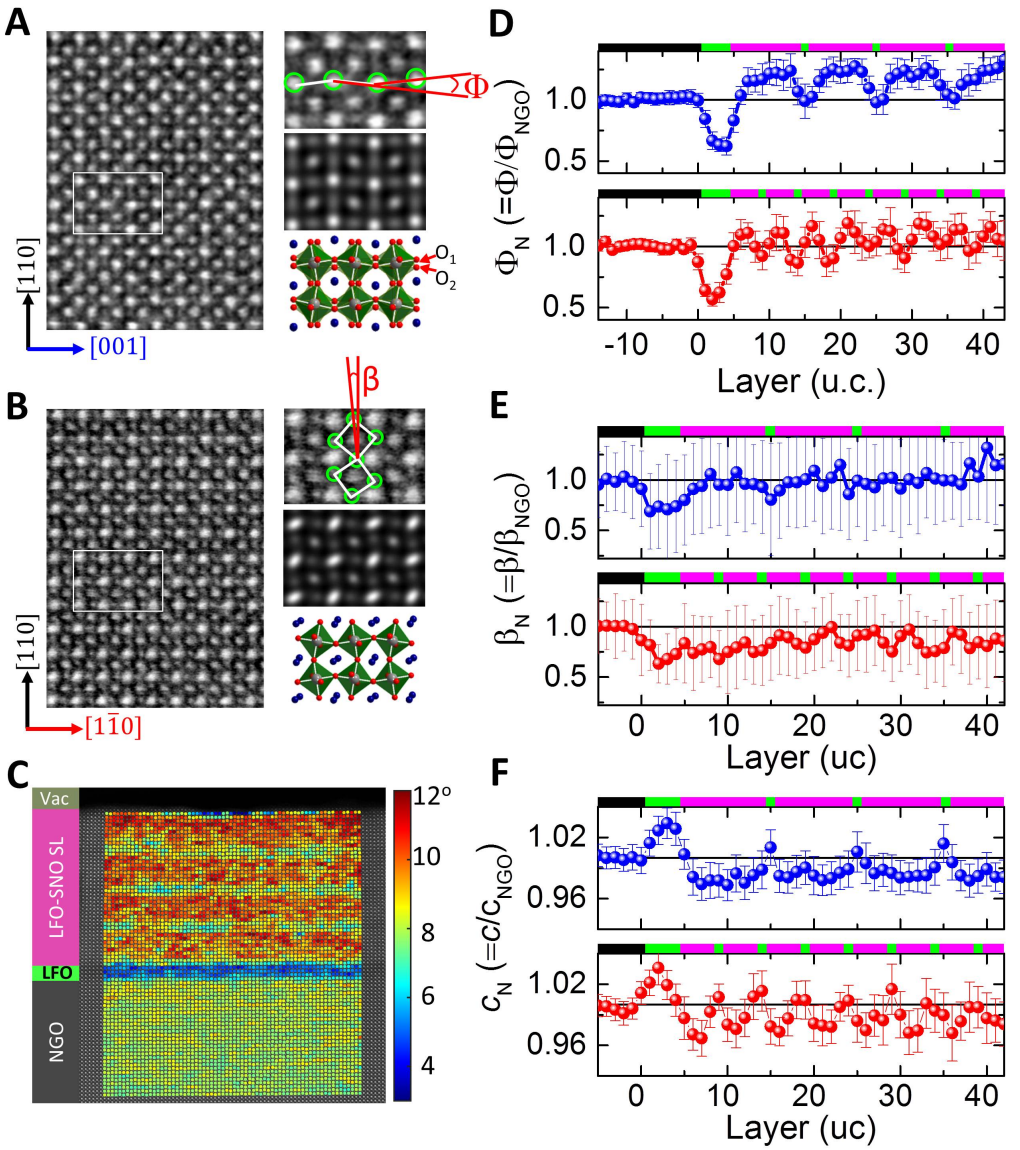

Figure 8.2 | **Atomic scale lattice structural characterization.** Inversed ABF images of LFO_1-SNO_4 with zone axis along (A) [1-10] and (B) [001] directions. Right next to (A) and (B) are magnifications of a selected region (top panel), simulated ABF-STEM images (middle) and structural models of bulk $SmNiO_3$ (bottom) for comparison. (C) 2D mapping of anti-polar A-site motions (ϕ) in LFO_1-SNO_{10}. The ϕ mapping is overlaid on a HAADF image from which the angle ϕ is calculated. The profile of (D) anti-polar motion (ϕ); (E) octahedral tilt (β); (F) out-of-plane lattice parameter c for LFO_1-SNO_4 (red) and LFO_1-SNO_{10} (blue). On top of each panels in (D)-(F) are the corresponding schematic view of chemical profiles with black (NGO), green (LFO) and purple (SNO).

across the superlattices (SI Appendix, Section 12.5). Figure 8.2C shows an example of the 2D mapping of the anti-polar A motion of LFO_1-SNO_{10} SL which is described by angle (ϕ) (see definition in Fig. 8.2A). The angle ϕ is correlated with amplitudes of rotations (α_R) and tilts (α_T) of the BO_6 octahedra: $\phi \propto \alpha_R \cdot \alpha_T$ ([178, 179]). The layer resolved profile of ϕ in LFO_1-SNO_{10} is shown in Fig. 8.2D. To avoid possible artefacts from the imaging technique itself, the profiles are normalized to the value of the NGO substrate ($\phi_N = \phi/\phi_{NGO}$). As shown in Fig. 8.2D, a relaxation of the angle ϕ_N is observed within the central part of the first 4 uc LFO layer, while near both the bottom LFO/NGO and top SNO/LFO interfaces this angle ϕ_N is larger, as expected from the geometric constraint effect discussed above in Fig. 8.1. Within the superlattice region a trapezoidal wave-like ϕ_N-profile is observed with a minimum angle exhibited by the LFO single layer and a plateau in the central part of each SNO layer. Closer to the LFO layer, the ϕ_N of SNO becomes smaller. Upon reducing the SNO to 4 uc, the whole SNO layer is now under the impact of interfacial structure constraint and thus the ϕ_N-profile is changed into a more triangular wave-like shape.

The profiles of octahedral tilt angle β_N ($=\beta/\beta_{NGO}$) around the [001] axis (see definition in Fig. 8.2B) are estimated from ABF images (SI Appendix, Section 12.5). This tilt angle β corresponds in fact to the projection of α_T on (001) planes. Similar to the anti-polar distortion ϕ_N, the β_N becomes smaller near the LFO/SNO interface and a periodic modulation of β_N is observed across the superlattice as shown in Fig. 8.2E. The modulation of the β_N of SNO layer is weakened when the SNO thickness is increased from 4 to 10 uc. The stretching or bending of the Ni-O bond should also change the lattice constant. This scenario is confirmed from the profile of out-of-plane lattice constant (c). As shown in Fig. 8.2F, the lattice parameter c of LFO within the superlattice region is smaller than that in the 4 uc LFO buffer region. Near the LFO/SNO interface, the c of the SNO becomes larger than that in the central region of the SNO layer. The larger (smaller) c of LFO or SNO corresponds to smaller (larger) tilt in LFO or SNO (see Fig. 8.2D-F). The mean value $<\phi_N>$ ($<\beta_N>$) of SNO in LFO1-SNO10 and $LFOi_1$-SNO_4 SLs are 1.178 (0.976) and 1.049 (0.852), respectively. The reduced tilts and anti-polar distortion demonstrate the effective control of octahedral distortion of SNO by intercalating single LFO layer.

The electronic structures of SNO have been investigated by X-ray absorption spectroscopy (XAS). As shown in Fig. 8.3A, both Ni L_2 and L_3 edges are split into two (A and B) peaks as occurring in bulk $RNiO_3$ ([180]). The peak splitting energy ΔE ($\equiv E_B$-E_A) in LFO_1-SNO_4 is smaller than in LFO_1-SNO_{10}, while in LFO_1-SNO_{10} is similar to that in SNO_{30}. As shown by the zoomed-in view of the Ni L2 edge in Fig. 8.3B, the two split peaks gradually merge with decreasing SNO thickness in LFO_1-SNO_n. The ΔE for the Ni L_3 edge is shown in Fig. 8.3C, clearly illustrating a smaller splitting energy due to the structure modulation by LFO. The splitting of the Ni L-edge is suggested to depend on both the magnitude of the breathing mode distortion and the size of the Ni-O-Ni hopping interaction ([181]). A smaller splitting energy indicates a smaller Ni-O-Ni interaction and a smaller breathing distortion (δd=(dL-dS)/2) where dL and dS are the long and short Ni-O bonds respectively ([181]). The XAS

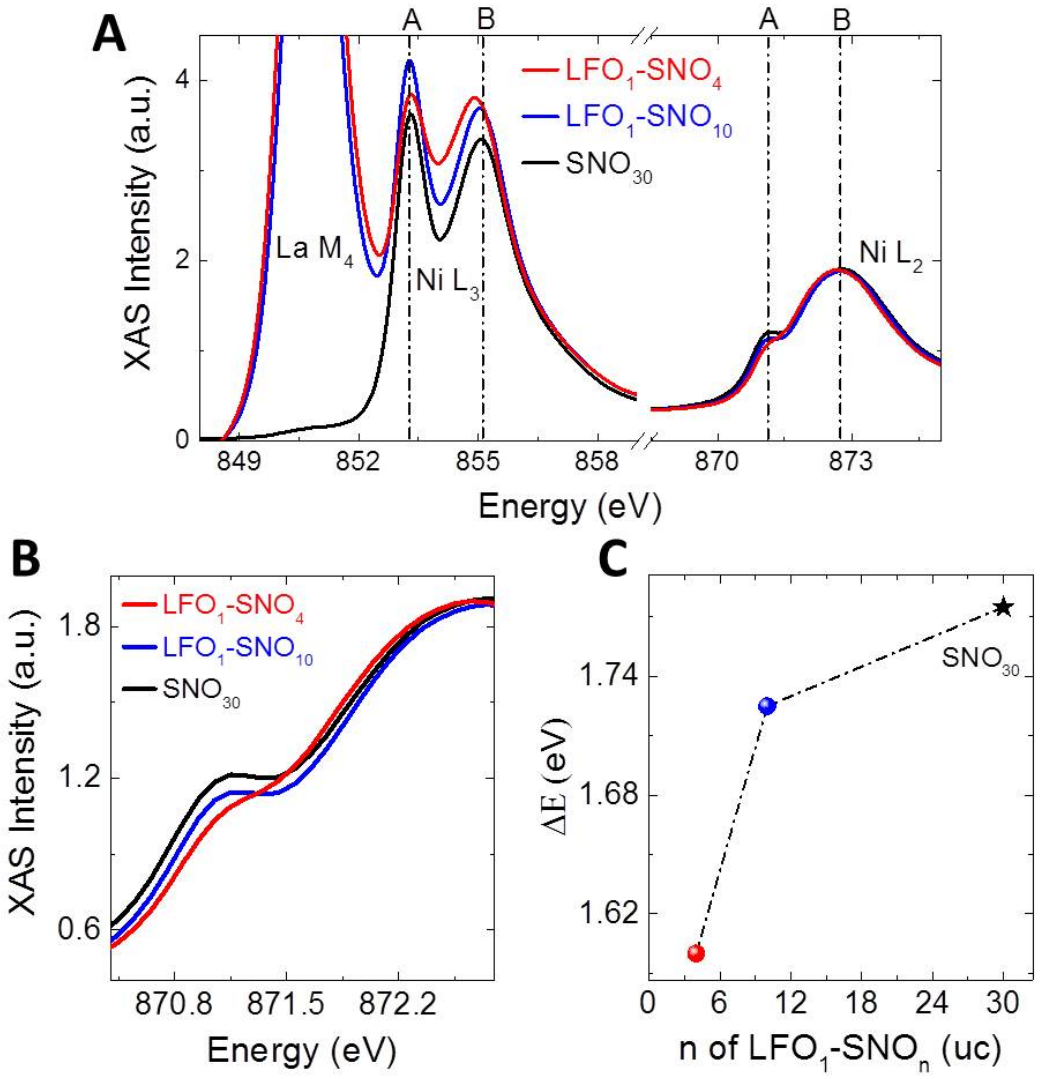

Figure 8.3 | **Electronic structure of nickelate superlattices.** (A) XAS of Ni $L_{2,3}$ edge; (B) zoomed-in spectra of Ni L_2 edge;(C) peak splitting energy $\Delta E=E_B-E_A$ of LFO_1-SNO_n superlattices and SNO_{30} film. The XAS was measured at 22 K

of Ni $L_{2,3}$ edge shown in Fig. 8.3A also suggests the absence of Ni_2^+ and no change of the valence of Ni, excluding possible charge transfer between LFO and SNO layers.

Concomitant to lattice and electronic structure modulations, a significant change of transport properties in LFO_1-SNO_n SLs has been achieved. As shown in Fig. 8.4A, a giant enhancement of conductivity is observed in LFO_1-SNO_4 SL. The characteristic MIT temperature T_{MIT} is reflected from the resistivity inflection point ($\frac{dln\rho}{d\frac{1}{T}}\Big|_{max}$) ([182]) as shown in inset of Fig. 8.4A. The T_{MIT} of LFO_1-SNO_4 is 78 K, much lower than that of SNO_{30} film (356 K). With increasing SNO thickness, the T_{MIT} moves toward that of bulk SNO films, coincident with the smaller structural modulation by LFO as the SNO thickness increases. The thickness (n) of SNO within LFO_1-SNO_n behaves similarly to the tolerance factor, monotonically controlling the transition temperatures (SI Appendix, Section 12.6).

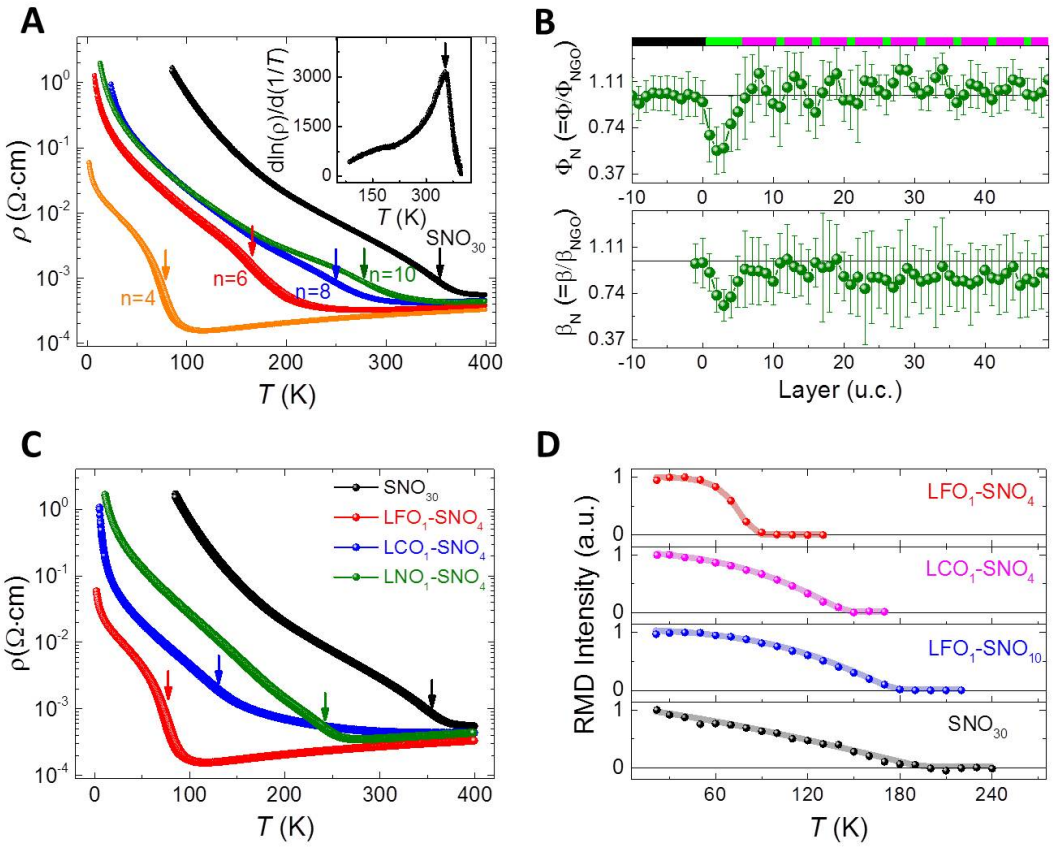

Figure 8.4 | **Transport and magnetic properties of tilt engineered nickelate superlattices.** (A) Temperature dependent resistivity of LFO_1-SNO_n superlattices (n=4-10) and 30 uc SNO film (SNO_{30}). Inset shows the first derivative $\frac{dln\rho}{d\frac{1}{T}}$ of SNO_{30} sample. The arrows in (A) and (C) indicate the resistive inflection points derived from $d\frac{dln\rho}{d\frac{1}{T}}\Big|_{max}$. (B) Layer dependent profiles of anti-polar motions (ϕ) and octahedral tilt angle (β) of LCO_1-SNO_4 superlattice. The chemical profile is schematically shown on top: black (NGO); green (LCO); purple (SNO). (D) Temperature dependent intensity of (1/4,1/4,1/4) magnetic Bragg reflection peak.

The decay nature of the geometric constraint imposed by the octahedral network across the interface allows us to rationally design the octahedral tilt distortion via either changing the thickness of the SNO layer or a delicate choice of the tilt-control-layer. As an illustration of the designed functionality by engineering the nature of TCL, a $LaCrO_3$ (LCO) layer was used to fabricate a LCO_1-SNO_4 SL and compare to the LFO_1-SNO_4 SL. LCO shares the same orthorhombic structure and similar octahedral tilt with LFO but has a smaller lattice mismatch of 0.6% with NGO than LFO/NGO of 1.8%. LCO is expected to exhibit more bending of the Cr-O-Cr bond, and therefore, have less impact on the tilt of the SNO ([176, 177]). The effect of LCO on the SNO structural modulation was investigated as well by STEM as shown in Fig. 8.4B. Near the LCO/SNO interface, both the ϕ_N and β_N of SNO are found to be reduced as occurring in LFO_1-SNO_4. However, the $<\phi_N>$ and $<\beta_N>$ of SNO within LCO_1-SNO_4 SL are 1.079 and 0.890, respectively, bigger than the values for LFO_1-SNO_4 as mentioned above. Accordingly, the LCO_1-SNO_4 SL shows higher conductivity than non-engineered SNO_{30}, but is less conductive than the LFO_1-SNO_4 SL (see Fig. 8.4C). The significant impact from LFO is further illustrated by comparing to $(LaNiO_3)_1$-SNO_4 (LNO_1-SNO_4) superlattice. As shown in Fig. 8.4C, the LNO_1-SNO_4 exhibits a much higher T_{MIT} (= 240 K) than LFO_1-SNO_4. Although LNO has a little smaller tilt in bulk (5.30) than that of bulk LFO (6.80), the LNO layer is under tensile strain which increases the tilt, in contrast to the highly compressive strain imposed on the LFO layer. The higher conductivity in LFO_1-SNO_4 than LNO_1-SNO_4 further reveals a pivotal role of the structural effect rather than any possible chemical reconstruction at the interface.

In addition, the Néel temperature (T_N) was measured using resonant magnetic diffraction (RMD) ([181, 183]). The RMD signal was taken at the Ni L_3 resonance. Figure 8.4D displays the temperature dependent intensity of the (1/4,1/4,1/4) magnetic Bragg reflection peak, which arises from the E'-type antiferromagnetic (E'-AFM) ordering of the nickelates. The Néel temperature is found to vary significantly when introducing interfacial structure modulation. The T_N of the SNO_{30} film is 194 K while it is 85 K for the LFO_1-SNO_4. For LFO_1-SNO_{10} the effect of the LFO layer becomes weaker and the T_N is around 176 K, close to the SNO_{30} film. The T_N of LCO_1-SNO_4 is 146 K, in between LFO_1-SNO_4 and LFO_1-SNO_{10}.

With the obtained T_N and T_{MIT}, a phase diagram is constructed using the mean Ni-O-Ni bond angle as control parameter (see Fig. 8.5). Here, the mean Ni-O-Ni bond angles are converted from mean values of β_N (See Materials and Methods 8.6). It is found that the T_{MIT} monotonically changes with the bond angle. For films with relatively small Ni-O-Ni bond angles and large T_{MIT} (> 200 K), T_N and T_{MIT} are decoupled and T_{MIT} decreases relatively abruptly as the bond angle increases. According to that trend, T_{MIT} should be below T_N at large bond angles; in that region however, the T_{MIT} is further promoted by the appearance of the E'-type AFM order and T_{MIT} becomes pinned at T_N, in line with the discussion in Ref. [17] and in agreement with bulk phase diagram ([4]). Therefore, the geometric design of the octahedral network produces a bulk-like phase diagram of the whole nickelate family but using only one compound $SmNiO_3$ (see Fig. 8.5 and SI Appendix, Section 12.6). Our results

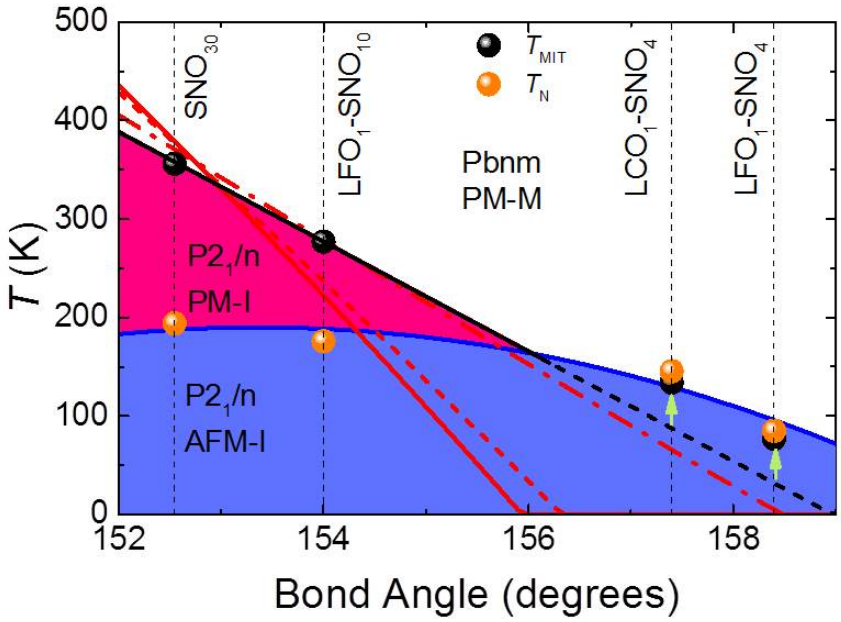

Figure 8.5 | **Temperature phase diagram of nickelate superlattices as a function of the mean Ni-O-Ni bond angle.** The mean bond angle is converted from mean tilt angle α_T (see Materials and Methods). The black dots (T_{MIT}) and orange dots (T_N) are experimental data. The theoretical evolution of T_{MIT} has been estimated while constraining the tilt angle α_T as imposed by the TCL and (i) relaxing self-consistently the rotation angle α_R ($\Delta\alpha_R \approx$ -1.5 %, full red line), (ii) constraining the rotation angle to keep it fixed ($\Delta\alpha_R$ = 0%, dashed red line) or (iii) constraining further the rotation angle to increase it slightly ($\Delta\alpha_R \approx$ +3%, dash-dot red line). See Materials and Methods Section for the explanation of the parameter $\Delta\alpha_R$.

also highlight the effect of local octahedral distortion at the atomic scale on the nickelate electronic states, confirming the central role the NiO_6 octahedral tilt in determining the properties of nickelates.

8.4.2 Theoretical Results

The explicit link between the controlled amplitude of the Ni-O-Ni bond angle and the observed evolution of T_{MIT} can be further supported theoretically using the Landau-type model of Ref. [17], assigning the MIT to a triggered phase transition arising from the softening of the breathing distortion by oxygen tilts and rotation and with parameters directly derived from first-principles. Starting from the set of parameters associated to the effective tolerance factor yielding a T_{MIT} equal to that of SNO_{30}, we can mimic the role of the TCL by forcing artificially the tilt mode amplitude (i.e. rescaling its energy curvature, see Materials and Methods) and investigating the subsequent impact on T_{MIT}. This can be done while allowing self-consistent relaxation of the rotation mode or by constraining it additionally so that it remains constant or is slightly amplified. The predictions of the model are summarized in Fig. 8.5 and compared with the experimentally obtained correlation between T_{MIT} and bond-angle. Note that here the model is restricted to structural degrees of freedom and

neglects the emergence of a magnetic order at T_N. The agreement observed between theory and experiment confirms the central role of the oxygen tilts in tuning T_{MIT}. The model further suggests that rotations might be slightly amplified as the tilts are reduced.

8.4.3 Application at room temperature

This efficient tuning is exploited practically to move T_{MIT} close to room temperature and switch the resistance by an external stimulus. Here, we propose and use a new approach to tune the resistance of nickelates through light illumination at specific wavelengths. The inset of Fig. 8.6A presents a sketch of the electronic structure of a nickelate in its insulating phase as usually understood today. The conduction band is formed by e_g^* states (antibonding states between Ni 3d and O 2p states, of predominant oxygen character) whose density of states shows a double peak shape with a local minimum ([102]). Below the Fermi level, the valence band has a similar character, in line with the negative-charge transfer nature of nickelates. Further down in energy lie the t_{2g}^* states, with dominant Ni 3d character. This electronic structure allows for three main optical transitions (see inset in Fig. 8.6A) ([129]). The deeper t_{2g}^* to e_g^* states transition (blue arrow) corresponds to transferring electrons from a 3d-like state to a O 2p-like state. Given that the occupancy of O 2p states is directly related to the level of covalence, a t_{2g}^* - e_g^* transition should intensify the covalent character and then enhance conductivity ([95]). More generally, photo-transfer of electrons from large to small Ni cages will bring the system closer to the metallic electronic configuration of the P*bnm* phase.

In order to realize room temperature oxide electronics for practical applications, several different tilt control layers have been explored to induce a first order room temperature metal-insulator transition, and $NdNiO_3$ (NNO) is found to be an ideal candidate (see Fig. 8.4 and SI Appendix Section 12.7). A first order MIT near room temperature was obtained in a $(NNO_1/SNO_2)_{10}$ (NNO_1-SNO_2) superlattice (see SI Appendix Section 12.7). Figure 8.6A shows its resistance at 70 K (well into the insulating state) upon low-power illumination at different photon energies. The resistance shows a minimum for an energy corresponding to the t_{2g}^* - e_g^* transition, which is consistent with the photo-doping mechanism described above. Figure 8.6B presents the temperature dependence of the resistance of the sample with and without 2.69 eV high-power blue light, non-isothermal illumination. The MIT temperature shifts down by 20 K with the light on, yielding a maximum light-induced resistance change near 300 K. Figure 8.6C shows the evolution of the resistance upon illumination with blue light pulses at different temperatures. Consistent with the data in Fig. 8.6B, the resistance switching effect is maximized at 300 K, amounting to nearly 150%. In the Supplementary Information, we show data for isothermal illumination and for a LFO_1-SNO_{10} superlattice. Since we were using long illumination pulses, sample heating due to light absorption was probably the main process at play, causing an apparent shift of the MIT temperature. However, the observed maximum optical switching near room temperature

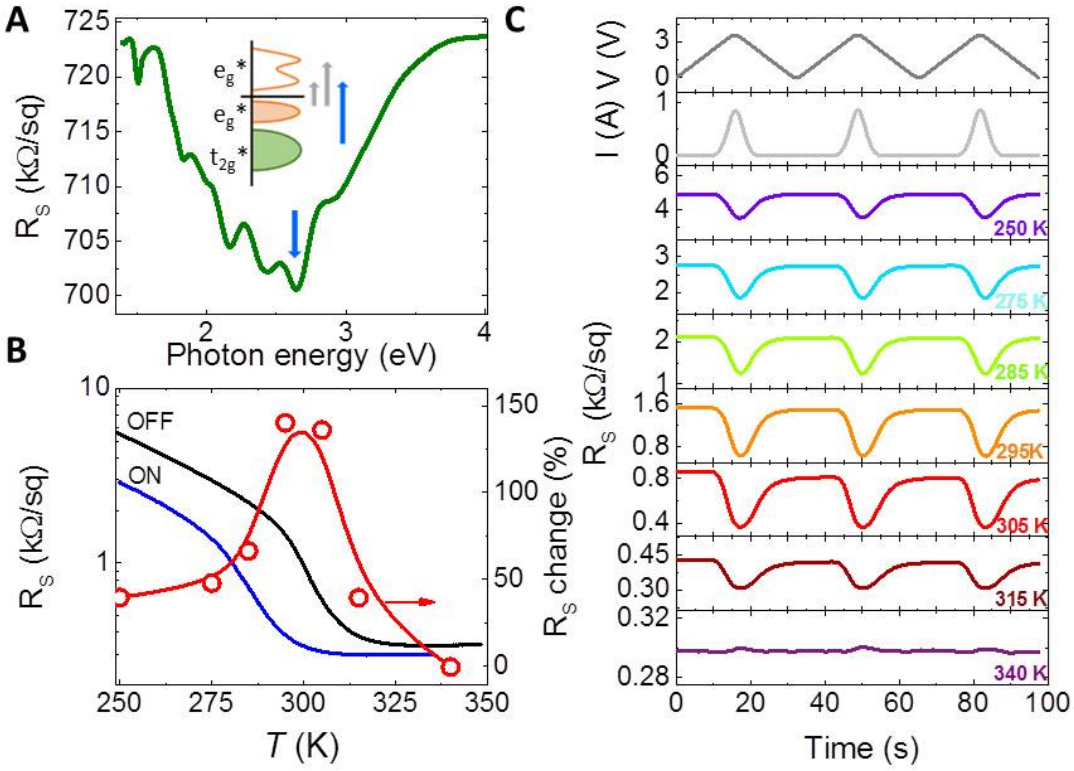

Figure 8.6 | **Light-induced resistance switching in nickelate superlattices.** (A) Dependence of the sheet resistance with illuminating photon energy at 70 K for a NNO_1-SNO_2 superlattice. The sketch describes the different optical transitions in nickelates, and the down-pointing blue arrow shows the energy corresponding the $t_{2g}^* \rightarrow e_g^*$ transition at ∝2.7 eV. (B) Temperature dependence of the sheet resistance a NNO_1-SNO_2 superlattice (left axis) without (black) and with illumination (blue) with a blue LED ($h\nu$ = 2.69 eV) powered with 1 A. Relative resistance change (right axis) induced by illumination. The symbols (right axis) correspond to the data of panel (C). (C) Top two panels: voltage and current applied to the blue LED vs time. Bottom seven panels: time dependence of the resistance upon illuminating the NNO_1-SNO_2 sample with the blue LED at different temperatures.

would strongly imply that the photo-doping mechanism proposed above should also yield a resistance switching effect for ultrafast (sub ps) pulses with a photon energy corresponding to the t_{2g}^{*} - e_{g}^{*} transition (see also SI Appendix Section 12.8). In any case, our data qualify engineered nickelates as room-temperature photoresistors based on a correlated material.

8.5 Conclusions

In conclusion, we demonstrated the remote control of ground state properties of nickelates through interfacial tilt patterns modulation using a tilt control layer. By manipulating two independent adjustable parameters-the nature of the tilt-control material and the relative thicknesses of the target and tilt-control materials, we obtained pseudo-continuous modulation of octahedral tilt and fine-tuning of the materials properties. Our results visualized the monotonic change of the metal-insulator transition with varying octahedral tilt, remarkably underlining the role of the Ni-O-Ni bond angle in determining the electronic ground state of the nickelates and supporting the structurally triggered mechanism proposed in Ref. [17]. By finely tuning the oxygen network, we are already able to achieve a near room temperature metal-insulator transition and a giant room temperature optical switching of resistance. The interfacial tilt pattern modulation using a tilt control layer can be viewed as a structural analogue of modulation doping in semiconductors, which has been a breakthrough discovery and led to both the observation of the fractional quantum Hall effect and to faster microelectronic circuits. This interface modulation tilt control can be applied directly to other perovksite materials, opening up new perspectives for the rational design of new classes of quantum materials for next generation electronics applications.

8.6 Materials and Methods

The $SmNiO_3$ (SNO), $LaNiO_3$ (LNO), $LaFeO_3$ (LFO) and $LaCrO_3$ (LCO) films or layers were deposited on atomic flat $NdGaO_3$ (110) (NGO) substrates at a laser fluence of 2 $\frac{J}{cm^2}$ by pulsed laser deposition (PLD) technique. The XRD was performed by PANalytical-X'Pert materials research diffractometer (MRD) at high resolution mode. Transport properties were measured by using a Quantum Design Physical Properties Measurement System (PPMS) in a van-der-Pauw geometry.

Scanning transmission electron microscopy (STEM) was performed on the X-Ant-Em instrument at the University of Antwerp. Cross-sectional cuts of the samples along the [1-10] and [001] directions were prepared using a FEI Helios 650 dual-beam Focused Ion Beam device. Satisfactory samples were prepared using low energy ion beam final thinning subsequent to a protection of the sample surface by sputtering of a 30 nm thick carbon protection layer, followed by E-beam deposition of Platinum as a first step to the FIB lamella preparation procedure. For imaging and EELS, the microscope was operated in STEM at 300 kV acceleration voltage with a convergence semi-angle of 21 mrad, providing a probe size

of ∝0.8 **r**A. The collection semi-angle ranges from 8-17 mrad and 44-190 mrad for ABF and ADF imaging respectively. The collection angle for EELS was 69 mrad. Image processing and analysis is detailed in the supporting Information. Simulations of ABF-STEM images of $SmNiO_3$ along [001]or and [1-10]or zone-axes were made with QSTEM at conditions of probe size 0.7 **r**A, 300 kV, de focus -1.7 nm, C3 = 1 micron, convergence angle 21 mrad, 15 configurations for TDS, collection angle 8-17 mrad, 15 nm thickness.

The x-ray absorption spectroscopy (XAS) and resonant magnetic diffraction (RMD) were performed using an in-vacuum 4-circle diffractometer at the Resonant Elastic and Inelastic X-ray Scattering (REIXS) beamline at Canadian Light Source (CLS) in Saskatoon, Canada. The beamline has a flux of 5×10^{12} $\frac{photon}{s}$ and photon energy resolution of 10^{-4} eV. The base pressure of the diffractometer chamber was kept lower than 10^{-9} Torr. The XAS spectra were measured using the total electron yield method, with the incident photons at an angle of 30 degrees from the surface. At the Ni $L_{2,3}$ edge, measurements with π and σ polarizations were averaged.

The Landau-type modeling was performed relying on the expression provided in Ref. [17] and related set of parameters directly fitted from first-principles DFT calculations (see Supplementary Material of Ref. [17]). The effective tolerance factor was selected to get a MIT corresponding to that experimentally observed in the SNO_{30} sample (T_{MIT} = 356 K). Then, in order to mimic the role of the TCL on the tilt mode, the energy curvature of the latter was renormalized by adding a prefactor (1-x) in front of the tilt quadratic coefficient. Tuning x, we can get the evolution of the tilt amplitude at room temperature (α_T directly linked to the Ni-O-Ni bond angle) and of the corresponding T_{MIT} in term of the external constraint imposed on the tilt mode. Results are reported in Fig. 8.5 in which we plot the evolution of T_{MIT} with respect to that of the Ni-O-Ni bond angle at room temperature for direct comparison with experimental data. Since tilt and rotation modes are coupled within the Landau model through a bi-quadratic term, tuning the tilt amplitude also indirectly affects the rotation angle. Since we have no direct information on the effects of the TCL and epitaxial strain on the latter, calculations were performed (i) relaxing self-consistently the rotation angle α_R which progressively evolves with α_T (for the largest constraint imposed on α_T in Fig. 8.5, the deviation of α_R at T_{MIT} with respect to its natural amplitude - i.e. value in bulk without constraint – is $\Delta\alpha_R \approx$ -1.5 %). (ii) constraining the rotation angle in order to force it to remain unaffected ($\Delta\alpha_R$ = 0%) and (iii) constraining the rotation angle in order to increase it slightly (here the coupling between rotations and tilts has been slightly modified so that for the largest constraint imposed on α_T in Fig. 8.5, $\Delta\alpha_R \approx$ +3 %). The tilt angle amplitude α_T, as accessible from the Landau model, and its projection on (001) planes, as measured experimentally, are both related to the Ni-O-Ni bond angle reported in Fig. 8.5 through : $\theta = 180 - 2\,\alpha_T = 2\,\sin^{-1}[1/(1+2\tan 2\,\beta)1/2]$.

Transport measurements under illumination were performed in a MONTANA cryostation with uncoated windows presenting 90% transmittance in the visible range. Two different configurations were used for characterizing the thermal response of the samples. In

Setup-1, the layer was thermally connected to the cold finger of the cryostat. To do so we added thermal grease to the edges of the sample in such a way that the $NdGaO_3$ substrate was thermally connected to the sample holder. In Setup-2, an insulating layer was added between the sample and the sample holder such that there was no thermal contact between the layer and the cold finger of the cryostat. The sheet resistance was determined by biasing with a current of 10 μA.

8.7 Acknowledgements

We would like to acknowledge Prof. Z. Zhong for stimulated discussion. M.H., G.K. and G.R. acknowledge funding from DESCO program of the Dutch Foundation for Fundamental Research on Matter (FOM) with financial support from the Netherlands Organization for Scientific Research (NWO). This work was funded by the European Union Council under the 7th Framework Program (FP7) grant nr NMP3-LA-2010-246102 IFOX. J.V., S.V.A, N.G. and K.M.C. acknowledge funding from FWO projects G.0044.13N, G.0374.13N, G. 0368.15N, and G.0369.15N. The Qu-Ant-EM microscope was partly funded by the Hercules fund from the Flemish Government. N.G. acknowledges funding from the European Research Council under the 7th Framework Program (FP7), ERC Starting Grant 278510 VORTEX. N.G. and J.V. acknowledge financial support from the European Union under the Seventh Framework Program under a contract for an Integrated Infrastructure Initiative (Reference No. 312483-ESTEEM2). The Canadian work was supported by NSERC and the Max Planck-UBC Centre for Quantum Materials. Some experiments for this work were performed at the Canadian Light Source, which is funded by the Canada Foundation for Innovation, NSERC, the National Research Council of Canada, the Canadian Institutes of Health Research, the Government of Saskatchewan, Western Economic Diversification Canada, and the University of Saskatchewan. MB acknowledges funding from the European Research Council under the 7th Framework Program (FP7), ERC CoG grant MINT #615759. A.M. and Ph.G. were supported by the ARC project AIMED and F.R.S-FNRS PDR project HiT4FiT and acknowledge access to Céci computing facilities funded by F.R.S-FNRS (Grant No 2.5020.1), Tier-1 supercomputer of the Fédération Wallonie-Bruxelles funded by the Walloon Region (Grant No 1117545) and HPC resources from the PRACE project Megapasta.

8.8 Conclusion of the article

To allow experimentalists to work independetly of the nickelates compounds on the MIT at room temperature, this paper explains how the critical temperature can be shifted by only affecting the structural contribution. In the next chapter, I will show how the electronic contribution, on its side, can be tuned to affect the MIT.

9 | Length-scales of interfacial coupling between metal-insulator phases in oxides

Claribel Domínguez[1], *Alexandru B.* Georgescu[2], *Bernat* Mundet[1,3], *Yajun* Zhang[4], *Jennifer* Fowlie[1], *Alain* Mercy[4], *Adrien* Waelchli[1], *Sara* Catalano[1], *Duncan T.L.* Alexander[3], *Philippe* Ghosez[4], *Antoine* Georges[1,2,5,6], *Andrew J.* Millis[2,7], *Marta* Gibert[8], and *Jean-Marc* Triscone[1]

[1]Department of Quantum Matter Physics, University of Geneva, Geneva, Switzerland [2]Center for Computational Quantum Physics, Flatiron Institute, New York, USA [3]Electron Spectrometry and Microscopy Laboratory (LSME), Institute of Physics (IPHYS), École Polytechnique Fédérale de Lausanne (EPFL), Lausanne, Switzerland [5]Collège de France, 11 place Marcelin Berthelot, 75005 Paris, France [6]Centre de Physique Théorique (CPHT), CNRS, Institut Polytechnique de Paris, France [7]Department of Physics, Columbia University, New York, USA [8]Physik-Institut, University of Zurich, Winterthurerstrasse 190, 8057 Zurich, Switzerland [4]Theoretical Materials Physics, Q-MAT, CESAM, University of Liège, B-4000 Liège, Belgium

9.1 Introduction to the article

On arXiv:1909.06287 and submitted to Nature Materials (2020)

In the previous chapter, the structural properties were tweaked to control the MIT critical temperature. Even though the triggering of the breathing by the rotations does still play a major role in the MIT, the explanation of the results in the supplementary of the previous chapter is completed with the interpretation done in the current chapter. Indeed, Liao et al.[33] obtained only one temperature, as predicted in this chapter due to the small number of slices, for the NNO-SNO superlatices which depends on the NNO/SNO ratio. As a last step, in this thesis, the electronic structure is deeply analysed to also explain the shift and/or split of the TMI.

9.2 Abstract

Controlling phase transitions in transition metal oxides remains a central feature of both technological and fundamental scientific relevance. A well-known example is the metal-insulator transition which has been shown to be highly controllable. A less well understood aspect of this phenomenon is the length scale over which the phases can be established. To gain further insight into this issue, we have atomically engineered an artificially phase separated system through fabricating epitaxial superlattices consisting of $SmNiO_3$ and $NdNiO_3$, two materials undergoing a metal-to-insulator transition at different temperatures. By combining advanced experimental techniques and theoretical modeling, we demonstrate that the length scale of interfacial coupling between metal-insulator phases is determined by balancing the energy cost of the boundary between a metal and an insulator and the bulk phase energies. Notably, we show that the length scale of this effect exceeds that of the physical coupling of structural motifs, introducing a new framework for interface-engineering properties at temperatures against the bulk energetics.

9.3 Introduction

Phase transitions characterized by a strong coupling of charge, spin, orbital and lattice degrees of freedom are ubiquitous in transition metal oxide materials[3]. A well-known example is the metal-insulator transition, which is typically first-order and exhibits regions of phase coexistence. Many studies have focused on manipulating the metal-to-insulator transition (MIT) through intrinsic and extrinsic effects[123, 184–186]. Moreover, experimental techniques such as photoemission electron microscopy and near-field scanning optical microscopy have been used to observe the phase coexistence at the MIT[187, 188]. However, remarkably little is known about the characteristic lengths of the two possible phases. Important open issues include the minimum length-scale over which a metallic or an insulating state can be established and the physics that sets this length-scale. Is this length-scale controlled by propagation of lattice distortions or more subtle interfacial effects? Answering these questions is important both for understanding the fundamental physics of the metal-insulator transition and for obtaining the control that is essential for application in new generations of electronic devices.

In this paper we present experimental and theoretical analyses of a series of specially-designed structures of two oxide materials that undergo metal-to-insulator transitions at different temperatures while sharing the same order parameter. We create atomic-precision epitaxial superlattices consisting of alternating layers of the two materials and we study the temperature dependence of their conductivity as a function of layer thickness. For thicker layers, two separate transitions are observed such that the engineered bi-component system mirrors the independent properties of the individual layers. For thinner layers the system behaves like one material, with a single metal-insulator transition, implying that we have

engineered properties unique to this superlattice system. The characteristic length-scale above which two separate transitions are observed implies a critical minimum thickness of around 3 nm. This is remarkably large considering the first-order nature of the metal-insulator transition which is not associated with diverging length scales. By combining our data with theoretical modeling, we demonstrate that the length-scale of interfacial coupling between metal-insulator phases in the superlattices is set neither by the length-scale of the propagation of structural motifs nor by that of the electronic order parameter from one material to the other. Rather, the length scale is set by the competition between interface and bulk energetics, the interplay between the two having recently been brought to light, for instance, in the context of VO_2[184]. The nickelate superlattices investigated here showcase how atomically-engineered layered materials provide a new path for understanding fundamental physics and for engineering functional properties that are against the bulk energetics.

As a model system for this study we take $NdNiO_3$ and $SmNiO_3$, two members of the rare earth nickelate family $RNiO_3$, where R is a rare earth cation. The rare earth nickelate materials are well known for the sharp MIT, observed when the temperature is decreased below a characteristic temperature T_{MI}, which depends on the choice of rare earth ion R[7, 99, 126, 189]. The T_{MI} for bulk $SmNiO_3$ is 400 K; and for bulk $NdNiO_3$, 200 K. The rare earth nickelates crystallize in slightly distorted versions of the perovskite structure, which can be visualized as a network of corner-sharing NiO_6 octahedra with the rare earth ions occupying the spaces in between. The distortions involve rotations and tilts of the octahedra, which are controlled by the ionic radius of the rare earth ions. The rotations and tilts modify the Ni-O-Ni bond angle (ϕ), which sensitively determines the bandwidth of the system and also T_{MI} ($\phi_{NdNiO_3} \approx 157°$ and $\phi_{SmNiO_3} \approx 153°$ at room temperature in bulk)[4, 5, 17, 99]. The MIT further involves a two-sublattice modulation of electron density (often referred to as "charge order" although the terms "bond density wave" or "charge density disproportionation" as well as "site-selective Mott transition" may be more appropriate[21]) accompanied by a two-sublattice breathing distortion of the NiO_6 octahedra, which can be understood as alternating larger and smaller NiO_6 octahedra. However, understanding and controlling the length-scale over which a MIT can develop is a less well-understood aspect of this phenomenon.

9.4 Results

To address these questions, epitaxial superlattices consisting of L repetitions of the basic $((SmNiO_3)_m/(NdNiO_3)_m)$ unit (m unit cells (u.c.) of $SmNiO_3$ and m u.c. of $NdNiO_3$), were deposited on top of $[001]_{pc}$-oriented $LaAlO_3$ substrates. The total thickness of all the samples was kept at $\approx$ 30 nm. Therefore, in order to match this thickness, the number of repetitions, L, was adjusted for each $((SmNiO_3)_m/(NdNiO_3)_m)$ unit or superlattice wavelength Λ (in u.c.) equal to $2m$ (m in pseudocubic (pc) u.c.), see Fig. 9.1a. The superlattices were

characterized ex-situ by X-ray diffraction, atomic force microscopy and aberration-corrected scanning transmission electron microscopy in combination with electron energy-loss spectroscopy (STEM-EELS). As shown in Fig. 9.1b, finite thickness oscillations and satellite peaks corresponding to the superlattice periodicity are observed, indicating high quality samples and good agreement with the designed layering. The atomically-flat surface reveals that the superlattices preserve the step-like topography of the substrate (see the corresponding inset in Fig. 9.1b). Reciprocal space mapping confirms that all superlattices are coherently strained to the substrate (see Supplementary Fig. 13.1). The structural properties and the chemical composition of the designed $(m,m)_L$ superlattices have been evaluated in detail by means of STEM-EELS. Fig. 9.1c shows a gray-scale high angle annular dark field (HAADF), i.e. Z-contrast, image of a $(5,5)_{10}$ superlattice viewed along the $[100]_{pc}$ zone axis of the $LaAlO_3$ substrate. The HAADF image confirms that the superlattice is fully epitaxial with the substrate and that no obvious defects such as dislocations or Ruddlesden-Popper faults are generated, either within the crystal or at the interfaces. EELS compositional maps obtained from the area indicated on the HAADF image are displayed in panel d where the La, Nd, Sm, and Ni signal intensities are represented in orange, red, green and blue respectively. All the imaged interfaces are atomically sharp and no obvious cationic intermixing between the $NdNiO_3$ and $SmNiO_3$ layers is identified. We also note that the oxygen content is constant over the structure, as shown in Fig. 13.5. The same crystal texture and interface quality have been observed in a $(12,12)_4$ superlattice, as can be seen in Fig. 13.6.

Fig. 9.2 displays the resistivity as a function of temperature for three $SmNiO_3/NdNiO_3$ superlattices with different periods Λ. The dashed lines indicate the T_{MI} of 10 nm thick $NdNiO_3$ and $SmNiO_3$ films grown on $[001]_{pc}$-oriented $LaAlO_3$. As can be seen in Fig. 9.2, superlattices with large Λ, i.e. thick $SmNiO_3$ and $NdNiO_3$ layers ($(10,10)_5$ and $(15,15)_4$), display two distinct MITs. The lower MIT seen at 100 K < T_L < 200 K is accompanied by a hysteresis loop and resembles the MIT behavior observed in $NdNiO_3$[190]. The second MIT manifests at higher temperatures, 300 K < T_H < 400 K, and resembles the MIT of $SmNiO_3$. In contrast, superlattices with short Λ (see for instance $(7,7)_8$) go from a fully metallic to a fully insulating state through a single MIT. By analyzing the entire data set (see Supplementary Fig. 13.2), we see that the conductive behavior of the higher period $SmNiO_3/NdNiO_3$ superlattices tends toward the independent $SmNiO_3$ and $NdNiO_3$ single film behaviors. With decreasing Λ, the two MITs come closer together in temperature until a joint MIT is measured at a temperature of $T_J \approx 155$ K. This behavior with a unique MIT is observed below a critical wavelength, Λ_c, of 16 u.c. These results are summarized on Fig. 9.4a, to which we will return shortly. Additional transport data, including Hall effect, is shown in the Supplementary information section 13.2.

The resistivity trends clearly demonstrate that a remarkably long length-scale of 8 u.c. (3 nm) is required to decouple the two materials and to establish independent phases determined by the bulk energetics. We now consider possible explanations for this long length-scale. As a first step we address the issue of cationic intermixing. We observe that a solid

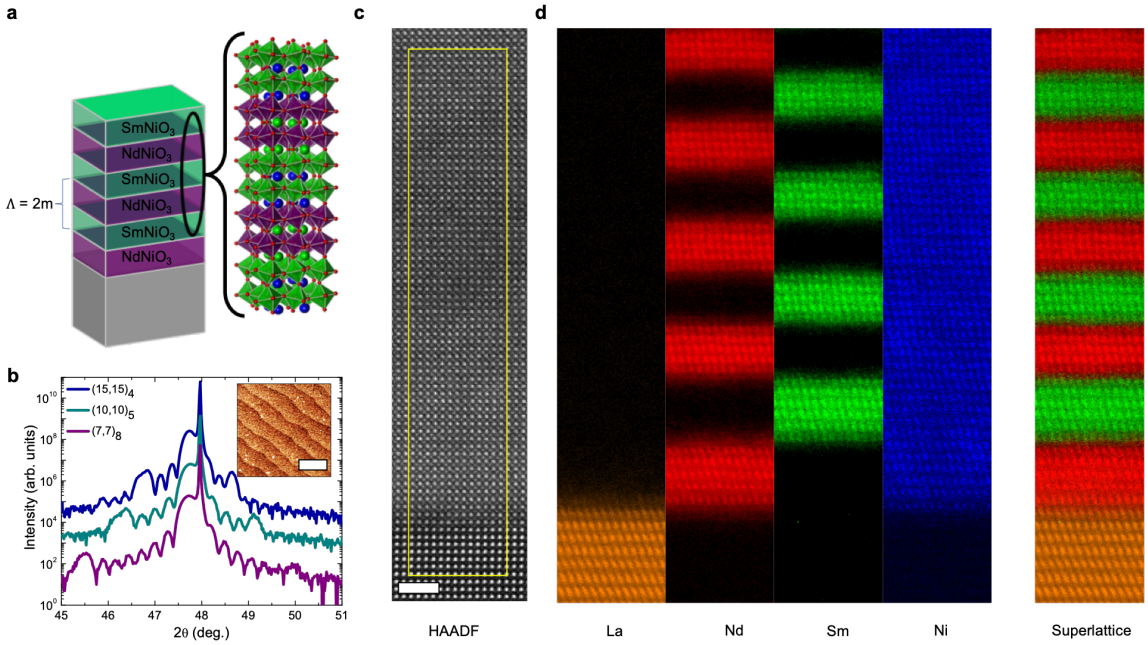

Figure 9.1 | **Detailed characterization of the $(m\mathbf{SmNiO_3}/m\mathbf{NdNiO_3})_L$ superlattices. a**, Schematic representation of the superlattice heterostructures, Λ indicates the superlattice period. **b**, X-ray diffractograms for $(7,7)_8$, $(10,10)_5$ and $(15,15)_4$ superlattices. The satellite peaks indicate the periodicity of the superlattices. **Inset**: Typical atomic force microscope topography of a $(7,7)_8$ superlattice. Scale bar: 500 nm. **c**, Cross sectional HAADF image of a $(5,5)_{10}$ superlattice viewed along the $[100]_{pc}$ zone axis direction of the $LaAlO_3$ substrate. The scale bar corresponds to 2 nm. **d**, EELS compositional maps obtained from the area indicated in (c). The La, Nd, Sm and Ni signals are represented in orange, red, green and blue colors, respectively. The La, Nd and Sm signals are displayed together in the superlattice map.

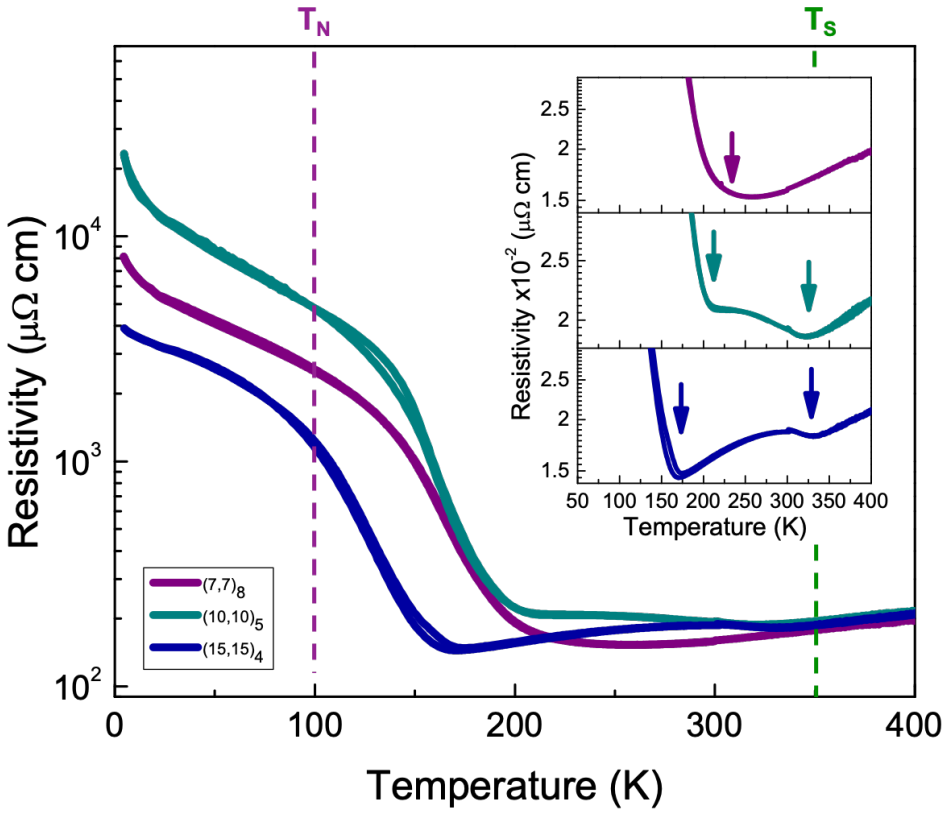

Figure 9.2 | **Transport measurements.** Resistivity vs temperature of the $(7,7)_8$, $(10,10)_5$ and $(15,15)_4$ $[001]_{pc}$-oriented $SmNiO_3/NdNiO_3$ superlattices. The dashed lines indicate the MIT temperatures of $NdNiO_3$ (T_N) and $SmNiO_3$ (T_S) films of 10 nm thickness on $[001]_{pc}$-oriented $LaAlO_3$ substrates to be compared with the values obtained for the superlattices. **Inset**: Close ups of the transitions.

solution $Sm_{0.5}Nd_{0.5}NiO_3$ exhibits a single MIT at approximately the same temperature as that of the short-wavelength superlattices, see Supplementary information Fig. 13.2. However, as can be seen from Fig. 9.1d, STEM analyses performed on a $(5,5)_{10}$ superlattice show that intermixing is extremely limited in these structures and does not extend further than 1 u.c. from the interfaces. We can therefore safely say that the long coupling length-scale is not chemical in origin.

A second possibility is interfacial structural coupling, shown in previous studies to be important in many perovskite superlattices[174, 191–193]. In particular, several works have found that rotations and tilts of the oxygen octahedral cages, determining the B-O-B bond angle in ABO_3 perovskites, can be modulated across interfaces[33, 124, 194, 195]. We also consider for this specific nickelate system that the breathing distortion (bond disproportionation) could gradually propagate from one material to the other. In order to investigate interfacial structural coupling, we determined the crystal structure of $SmNiO_3/NdNiO_3$ superlattices from density functional theory (DFT) + U calculations and corroborated our findings using STEM analyses that allowed the oxygen positions to be resolved. In the calculations, we considered the low temperature phases of $SmNiO_3$ and $NdNiO_3$, which have $P2_1n$ symmetry (with Glazer notation $a^-b^+a^-$), and the in-phase rotation axis has been oriented in-plane as predicted from the calculations and observed in our STEM measurements. Further details are reported in the methods section and Supplementary information.

Fig. 9.3a displays the calculated layer-resolved (z-direction) equatorial and apical Ni-O-Ni bond angle ϕ, two equatorial angles coming from the low symmetry. We see that ϕ reverts to a value characteristic of the given nickelate block within only 1 Ni layer of the interface. The STEM imaging is now used to compare the real structure of our $RNiO_3$ superlattices with those simulated by DFT, and to corroborate the predicted short-range coupling of the Ni-O-Ni bond angle at the $SmNiO_3/NdNiO_3$ interfaces. In order to evaluate how these rotations vary through the film depth (z-direction), we imaged the films along two different orthorhombic (ort) zone axes: the $[101]_{ort}$ and $[010]_{ort}$. The former allows evaluation of the rare earth anti-polar shifts (ΔZ) typical of *Pnma* structures, featuring a zig-zag pattern along the $[010]_{ort}$ direction, which in itself is an indirect signature of the amplitude of octahedral tilting[33, 196]. The latter, $[010]_{ort}$ zone axis is instead the optimum orientation for measuring ϕ, as the oxygen octahedra only rotate in phase along the $[010]_{ort}$ direction, and therefore all the oxygen atoms belonging to the same atomic column are projected at the same position of the image. Imaging is done using the HAADF and annular bright field imaging (ABF) detectors simultaneously in order to identify the oxygen columns as well as the cation positions. Fig. 9.3c and 9.3d show HAADF and contrast-inverted ABF images obtained from a central region of the $(5,5)_{10}$ superlattice sample. Each image was acquired from equivalent but distinct sample regions, along their corresponding zone axes. An amplified view of the contrast-inverted ABF image is displayed in Fig. 13.7 of the Supplementary information. From the HAADF and contrast-inverted ABF images, we have quantified both the ΔZ and ϕ structural parameters across the superlattice layers,

as plotted in Fig. 9.3e and 9.3f. Both parameters evolve similarly along the z-direction: switching from a specific $NdNiO_3$ value (30 pm and 164°) to another for the $SmNiO_3$ layer (38 pm and 160°), and back again, over only 1 u.c. from the $SmNiO_3/NdNiO_3$ interfaces. Furthermore, the Ni-O-Ni bond angle and antipolar motion amplitude values calculated from the DFT-simulated structure projected along the imaged planes are also displayed in these plots (solid blue circles), reproducing the same sharp interfacial structural evolution as the one observed from the STEM measurements. We therefore conclude that propagation of bond angles is not the reason for the long length scale we observe.

The breathing distortion yields a bond disproportionation (BD), which can be quantified as the difference between the lengths of the long and short Ni-O bonds (B_L and B_S respectively), $BD = \frac{B_L - B_S}{2}$. In the insulating phase, the BD is slightly greater in $SmNiO_3$ than in $NdNiO_3$, so some coupling of the BD magnitude across the interface may be expected. Fig. 9.3b illustrates the ab-initio determined BD magnitude across the $SmNiO_3/NdNiO_3$ interface. Similar to the bond angle, it can be seen that this parameter returns to the value characteristic of the given nickelate layer after just 1 u.c. of interface effect.

From the DFT and the STEM investigations, we conclude that neither bond angle nor bond disproportionation structural motifs propagate beyond 1 u.c. from the interface. This indicates that the effect of purely structural propagation across interfaces cannot account for the persistence of the joint behavior up to a superlattice period of as long as 16 u.c. Importantly, this suggests that the transition temperature in these heterostructures is not directly set by the local octahedral rotation as in the case of the bulk, but rather by the interplay of local bulk and interfacial physics. Remarkable within the field of oxide heterostructures, this behavior propagates up to around 8 u.c. into each material, while other physical modes (with the exception of strain) do not propagate past a few unit cells.

We find that the observed behavior is instead due to the energy cost of establishing a phase boundary – linked to the short-range mismatch of the coupled electronic and structural order parameters corresponding to the metal-insulator transition across the interface. As the structural and electronic order parameters are strongly coupled we can focus on just one. We set the theory in terms of N – the electronic disproportionation characterizing the nickelate insulating state. N is defined as the difference between the occupation of the long bond and short bond Ni sites ($N = N_{LB} - N_{SB}$) within a low energy, extended anti-bonding e_g orbital picture[128]. Previous theoretical calculations have found that $N = 0$ in the metallic state (e_g^1-e_g^1) and in the insulating state is around 1.2 - 1.5, depending on the material[23, 37, 127, 128].

Based on this electronic disproportionation order parameter we develop a Landau theory, which is described in detail in the Supplementary information. In the simplest description, the key ingredients in the model are the relative free energies of the metallic and insulating phases of the two components of the superlattice, and the energy cost of the phase boundary separating them. Without loss of generality we set the free energy of the metallic phase to zero, $E_M(T) = 0$, and refer to the free energy (per unit cell volume (J/m^3)) of the

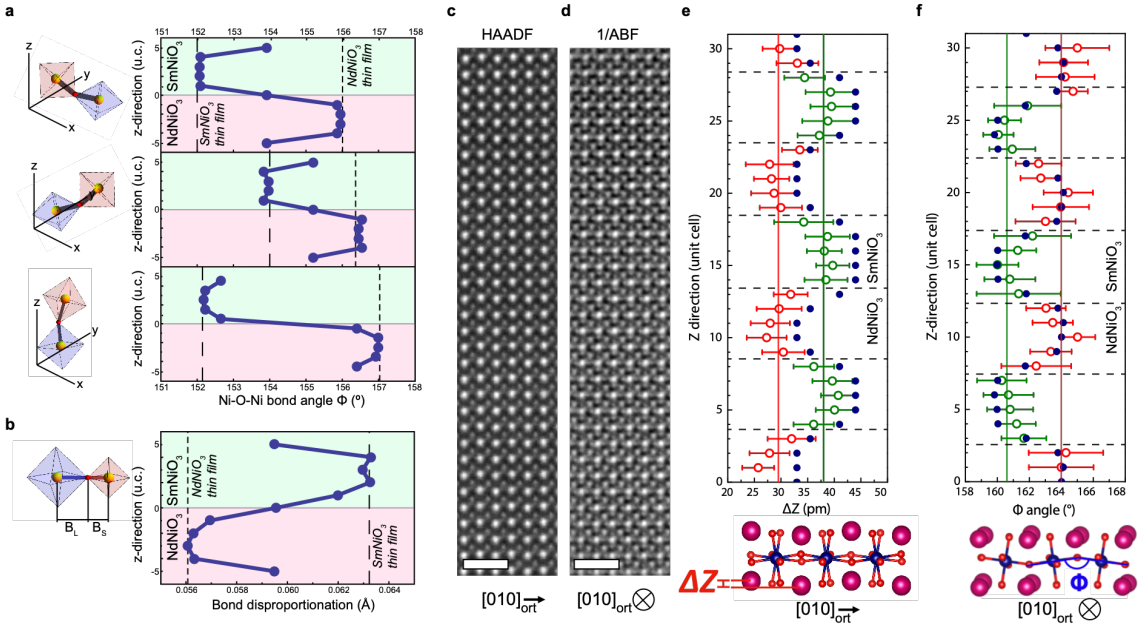

Figure 9.3 | **DFT + U calculations performed at 0 K (both materials in the $P21/n$ phase) of the layer-resolved bond angle and bond disproportionation in the superlattices and STEM structural analyses of the superlattices.** Layer-resolution of the **a**, Equatorial and apical Ni-O-Ni angles **b**, BD magnitude for a $(5,5)_{10}$ superlattice as calculated from DFT. Short and long dashed lines indicate the same calculated parameters for strained thin films of $NdNiO_3$ and $SmNiO_3$ respectively. Schemas are included beside each plot to illustrate the relevant structural parameter. The two equatorial angles result from the low symmetry. Cropped areas of a c, HAADF and a d, contrast-inverted ABF image obtained from a central region of a $(5,5)_{10}$ superlattice. Scale bar: 1 nm. **e - f**, ΔZ and ϕ depth-profiles. Structural models are shown below the plots, in which Nd/Sm, Ni and O atoms are represented with magenta, blue and red spheres respectively. On the plots, the solid blue circles represent the corresponding structural parameter calculated from the DFT-simulated structure projected onto the a-c plane. The exact amount of unit cells at each specific layer of the DFT-derived plots has been slightly modified in order to fit the experimental data. The solid lines represent the corresponding mean values of these parameters calculated from the interior layers of either the $NdNiO_3$ (magenta) or $SmNiO_3$ (green) blocks. The positions of the $SmNiO_3$/$NdNiO_3$interfaces are indicated with dashed lines.

insulating phase as $E_I(T)$, noting that only the difference between the two is of physical relevance. We take the phase boundary energy between two metallic or two insulating phases to be zero, although in reality an interfacial energy cost associated to the difference between the two materials is expected, but its magnitude should be minimal compared to the energy of the phase boundary separating the metallic and insulating states. The latter is taken to be E_{PB}, which is an energy per surface area (J/m^2). We assume that near the transition temperature the E_I have a linear temperature dependence:

$$E_I^{N,S} = K_{N,S}\frac{(T - T_{N,S})}{T_{N,S}} \tag{9.1}$$

Here K is a material dependent constant describing the stabilization energy (per unit cell) of the insulating phase relative to the high temperature metallic phase in $SmNiO_3$ (K_S) and $NdNiO_3$ (K_N). T_N and T_S are the experimental T_{MI}s of an individual film of $NdNiO_3$ and $SmNiO_3$ respectively.

We now compute the energy of the three possible states for our $(SmNiO_3)_m/(NdNiO_3)_m$ superlattices.

1) Both materials are metallic:

$$E_{MM} = mE_M^N + mE_M^S = 0 \tag{9.2}$$

2) $NdNiO_3$ is metallic and $SmNiO_3$ is insulating:

$$E_{MI} = mE_M^N + 2E_{PB} + mE_I^S(T) = 2E_{PB} + mE_I^S(T) \tag{9.3}$$

3) And both materials are insulating:

$$E_{II} = mE_I^N(T) + mE_I^S(T) \tag{9.4}$$

Keeping in mind that Λ_c ($\Lambda_c = 2m_c$) and T_J are the critical wavelength of the bifurcation and the temperature of the joint T_{MI} coming from experiment respectively and that m designates the number of unit cells of each nickelate block in the repeating unit, one can write three simple equations.

At the bifurcation point, the energies of having both materials insulating ("insulating-insulating"), both metallic ("metallic-metallic") and $NdNiO_3$ metallic and $SmNiO_3$ insulating ("metallic-insulating" phase coexistence with a phase boundary in between costing energy) are equal:

$$m_cE_I^N(T_J) + m_cE_I^S(T_J) = m_cE_M^N(T_J) + m_cE_m^S(T_J) = m_cE_M^N(T_J) + m_cE_I^S(T_J) + 2E_{PB} \tag{9.5}$$

We may now write an equation for the higher temperature metal-insulator transition (T_H), at which E_{MM} becomes equal to E_{MI}:

$$mE_M^N(T_H) + mE_M^S(T_H) = mE_M^N(T_H) + mE_I^S(T_H) + 2E_{PB} \tag{9.6}$$

And the lower transition temperature (T_L) at which E_{II} becomes equal to E_{MI}:

$$mE_I^N(T_L) + mE_I^S(T_L) = mE_M^N(T_L) + mE_I^S(T_L) + 2E_{PB} \tag{9.7}$$

Solving this system of equations, the following expressions for $T_L(m)$ and $T_H(m)$ are obtained:

$$T_L = T_N\left(1 + \frac{2E_{PB}}{mK_N}\right) \tag{9.8}$$

$$\tag{9.9}$$

$$T_H = T_S\left(1 - \frac{2E_{PB}}{mK_S}\right) \tag{9.10}$$

For large m (large Λ) the two transitions tend toward the $T_{MI}s$ for individual layers of $NdNiO_3$ and $SmNiO_3$ (T_N and T_S). When $T_L = T_H$, we obtain the critical wavelength Λ_c:

$$\frac{\Lambda_c}{2} = m_c = 2E_{PB}\frac{T_S K_N + T_N K_S}{K_S K_N (T_S - T_N)} \tag{9.11}$$

And T_J (assuming $K_N = K_S$):

$$T_J = \frac{2T_N T_S}{T_N + T_S} \tag{9.12}$$

The bifurcation point, Λ_c, is therefore the layer thickness at which the high energy cost of forming a phase boundary between insulating $SmNiO_3$ and metallic $NdNiO_3$ is entirely compensated by the energy gain of the bulk-like phases of the individual layers, making a phase coexisting state, for $\Lambda > \Lambda_c$, energetically feasible.

This simple description provides a qualitative and semi-quantitative explanation of the behavior observed in our superlattices, as shown by the dotted line in Fig. 9.4a. Also, T_J is elegantly predicted by this version of the model. Using the experimental values for $SmNiO_3$ and $NdNiO_3$ individual layers (T_S = 352 K and T_N = 100 K), the joint transition temperature (T_J) is estimated at 156 K, in remarkable agreement with experiment.

For the higher temperature branch, however, the fit can be quantitatively improved by refining the model, i.e. introducing a saturation temperature (T_{Sat}), releasing the assumption $K_N = K_S$ and using the measured T_J as an input parameter. Better reflecting the physical nature of phase transitions, T_{Sat} restricts the linear temperature dependence of the energy of the $SmNiO_3$ insulating state to a temperature range close to T_s (for $T > T_{Sat}$, $E_I^S(T) = K_S\frac{T-T_S}{T_S}$ while for $T < T_{Sat}$, $E_I^S = K_S\frac{(T_{Sat}-T_S)}{T_S}$). From this input and an estimated value of T_{Sat} (280 K) we can obtain the following expressions:

$$\frac{K_N}{K_S} = \frac{T_N(T_S - T_{Sat})}{T_S(T_J - T_N)} \tag{9.13}$$

(9.14)

$$\frac{E_{PB}}{K_N} = \Lambda_c \frac{K_S}{K_N} \frac{(T_S - T_{Stat})}{2T_S} \tag{9.15}$$

The equations for T_H and T_L remain the same, however, their values are now computed from the newly determined ratios, $K_N/K_S = 0.4$ and $E_{PB}/K_N = 4.8$. The excellent fit (dashed line) obtained can be seen in Fig. 9.4a that summarizes the experimental data and the output of the Landau theory.

Fig. 9.4b and 9.4c display the calculated energies of the three possible phases – insulating-insulating (gray), insulating-metallic (gray/purple) and metallic-metallic (purple) – versus temperature. This is shown for two superlattice wavelengths: $\Lambda = 10$ u.c. for which, experimentally, the system transitions from a fully metallic state to a fully insulating one and $\Lambda = 20$ u.c. for which a coexistence of a metallic and an insulating phase is found at intermediate temperatures. As can be seen in Fig. 9.4b, in the case of $\Lambda = 10$ u.c., the lowest energy is the metallic-metallic phase at high temperature with a transition to an insulating-insulating phase at 160 K. Examining the calculations for the $\Lambda = 20$ u.c. case (Fig. 9.4c), two transitions are seen to occur: a first one from a high temperature metallic-metallic phase to a mixed (metallic-insulating) phase and, at a lower temperature, a second one from the mixed (metallic-insulating) phase to the insulating-insulating one – neatly reproducing what is observed experimentally, as shown in Fig. 9.4a.

Fig. 9.4d and 9.4e show the evolution of the order parameter, N, across the interface of two different wavelength superlattices, $\Lambda = 10$ u.c., 20 u.c., for the various possible phases. As shown in Fig. 9.4e, at an interface between an insulating region and a metallic one, the order parameter has to go from a value of 1.2 to 0 and the energy cost of bending the order parameter goes as $(\nabla N)^2$. It is only in Fig. 9.4e, for $\Lambda = 20$ u.c., that the phase coexistence is stable. However, with a reduced superlattice wavelength of 10 u.c. (Fig. 9.4d), the higher density of phase boundaries makes the cost of bending the order parameter between the two distinct electronic phases higher than the energy gained by the individual component materials being in their optimal states. Thus, for $\Lambda = 10$ u.c., phase coexistence is never stable and, over some temperature range, the phase boundary energy forces either $SmNiO_3$ to be metallic or $NdNiO_3$ to be insulating against the energetics of the bulk phases.

The critical wavelength of 16 u.c is now readily understood despite being rather long given the short-range extension of the structural motifs, and of the order parameter itself. As we have demonstrated, the Landau expansion based on a first-order transition describes the phase separation size dependence of the phase transition in this superlattice system qualitatively and quantitatively. The ratio between the phase boundary energy and the free energy cost of the thin films to be in the unfavored state is thus the main parameter that

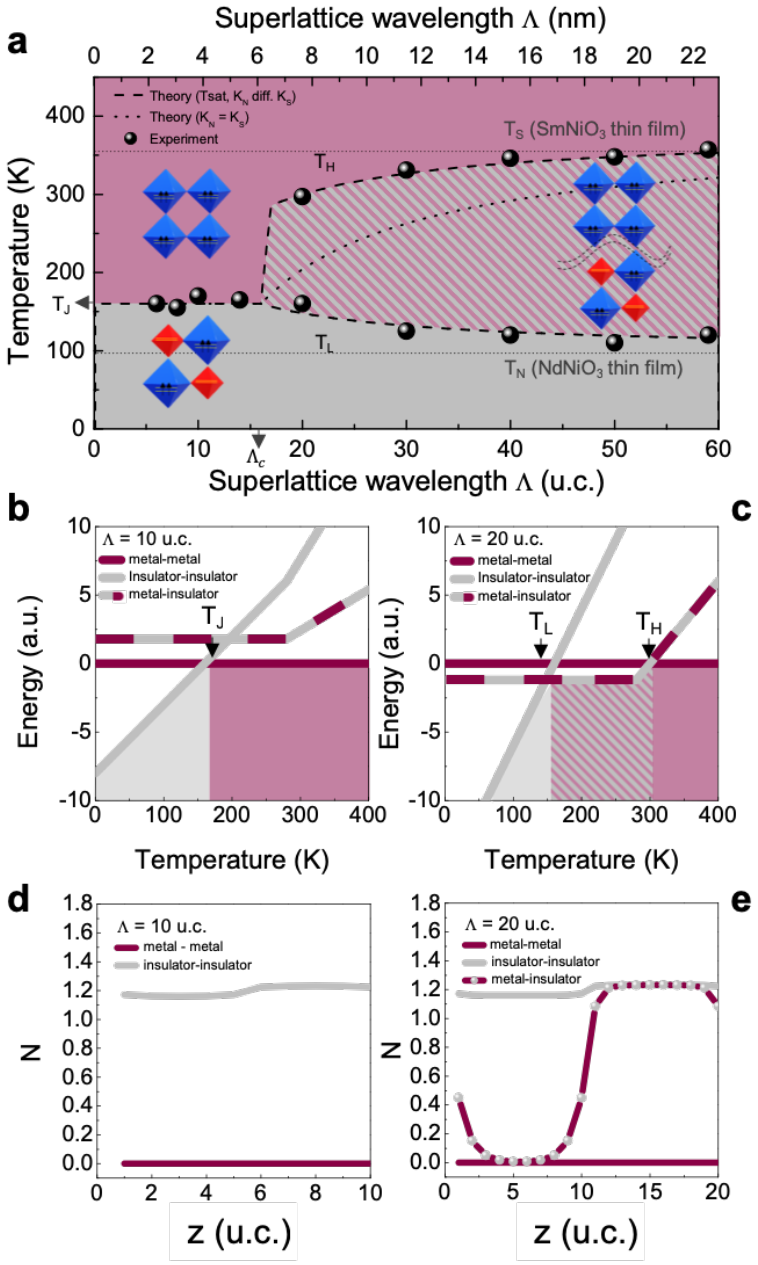

Figure 9.4 | **Output of the Landau model and experimental data.** **a**, Theoretical MIT temperatures (dotted and dashed lines indicate the model results assuming $K_N = K_S$ and introducing T_{Sat} with $K_N \neq K_S$, respectively) as a function of superlattice wavelength and comparison to the experimental data (filled circles). **b - c**, Energy as a function of temperature for the three possible cases, in two different superlattices (Λ = 10 u.c. and Λ = 20 u.c.). **d-e**, z- evolution of the order parameter N across the interface for Λ = 10 u.c. and Λ = 20 u.c. for the different possible cases, as calculated in the full Landau theory described in the Supplementary information.

determines the physics of the system. The phase boundary energy is determined by two factors: the local elastic cost of the structural mismatch between the phases, and the energy cost of interpolating the order parameter between the two values. This latter cost depends crucially on the energy landscape: in a first order situation the order parameter goes from one minimum to the other by passing over a local maximum, the height of which is an important component of the interface energy. An estimate of the energy cost of the phase boundary can be made by DFT + U, as described in the Supplementary information.

9.5 Conclusions

Through engineering specifically-designed superlattices, we were able to clearly isolate the role of the different physical phenomena in setting the length-scale of the MIT in the nickelates. We found that the length-scale of coupling between metal-insulator phases is controlled by an interfacial phase boundary energy. Notably, it is not determined by long-range propagation of bond disproportionation nor by the direct long-range physical coupling of bond angles, which up until now has been the standard approach to understanding interfacially-coupled behavior. This result highlights a framework for engineering functional properties in heterostructures and can be applied to other combinations of materials, such as vanadium and manganese oxides as well as to the naturally-occurring phase coexistence at a first-order phase transition. Further, we have shown that heterostructures can be used not only to engineer temperature-dependent properties to go against the bulk energetics, but as a model system to provide new insights into the fundamental physical energy scales of the bulk materials themselves.

9.6 Methods

9.6.1 Sample preparation

We used radiofrequency off-axis magnetron sputtering at a temperature of 460 °C and a pressure of 0.18 Torr (Ar:O_2 mix of ratio 3:1) to grow epitaxial superlattices consisting of L repetitions of the basic $((SmNiO_3)_m/(NdNiO_3)_m)$ unit (m unit cells of $SmNiO_3$ and m unit cells of $NdNiO_3$) on top of $[001]_{pc}$-oriented $LaAlO_3$ substrates. Prior to deposition, the $LaAlO_3$ substrates were thermally treated to ensure atomically flat terraces and step-like topography. Bulk $SmNiO_3$ and $NdNiO_3$ have pseudocubic lattice constants of $a_{pc} = 3.799$ Å and $a_{pc} = 3.808$ Å respectively; whereas $a_{pc} = 3.787$ Å for $LaAlO_3$. Hence the corresponding lattice mismatch $(a_{substrate} - a_{film})/a_{film}$ to the substrate is $\epsilon_{xx} = -0.3\%$ and $\epsilon_{xx} = -0.6\%$ for the $SmNiO_3$ and $NdNiO_3$ layers, respectively.

9.6.2 Transport measurements

Transport measurements were carried out in a 4 point configuration, after being patterned with UV lithography in standard Hall bar geometry with Pt contacts, in the temperature range 4 K < T < 400 K. Below 300 K, the samples were slowly dipped into a liquid helium bath while higher-than-room temperature measurements were achieved using two Peltier elements. The T_{MI} of the superlattices was determined from the maximum of $-d(lnR)/dT$ on heating[197].

9.6.3 Aberration-corrected STEM measurements

STEM specimens were prepared by mechanical tripod polishing, followed by argon ion beam milling to electron transparency with a Gatan PIPS II. Simultaneous series of high angle annular dark field (HAADF) and annular bright field (ABF) STEM images were acquired using a double-aberration-corrected FEI Titan Themis 60-300 microscope located at the CIME (EPFL). The instrument was operated at 300 kV high voltage, using an approximately 20 mrad convergence semi-angle for the electron probe. From each image series, the Smart Align software was used to produce an averaged image with reduced statistical image noise and correction of linear and non-linear scan distortions[198]. The central position associated to each atomic column has been localized by using a 2D Gaussian fitting procedure[199]. From the obtained set of coordinates, one per atomic sub-lattice, we have estimated the depth-evolution of the structural parameters. Each data point shown in Fig. 9.3e and 9.3f corresponds to the mean over around 25 u.c. and the error bars derive from the standard deviation.

STEM-EELS spectrum image (SI) datasets were acquired with a Gatan GIF Quantum ERS spectrometer, using the following conditions: a collection semi-angle of ≈47 mrad; 0.01 s acquisition time per pixel; 0.5 eV/ch energy dispersion and 2048 channels, thus covering all the spectral edges located between 400 – 1424 eV in energy loss. Principal component analysis was used to improve the signal-to-noise ratio of the EELS-SI datasets using a plugin in Gatan DigitalMicrograph (DM)[200, 201]. In particular, we used the first 14 principal components to reconstruct the EELS-SI for the maps shown in Fig. 9.1c. The La M_{45}, the Ni L_{23}, Sm M_{45} and Nd M_{45} edges were used for mapping the relative composition of the superlattices. A power-law dependency was used to fit and subtract the background signal from the edges. The multiple linear least squares plugin within DM was used to deconvolute the La M_{45} and Ni L_{23} peak signals, as they are substantially overlapped.

9.6.4 DFT

Our first-principles calculations were carried out using density functional theory (DFT) with Projector Augmented Wave (PAW) method as implemented in the Vienna ab initio simulation package (VASP)[202–204]. We used the PBEsol[115] exchange-correlation energy functional. In line with recent work on RNiO$_3$ compounds[22, 205], an on-site Coulomb

interaction[206] U = 2 eV was added to the $3d$ orbitals of Ni according to the method of Dudarev[207]. The plane-wave energy cutoff was set to 700 eV. The $(SmNiO_3)_1/(NdNiO_3)_1$, $(SmNiO_3)_3/(NdNiO_3)_3$ and $(SmNiO_3)_5/(NdNiO_3)_5$ superlattices were simulated respectively using $2 \times 2 \times 10$, $2 \times 2 \times 6$ and $2 \times 2 \times 10$ supercells and $6 \times 6 \times 1$, $6 \times 6 \times 2$ and $6 \times 6 \times 1$ Monkhorst-Pack k-point meshes[56]. The lattice constants of fully relaxed bulk $NdNiO_3$ and $SmNiO_3$ are in good agreement with experimental data (see Supplementary Table 13.1). In order to simulate properly the epitaxial strain imposed experimentally to $NdNiO_3$and $SmNiO_3$ on a $LaAlO_3$ substrate, the in-plane lattice parameters of the superlattices were fixed to be 3.77 Å. The oxygen rotation pattern was oriented with the long axis (c^+) in-plane (see Supplementary information). The out-of-plane lattice parameters and internal atomic coordinates were relaxed until the total energy and Hellman-Feynman force were converged to 10^{-7} eV and 10^{-3} eV/Å respectively. For simplicity, all the calculations were performed in the ferromagnetic state. Bond lengths and bond angles were calculated using the VESTA package[208].

9.7 Acknowledgements

We thank Hugo Strand and Manuel Zingl for fruitful discussions and acknowledge Marco Lopes and Siébastien Muller for their invaluable technical support. This work was partly supported by the Swiss National Science Foundation through Division II. The research leading to these results has received funding from the European Research Council under the European Union's Seventh Framework Program (FP7/2007-2013)/ERC Grant Agreement 319286 Q-MAC). The authors acknowledge access to the electron microscopy facilities at the Interdisciplinary Centre for Electron Microscopy (CIME), EPFL. The Flatiron Institute is a division of the Simons Foundation. Ph.G., Y.Z. and A.M. acknowledge support from ARC project AIMED and M-ERA.NET project SIOX as well as access to computational resources provided by the Consortium des Equipements de Calcul Intensif (CECI), funded by the Belgian F.R.S.-FNRS under the Grant No. 2.5020.11 and the Tier-1 supercomputer of the Fédération Wallonie-Bruxelles funded by the Walloon Region of Belgium under the Grant No 1117545. M.G acknowledges support by the Swiss National Science Foundation under grant No. PP00P2170564.

9.8 Conclusion of the article

Here, the electronic propagation through the boundary from one compound to the other, in nickelates heterosctructures, explains the variationof the TMI. Even if the structural properties do not seem to be affected in those systems, they are still a key ingredient in the triggering of the MIT.

Part V

Conclusion

Conclusions

From bulk to heterostructures, Density Functional Theory has shown its ability to deal with rare-earth nickelates, allowing us to characterise self consistently their properties at the structural, electronic and magnetic levels.

The metal insulator phase transition in the whole family of bulk compounds has been explained thanks to a structurally triggered Peierls Instability. For the sake of generality, this mechanism has been shown to apply to the ferrite family and it is a first step to extend it to the Jahn-Teller community that is a dare challenge for the future. The antiferromagnetic order has been explained as a strong fourth neighbor antiferromagnetic interaction. The characteristic double peaks in the optical spectrum have been reproduced and explained highlighting that the description of the nickelates behaviour cannot be restricted to a small e_g subspace but needs the whole d shell of the nickel atoms.

Nowadays, the development of devices based on transition Metal oxides is of great interest. Based on the discussed general theory, both structural and electronic properties can affect the physical properties. Nickelates seem a nice family for further developments. Nevertheless, some fundamental questions remain open.

The first one concerns the theoretical approach: DFT+U and DFT+DMFT suggest two distinct physics. However, they are not incompatible and both could even be at the origin of the explanation for the MIT. Indeed, previous DMFT analysis did not take into account the dynamic of the nuclei but the DFT did not take into account the dynamic correlation of the electrons too. In real life, both are of course dynamic and temperature dependent.

The second one is the fact that, even if the first-principles analysis suggests a structurally triggered Peierls mechanism as being a possible explanation of the MIT, none of the available experiment highlights the softening of the breathing mode as a function of the temperature. The main reason is that it is a hard task for the experimentalists. Indeed, the breathing mode is mixed with other modes in the metallic *Pbnm* phase. Thus, it is not straightforward to catch the modes among a huge number of experimental results. Because of that, it would be interesting to study nickelate compounds in temperature at the theoretical level. Thanks to this kind of analysis, theoreticians could suggest the range of energy that has to be treated. Based on first principles results, such an analysis in temperature is possible thanks to a second principle study[209]. Due to the complex behaviour of nickelates, structural, electronic and magnetic properties have to be taken into account. Multibinit is one of the code that

could be operational for such study but is under implementation[131]. It would allow us to make, in an easy and friendly way, second principles study from Abinit results in the future.

Another question is the triggering of the breathing explained in the cubic symmetric phase is still available in the *Pbnm* phase. It is again due to the mixing with other modes.

Concerning the magnetism, even if we are convinced about the $0 \uparrow 0 \downarrow$ configuration at the bulk level at oK, it would be interesting to characterize it close to the transition. Mainly for the case where the MIT and the magnetic phase transitions are concomittent. Indeed, it could be a configuration where all the nickel atoms are magnetic and a polar P_{21} phase allowed. In the same spirit, thin film could be a key ingredient to induce such polar phase thanks to the magnetism.

At the end, I would recommend to study further the reason why we have a cost of energy at the boundary between metallic and insulating phases for nickelates superlattices. I am anticipating that it is due to the Peierls mechanism which is not allowed in the region where the rotations are not big enough to induce the breathing mode...

Part VI

Appendix

10 | Supplementary Materials: Structurally triggered MIT in rare-earth nickelates

Alain Mercy[1], *Jordan* Bieder[1,2], *Jorge* Íñiguez [3] and *Philippe* Ghosez[1]

[1]Theoretical Materials Physics, Q-MAT, CESAM, University of Liège, B-4000 Liège, Belgium [2]CEA DAM-DIF, F-91297 Arpajon, France [3]Department of Materials Research and Technology, Luxembourg Institute of Science and Technology, L-4362 Esch/Alzette, Luxembourg

10.1 Supplementary Note 1. Validation of the DFT+U approach

In order to assess the validity of our DFT+U approach and determine the appropriate U parameter, we have considered a wide range of possible values for U (from 0 to 8 eV) and have compared the computed structural, magnetic and electronic properties to experimental data.

The results are summarized below for $YNiO_3$ considered as a test case. In line with what was reported independently in Ref. [103], it appears that a DFT approach with a moderate U value of 1.5 eV provides for nickelates an unprecedented agreement with experimental data, combining accurate description not only of the structural but also of the magnetic and electronic properties. It therefore offers a robust and ideal framework for the study of the interplay between these properties.

10.2 Supplementary Note 2. Atomic structure

In Supplementary Figure 10.1, we report the relative deviations respect to experimental data at low temperature [120] for the lattice parameters and atomic distortions in the E'-type AFM $P2_1/n$ phase of $YNiO_3$ in terms of the amplitude of the U parameter. The atomic distortions are those with respect to the $Pm\bar{3}m$ phase and are quantified from a symmetry-adapted mode analysis performed with AMPLIMODE [118, 119]. The labels of the modes

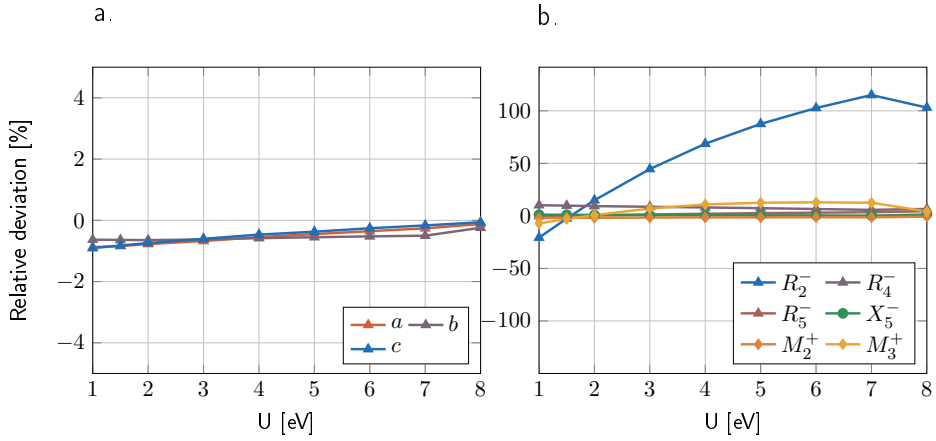

Figure 10.1 | **Evolution of the structural properties with U for $YNiO_3$.** Relative deviations respect to experimental data at low temperature [120] for the lattice parameters (a) and atomic distortions (b) in the E'-type AFM $P2_1/n$ phase of $YNiO_3$ in terms of the amplitude of the U parameter. Atomic distortions are quantified from a symmetry-adapted mode analysis (see Supplementary Table 10.1). The R_3^- and M_5^+ distortions which have negligible amplitudes (< 0.05) are not shown.

Labels	Atomic motion	$Pbnm$	$P2_1/n$
R_5^-	**Anti-phase rotations of O octahedra along x and y (R_{xy})**	**x**	**x**
M_2^+	**In-phase rotations of O octahedra along z (M_z)**	**x**	**x**
X_5^-	Anti-polar (layered) motion of R cations (X_{AP})	x	x
M_3^+	Jahn-Teller distortion of O octahedra (Q_2^+)	x	x
R_4^-	Anti-polar motion (rocksalt) of R cations (R_{AP})	x	x
R_2^-	**Breathing distortion of the O octahedra (B_{OC})**		**x**
M_5^+	Anti-polar motion of O (M_{AP})		x
R_3^-	Jahn-Teller distortion of O octahedra (Q_2^-)		x

Table 10.1 | **Structural distortions in nickelates.** Labels and description of the distortions of the $Pm\bar{3}m$ phase allowed by symmetry in the $Pbnm$ and $P2_1/n$ phases of $RNiO_3$ compounds. The main distortions are in bold.

that are allowed by symmetry in the $Pbnm$ and $P2_1/n$ phases and a brief description of the related atomic motions are reported in Supplementary Table 10.1.

We see in Supplementary Figure 10.1 that the lattice parameters are rather independent of U and well described within the whole range (error smaller than 1%). At the level of the atomic distortions, the amplitude of breathing mode B_{OC} (R_2^-) is only properly described in the limit of small U values. For the dominant modes like R_{xy} (R_5^-) or M_z (M_2^+), although the relative errors remain reasonably small for any U, the absolute amplitude evolves significantly with U and also converge to the correct values at low U.

In Supplementary Figure 10.2, we report comparison with experiment data [120] of the absolute amplitudes of the atomic distortions and lattice parameters in the E'-type AFM $P2_1/n$ phase of $YNiO_3$ as computed in DFT with U = 1.5 eV. It confirms that the atomic structure of $YNiO_3$ is very accurately described in DFT using PBESol and a U parameter of

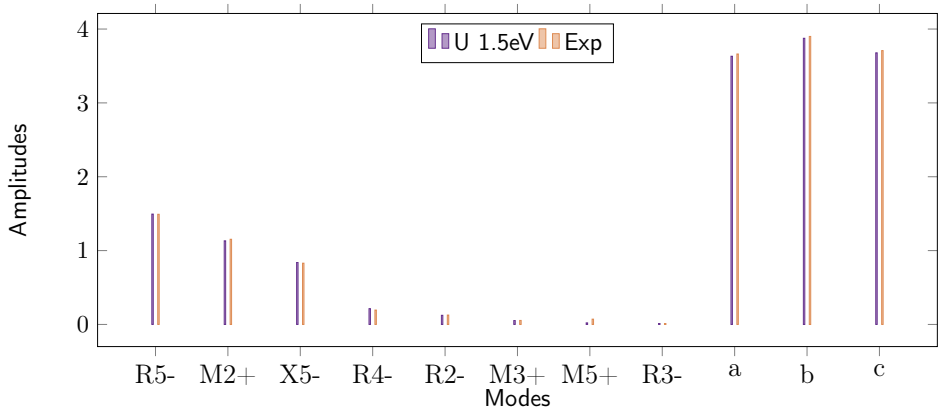

Figure 10.2 | **Experimental and theoretical structural properties for $YNiO_3$.** Comparison of the absolute amplitudes (Å) of the atomic distortions and lattice parameters in the E'-type AFM $P2_1/n$ phase of $YNiO_3$ as computed in DFT with U = 1.5 eV (purple) and as measured experimentally (orange). The E'-type AFM $P2_1/n$ ground state has a 80-atoms unit cell with lattice parameters $(a', b', c') = (2\sqrt{2}a, \sqrt{2}b, 4c)$.

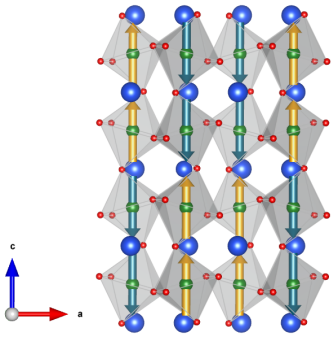

Figure 10.3 | **Ground State spin coniguration for $YNiO_3$.** Spin order associated to the E'-type antiferromagnetic (AFM-E') ground state.

1.5 eV.

10.3 Supplementary Note 3. Magnetic properties

In order to determine the magnetic ground state of the $P2_1/n$ phase of $YNiO_3$, we performed calculations for various magnetic orders associated to supercells of up to 80 atoms. While U values larger than 2 systematically favour a FM spin order, U = 1.5 eV properly stabilizes the E'-type spin ordering illustrated in Supplementary Figure 10.3 as the ground state. It corresponds to an "up-up-down-down" spin arrangement related to a Bragg vector $\mathbf{q} = (1/4, 1/4, 1/4)$ in pseudocubic notations.

In our calculations, we get a magnetic moment $\mu = 1.2\mu_B$ on the Ni atoms associated to the large oxygen octahedra and $\mu \approx 0\mu_B$ on the Ni atoms associated to the small octahedra. This is similar with what has been reported in Ref. [103, 210] and in line with the $d^8 - d^8L^2$ picture [105]. It is also compatible with experimental data as discussed in Ref. [211].

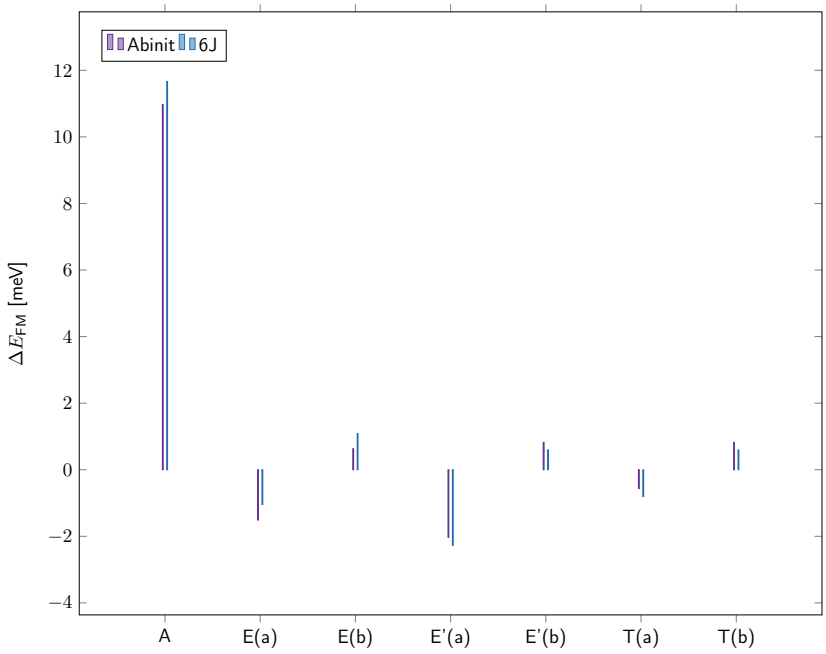

Figure 10.4 | **Heisenberg versus Abinit results for $YNiO_3$.** Comparison of the energy associated to various spin orders, respect to the FM order taken as reference, as obtained from our DFT calculations (purple) and simple spin model (blue). The A-type ordering corresponds to an antiferromagnetic stacking along the *c* direction of FM ordered *ab* planes. The E(a)-type order corresponds to an "up-up-down-down" zigzag chain along the *a* (orthorhombic) direction, and a FM order along the *c* direction. The E(b)-type order is characterised by the same "up-up-down-down" zigzag chain but along the *b* (orthorhombic) direction. The E'(a), E'(b), T(a) and T(b) types of order have the same in-plane properties too. However, the stacking along the *c* direction is different : E'(a) and E'(b) have two FM-order layers, AFM coupled with the next two layers while in the T(a) and T(b) configurations, the zigzag chain shifts about one spin along the chain direction at the same time one passes throught the *c* direction. The ground state is E'(a) as illustrated in Supplementary Figure 10.3 and simply called E' within the manuscript.

Beyond the fact that DFT calculations with U = 1.5 eV provides the right magnetic ground state, it is interesting to check if it properly accounts for the strength of the magnetic interactions. To that end, we built a simple spin model $E_{mag} = (1/2)\sum J_{ij} S_i S_j$ including J_{ij} interactions up to fourth neighbours (6 independent parameters) and fitted the parameters on our first-principles data [17]. As illustrated in Supplementary Figure 10.4 for $YNiO_3$ this spin model properly reproduces the energetics of the first-principles calculations.

Monte-Carlo simulations (using large boxes up to 1728 Ni atoms) from this spin-model [17] (i) confirmed the E'-type ground state and (ii) provided a Neel temperature $T_N = 154$ K, very similar to the mean-field estimate of 166 K and in close agreement with the experimental value of 150 K for $YNiO_3$ [97].

This demonstrates that our DFT calculations with U = 1.5 eV reproduces not only the correct E'-type magnetic ground state of nickelates but also properly describes the strength and anisotropy of their magnetic interactions.

10.4 Supplementary Note 4. Electronic properties

Our DFT calculations with U = 1.5 eV properly accounts for the insulating character of the E'-type AFM $P2_1/n$ ground state of $YNiO_3$. For the electronic bandgap, we get a value of 0.46 eV in reasonable agreement with the experimental estimate of 0.305 eV [155].

The electronic properties are further discussed in the manuscript. As it appears clearer there, the structural and electronic properties are intimately linked together in nickelates. Hence, the fact that our simulations describe accurately the structural properties of these compounds strongly suggests that they can also be trusted to investigate their electronic properties.

10.5 Supplementary Note 5. Phonon dispersion curves

In Supplementary Figure 10.5, we report the full phonon dispersion curves of the $Pm\bar{3}m$ phase of $YNiO_3$, as calculated for a FM spin ordering at the volume of the $P2_1/n$ AFM-E' phase ($a_{pc} = 3.728$Å). Similar curves have been obtained at the relaxed volume ($a_0 = 3.695$Å). Interpolation of these phonon dispersion curves relies on the calculation of the interatomic force constants within a $2 \times 2 \times 2$ supercell. Although this might not be totally sufficient to get a fully converged interpolation, it provides already a good estimate of the shape of the dispersion curves. It is worth to notice that the frequencies at the high-symmetry points, which are the only ones discussed below and in the manuscript, are not interpolated but calculated explicitly within our approach.

On the one hand, the phonon dispersion curves highlight strong instabilities at the R and M q–points of the BZ, associated to the R_{xy} and M_z distortions. On the other hand, and quite amazingly, the breathing distortion, B_{OC} located at the R point, which finally produces the MIT, is associated to the hardest mode in the cubic phase. Clearly, such hard mode cannot

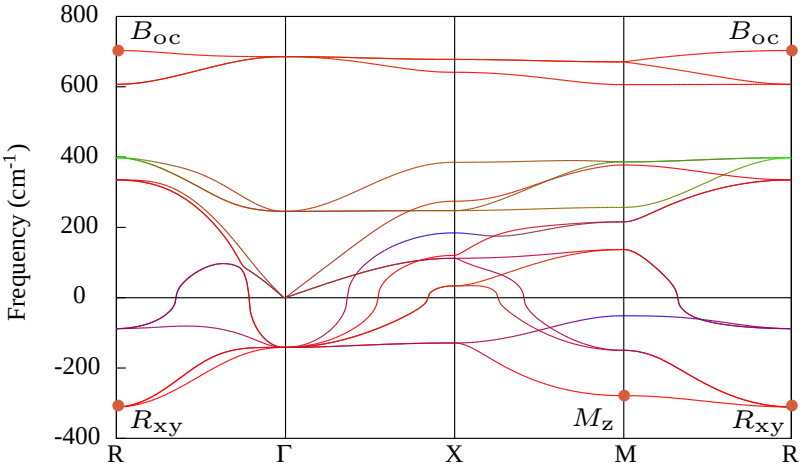

Figure 10.5 | **Cubic phonon dispersion curve for $YNiO_3$.** Phonon dispersion curve for the $Pm\bar{3}m$ phase of $YNiO_3$, at the $P2_1/n$ ground state volume and for a FM spin ordering (U=1.5 eV). Colors have been associated to the curves according to the involvement of each cation in the eigendisplacement of each mode (*R* in blue, Ni in green and O in red). Imaginary frequencies (unstable modes) appear as negative values.

spontaneously condense within the cubic structure.

We further notice the presence of two (triply-degenerated) unstable modes at Γ with very close frequencies. The softest one is associated to a polar-type motion involving *R* and O atoms; this kind of instability is expected for perovskites with small tolerance factors as $YNiO_3$. The second one is the silent butterfly motion of the O atoms.

10.6 Supplementary Note 6. Landau Model

Based on our DFT results, we have built a simple Landau-type model. In order to highlight the triggered mechanism, we restricted ourselves to the simplest possible model including only R_{xy}, M_z and B_{OC} degrees of freedom and lowest-order terms.

10.7 Supplementary Note 7. Expression

Within our Landau-type model, the free energy in terms of the amplitudes Q_R, Q_M and Q_B (of R_{xy}, M_z and B_{OC} respectively) reads:

$$\begin{aligned} E(Q_M, Q_R, Q_B) = \quad & \alpha_R Q_R^2 + \beta_R Q_R^4 + \alpha_M Q_M^2 + \beta_M Q_M^4 + \alpha_B Q_B^2 + \beta_B Q_B^4 \\ & + \lambda_{MR} Q_M^2 Q_R^2 + \lambda_{MB} Q_M^2 Q_B^2 + \lambda_{RB} Q_R^2 Q_B^2 \end{aligned} \tag{10.1}$$

The parameters α_R and α_M are assumed to be temperature dependent as

$$\alpha_R = \gamma_R(T_{0R} - T) \quad \text{and} \quad \alpha_M = \gamma_M(T_{0M} - T) \tag{10.2}$$

while all the other parameters are supposed to be constant.

Other modes allowed by symmetry (see Supplementary Table 10.1) in the $Pbnm$ and $P2_1/n$ phases have not be explicitly included within the model. Some of them, like X_5^- (and to a lesser extent R_4^- and M_3^+), take however a significant amplitude and are crucial to stabilize the $Pbnm$ phase. They are implicitly included through a renormalization of the λ_{MR} parameter as it will appear more clearly in the next section.

The strain degrees of freedom have not been explicitly included within the model to highlight the key role of phonon-phonon couplings, which appear sufficient to reproduce experimental data on bulk compounds. However, this model could be naturally extended to strain degrees of freedom and their couplings with lattice modes. This might be useful to quantify for instance the role of epitaxial strain in thin films but is beyond the scope of this work.

The expansion has been limited to 4^{th} order for all three order parameters including Q_{B}. This is justified by the fact that, from the fit of the parameters, the triggered transition appears to be second order . We notice however that explicit treatment of the strain (neglected here) could affect the order of the phase transition as further discussed below.

10.8 Supplementary Note 8. Fit from DFT

Parameters of our Landau-type model have been fitted on first-principles results. At first, we focused on $YNiO_3$.

We considered in our calculations a fixed cubic $Pm\bar{3}m$ cell at a volume similar to that of the $P2_1/n$ AFM-E' ground-state (a_{pc} = 3.728Å), which corresponds to imposing a negative strain of 0.9%. At this volume, relaxing within the $P2_1/n$ symmetry while keeping the unit cell fixed yields amplitudes of distortion comparable to the ground-state. We notice that, as illustrated in Supplementary Figure 10.6, similar calculations performed at the relaxed lattice constant (a_0 = 3.695Å) yield very similar results. Even calculations performed while relaxing the lattice parameters at fixed mode amplitudes (in reduced coordinates) do not provide any significant change.

The calculations have been performed with a FM spin order which does not break any symmetry. We checked explicitly that the key physical features and conclusions (cooperative bi-quadratic coupling between rotations and breathing and triggered mechanism) remain similar for different AFM spin orders. The results remain even very similar in a non-magnetic (NM) calculation (with or without U correction) although, in that case, the amplitude of rotations required to destabilise B_{OC} is slightly larger ($\approx$ 160%); this last result illustrates that electronic Hund's rule energy, although playing a role, is not driving alone the appearance of B_{OC} as sometimes suggested [104].

The parameters of the Landau model at 0 K have then been extracted from DFT data as follows.

- $\alpha_{\mathrm{R}}^0 (= \gamma_{\mathrm{R}} T_{0\mathrm{R}})$, $\alpha_{\mathrm{M}}^0 (= \gamma_{\mathrm{M}} T_{0\mathrm{M}})$, β_{R} and β_{M} were fitted on the individual double wells

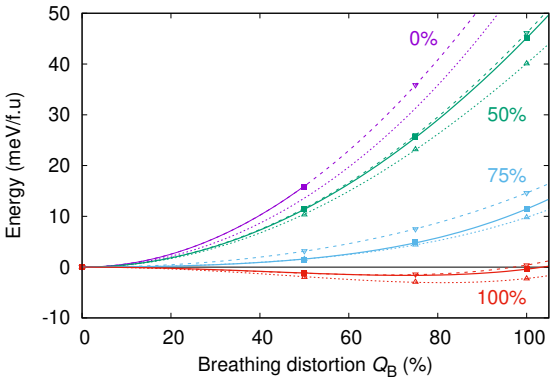

Figure 10.6 | **Breathing mode in $YNiO_3$ as a function of rotation modes.** Evolution of the energy of $YNiO_3$ in terms of the amplitude of the breathing distortion for fixed amplitude of oxygen rotations ($Q_R = Q_M$, from 0% to 100%) in a FM configuration and either a fixed cubic cell (dotted line and triangles: $a_{pc} = 3.728$ Å; dashed line and back triangles: $a_0 = 3.695$ Å) or when relaxing fully the lattice parameters (full line and squares).

associated to R_{xy} and M_z (Figure 4.1).

- λ_{RM} was fitted to reproduce the energy of a relaxed *Pbnm*-like phase (full atomic relaxation while keeping the cubic cell fixed). From this, we renormalize the natural competition between R_{xy} and M_z by including implicitly the stabilising effect of X_5^-, R_4^- and M_3^+ modes. We notice that in all compounds, R_{xy} and M_z compete with each other and should yield $\lambda_{RM} > 0$. However, because of the renormalization due to the implicit presence of the other modes, λ_{RM} becomes negative for large cations (i.e. X_5^- helps stabilizing the *Pbnm* phase consistently with the discussion in Ref. [96].

- α_B was fitted on the single well associated to B_{OC} (Figure 4.1).

- λ_{BR} and λ_{BM} were fitted from the change of curvature of the well of B_{OC} when freezing 100% of Q_R and Q_M respectively (Figure 4.2).

- β_B was fitted to reproduce the right amplitude of B_{OC} in the ground state of the model and it was checked that the result still properly describes the single well associated to B_{OC}.

Within the model, the amplitude for the atomic distortion are renormalised to the one obtained from DFT calculation for the $YNiO_3$ ground state. This means 1 for rotation, tilts and breathing mode correspond to the amplitude of these modes in a cubic box with lattice parameters coresponding to 3.728 Å.

We applied the same procedure to $GdNiO_3$ and $SmNiO_3$. All the computed parameters are summarized in Table 10.2.

As illustrated in Supplementary Figure 10.7, all the parameters have an almost linear dependence in terms of the tolerance factor t. So, in our model, we assumed such a linear dependence to determine the value of the parameters at arbitrary t.

parameter	Y	Gd	Sm
t	0.920	0.938	0.947
α_B	58.1	52.6	50.6
β_B	10.0	16.0	31.0
α_M^0	-578.3	-385.5	-277.3
T_{0M}	3918	2571	1897
β_M	213.9	209.4	201.0
α_R^0	-1288.1	-1081.2	-920.9
T_{0R}	3918	3195	2833
β_R	648.8	754.9	750.4
λ_{MR}	31.8	-57.7	-99.4
λ_{MB}	-26.0	-29.0	-29.4
λ_{RB}	-35.8	-42.2	-42.4

Table 10.2 | **Fitted Landau parameters as a function of the tolerance factor.** Landau model parameters (meV/f.u. or K) as fitted on first-principles data, using the mode normalisation described in the Methods section.

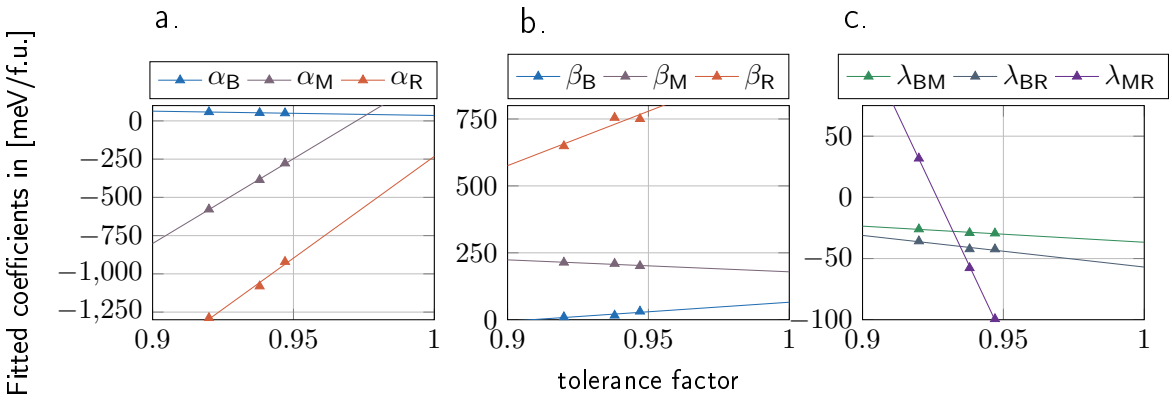

Figure 10.7 | **Landau parameters as a function of the tolerance factor.** Evolution of the model parameters (meV/f.u.) with the tolerance factor.

Finally, knowing $\alpha_{R,M}$ at 0 K (from the DFT calculations), their temperature dependence was estimated as follows. Focusing first on $YNiO_3$ we adjusted $T_{0R} = T_{0M}$ so that within our model, B_{OC} appears at the experimental value of 585K [5] and we deduced $\gamma_{M,R} = \alpha^0_{R,M}/T_{0R,M}$: $\gamma_M = 0.148 meV/f.u.$ and $\gamma_R = 0.331 meV/f.u.$. Then, assuming $\gamma_{M,R}$ constant within the whole family the evolution of T_{0R} and T_{0M} with the tolerance factor were obtained as: $T_{0R,M} = \alpha^0_{R,M}/\gamma_{M,R}$.

From this, we get the following final Landau-type expression for the free energy, allowing us to determine the values of Q_R,Q_M and Q_B for any value of the temperature T and tolerance factor t :

$$\begin{aligned} &E(Q_M, Q_R, Q_B) = \\ &(-281.9 \times t + 317.4)Q_B^2 + (714.3 \times t - 648.9)Q_B^4 \\ &-0.15 \times (-74891.2 \times t + 72818.6 - T) \times Q_M^2 + (-446.3 \times t + 625.3) \times_M^4 \\ &-0.33 \times (-40212.2 \times t + 40913.9 - T) \times Q_R^2 + (4067.9 \times t - 3085.5) \times Q_R^4 \\ &+(-4875.7 \times t + 4517)Q_M^2 Q_R^2 + (-131.6 \times t + 94.9) \times Q_M^2 Q_B^2 + (-258.6 \times t + 201.6) \times Q_R^2 Q_B^2 \end{aligned} \tag{10.3}$$

10.9 Supplementary Note 9. Analytical solution

From this model, T_{MI} can be determined analytically.

We start from the expression:

$$\begin{aligned} E(Q_M, Q_R, Q_B) = \quad & \alpha_B Q_B^2 + \beta_B Q_B^4 \\ & +\gamma_M \times (T_{0M} - T) \times Q_M^2 + \beta_M Q_M^4 \\ & +\gamma_R \times (T_{0R} - T) \times Q_R^2 + \beta_R Q_R^4 \\ & +\lambda_{MR} Q_M^2 Q_R^2 + \lambda_{MB} Q_M^2 Q_B^2 + \lambda_{RB} Q_R^2 Q_B^2 \end{aligned} \tag{10.4}$$

At the energy minimum, we should have :

$$\frac{\partial E}{\partial Q_M} = 0 \text{ and } \frac{\partial E}{\partial Q_R} = 0. \tag{10.5}$$

The solutions for that, other than $Q_M = 0$ and $Q_R = 0$, are :

$$\begin{aligned} Q_M^2 = \quad & \frac{-2T_{0M}\gamma_M\beta_R + T_{0R}\gamma_R\lambda_{MR} + T(2\gamma_M\beta_R - \gamma_R\lambda_{MR})}{4\beta_M\beta_R - \lambda_{MR}^2} \\ + \quad & \frac{(-2\beta_R\lambda_{MB} + \lambda_{MR}\lambda_{RB})}{4\beta_M\beta_R - \lambda_{MR}^2} Q_B^2 \\ Q_R^2 = \quad & \frac{-2T_{0M}\gamma_M\beta_R + T_{0R}\gamma_R\lambda_{MR} + T(2\gamma_M\beta_R - \gamma_R\lambda_{MR})}{4\beta_M\beta_R - \lambda_{MR}^2} \\ + \quad & \frac{(-2\beta_R\lambda_{MB} + \lambda_{MR}\lambda_{RB})}{4\beta_M\beta_R - \lambda_{MR}^2} Q_B^2 \end{aligned} \tag{10.6}$$

Introducing this in Supplementary Eq. (10.4) we get :

$$E(Q_B) = \alpha'_B Q_B^2 + \beta'_B Q_B^4 \tag{10.7}$$

where

$$\begin{aligned} \alpha'_B = \quad & \alpha_B + \frac{(\gamma_M \lambda_{MR} \lambda_{RB} - 2\gamma_M \beta_R \lambda_{MB})}{4\beta_M \beta_R - \lambda_{MR}^2}(T_{0M} - T) \\ + \quad & \frac{(\gamma_R \lambda_{MB} \lambda_{MR} - 2\gamma_R \beta_M \lambda_{RB})}{4\beta_M \beta_R - \lambda_{MR}^2}(T_{0R} - T) \end{aligned} \tag{10.8}$$

$$\beta'_B = \quad \beta_B + \frac{\lambda_{MB} \lambda_{MR} \lambda_{RB} - \beta_M \lambda_{RB}^2 - \beta_R \lambda_{MB}^2}{4\beta_M \beta_R - \lambda_{MR}^2} \tag{10.9}$$

$$\tag{10.10}$$

The MIT is linked to the appearance of the B_{OC}. This will appear at a temperature T_{MI} at which $\alpha'_B = 0$. This critical temperature is given by :

$$\begin{aligned} T_{MI} = \quad & \frac{\alpha_B(-4\beta_M \beta_R + \lambda_{MR}^2)}{2\gamma_M \beta_R \lambda_{MB} - \gamma_R \lambda_{MB} \lambda_{MR} + 2\gamma_R \beta_M \lambda_{RB} - \gamma_M \lambda_{MR} \lambda_{RB}} \\ + \quad & \frac{T_{0R} \gamma_R(-\lambda_{MB} \lambda_{MR} + 2\beta_M \lambda_{RB})}{2\gamma_M \beta_R \lambda_{MB} - \gamma_R \lambda_{MB} \lambda_{MR} + 2\gamma_R \beta_M \lambda_{RB} - \gamma_M \lambda_{MR} \lambda_{RB}} \\ + \quad & \frac{T_{0M} \gamma_M(2\beta_R \lambda_{MB} - \lambda_{MR} \lambda_{RB}))}{2\gamma_M \beta_R \lambda_{MB} - \gamma_R \lambda_{MB} \lambda_{MR} + 2\gamma_R \beta_M \lambda_{RB} - \gamma_M \lambda_{MR} \lambda_{RB}} \end{aligned} \tag{10.11}$$

Furthermore, supposing a linear dependence for all the coefficients with respect to the tolerance factor, we get a generic expression :

$$T_{MI} = \frac{a + t \times (b + (c + d \times t)t)}{e + t \times (f + g \times t)} \tag{10.12}$$

where t is the tolerance factor and a, b, c, d, e, f and g are a combination of model parameters.

Using the coefficients determined from DFT calculations in the previous Section, we can predict the evolution of T_{MI} as a function of the tolerance factor as illusrated in Figure 4.2b, blue line.

Independently, we can also fit the experimental data point using Supplementary Eq. 10.12. Making such a fit, while excluding Nd and Pr compounds, we get the dashed blue line in Figure 4.2b.

10.10 Supplementary Note 10. Order of the transition

Experimentally, there is still some debate about the order of the MIT. For large cations ($T_{MI} = T_N$), the MIT is rather abrupt and hysteretic and unanimously considered as being first order [5]. The magnetic transition that takes place at the same temperature is also first order [112]. For small cations ($T_{MI} > T_N$), the MIT is less hysteretic and sometimes considered as evolving to second-order. Some studies seem however to show that it stays first-order

[212, 213], while the less hysteretic behavior could be related to the fact that kinetics are better at higher temperatures [5]. For these compounds the magnetic transition is second-order.

As previously mentioned, the MIT is predicted to be second-order within our very simple model. As highlighted in Supplementary Table 10.2, computed β_B is positive for all compounds. From Supplementary Eq. 10.10, the oxygen rotations renormalize the fourth-order term coefficient and a negative value of β'_B would give rise to a first-order transition (it would then further require including 6^{th} order terms in Q_B). Although this renormalization is negative, β'_B stays nevertheless positive in all cases (β'_B = 9, 14 and 29 respectively for $YNiO_3$, $GdNiO_3$ and $SmNiO_3$ respectively) corresponding therefore to a second-order transition.

Yet, we have to stress that our approach does not allow us to address the order of the transition conclusively. First, our model is built at fixed cubic cell and does not include strain relaxation. Explicit treatment of the latter will further renormalize the 4^{th}-order term and might potentially make it negative, so eventually changing the order of the transition. Second, at a more fundamental level, even if our DFT+U results suggest that Q_B undergoes a second-order transition, that does not rule out the possibility that thermal effects effectively render a first-order transformation driven by temperature. The ferroelectric phase transitions of $BaTiO_3$, a well studied case, are a concrete example of this [214], and also illustrate the critical role of strains to enhance the discontinuous character of the transformation [215]. Hence, discussing the character of the transition from first-principles would require explicitly statistical simulations that fall beyond of the scope of this work. The Landau model introduced here was kept simple on purpose in order to highlight the key role of the triggered mechanism and it shows that, based on our first-principles results and a minimal experimental input, the main features of the phase diagram can be readily reproduced. Further, the main trends (regarding ionic size, amplitude of the different rotations, ...) are properly captured by this simple model, which moreover provides us with insights about how to tune the behaviour of these materials. In this sense, we consider that the proposed Landau model is valid and useful although, admittedly, it is not suitable for a definite discussion of the order of the transition.

For large cations (Nd and Pr), our model predicts that the MIT can no more be fully triggered by the oxygen rotations (which are reduced); for those compounds, it is complementarily promoted by the appearance of the AFM-E' magnetic order. In such case, the MIT takes place at $T_{MI} = T_N$; it is expected to be more abrupt and to be first order. Such coupling between the structural and magnetic transition for large cations is in line with the conclusions of Vobornik *et al.* in Ref. [112]: they suggest indeed that, contrary to other cases, there is a possible interplay between electronic and magnetic degrees of freedom when $T_{MI} = T_N$ and that any further model of the MIT should address that fact. Our manuscript explicitly addresses that point and we believe that it convincingly answers their questioning.

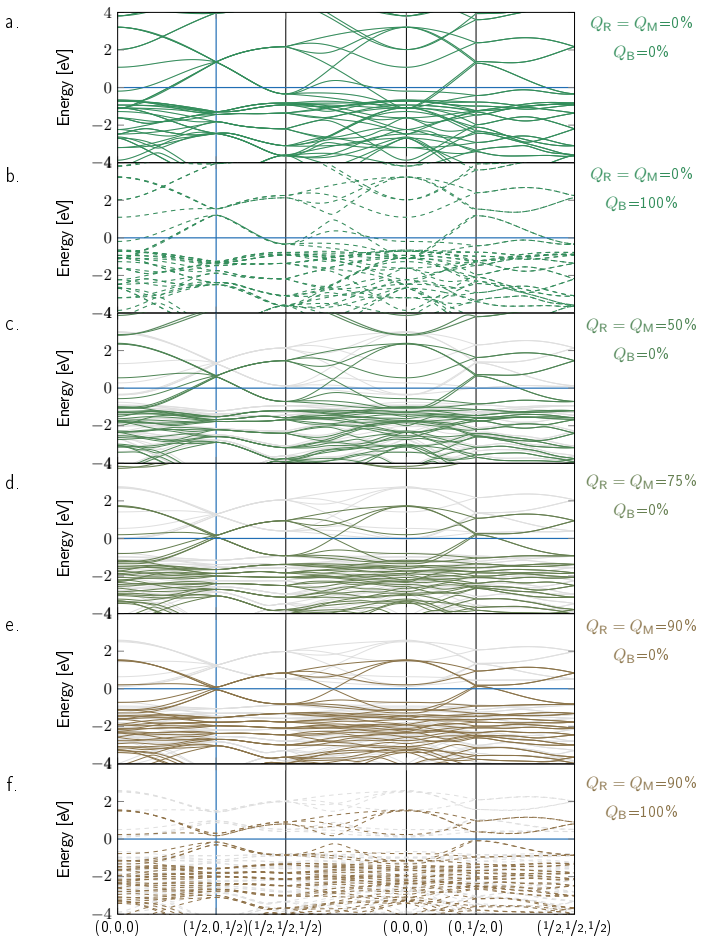

Figure 10.8 | **$YNiO_3$ FM electronic band structures.** $YNiO_3$, FM spin order. Evolution of the electronic dispersion curves around the Fermi energy E_f when freezing into the $Pm\bar{3}m$ phase increasing amplitudes of oxygen rotations ($Q_R = Q_M =$ (**a**) 0%, (**c**) 50%, (**d**) 75% and (**e**) 90%, lines) and eventually adding the breathing distortion ($Q_B = 100\%$ with $Q_R = Q_M =$ (**b**) 0% and (**f**) 90%, dashed lines). The graph connects high-symmetry points in the Brillouin zone of the $Pbnm$ or $P2_1/n$ 20-atom cell. Majority spins are in colors and minority spins in light grey.

10.11 Supplementary Note 11. Electronic band structures

In Supplementary Figure 10.8, we report the electronic dispersion curves of $YNiO_3$ with a FM spin order, along a more exhaustive path of the Brillouin zone of the $Pbnm$ or $P2_1/n$ 20-atom cell. The majority spins are in colors while the minority spins are in light grey. The latter have been omitted for clarity in the main manuscript. We notice that the cubic phase is essentially non magnetic (up and down spin bands nearly degenerate) and magnetism starts to develop with the rotations.

In Supplementary Figure 10.9, we report similarly the electronic dispersion curves of $YNiO_3$ but with an AFM-A spin order. This figure is very similar to the previous one, demonstrating that our results are not dependent of the specific choice of spin order.

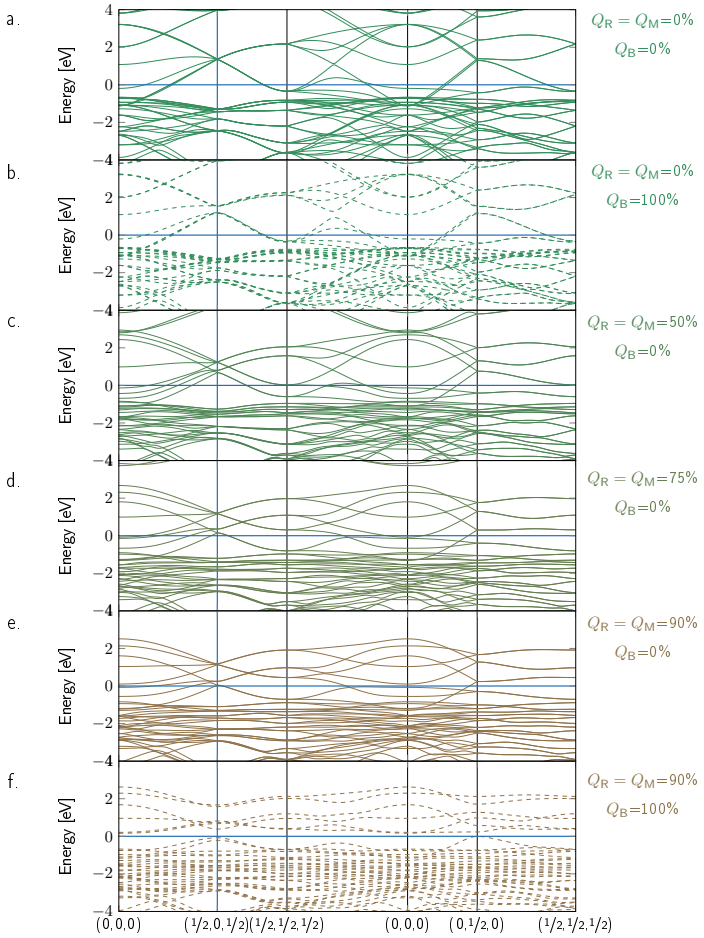

Figure 10.9 | **$YNiO_3$ AFM-A electronic band structures.** $YNiO_3$, AFM-A spin order. Evolution of the electronic dispersion curves around the Fermi energy E_f when freezing into the $Pm\bar{3}m$ phase increasing amplitudes of oxygen rotations ($Q_R = Q_M$ = (**a**) 0%, (**c**) 50%, (**d**) 75% and (**e**) 90%, lines) and eventually adding the breathing distortion (Q_B = 100% with $Q_R = Q_M$ = (**b**) 0% and (**f**) 90%, dashed lines). The graph connects high-symmetry points in the Brillouin zone of the $Pbnm$ or $P2_1/n$ 20-atom cell.

11 | Supplementary Materials: From charge- to orbital-ordered MIT in alkaline-earth ferrites

Yajun Zhang[1,2], *Michael Marcus* Schmitt[1], *Alain* Mercy[1], *Jie* Wang[2] and *Philippe* Ghosez[1]

[1]Theoretical Materials Physics, Q-MAT, CESAM, University of Liège, B-4000 Liège, Belgium [2]Department of Engineering Mechanics, School of Aeronautics and Astronautics, Zhejiang University,38 Zheda Road, Hangzhou 310007, China

11.1 Supplementary Note 1. Choice of (U|J) Parameters

For our first-principles study of the $AFeO_3$ family we used density functional theory (DFT) as implemented in the *Vienna Ab-Initio Simulation Package* (*VASP*) with the *PBEsol* exchange-correlation functional adding a *Liecthenstein* (U|J) correction of (U|J)=(7.2|2) eV. Those parameters where determined by comparing the magnetic, electronic, and structural ground-state of our calculation to experimental values on which we give additional informations in the following two sections.

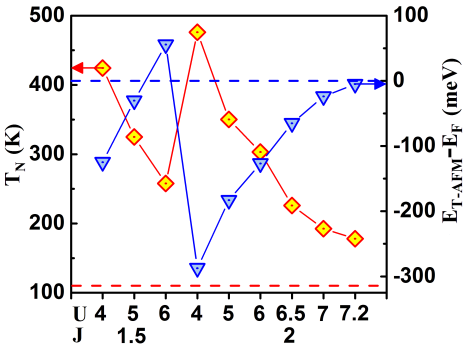

Figure 11.1 | Effect of U and J value on the Néel temperature T_N (orange curve) and energy difference between T-AFM (or S-AFM) state and FM state (blue curve).

11.1.1 Supplementary Note 1.1 Magnetic and Electronic Properties

In Fig. 11.1 and Table 11.1 magnetic and electronic informations of our DFT-PBEsol + (U|J) calculations and experimental values are gathered.

Experimentally, $CaFeO_3$ exhibits an antiferromagnetic (AFM) transition at the Néel temperature T_N = 115 K. Below, the magnetic state is proposed to be either a spiral spin structure with alternating incommensurate magnetic moments of 2.70 and 3.52 μ_B or a sinusoidal structure with alternating moments of 3.6 and 5.06 μ_B. The helical axis of the spiral structure was proposed to lie along or close to the pseudocubic [111] direction, the sinusoidal axis in or close to the pseudocubic [101] direction. Both spin-waves exhibit periodicity close to $k = \frac{\pi}{3}$. The nearest-neighbor interaction is suggested to be ferromagnetic, the next-nearest anti-ferromagnetic.

In our calculations, the magnetic ground-state was probed at the collinear level on various magnetic cells up to 16 formula units (ferromagnetic (FM), simple A-type, C-type, and G-type AFM-orders, and more complex E-type, S-type and T-type AFM states as defined in [29]). In the limit of these unit-cells S- and T-type AFM states are the closest to the spiral model of *Woodward et al.* showing ⇑↑⇓↓ sequences along the [111] direction, where ⇑ stands for the larger magnetic moment and ↑ for the smaller ones. For most tested (U|J) values AFM-S or T-type were the ground state, with marginal energy differences in between them. We extracted isotropic spin-exchange parameters until the fourth neighbor and calculated T_N from mean field theory. For U = 7.2 eV and J = 2 eV we found the lowest T_N of about 180 K in decent proximity to the experimental one, where T-type AFM is the ground-state. The nearest neighbor exchange is FM (J_1 = 5.09meV/fu), while second and third neighbor interactions are negligible (J_2 = 0.74meV/fu, J_3 = 0.31meV/fu). The fourth nearest-neighbor exchange constant (second nearest along the [001] pseudocubic axis) is strongly AFM (J_4 = −3.69meV/fu), showing the magnetic frustration of the system which would lead to spiral magnetic structures in non-collinear calculations. The corresponding magnetic moments at U = 7.2 eV and J = 2 eV of 2.72 μ_B and 4.07 μ_B for two nearest-neighboring Fe atoms match sufficiently the experimental results. We further check the band gap with U = 7.2 eV and J = 2 eV. The result of 0.96 eV compares well with the previous result of 0.9 eV obtained from Hartree-Fock calculations[158].

11.1.2 Supplementary Note 1.2 Structural Optimization

In Fig. 11.2(a), (b), as well as Table 11.1 we present structural values in dependency of the (U|J) parameters for $CaFeO_3$. All tested quantities are excellently reproduced by the choice of (U|J)=(7.2|2) eV. In Fig 11.2 (c) we additionally show that the experimental cubic lattice parameters of $SrFeO_3$ and $BaFeO_3$ are equally well reproduced by the same calculation approach.

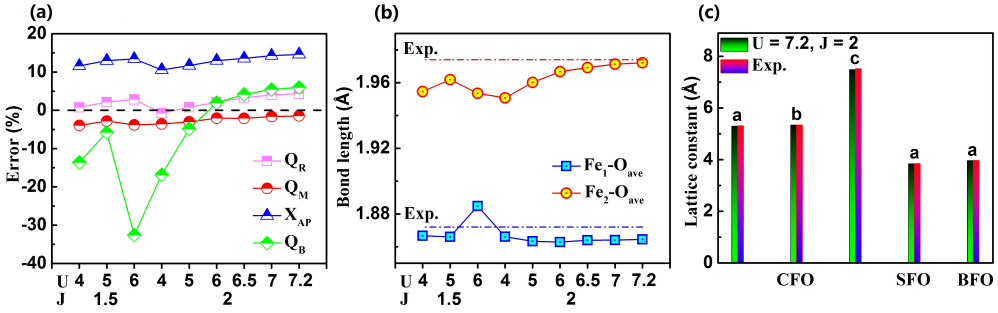

Figure 11.2 | Effect of U and J value on the (a) Error of the distortions for the lowest energy structure compared to experimental results, (b) average bond length of Fe1 and Fe2 sites in the optimized ground state, (c) lattice constant of T-AFM $CaFeO_3$ and ferromagnetic $SrFeO_3$ and $BaFeO_3$ with U equal to 7.2 eV and J equal to 2 eV. The ISOTROPY program was used to quantify the distortion modes amplitudes [156]

11.2 Supplementary Note 2. Closing of the Band-Gap at the Phase Boundary between Charge- and Orbital-Order under Epitaxial Strain

The transition from charge to orbital-ordering takes place precisely, when the band-gap is closed at 3% tensile epitaxial strain. At this strain the Charge-Ordered state becomes semimetallic, where the indirect band-gap is closed down. An electron pocket is formed along the path $\overline{\mathbf{SY}}$, a complementary hole pocket is formed around the **U** point in the Brillouin-Zone of the orthorhombic 20-atoms unit cell. These pockets are removed with the appearance of the M_{JT} distortions and the magnetic transition from FM to AFM-A (See Fig. 11.3.

11.3 Supplementary Note 3. Reduction of MIT Temperature in $Ca/SrFeO_3$ Solid Solutions

In Table 11.2 we present the results of structural optimizations of $CaFeO_3$, $SrFeO_3$, and the solid solution $Ca_{0.5}Sr_{0.5}FeO_3$ ordered along the [001] pseudocubic axis. As it is obvious from Table 11.2 the triggering mechanism we present in the main manuscript is able to

$U\|J$ (eV)	a (Å)	b (Å)	c (Å)	Q_B (Å)	Q_M (Å)	Q_R (Å)	T_N (K)	E_{Gap} (eV)
7.2|2	5.29	5.34	7.48	0.19	0.81	1.11	180	0.96
3|0 [151]	5.29	5.33	7.49	0.08	0.81	1.10	-	0.18
Exp. [148]	5.31	5.35	7-52	0.18	0.83	1.06	115	-

Table 11.1 | Comparison of the lattice parameters, amplitudes of relevant atomic disortions (from ISOTROPY [216], Néel temperature T_N and electronic band gap of the $P2_1/n$-phase of $CaFeO_3$ as obtained in the T-AFM state from PBEsol + (7.2|2) method (present), in the FM state from PBEsol + (3.0|0) and experimental results .

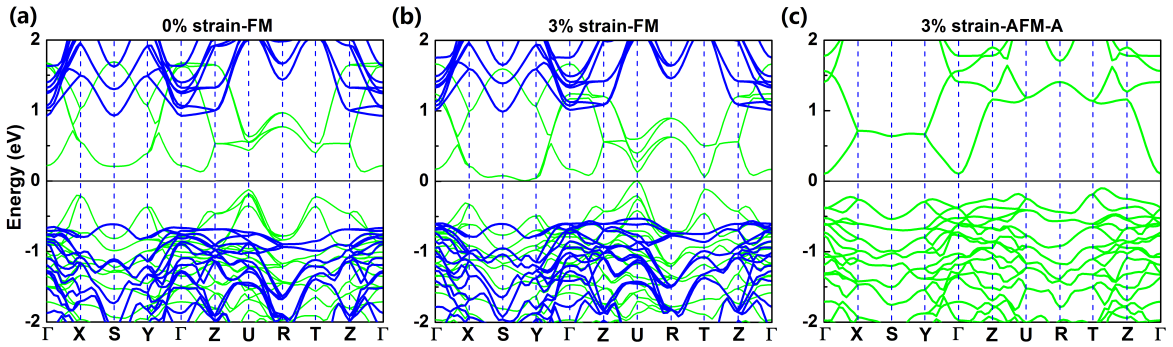

Figure 11.3 | Electronic Band Structures of (a) FM-CO state under 0% strain, (b) FM-CO state under 3% strain and (c) AFM-A-OO state under 3% strain. Green lines represent the majority, blue lines the minority spin channels, respectively.

explain the band gap reduction from $CaFeO_3$ to the solid solution and the other way around the opening of it when starting from pure $SrFeO_3$. In Fig. 11.4 we provide additionally the calculated electronic band structures of the three materials.

Table 11.2 | Optimized Lattice Constants and distortion mode amplitudes of $B_{oc}(Q_B)$, $R_{xy}(Q_R)$ and $M_z(Q_M)$ for $CaFeO_3$, $Ca_{0.5}Sr_{0.5}FeO_3$, and $SrFeO_3$.

	a (Å)	b (Å)	c (Å)	Q_B(Å)	Q_M(Å)	Q_B(Å)
$CaFeO_3$	5.3	5.35	7.5	0.14	0.9	1.11
$Ca_{0.5}Sr_{0.5}FeO_3$	5.39	5.37	7.59	0.11	0.49	0.82
$SrFeO_3$	5.43	5.43	7.68	0	0	0

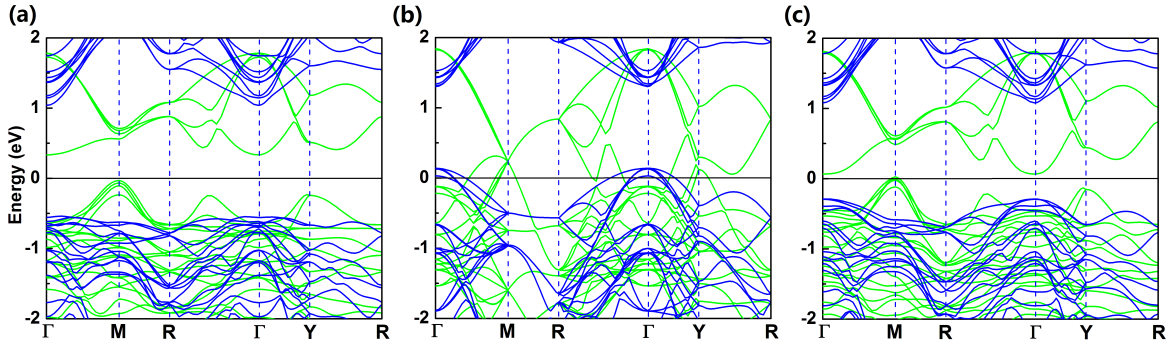

Figure 11.4 | Band structure of (a) $CaFeO_3$, (b) $SrFeO_3$ and (c) $Ca_{0.5}Sr_{0.5}FeO_3$ ordered along [001] in ferromagnetic state along the high-symmetry path **Γ**(0, 0, 0)-**M** (1/2, 0, 1/2)-**R**(1/2, 1/2, 1/2)-**Γ**(0, 0, 0)-**Y**(0, 1/2, 0)-**R**(1/2, 1/2, 1/2) of the Brillouin zone of orthorhombic lattice.

11.4 Supplementary Note 4. Coupling Parameters and Decomposotion of the Linear Term $\gamma Q_R Q_X Q_{JT}$

Table 11.3 represents an extended version of Table 11.1 of the main manuscript. We additionally note the coupling parameters resulting a polynomial fit of the potential energy

surfaces presented in Fig. 7.3 (a) and (b) in the main manuscript. The energy contributions to ΔE_{JT} ($\Delta E_{JT} = \sum_i \Delta E_{JT}^i$), where then obtained by simple multiplications of the distortion amplitudes with the coupling parameters according to Eq. (7.2) of the main manuscript. In Table 11.3 we disentangle the oxygen motion Q_X^O and cation motion Q_X^A appearing in the same irreducible representation X_5^- and investigate the potential energy surface with respect to those displacements. It turns out to be more appropriate to associate individual coupling parameters to Q_X^O and Q_X^A and write

$$\begin{aligned}\gamma_{RXJT} Q_X Q_R Q_{JT} &= \gamma_{RXJT}^A Q_X^A Q_R Q_{JT} \\ &+\gamma_{RXJT}^O Q_X^O Q_R Q_{JT}\end{aligned} \tag{11.1}$$

Comparing the amplitudes Q_X^O, Q_X^A and the energy well with respect to Q_{JT} associated with the above coupling(Fig. 11.5) for CO and OO phase at 0% strain, it becomes apparent that the asymmetric energy contribution ΔE_{JT}^3 in OO phase stems primarily from the change of the relative amplitudes Q_X^O/Q_X^A as γ_{RXJT}^O and γ_{RXJT}^A are rather constant in the two phases.

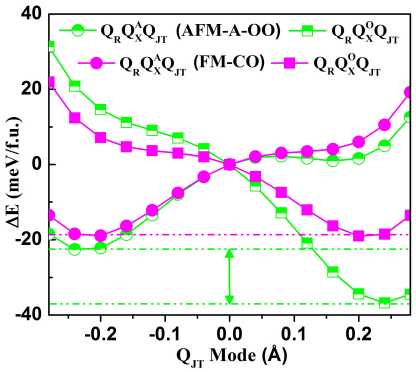

Figure 11.5 | Decomposition of the trilinear term $\gamma_{RXJT} Q_X Q_R Q_{JT}$ into the motion of the cations $\gamma_{RXJT}^A Q_X^A Q_R Q_{JT}$ and oxygens $\gamma_{RXJT}^O Q_X^O Q_R Q_{JT}$ by fixing Q_X^A, Q_X^O and Q_R obtained from AFM-A OO phase (green curve) and FM CO phase (Magenta curve) at 0% strain (a=3.76Å).

Table 11.3 | Extended Version of Table 7.1 in the main manuscript. Amplitude of distortion modes of $CaFeO_3$ thin film under 0%(=3.76Å) and 4% (=3.91Å) in CO and OO phases, coupling parameters, energy gains ΔE^i_{JT} related to the condensation of Q_{JT} mode, and the energy cost related to AFM-A magnetic order. Calculations were executed in FM for the CO-phase and AFM-A for the OO-phases. The units of the coupling parameters are (meV/(Åfu)), where d stands for the dimension of the term the parameters is associated to.

Amplitudes (Å)	Q_{JT}	Q_B	Q_M	Q_R	Q_X	Q^A_X	Q^O_X
a = 3.76Å-CO	0.007	0.137	0.788	1.111	0.440	0.413	-0.149
a = 3.76Å-OO	0.256	0.000	0.717	1.194	0.457	0.371	-0.270
a = 3.91Å-OO	0.400	0.000	0.676	1.309	0.552	0.407	-0.374
Parameters (meV/(Åfu))	α_{JT}	λ_{MJT}	λ_{RJT}	γ_{RXJT}	γ^A_{RXJT}	γ^O_{RXJT}	
a = 3.76Å-CO	102.4	-183.0	-375.8	7.2	-131.5	-389.2	
a = 3.76Å-OO	66.7	-181.1	-401.2	-113.0	-129.7	-372.5	
a = 3.91Å-OO	-651.7	-69.9	-276.3	-107.1	-106.5	-280.0	
Energies (meV/fu)	ΔE^1_{JT}	ΔE^2_{JT}	ΔE^3_{JT}	ΔE_{JT}	ΔE_{AFMA}		
a = 3.76Å-CO	6.7	-37.8	-0.9	-32.0	62.3		
a = 3.76Å-OO	4.4	-43.6	-15.8	-55.0	74.5		
a = 3.91Å-OO	-104.3	-80.9	-31.0	-216.2	49.3		

12 | Supplementary Materials: Modulation tilt control engineered metal-insulator transitions in perovskites nickelates for room temperature optical switching

Zhaoliang Liao[1], *Nicolas* Gauquelin[2], *Robert* J. Green[345], *Knut* Müller-Caspary[2], *Ivan* Lobato[2], *Lin* Li[1], *Sandra* Van Aert[2], *Johan* Verbeeck[2], *Mark* Huijben[1], *Mathieu* N. Grisolia[6], *Victor* Rouco[6], *Ralph* El Hage[6], *Javier* E. Villegas[6], *Alain* Mercy[7], *Manuel* Bibes[6], *Philippe* Ghosez[7], *George* A. Sawatzky[34], *Guus* Rijnders[1], and *Gertjan* Koster[1]

[1]MESA Institute for Nanotechnology, University of Twente, 7500 AE Enschede, The Netherlands [2]Electron Microscopy for Materials Science (EMAT),University of Antwerp, 2020 Antwerp, Belgium [3]Quantum Matter Institute, University of British Columbia, Vancouver, V6T 1Z4, Canada [4]Department of Physicsand Astronomy, University of British Columbia, Vancouver, V6T 1Z4, Canada [5]Department of Physics and Engineering Physics, University of Saskatchewan,Saskatoon, S7N 5E2, Canada [6]Unité Mixte de Physique CNRS/Thales, Université Paris-Saclay, 91767 Palaiseau, France [7]Theoretical Materials Physics,Quantum Materials Center (Q-MAT), Complex and Entangled Systems from Atoms to Materials (CESAM), Université de Liège, B-4000 Liège, Belgium

12.1 Supplementary Note 1. Growth of the samples

The atomic flat $NdGaO_3(110)$ (NGO) substrates were treated by the etching of modified HF buffer solution and annealing at 1050 ° C for 4 hour (1). All the materials of $SmNiO_3$(SNO), $NdNiO_3$(NNO), $LaNiO_3$(LNO), $LaFeO_3$(LFO) and $LaCrO_3$(LCO) mentioned in the main text were deposited using pulsed laser deposition (PLD) technique at a laserfluence of $2\frac{J}{cm^2}$. During the growth, the temperature was maintained at 600 °C and oxygen pressure was 0.3 *mbar*. In-situ reflection high-energy electron diffraction (RHEED) was used to moni-

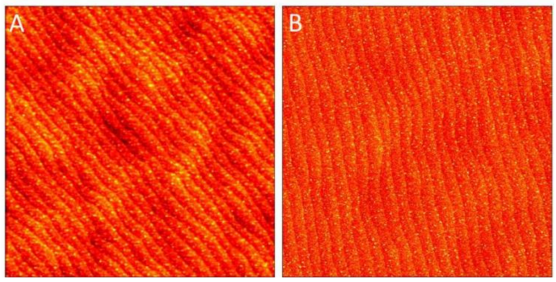

Figure 12.1 | Surface morphology of (A) $(LFO_1/SNO_4)_{10}$ and (B) $(LFO_1/SNO_{10})_4$ superlattices by AFM. The size of the imaged area is 10x10 μm^2.

tor the growthand confirmed a layer by layer growth fashion. After the growth, the samples were cooled down at 200 *mbar* at a cooling rate of 25 $\frac{^\circ C}{min}$. For $(LFO_1/SNO_n)_m$ and $(LCO_1/SNO_n)_m$ superlattice growth, four unit cells (uc) of LFO and LCO layers were first deposited on NGO respectively and subsequent the superlattices were grown. For superlattices growth, it started from SNO layers. Since the LNO films with thickness more than about 3 unit cell (uc) are metallic, the $(LNO_1/SNO_n)_m$ superlattices were directly grown on NGO substrates. The surface morphologies of the films were characterized by atomic force microscopy (AFM). Figure 12.1A and 12.1B show respectively the AFM images of $(LFO_1/SNO_4)_{10}$ and $(LFO_1/SNO_{10})_4$ superlattices grown on NGO (110) substrates which confirm atomic flat surfaces with clearly visible terraces.

12.2 Supplementary Note 2. Structure characterization of nickelate superlattices

The lattice structures of the nickelate superlattices were characterized by X-ray diffraction (XRD) using PANalytical-X'Pert materials research diffractometer (MRD) at high resolution mode. Figure 12.2 presents the X-ray diffraction θ-2θ scan of LFO_1-SNO_4 superlattice which shows satellite peaks originating from the superlattice structure. The superlattice peaks (SL0, SL+1, SL-1) reveal a superlattice period of 1.92 nm, fully consistent with the designed period controlled during growth by RHEED intensity oscillation. The presence of Pendellosung fringes further confirms the smoothness of the surface and the high quality ordering of the superlattice. The high structural quality of a bare 30 uc SNO film (SNO_{30}) is also indicated by XRD in Fig. 12.2A.

The lattice structures of LFO_1-SNO_n superlattices and SNO films have been characterized by high resolution X-ray reciprocal space mapping (RSM). Figure 12.2B and 12.2C show respectively the RSMs of the (420), (240), (332) and (33-2) reflections of SNO_{30} film and LFO_1-SNO_4 superlattice, which both indicate orthorhombic structures. Note that upon conversion of this (110)-oriented orthorhombic structure into a pseudocubic unit cell, a monoclinic tilt angle α appears. The out-of-plane lattice parameter c and monoclinic tilt angle α of SLs in pseudocubic unit cell exhibit a gradual change with increasing SNO thickness

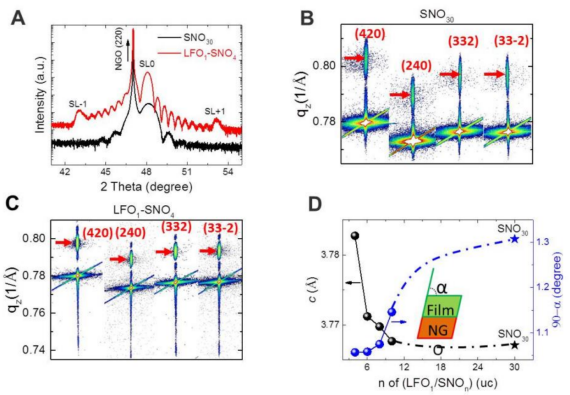

Figure 12.2 | (A) X-ray diffraction θ-2θ scan of SNO_{30}film and LFO_1-SNO_4 superlattice. (B) Reciprocal space mapping of the (420), (240), (332) and (33-2) reflections of (B) SNO_{30} film and (C) LFO_1-SNO_4 superlattice. The peaks are noted in orthorhombic indices. (D) Lattice parameters of LFO_1-SNO_n superlattice (sphere dots) as a function of SNO layer thickness and SNO_{30} film (star symbol).

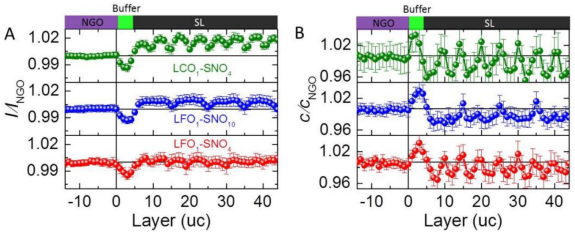

Figure 12.3 | (A) Normalized HAADF-STEM intensity (I/I_{NGO}) profiles and (B) normalized lattice constant (c/c_{NGO}) profiles for three superlattices: $(LFO_1/SNO_4)_{10}$ (red), $(LFO_1/SNO_{10})_4$ (blue) and $(LCO_1/LFO_4)_{10}$ (green).

n. As shown in Fig. 12.2D, c gradually decays to that of bulk SNO film value and $\frac{\pi}{2} - \alpha$ gradually increases to that of bulk SNO film, suggesting reduced structural distortion in SLs when the SNO layer is very thin and the impact of the LFO is strong.

12.3 Supplementary Note 3. Chemical contrast across the nickelate superlattices

All scanning transmission electron microscopy (STEM) images were processed as follow: 20 images were acquired with a beam current of 40 pA and a fast acquisition time of 0.1 μs/pixel. Each image resolution was 4096*4096 pixels. These images were then aligned and drift corrected as described in Ref. [217]. From the corrected images, the StatSTEM software was used to measure the position coordinates of each atomic column using statistical parameter estimation theory ([218]). All subsequent parameters (tilt angles, intensity profiles, c lattice parameter, strain, etc.) were extracted using the ImageEval software ([219]).

The limited contrast between LFO and SNO in high angle annular dark field (HAADF) STEM images is due to the high similarity of their atomic number for Sm (62), Nd (60) and La (57) on the A-sites, as well as Ni (28) and Fe (26) on the B-sites. The intensity of

a STEM image depends on the atomic number (Z) and a larger Z will give rise to a higher intensity. Therefore, there should be still intensity contrast although it is small and may be too small to be resolved by eye directly from a HAADF-STEM image. Figure 12.3A plots the STEM intensity profiles for three different samples of $(LFO_1/SNO_4)_{10}$, $(LFO_1/SNO_{10})_4$ and $(LCO_1/LFO_4)_{10}$ superlattices. The intensities are calculated from their HAADF images with zone axis along [1-10] and the intensities are normalized to the intensity of the NGO substrates. The intensity contrast indeed is very low. For example, the intensity of LFO from buffered region is only about 2% lower than that of the NGO substrate. However, the contrast can be still resolved in intensity-profile where the valley positions indicate the LFO layers and peak positions suggest the center of the SNO layers. A periodic modulation of the intensity can be observed for all three $(LFO_1/SNO_4)_{10}$, $(LFO_1/SNO_{10})_4$ and $(LCO_1/LFO_4)_{10}$ superlattices, confirming the superlattice structures.

The chemical contrast can also be reflected from the profile of out-of-plane lattice parameter (c). Since the LFO or LCO will have larger lattice constant than NGO or SNO, peak positions can then suggest us the location of the LFO or LCO layers. As shown in Fig. 12.3B, a larger *c* lattice parameter is observed in the buffer LFO or LCO regions. Within the superlattice area, a periodic modulation of *c* axis length is observed with larger (smaller) values in LFO (SNO) layers. Due to interfacial octahedral coupling effect, there are mutual geometry constraint of octahedral tilt of SNO and LFO. The LFO will reduce the tilt of SNO at the LFO/SNO interfaces, but the SNO reciprocally forces the tilt of LFO to be larger. This effect will make the tilts of LFO within the superlattice region larger than that of the first 4 uc LFO buffer. As a result, the *c* of LFO within superlattice is also smaller than the LFO buffer. In contrast, the SNO will have larger *c* near LFO/SNO interfaces and smaller *c* in the central part of SNO (see red and blue curves in Fig. 12.3B). Similar scenario occurs for $(LCO_1/SNO_4)_{10}$ superlattice (see green curve in Fig. 12.3B).

12.4 Supplementary Note 4. Electron energy loss spectroscopy (EELS) maps

The chemical contrast across the nickelate superlattice has also been characterized by electron energy loss spectroscopy (EELS) mapping. Figure 12.4 shows the EELS mapping of $(LFO_1/SNO_4)_{10}$ superlattice. The first panel is the simultaneously acquired annular dark field (ADF) image, indicating consistent atomic ordering across the superlattice. The good quality of the superlattice and atomic sharpness of the interfaces within the superlattice is suggested from the atomic resolved EELS mapping of Sm $M_{4,5}$, La $M_{4,5}$, Fe $L_{2,3}$, Ni $L_{2,3}$. EELS mapping shows a periodic stacking of 4 uc SNO and 1 uc LFO. There is slight diffusion of La at the LFO/SNO interface. The LFO layer always consists of one FeO_2 layer followed by a LaO layer. This indicates that the layer stacking at the SNO_4-LFO_1-SNO_4 interfaces has the following sequence: NiO_2-SmO-FeO_2-LaO-NiO_2-SmO.

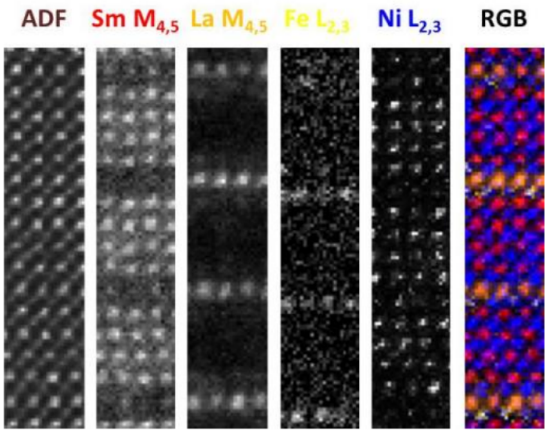

Figure 12.4 | Atomically resolved EELS mapping of Sm $M_{4,5}$, La $M_{4,5}$, Fe $L_{2,3}$, Ni $L_{2,3}$ at the $(LFO_1/SNO_4)_{10}$ superlattices. The first panel is the simultaneously acquired annular dark field (ADF) image. For RGB composite at last panel, the following color was used: Red: Sm; Orange: La; Yellow: Fe; Blue: Ni.

12.5 Supplementary Note 5. Estimation of lattice parameters profiles

Using statistical parameter estimation theory, atomic column positions (X,Y) in scanning transmission electron microscopy images can be precisely determined ([218, 220–222]) and thus detailed lattice structure parameters can be quantified statistically. To quantify the layer-position dependent octahedral tilt distortion, inversed annular bright field STEM (ABF-STEM) images which enable us to resolve the oxygen sites are used while for the A-site displacement quantification, HAADF images which have better contrast for heavier elements are chosen. Figure 12.5A shows a 2D mapping of the angle ϕ for a $(LFO_1/SNO_{10})_4$ superlattice. The definition of the angle is shown in the inset of Fig. 12.5A. The angle ϕ is the angle between three successive A-sites in the same row in (1-10) plane. To reflect the rumpling feature of A-sites we define ϕ_{A2} as $\angle A_1A_2A_3$-π while ϕ_{A3} as π - $\angle A_2A_3A_4$, thus we will have an alternated sign of ϕ (...+-+-+-...). Figure 12.5A shows a 2D mapping of the signed ϕ of $(LFO_1/SNO_{10})_4$sample from a HAADF image. The mapping of ϕ is overlaid on the HAADF image. A checkboard pattern can be seen in the signed ϕ mapping due to the alternated sign of the ϕ. We can also use the unsigned ϕ by taking the absolute value of this angle and obtain a mapping of unsigned ϕ as shown in Fig. 12.5B. Figure 12.5C also shows a 2D mapping of unsigned ϕ for $(LFO_1/SNO_4)_{10}$ superlattice. With these 2D maps, we can average the unsigned ϕ in the same layer and then obtain the layer-position dependent mean ϕ together with its standard deviation across the samples presented in Fig 8.3D of the main text.

The out-of-plane lattice parameter (c) profile is calculated from the 2D mapping of c. The definition of the c-axis is shown in inset of Fig. 12.5D, which is the lattice spacing between two nearest neighboring AO planes. An example of the 2D mapping of c of

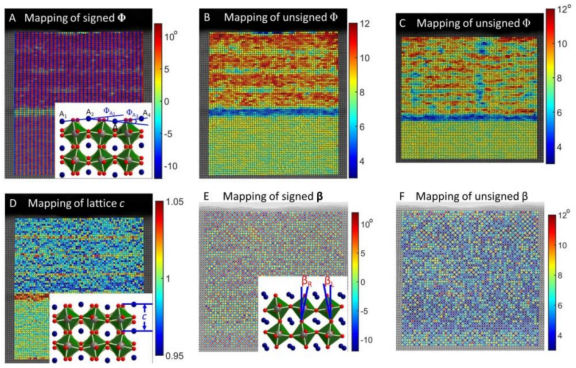

Figure 12.5 | 2D mapping of (A) signed and (B) unsigned anti-polar A-site motion (ϕ) in $(LFO_1/SNO_{10})_4$superlattice. (C) 2D mapping of unsigned ϕ angle in $(LFO_1/SNO_4)_{10}$ superlattice. (D) 2D mapping of out-of-plane lattice parameter c in $(LFO_1/SNO_{10})_4$ superlattice. The c is normalized to the lattice c of NGO substrate. 2D mapping of (E) signed β and (F) unsigned β angle in $(LFO_1/SNO_4)_{10}$ superlattice. For all mappings, each color pixel represents a local angle at a specific local A-site (A)-(C), local lattice parameter c at a specific single unit cell (D) or local octahedra tilt angle β at a local specific BO_6 octahedron (E)-(F). The 2D mappings are overlaid on HAADF images or ABF images from which corresponding lattice structure parameters are calculated

$(LFO_1/SNO_{10})_4$ superlattice is shown in Fig. 12.5D. Here, the c is normalized to the substrate NGO c value. Similar to the calculation of ϕ-profile, we can also average the c in each layer and then obtain the layer position dependent mean c together with its standard deviation presented in Fig. 8.3F of the main text.

While the profile of octahedral tilt angle β around the [001] axes is determined from the 2D mapping of β from ABF images. Figure 12.5E shows a 2D mapping of the signed β angle of $(LFO_1/SNO_4)_{10}$ superlattice. The definition of β is shown in inset of Fig. 12.5E. The β of left tilted octahedron is defined as negative value and right tilted octahedron as positive value. Taking the absolute value of the β, the signed β mapping is then converted into unsigned β mapping as shown in Fig. 12.5F. By averaging the unsigned β in the same layer, the layer-position dependent mean β together with its standard deviation across the samples presented in Fig 8.3E of the main text is obtained.

12.6 Supplementary Note 6. Phase diagram of $(LaFeO_3)_1$-$(SmNiO_3)_n$ superlattices

The thickness (n) of SNO within LFO_1-SNO_n SLs effectively controls the transition temperatures. By plotting the MIT temperature (T_{MIT}) and Néel temperature (T_N) as a function of SNO thickness (n), a phase diagram is constructed and shown in Fig. 12.6. The T_{MIT} monotonically increases the increasing n. The phase diagram is similar to bulk phase diagram where the tolerance factor is used as control parameter. For superlattices with a relatively low T_{MIT} ($< \approx 200$ K), their T_N is coincident with T_{MIT}. For superlattices with T_{MIT} larger than ≈ 200 K, the T_N and T_{MIT} are decoupled and show an increase in temperature differ-

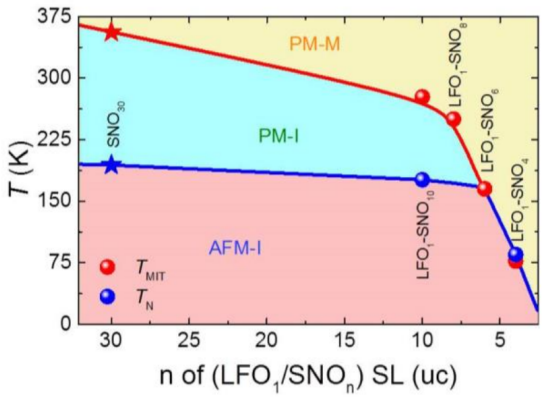

Figure 12.6 | Controlled transition temperature (T_{MIT}, T_N) by changing the thickness of the SNO layers in LFO_1-SNO_n superlattices.

ence with increasing T_{MIT}.

12.7 Supplementary Note 7. Metal-insulator transition in $NdNiO_3$-$SmNiO_3$ superlattices

In order to realize room temperature oxide electronics for practical application, a proper tilt control layer is explored to induce first order room temperature metal-insulator transition. Several tilt control layers have been tried, such as $LaFeO_3$, $LaCrO_3$, $LaNiO_3$, and $NdNiO_3$. Among those tilt control layers, the $NdNiO_3$ is found to be an ideal candidate to induce sharp first order room temperature metal-insulator transition. The tilting of octahedra can be controlled by constructing $((NdNiO_3)_m/(SmNiO_3)_n)_N$ superlattices on NGO (110) substrates which is denoted by NNO_m-SNO_n for simplify. The thickness of the superlattice is maintained to be $\approx$ 30 uc. Since the tilt of NNO is smaller, their combination will lead to an octahedral tilt in between NNO and SNO, thus tuning the T_{MIT} in between that of NNO and SNO depending on the ratio of n/m. As shown in Fig. 12.7, increasing the n/m from 2/2 to 3/1 gradually increases T_{MIT}. The first order metal insulator transition is obtained for NNO_2-SNO_2 and NNO_1-SNO_2 superlattices while it is more cross-over like in NNO_1-SNO_3 superlattice. Interestingly, near room temperature sharp metal-insulator (T_{MIT}= 293 K) is obtained for NNO_1-SNO_2 superlattice, providing great opportunity for fabricating room temperature electronics device.

12.8 Supplementary Note 8. Optical experiments in nickelate superlattices

Transport measurements under illumination were performed in a MONTANA cryostation with uncoated windows presenting 90% transmittance in the visible range. Two different configurations were used for characterizing the thermal response of the samples. In Setup-1, the layer was thermally connected to the cold finger of the cryostat. To do so we added

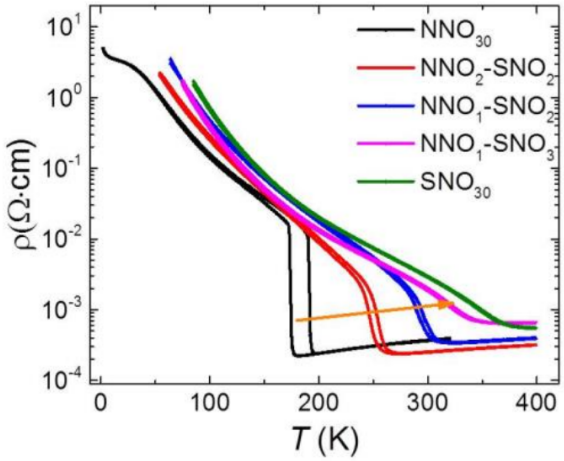

Figure 12.7 | Metal-insulator transition in NNO_m-SNO_n superlattices. The orange arrow indicates the tendency of the change of T_{MIT} with increasing n/m ratio.

thermal grease to the edges of the sample in such a way that the $NdGaO_3$ substrate was thermally connected to the sample holder. In Setup-2, an insulating layer was added between the sample and the sample holder such that there was no thermal contact between the layer and the cold finger of the cryostat. The sheet resistance was determined by biasing with a current of 10 μA. Figure 12.8 presents the results of these experiments on two superlattices: SNO_{10}-LFO_1 (panels a and b) and SNO_3-NNO_2 (panels c and d) with Setup-1 (panels a and c) and Setup-2 (panels b and d). In isothermal illumination (Setup-1, panels a and c), a very small resistance change is observed, showing a peak in temperature reminiscent of the metal-insulator transition. Note that for the SNO_3-NNO_2 sample, this peak is superimposed with a negative background reflecting a slight change of the overall sample resistance between the two consecutive temperature sweeps. In non-isothermal illumination (Setup-2, panels b and d), the relative resistance change is much stronger, up to a factor 2-3. Again, for both samples, its temperature dependence shows a peak related to the metal-insulator transition (for the SNO_{10}-LFO_1 sample this peak is superimposed with a decrease, reflecting the thermally activated transport behavior in the insulating state). The difference in the response between both setups strongly suggests that light illumination promotes sample heating, however with a specific wavelength dependence as we discuss in the manuscript.

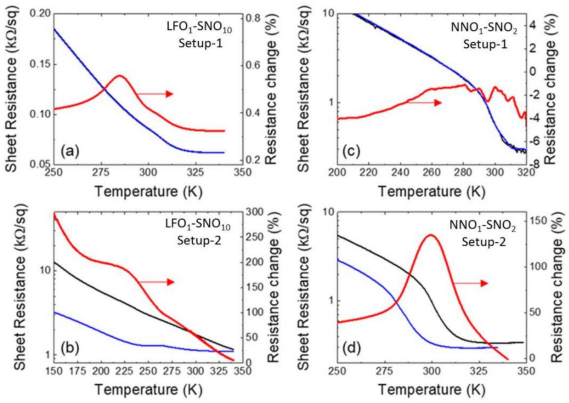

Figure 12.8 | Temperature dependence of the resistance for LFO_1-SNO_{10} and NNO_1-SNO_2 superlattices in two experimental configurations (Setup-1 and Setup-2).

13 | Supplementary Materials: Length-scales of interfacial coupling between metal-insulator phases in oxides

Claribel Domínguez[1], *Alexandru B.* Georgescu[2], *Bernat* Mundet[1,3], *Yajun* Zhang[4], *Jennifer* Fowlie[1], *Alain* Mercy[4], *Adrien* Waelchli[1], *Sara* Catalano[1], *Duncan T.L.* Alexander[3], *Philippe* Ghosez[4], *Antoine* Georges[1,2,5,6], *Andrew J.* Millis[2,7], *Marta* Gibert[8], and *Jean-Marc* Triscone[1]

[1]Department of Quantum Matter Physics, University of Geneva, Geneva, Switzerland [2]Center for Computational Quantum Physics, Flatiron Institute, New York, USA [3]Electron Spectrometry and Microscopy Laboratory (LSME), Institute of Physics (IPHYS), École Polytechnique Fédérale de Lausanne (EPFL), Lausanne, Switzerland [5]Collège de France, 11 place Marcelin Berthelot, 75005 Paris, France [6]Centre de Physique Théorique (CPHT), CNRS, Institut Polytechnique de Paris, France [7]Department of Physics, Columbia University, New York, USA [8]Physik-Institut, University of Zurich, Winterthurerstrasse 190, 8057 Zurich, Switzerland [4]Theoretical Materials Physics, Q-MAT, CESAM, University of Liège, B-4000 Liège, Belgium

13.1 Supplementary Note 1. X-ray reciprocal space mapping of $SmNiO_3/NdNiO_3$ superlattices

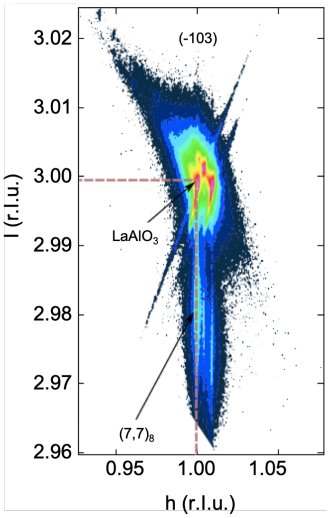

Figure 13.1 | **Supplementary Figure S1.** Representative X-ray diffraction reciprocal space map corresponding to a $(7,7)_8$ superlattice around the (-103) reflection, confirming coherent growth of the superlattices.

13.2 Supplementary Note 2. Transport measurements

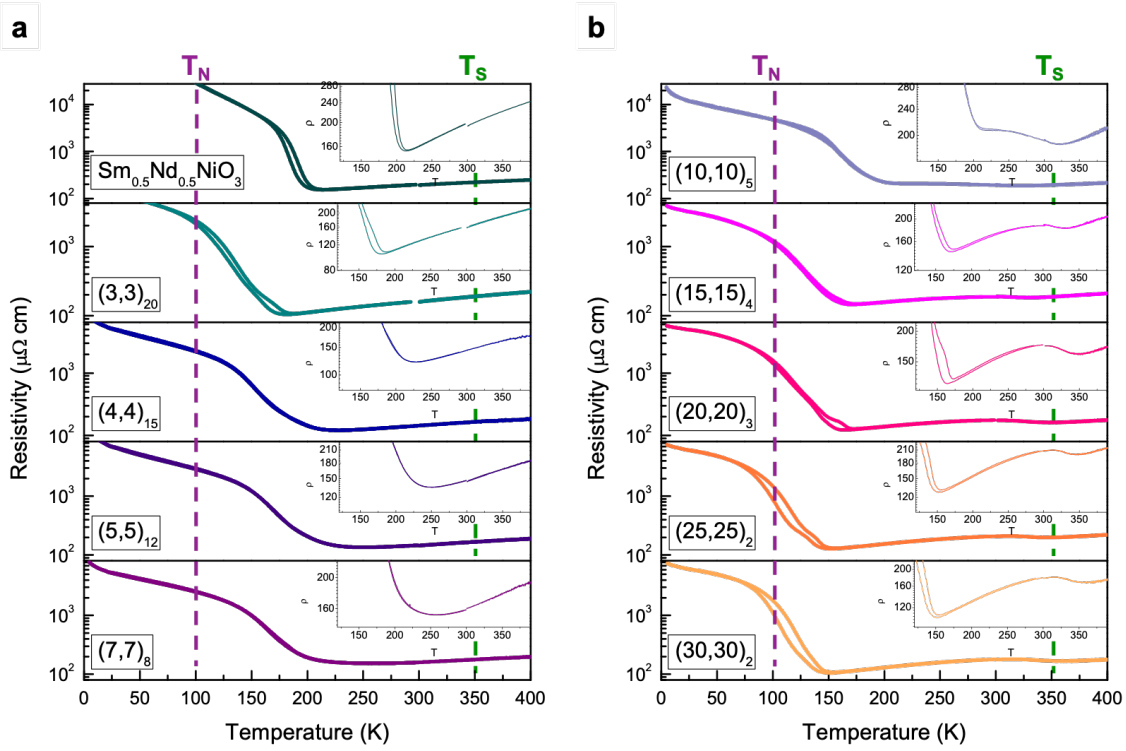

Figure 13.2 | **Supplementary Figure S2.** Resistivity vs temperature of all investigated $[001]_{pc}$-oriented $SmNiO_3/NdNiO_3$ superlattices with different periods. **a**, $Sm_{0.5}Nd_{0.5}NiO_3$ and short-wavelength superlattices displaying a single MIT. **b**, Large-wavelength superlattices showing two distinct MITs. The dashed lines indicate the MIT temperatures of the corresponding $NdNiO_3$ (T_N) and $SmNiO_3$ (T_S) films 10 nm thick, to be compared with the values obtained for the superlattices. **Inset**: Close ups of the transitions.

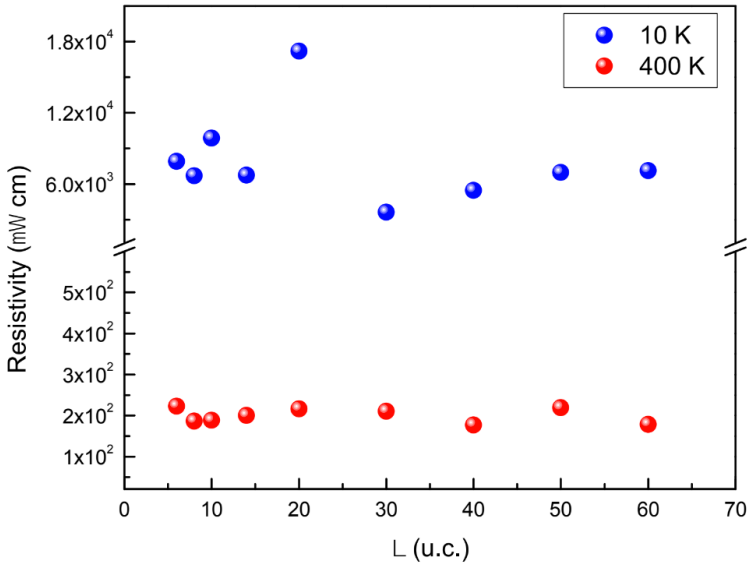

Figure 13.3 | **Supplementary Figure S3.** High and low temperature resistivities as a function of superlattice wavelength Λ.

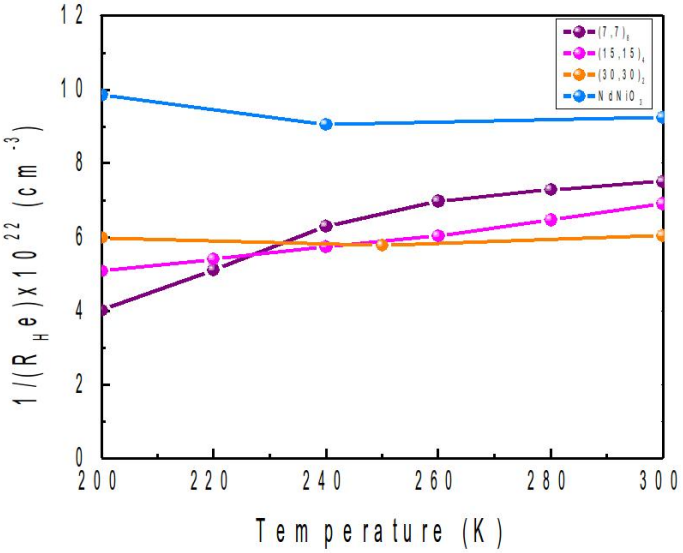

Figure 13.4 | **Supplementary Figure S4.** Inverse Hall coefficient measured as a function of temperature for a 30 u.c. thick (10nm) $NdNiO_3$ film and $(7,7)_8$, $(15,15)_4$ and $(30,30)_2$ superlattices.

13.3 Supplementary Note 3. Additional STEM-EELS analyses

Even though electron energy-loss spectroscopy (EELS) is not the best technique for quantifying the amount of oxygen vacancies (V_O) that are present in the $SmNiO_3/NdNiO_3$ superlattices, it can be used for mapping how these V_O (if any are present) are distributed through the lattice. This technique resembles X-ray absorption spectroscopy (XAS) but, instead of using polarized light, an electron probe is used as the excitation source thus providing spatial resolution as well.

Pursuant to this, we have analyzed the fine structure of the 0K edge at different positions in a $(5,5)_{10}$ superlattice, one of those displaying a single MIT, as shown in Fig.13.5a. Like in the XAS experiments performed in single crystal samples, the 0K edge is composed of a pre-peak located at 528.5 eV (orange arrow) and two main peaks centered at 535 eV and 543 eV[223]. The pre-peak arises due to excitation of electrons from the filled O 1s band into the empty O 2p states that are hybridized with the Ni 3d states. Accordingly, the spectral shape of this pre-peak is very sensitive to subtle changes in the Ni-O coordination, and therefore to the presence of V_O. As previously reported, an increase of Vo would lead to a lowering of the pre-peak intensity[223, 224].

Fig. 13.5b shows a simultaneously acquired high angle annular dark field (HAADF) image and La, Sm and Nd EELS compositional maps obtained from the $(5,5)_{12}$ superlattice. The EEL spectra shown in Fig. 13.5a were derived by lateral integration of the pixel-by-pixel EELS mapping data at different vertical positions in the superlattice, as indicated by the colored arrows in Fig. 13.5b. In particular, the positions indicated with black and green arrows correspond to the central area of either a $SmNiO_3$ or $NdNiO_3$ layer whereas the other two regions (green and blue arrows) relate to regions located close to their interface. The fact that no significant spectral changes are identified in the 0K edge pre-peak when comparing all the acquired EEL spectra confirms that the same concentration of V_O is present in both layers as well as at their interface.

In order to extend this analysis to all the interfaces belonging to this $(5,5)_{12}$ superlattice, we have mapped within the whole superlattice the intensity ratio between the main peak and the pre-peak of the 0K edge. This procedure has been done in order to minimize possible undesired effects related to modulations in the specimen thickness. The obtained values are plotted in the map shown in Fig. 13.5d. No significant color-wise changes are identified, thus confirming that if some V_O are present, they are homogeneously distributed within the whole superlattice. The increase of the signal observed in the substrate occurs since no 0K edge pre-peak is present in the $LaAlO_3$ substrate compound.

In Fig. 13.5d we also evaluate the spectral shape of the Ni L_2 peak at the same positions marked with colored arrows in Fig. 13.5b. The fine structure of this particular peak is very sensitive to subtle changes in the Ni valence, since it splits into two peaks when the Ni is reduced from Ni^{3+} to Ni^{2+}[224, 225]. The fact that no substantial spectral modifications are identified in the Ni L_2 peak between the EEL spectra acquired at different positions of the superlattice evidences that the Ni valence remains constant and, therefore, that no charge is transferred from one layer to the other at the interfaces.

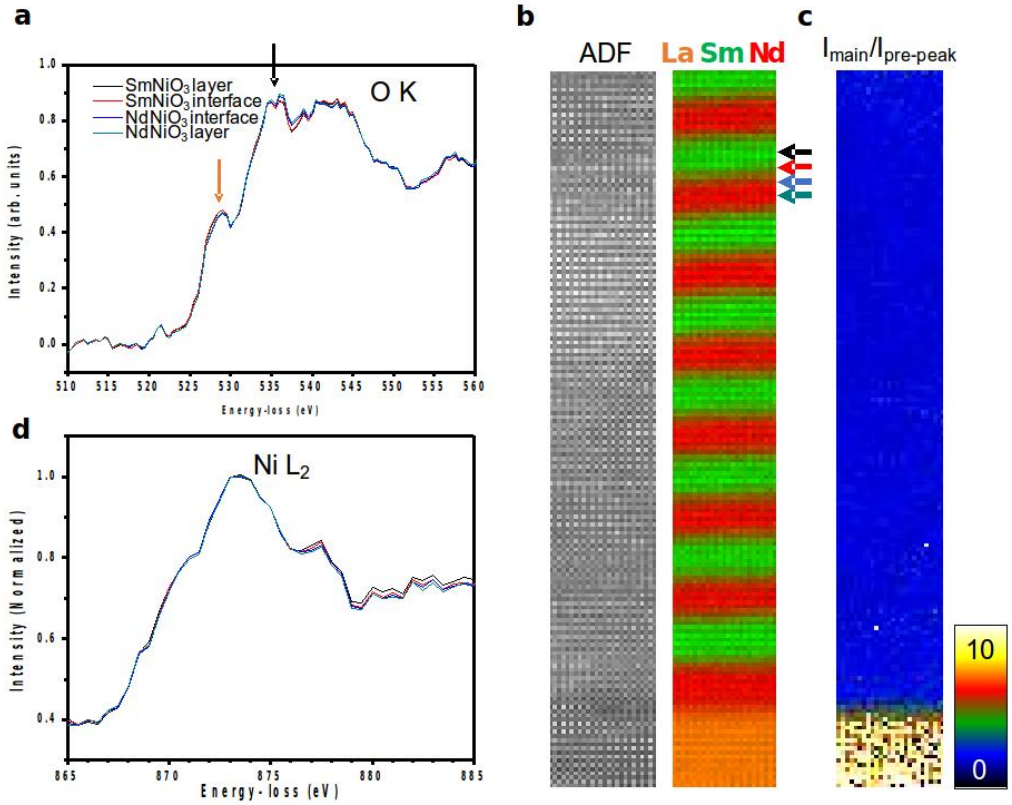

Figure 13.5 | **Supplementary Figure S5. a**, 0K edge EEL spectra obtained from the vertical positions of the $(5,5)_{12}$ superlattice indicated with colored arrows in b. The black and orange arrows respectively point to the main peak and pre-peak of the 0K edge. **b**, Simultaneously acquired ADF image and La/Sm/Nd EELS compositional map of the $(5,5)_{12}$ superlattice. The La (orange), Sm (green) and Nd (red) signals are obtained from the La M, Sm M and Nd M edges, respectively. **c**, Map showing the intensity ratio between the main peak and the pre-peak belonging to the 0K edge in the whole superlattice. **d**, Ni L_2 edge EEL spectra obtained from the crystal positions indicated with colored arrows in b.

13.4 Supplementary Note 4. Additional STEM

In order to confirm that all superlattices present a similar length coupling for the octahedral rotations at the $SmNiO_3/NdNiO_3$ interfaces, we have also characterized the structural properties of a superlattice with a larger wavelength than the critical value (Λ_c= 16 u.c.). In particular, we have chosen one with 12 u.c. repetitions per layer (Λ=24 u.c.). Fig. 13.6a shows the La (orange), Ni (blue), Nd (red) and Sm (green) EELS compositional maps obtained from this superlattice. As in the $(5,5)_{12}$ superlattice, the $SmNiO_3/NdNiO_3$ interfaces are atomically sharp and no cationic intermixing is identified in the layers. As described in the main text, from the atomic positions of the HAADF and contrast-inverted ABF images that are shown in Fig. 13.6b and 13.6d respectively, we have measured the evolution across the superlattice of both the amplitude of the antipolar motion and the Ni-O-Ni bond angle (ϕ). The corresponding depth-profiles are displayed in Fig. 13.6c and 13.6e. As in the $(5,5)_{12}$ superlattice, two different ΔZ and ϕ values are clearly identified, corresponding to either $NdNiO_3$ or $SmNiO_3$ layers. Besides, the system switches from one value to the other

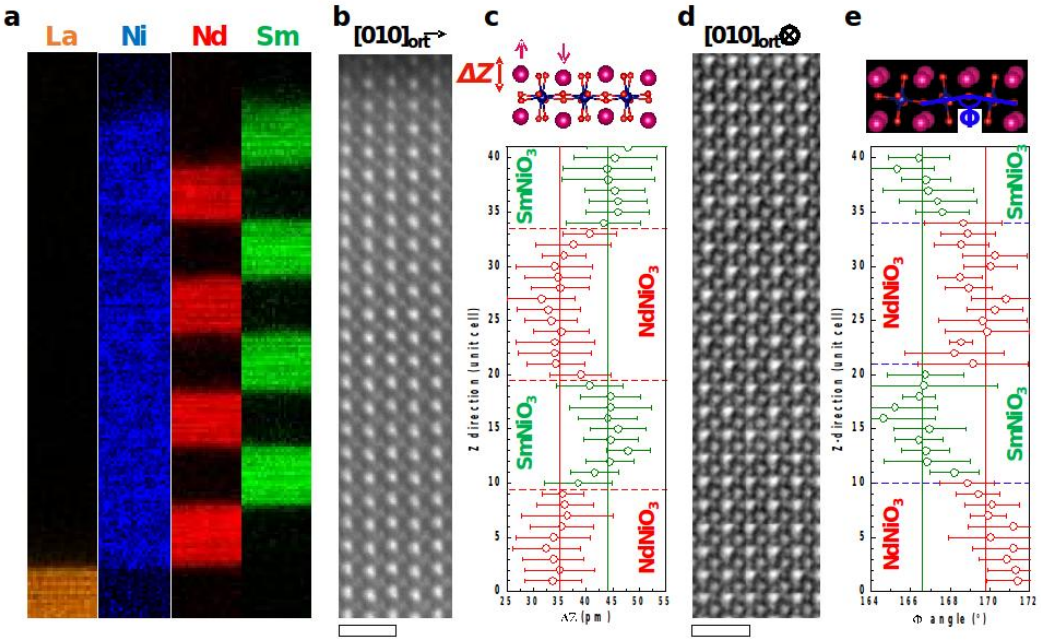

Figure 13.6 | **Supplementary Figure 6. a**, La (orange), Ni (blue), Nd (red) and Sm (green) EELS compositional maps acquired in a $(12,12)_4$ superlattice obtained from the La M, Ni L, Sm M and Nd M edges respectively. **b**, HAADF image showing a central area of the studied superlattice, which has been acquired along the $[100]_{pc}$ zone axis. **c**, Depth-profile of the measured antipolar motion amplitude (ΔZ). The top panel displays a sketch of the structure, the motion of the R cations (pink arrows) and the studied ΔZ. **d**, Contrast-inverted ABF image obtained from an equivalent area than the image shown in b acquired along the $[001]_{pc}$ zone axis. **e**, Depth-profile of the measured antipolar motion amplitude Ni-O-Ni bond angle (ϕ). The top panel displays a sketch of the structure and ϕ. The approximate position of the interfaces is indicated with dashed lines. The solid lines indicate the averaged ΔZ and ϕ values for either the $NdNiO_3$ (red) or $SmNiO_3$ (green) layers. Scale bars: 1nm.

one in approximately 1-2 u. c. at the interfaces, thus confirming the short length coupling of the octahedral tilts.

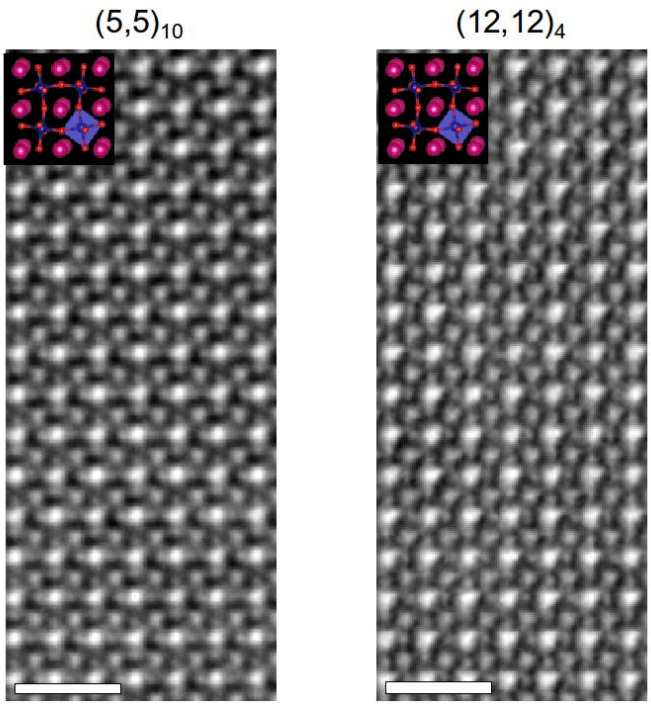

Figure 13.7 | **Supplementary Figure S7.** Amplified view of the contrast-inverted ABF images obtained from the (a) $(5,5)_{12}$ and $(12,12)_4$ superlattices. In the overlaid structural models, Nd/Sm, Ni and O atoms are represented with magenta, blue and red spheres respectively, scale bars: 1nm.

13.5 Supplementary Note 5. Structural considerations in the calculations

Both $SmNiO_3$ and $NdNiO_3$ are slightly distorted perovskite oxides. At higher temperatures both compounds are metallic and orthorhombic with $Pnma$ symmetry, and the rotations and tilts of oxygen octahedra are described by the $a^-a^-c^+$ pattern in Glazer notation. At lower temperatures, both compounds undergo a monoclinic distortion with $P2_1n$ symmetry, combining the same pattern of octahedral rotations and tilts with an additional breathing motion of the octahedra[25]. In the Table 13.1, we compare the lattice constants of the bulk $P2_1n$ phases, as reported experimentally and computed from DFT. We observe an excellent agreement, with only a systematic trend of the calculations to slightly underestimate the lattice constants (typically by less than 1%). It appears that $SmNiO_3$ has a much larger orthorhombic distortion ($b > a$) than $NdNiO_3$, features properly captured by the DFT + U calculations.

According to the information provided in the Supplementary Table 13.1, when growing $NdNiO_3$ and $SmNiO_3$ on top of $LaAlO_3$ (a_{pc} = 3.787 Å), one can expect that the epitaxial strain will not induce any strong preferential orientation for $NdNiO_3$, while it should favor the growth of $SmNiO_3$ with its c axis in-plane. Accordingly, the superlattices should preferentially grow with the same orientation. This is confirmed by the DFT calculations, showing

	$SmNiO_3$		$NdNiO_3$	
	Experimental[97]	DFT	Experimental[25]	DFT
a	5.327	5.258	5.386	5.370
b	5.437	5.430	5.382	5.353
c	7.565	7.500	7.607	7.565
$a/\sqrt{2}$	3.767	3.718	3.808	3.797
$b/\sqrt{2}$	3.845	3.840	3.806	3.785
$c/2$	3.783	3.750	3.803	3.783
ϵ_{zz}	+0.12	+0.53	-0.43	-0.33
ϵ_{xx}	-0.50	-0.25	-0.53	-0.56

Table 13.1 | **Supplementary Table 1.** Comparison of the experimental and theoretical (ferromagnetic configuration) lattice constants (in Å) of bulk $SmNiO_3$ and $NdNiO_3$ in their $P2_1n$ ground-state and related epitaxial strains (in %) on a $LaAlO_3$ substrate for a growth with c axis in-plane.

that the configuration with the c-axis in-plane is energetically favored with respect to the configuration with the c-axis out-of-plane. This is also corroborated experimentally by the STEM measurements. In order to reproduce an epitaxial strain state comparable to the experiment (see Supplementary Table 13.1), we considered in our calculations (that slightly underestimate lattice constants) a pseudo-cubic lattice constant of 3.77 Åfor $LaAlO_3$.

13.6 Supplementary Note 6. Energy of the phase boundary

In order to achieve better microscopic characterization of the phase boundary and related energy, E_{PB}, we performed additional DFT calculations. We considered $\Lambda = 6$, 10, 14 and 20 u.c. superlattices in three different cases: (i) breathing mode in both materials (as resulting from full atomic relaxation), (ii) breathing mode suppressed in $NdNiO_3$ but preserved in $SmNiO_3$ and (iii) breathing mode suppressed in both. The calculations were performed with ferromagnetic order for simplicity.

The results are summarized in Fig. 13.8 in which we quantify the charge disproportionation ΔN along the stack using, as a proxy, the difference in magnetic moments ΔM between unequal Ni sites in each layer. We observe that, with the breathing distortion present in both compounds, the charge disproportionation is large and rather constant along the whole stack, as assumed in our Landau model. Suppressing the breathing distortion in $NdNiO_3$, we see that ΔM propagates from $SmNiO_3$ within $NdNiO_3$ while decreasing from the interface according to a profile similar to that obtained in the Landau model in Fig. 9.4e.

From a comparison of the change of energy arising from the suppression of the breathing distortion in $NdNiO_3$ in the superlattices and in bulk, we can also estimate E_{PB}. For increasing Λ, E_{PB} quickly converges to a value of ≈20 meV per unit cell area. Layer-by layer contributions to E_{PB} are shown in green in Fig. 13.8, highlighting its local character. It is worth noticing, however, that the atomic configuration of the superlattice with the breathing mode suppressed in $NdNiO_3$ and preserved in $SmNiO_3$, which appears experimentally

at intermediate temperature, is not a metastable state in our DFT calculations at 0K. This means that there is no unique way to define this geometry and E_{PB} will depend on the convention arbitrarily chosen to do so. Using the same convention at all thicknesses allows us to demonstrate the existence of an energy cost located at the interface over a distance compatible with the bending of the order parameter but the absolute value of E_{PB} should be taken with care. This justifies why E_{PB} was taken as a free parameter of our Landau model. In addition, we note that for the same reason, DFT+U is likely to underestimate the disproportionation cost: as the metallic (0 disproportionation) structure is not metastable within DFT+U, and the energy landscape is that of a second-order phase transition[17], the first-order transition physics involving an energy barrier between the two states is not captured and the interfacial energy caused by going over this energy barrier is underestimated. This highlights the importance of not just energy minima, but of the local minima and energy landscape as well in the context of electronic structure methods.

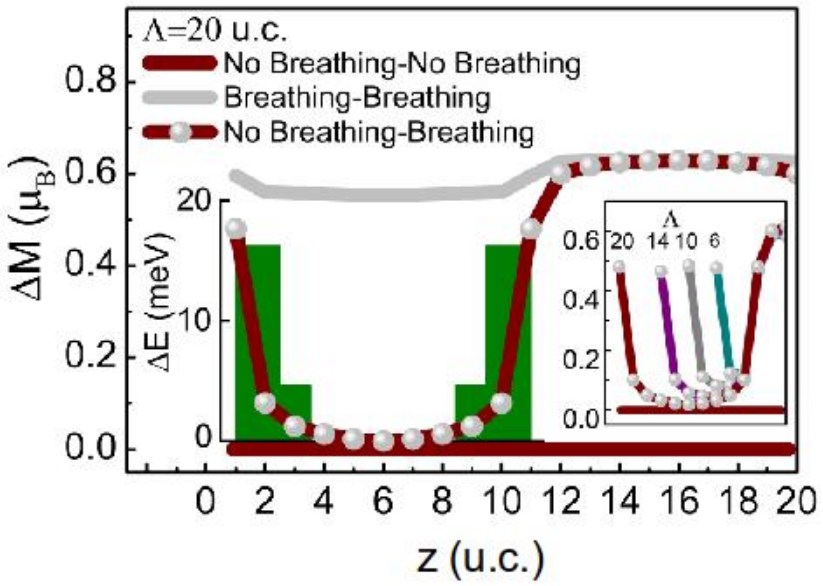

Figure 13.8 | **Supplementary Figure S8.** Z-evolution of the charge disproportionation as obtained from DFT + U calculations and quantified from the difference of magnetic moment (ΔM) at unequal Ni sites. The results are for Λ = 20 u.c. in three distinct cases: no breathing distortions in $SmNiO_3$ or $NdNiO_3$ (red), breathing distortion in both $SmNiO_3$ and $NdNiO_3$ (grey) and breathing distortion in $SmNiO_3$ but no breathing distortion in $NdNiO_3$ (red with grey balls). The layer-by-layer phase boundary energy is superimposed in green to the profile for Λ = 20 u.c. **Inset**: comparison of the charge disproportionation profile at distinct thicknesses Λ = 6, 10, 14 and 20 u.c.

As well as this microscopic approach to predicting the phase boundary energy, we can also estimate it by combining the information we have from the Landau theory and comparing to experiment. From the Landau theory we obtain that $\frac{K_N}{K_S} = 0.4$ and $\frac{E_{PB}}{K_N} = 4.8\times$pseudocubic unit cell length. At T=0K, the free energy difference is equal to the total energy difference between the metallic and insulating states, which we can obtain from first principles calculations, i.e. for $SmNiO_3$ for which we have an assumption about the asymptotic low-T

behavior of the free energy difference : $E_I^S - E_M^S = K_S \frac{(T_{Sat} - T_S)}{T_S}$, we can estimate $K_S \approx 10$ meV per 5 atom u.c. from the energy difference between the metallic and insulating state within DFT+U. From this and the ratios extracted from experiment, we obtain $E_{PB} \approx 100\ meV/a^2$, with a the pseudocubic lattice constant. Previous work within DFT+DMFT has estimated that the DFT+U energy difference between the metallic and insulating state is overestimated; using the DFT+DMFT energy difference of 5 meV per u.c we would obtain an estimate of 50 meV/a^2. While we did not make any assumptions about the low-T behaviour of $NdNiO_3$, it is worth mentioning that if we assume a linear dependence of the free energy difference between the metallic and insulating state down to T=0K, $E_I^N - E_M^N = K_N \frac{(T - T_N)}{T_N} = -K_N$, we would obtain $E_{PB} \approx 50\ meV/a^2$ using the DFT+U energy difference estimate and $E_{PB} \approx 25\ meV/a^2$ using the DFT+DMFT one. As $NdNiO_3$ is likely to have a similar asymptotic low T free energy behaviour to $SmNiO_3$, these numbers likely provide a lower bound.

Note that both our first principles calculations and fitting to the experiment yield rather similar values for E_{PB} of tens of meV.

13.7 Supplementary Note 7. Bulk Landau Theory

In order to study the transition in more detail and thereby justify the analytical approach in the main text, we also perform numerical calculations involving a full, layer dependent bulk Landau theory for the two component materials. The metal-insulator transition in the nickelates is characterized by a simultaneous electronic (N) and structural bond disproportionation (BD) from the high temperature metallic phase to the low temperature insulating phase. As one order parameter determines the other, without loss of generality, we select the electronic order parameter N to be the one determining the physical state of the system. As in the main text and previous work[23, 37, 127, 128] this is usually defined as the occupancy difference between the higher filling and the lower filling e_g frontier antibonding orbitals in a d-orbital only picture.

To model a superlattice of periodicity Λ we then define a total number of Λ points which we label by coordinate z, half of which corresponds to $NdNiO_3$ ($1 \leq z \leq \frac{\Lambda}{2}$), and half of which corresponds to $SmNiO_3$ ($\frac{\Lambda}{2} + 1 \leq z \leq \Lambda$). To each point z we then assign a polynomial form of the free energy. We pick a standard choice for a first-order free energy landscape for each point:

$$E_{Bulk}(z, N, T) = P(N) = \frac{A(z)N^6}{6} + \frac{B(z)N^4}{4} + \frac{C(z,T)N^2}{2} \tag{13.1}$$

As in the main text, this theory has a free energy of 0 for the metallic phase, independent of temperature at $N(z) = 0$ corresponding to the metallic phase. For the bulk insulating phase, we then use $N(z) = 1.2$ for the $NdNiO_3$ layers and $N(z) = 1.4$ electrons for the $SmNiO_3$ insulating state, consistent with previous DFT+DMFT work[23, 37, 127, 128], however noting that these values are not relevant in themselves as we will show later. For

each material we then determine the coefficients at the metal-insulator transition temperature of the respective material. We set $A(z) = 1$ for all z (which sets an overall normalization factor for the Landau theory) then determine $B(z)$ and $C(z, T_{MIT})$ from $E(z, N_I, T_{MIT}) = 0$ and $\frac{\partial E_{Bulk}(z,N_I,T_{MIT})}{\partial N} = 0$. In order to then tune the free energy to obtain a metal-insulator transition we vary the coefficient $C(T)$ with temperature as: $C(z,T) = C(z,T_{MIT})\left(1 + \alpha(z)\frac{T-T_{MIT}}{T_{MIT}}\right)$ with $0 \leq \alpha(z) \leq 1$ and $\alpha(z)$ taking one of two values we determine α_{NdNiO_3} or α_{SmNiO_3}. We note that this is equivalent to changing the susceptibility of the metallic phase as $C(z,T) = \chi_M^{-1}$, while keeping $C(z,T)$ in order to ensure the first-order nature of the metal-insulator transition.

To these we add a discretized gradient term that couples nearest neighbor layers by penalizing changes in the order parameter from one layer to the other:

$$E_{gradient} = \sum_z \frac{\xi^2}{2}(N(z) - N(z-1))^2 \tag{13.2}$$

where z are the integer values determining the layer number.

The total free energy is then:

$$E_{total} = \sum_z E_{Bulk}(z,N,T) + \sum_z \frac{\xi^2}{2}(N(z) - N(z-1))^2 \tag{13.3}$$

As the coefficients for the $E(z,N,T)$ are the same throughout each material, but different from one to the next, in the $\xi \to 0$ limit, we obtain a sum of two bulk energies as in the main text. For $\xi \neq 0$, an energy cost will appear from a combination of $N(z)$ not being at the optimum bulk values, and from the order parameter 'bending' across the interface, leading to a phase boundary energy cost. If this phase boundary is restricted in length compared to $\frac{\Lambda}{2}$, then this energy cost will be constant.

We now have effectively three adjustable parameters, α_{NdNiO_3}, α_{SmNiO_3} and ξ. Similar to the simplified theory in the main text, the ratio of the two α can be obtained from the joint transition temperature at the bifurcation point T_J(similar to the K constants in the main text), while ξ can be obtained from the critical wavelength of the bifurcation point Λ_c. Note that one can adjust the N_I for the insulating states of the materials as well, however as long as the α and ξ are determined as described above after setting the value of the N_I, the resulting transition temperatures will be the same (confirming that the main physics is in fact captured by the simplified model in the main text).

The final step is to initialize and solve the calculation for the three physically relevant configurations. To obtain a full metallic solution, we initialize the calculation with $N(z) = 0$ for all z, for a mixed $NdNiO_3$ metallic, $SmNiO_3$ insulating solution we initialize $N(z) = 0$ for $1 \leq z \leq \frac{\Lambda}{2}$ and $N(z) = N_I^{SNO}$ for $\frac{\Lambda}{2} + 1 \leq z \leq \Lambda$ and for the full insulating solution we initialize $N(z) = N_I$ with the N_I corresponding to the respective material. Then we minimize over the total free energy and depending on which initial state we started in we obtain a different minimum corresponding to one of the three possible solutions. Similar to the

simplified theory, we can additionally impose a saturation temperature for $C(z,t)$ for the $SmNiO_3$ layers:$C(z,T) = C(z,T_{MIT})\left(1+\alpha(z)\frac{T_{Saturation}-T_{MIT}}{T_{MIT}}\right)$ for $T < T_{Saturation}$.

13.8 Supplementary Note 8. About Landau Model

We find minima of the polynomial Landau theory numerically using a standard leapfrog scheme which is iterated to self-consistency. Calculations are initialized using all possible combinations of the solutions for bulk phases, thereby producing all insulating, all metallic and mixed solutions[226]

Bibliography

[1] M. Graef and E. McHenry, *Structure of materials: an introduction to crystallography, diffraction and symmetry* (Cambridge University Press, New York, NY, USA, 2012), 2nd ed., ISBN 9781107005877, URL https://doi.org/10.1017/CBO9781139051637.

[2] P. HAGENMULLER, in *Inorganic Solid Fluorides*, edited by P. Hagenmuller (Academic Press, 1985), p. xv, ISBN 978-0-12-313370-0, URL http://www.sciencedirect.com/science/article/pii/B9780123133700500050.

[3] D. I. Khomskii, *Transition Metal Coumpounds* (Cambridge University Press, 2014), ISBN 9781107020177, URL https://doi.org/10.1107/S2052520616003097.

[4] M. L. Medarde, Journal of Physics: Condensed Matter 9, 1679 (1997), ISSN 0953-8984, URL http://stacks.iop.org/0953-8984/9/i=8/a=003.

[5] G. Catalan, Phase Transitions 81, 729 (2008), ISSN 0141-1594, URL http://dx.doi.org/10.1080/01411590801992463.

[6] S. Catalano, M. Gibert, V. Bisogni, O. E. Peil, F. He, R. Sutarto, M. Viret, P. Zubko, R. Scherwitzl, A. Georges, et al., APL Materials 2, 116110 (2014), ISSN 2166-532X, URL http://scitation.aip.org/content/aip/journal/aplmater/2/11/10.1063/1.4902138.

[7] S. Middey, J. Chakhalian, P. Mahadevan, J. W. Freeland, A. J. Millis, and D. D. Sarma, Annual Review of Materials Research 46, 305 (2016), URL http://dx.doi.org/10.1146/annurev-matsci-070115-032057.

[8] G. Demazeau, A. Marbeuf, M. Pouchard, and P. Hagenmuller, Journal of Solid State Chemistry 3, 582 (1971), ISSN 0022-4596, URL http://www.sciencedirect.com/science/article/pii/0022459671901058.

[9] H. Y. Hwang, Y. Iwasa, M. Kawasaki, B. Keimer, N. Nagaosa, and Y. Tokura, Nature Materials 11, 103 (2012), URL https://doi.org/10.1038/nmat3223.

[10] M. Bibes, J. E. Villegas, and A. Barthélémy, Advances in Physics 60, 5 (2011), URL https://doi.org/10.1080/00018732.2010.534865.

[11] J. Mannhart and D. G. Schlom, Science 327, 1607 (2010), ISSN 0036-8075, https://science.sciencemag.org/content/327/5973/1607.full.pdf, URL https://science.sciencemag.org/content/327/5973/1607.

[12] V. M. Goldschmidt, Naturwissenschaften 14, 477 (1926), ISSN 1432-1904, URL https://doi.org/10.1007/BF01507527.

[13] M. Medarde, J. Mesot, P. Lacorre, S. Rosenkranz, P. Fischer, and K. Gobrecht, Physical Review B 52, 9248 (1995), URL http://link.aps.org/doi/10.1103/PhysRevB.52.9248.

[14] M. Medarde, M. T. Fernández-Díaz, and P. Lacorre, Physical Review B 78, 212101 (2008), URL http://link.aps.org/doi/10.1103/PhysRevB.78.212101.

[15] J. L. Garcia-Munoz, M. A. G. Aranda, J. A. Alonso, and M. J. Martinez-Lope, Phys. Rev. B 79, 134432 (2009), URL https://link.aps.org/doi/10.1103/PhysRevB.79.134432.

[16] A. Hampel, P. Liu, C. Franchini, and C. Ederer, npj Quantum Materials 4 (2019), URL https://doi.org/10.1038/s41535-019-0145-4.

[17] A. Mercy, J. Bieder, J. Iniguez, and P. Ghosez, Nature Communications (2017), URL https://www.nature.com/articles/s41467-017-01811-x.

[18] J. Varignon, M. Bibes, and A. Zunger, Phys. Rev. B 100, 035119 (2019), URL https://link.aps.org/doi/10.1103/PhysRevB.100.035119.

[19] U. Staub, G. I. Meijer, F. Fauth, R. Allenspach, J. G. Bednorz, J. Karpinski, S. M. Kazakov, L. Paolasini, and F. d'Acapito, Physical Review Letters 88, 126402 (2002), URL http://link.aps.org/doi/10.1103/PhysRevLett.88.126402.

[20] Y. Quan, V. Pardo, and W. E. Pickett, Phys. Rev. Lett. 109, 216401 (2012), URL https://link.aps.org/doi/10.1103/PhysRevLett.109.216401.

[21] H. Park, A. J. Millis, and C. A. Marianetti, Physical Review Letters 109, 156402 (2012), URL http://link.aps.org/doi/10.1103/PhysRevLett.109.156402.

[22] A. Hampel and C. Ederer, Phys. Rev. B 96, 165130 (2017), URL https://link.aps.org/doi/10.1103/PhysRevB.96.165130.

[23] O. E. Peil, A. Hampel, C. Ederer, and A. Georges, Phys. Rev. B 99, 245127 (2019), URL https://link.aps.org/doi/10.1103/PhysRevB.99.245127.

[24] J. Ruppen, J. Teyssier, I. Ardizzone, O. E. Peil, S. Catalano, M. Gibert, J.-M. Triscone, A. Georges, and D. van der Marel, Phys. Rev. B 96, 045120 (2017), URL https://link.aps.org/doi/10.1103/PhysRevB.96.045120.

[25] J. L. Garcia-Munoz, J. Rodriguez-Carvajal, P. Lacorre, and J. B. Torrance, Phys. Rev. B 46, 4414 (1992), URL https://link.aps.org/doi/10.1103/PhysRevB.46.4414.

[26] Y. Lu, D. Betto, K. Fürsich, H. Suzuki, H.-H. Kim, G. Cristiani, G. Logvenov, N. B. Brookes, E. Benckiser, M. W. Haverkort, et al., Phys. Rev. X 8, 031014 (2018), URL https://link.aps.org/doi/10.1103/PhysRevX.8.031014.

[27] S. Lee, R. Chen, and L. Balents, Physical Review Letters 106, 016405 (2011), URL http://link.aps.org/doi/10.1103/PhysRevLett.106.016405.

[28] V. Scagnoli, U. Staub, A. M. Mulders, M. Janousch, G. I. Meijer, G. Hammerl, J. M. Tonnerre, and N. Stojic, Phys. Rev. B 73, 100409 (2006), URL https://link.aps.org/doi/10.1103/PhysRevB.73.100409.

[29] G. Giovannetti, S. Kumar, D. Khomskii, S. Picozzi, and J. van den Brink, Physical Review Letters 103, 156401 (2009), URL http://link.aps.org/doi/10.1103/PhysRevLett.103.156401.

[30] D. J. Gawryluk, Y. M. Klein, T. Shang, D. Sheptyakov, L. Keller, N. Casati, P. Lacorre, M. T. Fernández-Díaz, J. Rodríguez-Carvajal, and M. Medarde, Phys. Rev. B 100, 205137 (2019), URL https://link.aps.org/doi/10.1103/PhysRevB.100.205137.

[31] K. Haule and G. Gheorghe, Scientific Reports 7, 2045 (2017), URL https://doi.org/10.1038/s41598-017-10374-2.

[32] M. Medarde, P. Lacorre, K. Conder, F. Fauth, and A. Furrer, Physical Review Letters 80, 2397 (1998), URL http://link.aps.org/doi/10.1103/PhysRevLett.80.2397.

[33] Z. Liao, N. Gauquelin, R. J. Green, K. Müller-Caspary, I. Lobato, L. Li, S. Van Aert, J. Verbeeck, M. Huijben, M. N. Grisolia, et al., Proceedings of the National Academy of Sciences 115, 9515 (2018), ISSN 0027-8424, URL https://www.pnas.org/content/115/38/9515.

[34] R. Scherwitzl, S. Gariglio, M. Gabay, P. Zubko, M. Gibert, and J.-M. Triscone, Phys. Rev. Lett. 106, 246403 (2011), URL https://link.aps.org/doi/10.1103/PhysRevLett.106.246403.

[35] S. Catalano, M. Gibert, V. Bisogni, F. He, R. Sutarto, M. Viret, P. Zubko, R. Scherwitzl, G. A. Sawatzky, T. Schmitt, et al., APL Materials 3, 062506 (2015), ISSN 2166-532X, URL http://scitation.aip.org/content/aip/journal/aplmater/3/6/10.1063/1.4919803.

[36] C. Domínguez, A. B. Georgescu, B. Mundet, Y. Zhang, J. Fowlie, A. Mercy, S. Catalano, D. T. L. Alexander, P. Ghosez, A. Georges, et al., *Length-scales of interfacial coupling between metal-insulator phases in oxides* (2019), 1910.06887.

[37] A. B. Georgescu, O. E. Peil, A. S. Disa, A. Georges, and A. J. Millis, Proceedings of the National Academy of Sciences 116, 14434 (2019), ISSN 0027-8424, URL https://www.pnas.org/content/116/29/14434.

[38] H. A. Jahn, E. Teller, and F. G. Donnan, Proceedings of the Royal Society of London. Series A - Mathematical and Physical Sciences 161, 220 (1937), URL https://royalsocietypublishing.org/doi/abs/10.1098/rspa.1937.0142.

[39] K. Yosida, *Theory of Magnetism* (Springer the language of Science, 1996), ISBN 3540606513, URL https://www.springer.com/gp/book/9783540606512.

[40] R. M. Martin, *Basic Theory and Practical Methods* (Cambridge University Press, 2004), ISBN 9780521782852.

[41] N. W. Ashcroft and N. D. Mermin, *Physique des solides* (EDP Sciences, 1976), ISBN 2868835775, URL https://laboutique.edpsciences.fr/produit/298/9782759801787/Physique%20des%20solides.

[42] E. Schrödinger, Phys. Rev. 28, 1049 (1926), URL https://link.aps.org/doi/10.1103/PhysRev.28.1049.

[43] X. Gonze, B. Amadon, P. M. Anglade, J. M. Beuken, F. Bottin, P. Boulanger, F. Bruneval, D. Caliste, R. Caracas, M. Côté, et al., Computer Physics Communications 180, 2582 (2009), ISSN 0010-4655, URL http://www.sciencedirect.com/science/article/pii/S0010465509002276.

[44] X. Gonze, J.-M. Beuken, R. Caracas, F. Detraux, M. Fuchs, G.-M. Rignanese, L. Sindic, M. Verstraete, G. Zerah, F. Jollet, et al., Computational Materials Science 25, 478 (2002), ISSN 0927-0256, URL http://www.sciencedirect.com/science/article/pii/S0927025602003257.

[45] X. Gonze, G. Rignanese, M. Verstraete, J. Betiken, Y. Pouillon, R. Caracas, F. Jollet, M. Torrent, G. Zerah, M. Mikami, et al., Zeitschrift fur Kristallographie.(Special issue on Computational Crystallography.) 220, 558 (2005), URL https://doi.org/10.1524/zkri.220.5.558.65066.

[46] M. Born and R. Oppenheimer, Annalen der Physik 389, 457 (1927), https://onlinelibrary.wiley.com/doi/pdf/10.1002/andp.19273892002, URL https://onlinelibrary.wiley.com/doi/abs/10.1002/andp.19273892002.

[47] P. Hohenberg and W. Kohn, Phys. Rev. 136, B864 (1964), URL http://link.aps.org/doi/10.1103/PhysRev.136.B864.

[48] W. Kohn and L. J. Sham, Physical Review 140, A1133 (1965), URL http://link.aps.org/doi/10.1103/PhysRev.140.A1133.

[49] V. Fock, Zeitschrift für Physik 61, 126 (1930), ISSN 0044-3328, URL https://doi.org/10.1007/BF01340294.

[50] R. O. Jones and O. Gunnarsson, Rev. Mod. Phys. 61, 689 (1989), URL https://link.aps.org/doi/10.1103/RevModPhys.61.689.

[51] D. M. Ceperley and B. J. Alder, Phys. Rev. Lett. 45, 566 (1980), URL https://link.aps.org/doi/10.1103/PhysRevLett.45.566.

[52] J. P. Perdew, K. Burke, and M. Ernzerhof, Physical Review Letters 77, 3865 (1996), URL http://link.aps.org/doi/10.1103/PhysRevLett.77.3865.

[53] D. R. Hartree, Mathematical Proceedings of the Cambridge Philosophical Society 24, 89–110 (1928).

[54] J. C. Slater, Phys. Rev. 32, 339 (1928), URL https://link.aps.org/doi/10.1103/PhysRev.32.339.

[55] A. D. Becke, The Journal of Chemical Physics 98, 1372 (1993), URL https://doi.org/10.1063/1.464304.

[56] H. J. Monkhorst and J. D. Pack, Phys. Rev. B 13, 5188 (1976), URL https://link.aps.org/doi/10.1103/PhysRevB.13.5188.

[57] P. E. Blöchl, Physical Review B 50, 17953 (1994), URL http://link.aps.org/doi/10.1103/PhysRevB.50.17953.

[58] M. Torrent (2012), URL https://pdfslide.net/documents/the-projector-augmented-wave-method-marc-torrent-francois-jollet-cea-bruyeres-le-chatel.html.

[59] J. Hubbard, Proc. R. Soc. Lond. A. 276 (1997), URL https://doi.org/10.1098/rspa.1963.0204.

[60] A. Georges, G. Kotliar, W. Krauth, and M. J. Rozenberg, Rev. Mod. Phys. 68, 13 (1996), URL https://link.aps.org/doi/10.1103/RevModPhys.68.13.

[61] M. Torrent, F. Jollet, F. Bottin, G. Zérah, and X. Gonze, Computational Materials Science 42, 337 (2008), ISSN 0927-0256, URL http://www.sciencedirect.com/science/article/pii/S0927025607002108.

[62] F. Jollet, M. Torrent, and N. Holzwarth, Computer Physics Communications 185, 1246 (2014), ISSN 0010-4655, URL http://www.sciencedirect.com/science/article/pii/S0010465513004359.

[63] X. Gonze (2004), URL www.abinit.org.

[64] J. Paier, R. Hirschl, M. Marsman, and G. Kresse, The Journal of Chemical Physics 122, 234102 (2005), ISSN 0021-9606, 1089-7690, URL http://scitation.aip.org/content/aip/journal/jcp/122/23/10.1063/1.1926272.

[65] G. H. Wannier, Phys. Rev. 52, 191 (1937), URL https://link.aps.org/doi/10.1103/PhysRev.52.191.

[66] A. G. Petukhov, I. I. Mazin, L. Chioncel, and A. I. Lichtenstein, Phys. Rev. B 67, 153106 (2003), URL https://link.aps.org/doi/10.1103/PhysRevB.67.153106.

[67] B. Amadon, F. Lechermann, A. Georges, F. Jollet, T. O. Wehling, and A. I. Lichtenstein, Phys. Rev. B 77, 205112 (2008), URL https://link.aps.org/doi/10.1103/PhysRevB.77.205112.

[68] A. I. Liechtenstein, V. I. Anisimov, and J. Zaanen, Phys. Rev. B 52, R5467 (1995), URL http://link.aps.org/doi/10.1103/PhysRevB.52.R5467.

[69] R. P. Feynman, Phys. Rev. 56, 340 (1939), URL https://link.aps.org/doi/10.1103/PhysRev.56.340.

[70] H. Hellmann, Deuticke, Leipzig (1937).

[71] C. G. Broyden, IMA Journal of Applied Mathematics 6, 76 (1970), ISSN 0272-4960, URL https://doi.org/10.1093/imamat/6.1.76.

[72] R. Fletcher, The Computer Journal 13, 317 (1970), ISSN 0010-4620, URL https://doi.org/10.1093/comjnl/13.3.317.

[73] D. Goldfarb, Math. Comp. 24, 23 (1970), URL https://doi.org/10.1090/S0025-5718-1970-0258249-6.

[74] D. F. Shanno, Mathematics of Computation 24, 647 (1970), ISSN 00255718, 10886842, URL http://www.jstor.org/stable/2004840.

[75] R. M. Pick, M. H. Cohen, and R. M. Martin, Phys. Rev. B 1, 910 (1970), URL https://link.aps.org/doi/10.1103/PhysRevB.1.910.

[76] S. Baroni, S. de Gironcoli, A. Dal Corso, and P. Giannozzi, Rev. Mod. Phys. 73, 515 (2001), URL https://link.aps.org/doi/10.1103/RevModPhys.73.515.

[77] X. Gonze, Phys. Rev. A 52, 1086 (1995), URL https://link.aps.org/doi/10.1103/PhysRevA.52.1086.

[78] X. Gonze, Phys. Rev. A 52, 1096 (1995), URL https://link.aps.org/doi/10.1103/PhysRevA.52.1096.

[79] X. Gonze and C. Lee, Phys. Rev. B 55, 10355 (1997), ISSN 0163-1829, 1095-3795, URL https://doi.org/10.1103/physrevb.55.10355.

[80] X. Gonze and J.-P. Vigneron, Phys. Rev. B 39, 13120 (1989), URL https://link.aps.org/doi/10.1103/PhysRevB.39.13120.

[81] M. Veithen, X. Gonze, and P. Ghosez, Phys. Rev. B 71, 125107 (2005), URL https://link.aps.org/doi/10.1103/PhysRevB.71.125107.

[82] A. Togo and I. Tanaka, Scr. Mater. 108, 1 (2015), URL https://atztogo.github.io/phonopy/.

[83] P. A. M. Dirac and N. H. D. Bohr, Proceedings of the Royal Society of London. Series A, Containing Papers of a Mathematical and Physical Character 114, 243 (1927), URL https://royalsocietypublishing.org/doi/abs/10.1098/rspa.1927.0039.

[84] S. Mazevet, J. Clérouin, V. Recoules, P. M. Anglade, and G. Zerah, Phys. Rev. Lett. 95, 085002 (2005), URL https://link.aps.org/doi/10.1103/PhysRevLett.95.085002.

[85] S. Mazevet, M. Torrent, V. Recoules, and F. Jollet, High Energy Density Physics 6, 84 (2010), URL http://www.sciencedirect.com/science/article/pii/S1574181809000664.

[86] J. Bieder and P. Ghosez, Under writing (2020).

[87] R. Kubo, Journal of the Physical Society of Japan 12, 570 (1957), URL https://doi.org/10.1143/JPSJ.12.570.

[88] D. A. Greenwood, Proceedings of the Physical Society 71, 585 (1958), URL https://doi.org/10.1088%2F0370-1328%2F71%2F4%2F306.

[89] L. Landau, Theory of phase transitions 1, 234 (1937).

[90] J. S. Smart, *Effective Field Theories of Magnetism* (W. B. AUNDERS COMPANY, Philadelphia et London, 1966), ISBN 6525648.

[91] J. Shi, S. D. Ha, Y. Zhou, F. Schoofs, and S. Ramanathan, Nature Communications 4, 2676 (2013), ISSN 2041-1723, URL http://www.nature.com/ncomms/2013/131031/ncomms3676/full/ncomms3676.html.

[92] Y. Zhou, X. Guan, H. Zhou, K. Ramadoss, S. Adam, H. Liu, S. Lee, J. Shi, M. Tsuchiya, D. D. Fong, et al., Nature 534, 231 (2016), ISSN 0028-0836, URL http://www.nature.com/nature/journal/v534/n7606/full/nature17653.html.

[93] M. Först, A. D. Caviglia, R. Scherwitzl, R. Mankowsky, P. Zubko, V. Khanna, H. Bromberger, S. B. Wilkins, Y.-D. Chuang, W. S. Lee, et al., Nature Materials 14, 883 (2015), ISSN 1476-1122, URL http://www.nature.com/nmat/journal/v14/n9/abs/nmat4341.html.

[94] T. H. Kim, D. Puggioni, Y. Yuan, L. Xie, H. Zhou, N. Campbell, P. J. Ryan, Y. Choi, J.-W. Kim, J. R. Patzner, et al., Nature 533, 68 (2016), ISSN 0028-0836, URL http://www.nature.com/nature/journal/v533/n7601/full/nature17628.html.

[95] M. N. Grisolia, J. Varignon, G. Sanchez-Santolino, A. Arora, S. Valencia, M. Varela, R. Abrudan, E. Weschke, E. Schierle, J. E. Rault, et al., Nature Physics 12, 484 (2016), ISSN 1745-2473, URL http://www.nature.com/nphys/journal/v12/n5/full/nphys3627.html.

[96] N. A. Benedek and C. J. Fennie, The Journal of Physical Chemistry C 117, 13339 (2013), URL http://dx.doi.org/10.1021/jp402046t.

[97] J. A. Alonso, J. L. García-Muñoz, M. T. Fernández-Díaz, M. A. G. Aranda, M. J. Martínez-Lope, and M. T. Casais, Physical Review Letters 82, 3871 (1999), URL http://link.aps.org/doi/10.1103/PhysRevLett.82.3871.

[98] J. L. García-Muñoz, J. Rodríguez-Carvajal, and P. Lacorre, Physical Review B 50, 978 (1994), URL http://link.aps.org/doi/10.1103/PhysRevB.50.978.

[99] J. B. Torrance, P. Lacorre, A. I. Nazzal, E. J. Ansaldo, and C. Niedermayer, Physical Review B 45, 8209 (1992), URL http://link.aps.org/doi/10.1103/PhysRevB.45.8209.

[100] T. Mizokawa, D. I. Khomskii, and G. A. Sawatzky, Physical Review B 61, 11263 (2000), URL http://link.aps.org/doi/10.1103/PhysRevB.61.11263.

[101] H. Raebiger, S. Lany, and A. Zunger, Nature 453, 763 (2008), ISSN 0028-0836, URL http://www.nature.com/nature/journal/v453/n7196/full/nature07009.html.

[102] J. Ruppen, J. Teyssier, O. E. Peil, S. Catalano, M. Gibert, J. Mravlje, J.-M. Triscone, A. Georges, and D. van der Marel, Physical Review B 92, 155145 (2015), URL http://link.aps.org/doi/10.1103/PhysRevB.92.155145.

[103] J. Varignon, M. N. Grisolia, J. Iniguez, A. Barthélémy, and M. Bibes, npj Quantum Materials 2, 21 (2017), URL https://www.nature.com/articles/s41535-017-0024-9.

[104] I. I. Mazin, D. I. Khomskii, R. Lengsdorf, J. A. Alonso, W. G. Marshall, R. M. Ibberson, A. Podlesnyak, M. J. Martínez-Lope, and M. M. Abd-Elmeguid, Physical Review Letters 98, 176406 (2007), URL http://link.aps.org/doi/10.1103/PhysRevLett.98.176406.

[105] S. Johnston, A. Mukherjee, I. Elfimov, M. Berciu, and G. A. Sawatzky, Physical Review Letters 112, 106404 (2014), URL http://link.aps.org/doi/10.1103/PhysRevLett.112.106404.

[106] V. Bisogni, S. Catalano, R. J. Green, M. Gibert, R. Scherwitzl, Y. Huang, V. N. Strocov, P. Zubko, S. Balandeh, J.-M. Triscone, et al., Nature Communications 7, 13017 (2016), ISSN 2041-1723, URL http://arxiv.org/abs/1607.06758.

[107] F. P. de la Cruz, C. Piamonteze, N. E. Massa, H. Salva, J. A. Alonso, M. J. Martínez-Lope, and M. T. Casais, Physical Review B 66, 153104 (2002), URL http://link.aps.org/doi/10.1103/PhysRevB.66.153104.

[108] P. V. Balachandran and J. M. Rondinelli, Physical Review B 88, 054101 (2013), URL http://link.aps.org/doi/10.1103/PhysRevB.88.054101.

[109] J. Holakovský, physica status solidi (b) 56, 615 (1973), URL https://onlinelibrary.wiley.com/doi/abs/10.1002/pssb.2220560224.

[110] I. N. Flerov, M. V. Gorev, V. N. Voronov, A. Tressaud, and J. Grannec, J. Solid State Chem. 3, 582 (1971).

[111] M. Iwata, C. H. Zhao, R. Aoyagi, M. Maeda, and Y. Ishibashi, Japonese Journal of Applied Physics 46, 5894 (2007), URL https://doi.org/10.1143%2Fjjap.46.5894.

[112] I. Vobornik, L. Perfetti, M. Zacchigna, M. Grioni, G. Margaritondo, J. Mesot, M. Medarde, and P. Lacorre, Phys. Rev. B 60, R8426 (1999), URL http://link.aps.org/doi/10.1103/PhysRevB.60.R8426.

[113] T. Akao, Y. Azuma, M. Usuda, Y. Nishihata, J. Mizuki, N. Hamada, N. Hayashi, T. Terashima, and M. Takano, Phys. Rev. Lett. 91, 156405 (2003), URL http://link.aps.org/doi/10.1103/PhysRevLett.91.156405.

[114] A. I. Liechtenstein, I. I. Mazin, C. O. Rodriguez, O. Jepsen, O. K. Andersen, and M. Methfessel, Phys. Rev. B 44, 5388 (1991), URL https://link.aps.org/doi/10.1103/PhysRevB.44.5388.

[115] J. P. Perdew, A. Ruzsinszky, G. I. Csonka, O. A. Vydrov, G. E. Scuseria, L. A. Constantin, X. Zhou, and K. Burke, Phys. Rev. Lett. 100, 136406 (2008), URL http://link.aps.org/doi/10.1103/PhysRevLett.100.136406.

[116] N. Benedek (1990), URL http://www.me.utexas.edu/~benedekgroup/ToleranceFactorCalculator/#home.

[117] M. W. Lufaso and P. M. Woodward, Acta Crystallogr. B 57, 725 (2001), URL https://doi.org/10.1107/S0108768101015282.

[118] D. Orobengoa, C. Capillas, M. I. Aroyo, and J. M. Perez-Mato, Journal of Applied Crystallography 42, 820 (2009), URL https://doi.org/10.1107/S0021889809028064.

[119] J. M. Perez-Mato, D. Orobengoa, and M. I. Aroyo, Acta Crystallographica Section A 66, 558 (2010), URL https://doi.org/10.1107/S0108767310016247.

[120] J. A. Alonso, M. J. Martínez-Lope, M. T. Casais, J. L. García-Muñoz, M. T. Fernández-Díaz, and M. A. G. Aranda, Physical Review B 64 (2001), ISSN 0163-1829, 1095-3795, URL http://link.aps.org/doi/10.1103/PhysRevB.64.094102.

[121] C. Girardot, J. Kreisel, S. Pignard, N. Caillault, and F. Weiss, Phys. Rev. B 78, 104101 (2008), URL https://link.aps.org/doi/10.1103/PhysRevB.78.104101.

[122] M. Imada, A. Fujimori, and Y. Tokura, Rev. Mod. Phys. 70, 1039 (1998), URL https://link.aps.org/doi/10.1103/RevModPhys.70.1039.

[123] P. Zubko, S. Gariglio, M. Gabay, P. Ghosez, and J.-M. Triscone, Annu. Rev. Conden. Ma. P. 2, 141 (2011), URL https://doi.org/10.1146/annurev-conmatphys-062910-140445.

[124] Y. Yuan, Y. Lu, G. Stone, K. Wang, C. M. Brooks, D. G. Schlom, S. B. Sinnott, H. Zhou, and V. Gopalan, Nature Communications 9, 5220 (2018), URL https://doi.org/10.1038/s41467-018-07665-1.

[125] S. R. Barman, A. Chainani, and D. D. Sarma, Phys. Rev. B 49, 8475 (1994), URL https://link.aps.org/doi/10.1103/PhysRevB.49.8475.

[126] S. Catalano, M. Gibert, J. Fowlie, J. Íñiguez, J.-M. Triscone, and J. Kreisel, Reports on Progress in Physics 81, 046501 (2018), URL https://doi.org/10.1088%2F1361-6633%2Faaa37a.

[127] P. Seth, O. E. Peil, L. Pourovskii, M. Betzinger, C. Friedrich, O. Parcollet, S. Biermann, F. Aryasetiawan, and A. Georges, Phys. Rev. B 96, 205139 (2017), URL https://link.aps.org/doi/10.1103/PhysRevB.96.205139.

[128] A. Subedi, O. E. Peil, and A. Georges, Physical Review B 91, 075128 (2015), URL http://link.aps.org/doi/10.1103/PhysRevB.91.075128.

[129] M. K. Stewart, J. Liu, M. Kareev, J. Chakhalian, and D. N. Basov, Phys. Rev. Lett. 107, 176401 (2011), URL https://link.aps.org/doi/10.1103/PhysRevLett.107.176401.

[130] B. Torriss, J. Margot, and M. Chaker, Scientific Reports 7, 40915 (2017), URL https://doi.org/10.1038/srep40915.

[131] X. Gonze, B. Amadon, G. Antonius, F. Arnardi, L. Baguet, J.-M. Beuken, J. Bieder, F. Bottin, J. Bouchet, E. Bousquet, et al., Computer Physics Communications 248, 107042 (2020), ISSN 0010-4655, URL http://www.sciencedirect.com/science/article/pii/S0010465519303741.

[132] J. Rodríguez-Carvajal, S. Rosenkranz, M. Medarde, P. Lacorre, M. T. Fernandez-Díaz, F. Fauth, and V. Trounov, Phys. Rev. B 57, 456 (1998), URL https://link.aps.org/doi/10.1103/PhysRevB.57.456.

[133] J. Perez-Mato, S. Gallego, L. Elcoro, E. Tasci, and M. Aroyo, Journal of Physics Condensed Matter 28, 286001 (2016), ISSN 09538984.

[134] J. Karpinski, E. Kaldis, K. Conder, S. Rusiecki, and E. Jilek, in *Gas Pressure Effects on Materials processing and design* (1992), vol. 251 of *MRS Symposium Proceedings*, pp. 291–305, ISBN 1-55899-145-X.

[135] J. Karpinski, Philosophycal Magazine 92, 2662 (2012), ISSN 1478-6435.

[136] J. Prakash, C. K. Blakely, and V. V. Poltavets, SOLID STATE SCIENCES 17, 72 (2013), ISSN 1293-2558.

[137] P. Fischer, G. Frey, M. Koch, M. Koennecke, V. Pomjakushin, J. Schefer, R. Thut, N. Schlumpf, R. Buerge, U. Greuter, et al., Journal of synchrotron radiation 20, 667 (2013).

[138] J. Schefer, P. Fischer, H. Heer, M. Koch, and R. Thut, Nuclear Instruments and Methods in Physics Research Section A: Accelerators, Spectrometers, Detectors and Associared Equipment 288, 477 (1990).

[139] J. J. Rodríguez-Carvajal, Physica B: Physics of Condensed Matter 192, 55 (1993).

[140] J. P. Brown, *International Tables for Crystallography* (International Union of Crystallography, 2006), vol. C: Mathematical, Physical and Chemical Tables, Section 4.4.5 (Magnetic Form Factors), pp. 454–461, ISBN 978-1-4020-1900-5, URL https://it.iucr.org/Cb/ch4o4v0001/sec4o4o5/.

[141] A. M. Glazer, Acta Crystallographica Section B Structural Crystallography and Crystal Chemistry 28, 3384 (1972), ISSN 05677408, URL http://scripts.iucr.org/cgi-bin/paper?S0567740872007976.

[142] J. Varignon, M. N. Grisolia, J. Iñiguez, A. Barthélémy, and M. Bibes, npj Quantum Materials 2, 21 (2017), ISSN 2397-4648, URL https://doi.org/10.1038/s41535-017-0024-9.

[143] T. Kimura, S. Ishihara, H. Shintani, T. Arima, K. T. Takahashi, K. Ishizaka, and Y. Tokura, Phys. Rev. B 68, 060403 (2003), URL http://link.aps.org/doi/10.1103/PhysRevB.68.060403.

[144] M. C. Sánchez, G. Subías, J. García, and J. Blasco, Phys. Rev. Lett. 90, 045503 (2003), URL http://link.aps.org/doi/10.1103/PhysRevLett.90.045503.

[145] J. B. MacChesney, R. C. Sherwood, and J. F. Potter, J. Chem. Phys. 43, 1907 (1965), URL http://scitation.aip.org/content/aip/journal/jcp/43/6/10.1063/1.1697052.

[146] N. Hayashi, T. Yamamoto, H. Kageyama, M. Nishi, Y. Watanabe, T. Kawakami, Y. Matsushita, A. Fujimori, and M. Takano, Angew. Chem. Int. Edit. 50, 12547 (2011), URL http://dx.doi.org/10.1002/anie.20110527.

[147] S. Kawasaki, M. Takano, R. Kanno, T. Takeda, and A. Fujimori, J. Phys. Soc. Jpn. 67, 1529 (1998), URL https://doi.org/10.1143/JPSJ.67.1529.

[148] P. M. Woodward, D. E. Cox, E. Moshopoulou, A. W. Sleight, and S. Morimoto, Phys. Rev. B 62, 844 (2000), URL http://link.aps.org/doi/10.1103/PhysRevB.62.844.

[149] J. Matsuno, T. Mizokawa, A. Fujimori, Y. Takeda, S. Kawasaki, and M. Takano, Phys. Rev. B 66, 193103 (2002), URL https://link.aps.org/doi/10.1103/PhysRevB.66.193103.

[150] S. Ghosh, N. Kamaraju, M. Seto, A. Fujimori, Y. Takeda, S. Ishiwata, S. Kawasaki, M. Azuma, M. Takano, and A. K. Sood, Phys. Rev. B 71, 245110 (2005), URL https://link.aps.org/doi/10.1103/PhysRevB.71.245110.

[151] A. Cammarata and J. M. Rondinelli, Phys. Rev. B 86, 195144 (2012), URL https://link.aps.org/doi/10.1103/PhysRevB.86.195144.

[152] P. C. Rogge, R. U. Chandrasena, A. Cammarata, R. J. Green, P. Shafer, B. M. Lefler, A. Huon, A. Arab, E. Arenholz, H. N. Lee, et al., Phys. Rev. Materials 2, 015002 (2018), URL https://link.aps.org/doi/10.1103/PhysRevMaterials.2.015002.

[153] G. Kresse and J. Hafner, Phys. Rev. B 47, 558 (1993), URL https://link.aps.org/doi/10.1103/PhysRevB.47.558.

[154] V. I. Anisimov, F. Aryasetiawan, and A. I. Lichtenstein, J. Phys.: Condens. Matter 9, 767 (1997), URL http://stacks.iop.org/0953-8984/9/i=4/a=002.

[155] T. Arima, Y. Tokura, and J. B. Torrance, Physical Review B 48, 17006 (1993), URL http://link.aps.org/doi/10.1103/PhysRevB.48.17006.

[156] B. J. Campbell, H. T. Stokes, D. E. Tanner, and D. M. Hatch, J. Appl. Crystallogr. 39, 607 (2006), URL http://dx.doi.org/10.1107/S0021889806014075.

[157] T. Takeda, R. Kanno, Y. Kawamoto, M. Takano, S. Kawasaki, T. Kamiyama, and F. Izumi, Solid State Sci. 2, 673 (2000), ISSN 1293-2558, URL http://www.sciencedirect.com/science/article/pii/S1293255800010888.

[158] M.-H. Whangbo, H.-J. Koo, A. Villesuzanne, and M. Pouchard, Inorg. Chem. 41, 1920 (2002), pMID: 11925189, URL https://doi.org/10.1021/ic0110427.

[159] J. Varignon, N. C. Bristowe, E. Bousquet, and P. Ghosez, Sci. Rep. 5, 15364 (2015), ISSN 2045-2322, URL http://www.ncbi.nlm.nih.gov/pmc/articles/PMC4612717/.

[160] M. A. Carpenter and C. J. Howard, Acta Crystallogr. B. 65, 134 (2009), URL https://doi.org/10.1107/S0108768109000974.

[161] W.-G. Yin, D. Volja, and W. Ku, Phys. Rev. Lett. 96, 116405 (2006), URL http://link.aps.org/doi/10.1103/PhysRevLett.96.116405.

[162] Z. He and A. J. Millis, Phys. Rev. B 91, 195138 (2015), URL https://link.aps.org/doi/10.1103/PhysRevB.91.195138.

[163] K. J. Choi, M. Biegalski, Y. L. Li, A. Sharan, J. Schubert, R. Uecker, P. Reiche, Y. B. Chen, X. Q. Pan, V. Gopalan, et al., Science 306, 1005 (2004), ISSN 0036-8075, URL https://science.sciencemag.org/content/306/5698/1005.

[164] G. Logvenov, A. Gozar, and I. Bozovic, Science 326, 699 (2009), ISSN 0036-8075, URL https://science.sciencemag.org/content/326/5953/699.

[165] A. V. Boris, Y. Matiks, E. Benckiser, A. Frano, P. Popovich, V. Hinkov, P. Wochner, M. Castro-Colin, E. Detemple, V. K. Malik, et al., Science 332, 937 (2011), ISSN 0036-8075, URL https://science.sciencemag.org/content/332/6032/937.

[166] A. K. Yadav, C. T. Nelson, S. L. Hsu, Z. Hong, J. D. Clarkson, C. M. Schlepütz, A. R. Damodaran, P. Shafer, E. Arenholz, L. R. Dedon, et al., Nature 530, 198 (2016), URL https://doi.org/10.1038/nature16463.

[167] J. Chakhalian, J. W. Freeland, H.-U. Habermeier, G. Cristiani, G. Khaliullin, M. van Veenendaal, and B. Keimer, Science 318, 1114 (2007), ISSN 0036-8075, URL https://science.sciencemag.org/content/318/5853/1114.

[168] E. Pavarini, S. Biermann, A. Poteryaev, A. I. Lichtenstein, A. Georges, and O. K. Andersen, Phys. Rev. Lett. 92, 176403 (2004), URL https://link.aps.org/doi/10.1103/PhysRevLett.92.176403.

[169] J.-S. Zhou and J. B. Goodenough, Phys. Rev. B 68, 144406 (2003), URL https://link.aps.org/doi/10.1103/PhysRevB.68.144406.

[170] P. D. C. King, H. I. Wei, Y. F. Nie, M. Uchida, C. Adamo, S. Zhu, X. He, I. Bozovic, D. G. Schlom, and K. M. Shen, Nature Nanotechnology 9, 443 (2014), URL https://doi.org/10.1038/NNANO.2014.59.

[171] J. c. v. Chaloupka and G. Khaliullin, Phys. Rev. Lett. 100, 016404 (2008), URL https://link.aps.org/doi/10.1103/PhysRevLett.100.016404.

[172] J.-S. Zhou, J. B. Goodenough, and B. Dabrowski, Phys. Rev. Lett. 95, 127204 (2005), URL https://link.aps.org/doi/10.1103/PhysRevLett.95.127204.

[173] Z. Y. Shi J and R. S, Nature Communications 5, 4860 (2014), URL https://www.nature.com/articles/ncomms5860.

[174] J. M. Rondinelli, S. J. May, and J. W. Freeland, MRS Bulletin 37, 261–270 (2012), URL https://doi.org/10.1557/mrs.2012.49.

[175] Z. Liao, M. Huijben, Z. Zhong, N. Gauquelin, S. Macke, R. Green, S. van Aert, J. Verbeeck, G. van Tendeloo, K. Held, et al., Nature materials 15, 425 (2016), ISSN 1476-1122, URL https://doi.org/10.1038/nmat4579.

[176] S. J. May, J.-W. Kim, J. M. Rondinelli, E. Karapetrova, N. A. Spaldin, A. Bhattacharya, and P. J. Ryan, Phys. Rev. B 82, 014110 (2010), URL https://link.aps.org/doi/10.1103/PhysRevB.82.014110.

[177] A. Vailionis, H. Boschker, W. Siemons, E. P. Houwman, D. H. A. Blank, G. Rijnders, and G. Koster, Phys. Rev. B 83, 064101 (2011), URL https://link.aps.org/doi/10.1103/PhysRevB.83.064101.

[178] S. Amisi, E. Bousquet, K. Katcho, and P. Ghosez, Phys. Rev. B 85, 064112 (2012), URL https://link.aps.org/doi/10.1103/PhysRevB.85.064112.

[179] N. Miao, N. C. Bristowe, B. Xu, M. J. Verstraete, and P. Ghosez, Journal of Physics: Condensed Matter 26, 035401 (2013), URL https://doi.org/10.1088%2F0953-8984%2F26%2F3%2F035401.

[180] J. W. Freeland, M. van Veenendaal, and J. Chakhalian, Journal of Electron Spectroscopy and Related Phenomena 208, 56 (2016), ISSN 0368-2048, special Issue: Electronic structure and function from state-of-the-art spectroscopy and theory, URL http://www.sciencedirect.com/science/article/pii/S0368204815001516.

[181] R. J. Green, M. W. Haverkort, and G. A. Sawatzky, Phys. Rev. B 94, 195127 (2016), URL https://link.aps.org/doi/10.1103/PhysRevB.94.195127.

[182] J. Liu, M. Kargarian, M. Kareev, B. Gray, P. Ryan, A. Cruz, N. Tahir, Y. Chuang, J. Guo, J. Rondinelli, et al., Nature Communications 4 (2013), ISSN 2041-1723, URL https://doi.org/10.1038/ncomms3714.

[183] D. G. Hawthorn, F. He, L. Venema, H. Davis, A. J. Achkar, J. Zhang, R. Sutarto, H. Wadati, A. Radi, T. Wilson, et al., Review of Scientific Instruments 82, 073104 (2011), URL https://doi.org/10.1063/1.3607438.

[184] D. Lee, B. Chung, Y. Shi, G.-Y. Kim, N. Campbell, F. Xue, K. Song, S.-Y. Choi, J. P. Podkaminer, T. H. Kim, et al., Science 362, 1037 (2018), ISSN 0036-8075, URL https://science.sciencemag.org/content/362/6418/1037.

[185] C. Cen, S. Thiel, G. Hammerl, C. W. Schneider, K. E. Andersen, C. S. Hellber, J. Mannhart, and J. Levy, Nature Materials 7, 298 (2008), URL https://doi.org/10.1038/nmat2136.

[186] S. Thiel, G. Hammerl, A. Schmehl, C. W. Schneider, and J. Mannhart, Science 313, 1942 (2006), ISSN 0036-8075, URL https://science.sciencemag.org/content/313/5795/1942.

[187] G. Mattoni, P. Zubko, F. Maccherozzi, A. van der Torren, D. B. Boltje, M. Hadjimichael, N. Manca, S. Catalano, M. Gibert, Y. Liu, et al., Nature Communications 7 (2016), URL https://www.nature.com/articles/ncomms13141#supplementary-information.

[188] K. W. Post, A. S. McLeod, M. Hepting, M. Bluschke, Y. Wang, G. Cristiani, G. Logvenov, A. Charnukha, G. X. Ni, P. Radhakrishnan, et al., Nature Physics 14 (2018), URL https://doi.org/10.1038/s41567-018-0201-1.

[189] P. Lacorre, J. Torrance, J. Pannetier, A. Nazzal, P. Wang, and T. Huang, Journal of Solid State Chemistry 91, 225 (1991), ISSN 0022-4596, URL http://www.sciencedirect.com/science/article/pii/002245969190077U.

[190] R. Scherwitzl, P. Zubko, I. G. Lezama, S. Ono, A. F. Morpurgo, G. Catalan, and J.-M. Triscone, Advanced Materials 22, 5517 (2010), URL https://onlinelibrary.wiley.com/doi/abs/10.1002/adma.201003241.

[191] S. J. May, C. R. Smith, J.-W. Kim, E. Karapetrova, A. Bhattacharya, and P. J. Ryan, Phys. Rev. B 83, 153411 (2011), URL https://link.aps.org/doi/10.1103/PhysRevB.83.153411.

[192] J. Rondinelli and N. Spaldin, Advanced Materials 23, 3363 (2011), ISSN 0935-9648, URL https://doi.org/10.1002/adma.201101152.

[193] J. Chakhalian, A. J. Millis, and J. Rondinelli, Nature Materials 11 (2012), URL https://doi.org/10.1038/nmat3225.

[194] E. J. Moon, R. Colby, Q. Wang, E. Karapetrova, C. M. Schlepütz, M. R. Fitzsimmons, and S. J. May, Nature Communications 5 (2014), URL https://doi.org/10.1038/ncomms6710.

[195] R. Aso, D. Kan, Y. Shimakawa, and H. Kurata, Scientific Reports 3, 2214 (2013), URL https://doi.org/10.1038/srep02214.

[196] J. Y. Zhang, J. Hwang, S. Raghavan, and S. Stemmer, Phys. Rev. Lett. 110, 256401 (2013), URL https://link.aps.org/doi/10.1103/PhysRevLett.110.256401.

[197] G. Catalan, R. M. Bowman, and J. M. Gregg, Phys. Rev. B 62, 7892 (2000), URL https://link.aps.org/doi/10.1103/PhysRevB.62.7892.

[198] L. Jones, H. Yang, T. J. Pennycook, M. S. J. Marshall, S. Van Aert, N. D. Browning, M. R. Castell, and P. D. Nellist, Advanced Structural and Chemical Imaging 1, 8 (2015), URL https://doi.org/10.1186/s40679-015-0008-4.

[199] M. Nord, P. E. Vullum, I. MacLaren, T. Tybell, and R. Holmestad, Advanced Structural and Chemical Imaging 3, 9 (2017), URL https://doi.org/10.1186/s40679-017-0042-5.

[200] M. Bosman, M. Watanabe, D. Alexander, and V. Keast, Ultramicroscopy 106, 1024 (2006), ISSN 0304-3991, proceedings of the International Workshop on Enhanced Data Generated by Electrons, URL http://www.sciencedirect.com/science/article/pii/S0304399106001021.

[201] G. Lucas, P. Burdet, M. Cantoni, and C. Hébert, Micron 52-53, 49 (2013), ISSN 0968-4328, URL http://www.sciencedirect.com/science/article/pii/S0968432813001261.

[202] G. Kresse and J. Furthmüller, Comput. Mater. Sci. 6, 15 (1996), ISSN 0927-0256, URL http://www.sciencedirect.com/science/article/pii/0927025696000080.

[203] G. Kresse and J. Furthmüller, Phys. Rev. B 54, 11169 (1996), URL https://link.aps.org/doi/10.1103/PhysRevB.54.11169.

[204] G. Kresse and D. Joubert, Phys. Rev. B 59, 1758 (1999), URL https://link.aps.org/doi/10.1103/PhysRevB.59.1758.

[205] J. Varignon, M. N. Grisolia, D. Preziosi, P. Ghosez, and M. Bibes, Phys. Rev. B 96, 235106 (2017), URL https://link.aps.org/doi/10.1103/PhysRevB.96.235106.

[206] C. Loschen, J. Carrasco, K. M. Neyman, and F. Illas, Phys. Rev. B 75, 035115 (2007), URL https://link.aps.org/doi/10.1103/PhysRevB.75.035115.

[207] S. L. Dudarev, G. A. Botton, S. Y. Savrasov, C. J. Humphreys, and A. P. Sutton, Phys. Rev. B 57, 1505 (1998), URL https://link.aps.org/doi/10.1103/PhysRevB.57.1505.

[208] K. Momma and F. Izumi, Journal of Applied Crystallography 41, 653 (2008), URL https://doi.org/10.1107/S0021889808012016.

[209] J. C. Wojdeł, P. Hermet, M. P. Ljungberg, P. Ghosez, and J. Íñiguez, Journal of Physics: Condensed Matter 25, 305401 (2013), URL http://stacks.iop.org/0953-8984/25/i=30/a=305401.

[210] S. Prosandeev, L. Bellaiche, and J. Íñiguez, Physical Review B 85, 214431 (2012), URL http://link.aps.org/doi/10.1103/PhysRevB.85.214431.

[211] A. Muñoz, J. A. Alonso, M. J. Martinez-Lope, and M. T. Fernandez-Diaz, Journal of Solid State Chemistry 182, 1982 (2009), ISSN 0022-4596, URL http://www.sciencedirect.com/science/article/pii/S0022459609002242.

[212] J. Perez-Cacho, J. Blasco, J. Garcia, M. Castro, and J. Stankiewicz, J. Phys.: Condens. Matter 11, 405 (1999), URL https://doi.org/10.1088%2F0953-8984%2F11%2F2%2F007.

[213] I. Nikulina, M. Novojilova, A. Kaulb, A. Maiorovab, and M. S.N., Materials Research Bulletin 39, 803 (2004).

[214] J. Iniguez, S. Ivantchev, J. M. Perez-Mato, and A. Garcia, Phys. Rev. B 63, 144103 (2001), URL http://link.aps.org/doi/10.1103/PhysRevB.63.144103.

[215] W. Zhong, D. Vanderbilt, and K. M. Rabe, Phys. Rev. B 52, 6301 (1995), URL http://link.aps.org/doi/10.1103/PhysRevB.52.6301.

[216] H. T. Stokes and D. M. Hatch, Journal of Applied Crystallography 38, 237 (2005), URL https://doi.org/10.1107/S0021889804031528.

[217] V. Leca, D. H. A. Blank, and G. Rijnders, arXiv e-prints arXiv:1202.2256 (2012), URL https://arxiv.org/abs/1202.2256.

[218] A. D. Backer, K. van den Bos, W. V. den Broek, J. Sijbers, and S. V. Aert, Ultramicroscopy 171, 104 (2016), ISSN 0304-3991, URL http://www.sciencedirect.com/science/article/pii/S0304399116301747.

[219] K. Müller-Caspary, T. Mehrtens, M. Schowalter, T. Grieb, A. Rosenauer, F. F. Krause, C. Mahr, and P. Potapov, *ImageEval. A software for the processing, evaluation and acquisition of (S)TEM images* (American Cancer Society, 2016), pp. 481–482, ISBN 9783527808465, URL https://onlinelibrary.wiley.com/doi/abs/10.1002/9783527808465.EMC2016.6143.

[220] A. den Dekker, S. V. Aert, A. van den Bos, and D. V. Dyck, Ultramicroscopy 104, 83 (2005), ISSN 0304-3991, URL http://www.sciencedirect.com/science/article/pii/S030439910500046X.

[221] S. V. Aert, A. den Dekker, A. van den Bos, D. V. Dyck, and J. Chen, Ultramicroscopy 104, 107 (2005), ISSN 0304-3991, URL http://www.sciencedirect.com/science/article/pii/S0304399105000471.

[222] N. Gauquelin, K. van den Bos, A. Béché, F. Krause, I. Lobato, S. Lazar, A. Rosenauer, S. V. Aert, and J. Verbeeck, Ultramicroscopy 181, 178 (2017), ISSN 0304-3991, URL http://www.sciencedirect.com/science/article/pii/S0304399117301262.

[223] M. Abbate, G. Zampieri, J. Okamoto, A. Fujimori, S. Kawasaki, and M. Takano, Phys. Rev. B 65, 165120 (2002), URL https://link.aps.org/doi/10.1103/PhysRevB.65.165120.

[224] S. Middey, P. Rivero, D. Meyers, M. Kareev, X. Liu, Y. Cao, J. W. Freeland, S. Barraza-Lopez, and J. Chakhalian, Scientific Reports 4, 6819 (2014), URL https://doi.org/10.1038/srep06819.

[225] M. Medarde, A. Fontaine, J. L. Garcia-Munoz, J. Rodriguez-Carvajal, M. de Santis, M. Sacchi, G. Rossi, and P. Lacorre, Phys. Rev. B 46, 14975 (1992), URL https://link.aps.org/doi/10.1103/PhysRevB.46.14975.

[226] W. T. Vetterling, S. A. Teukolsky, B. P. Flannery, and W. H. Press, *Numerical Recipes Example Book C++* (Cambridge University Press, New York, NY, USA, 2002), 2nd ed., ISBN 0521750342.

List of Tables

List of Figures

Contents